EXPLORING INTERFACIAL AND NANOSCALE ELECTRICAL EFFECTS IN SOLID STATE IONIC CONDUCTORS FOR APPLICATION IN LOW TEMPERATURE SOLID OXIDE FUEL CELLS AND SOLID STATE BATTERIES

A Dissertation
Presented to
The Academic Faculty

by

Benjamin Harris Rainwater

In Partial Fulfillment
Of the Requirements for the Degree
Doctorate of Philosophy in the
School of Materials Science and Engineering

Georgia Institute of Technology
May 2016

EXPLORING INTERFACIAL AND NANOSCALE ELECTRICAL EFFECTS IN SOLID STATE IONIC CONDUCTORS FOR APPLICATION IN LOW TEMPERATURE SOLID OXIDE FUEL CELLS AND SOLID STATE BATTERIES

Approved by:

Dr. Meilin Liu, Advisor
School of Materials Science and Engineering
Georgia Institute of Technology

Dr. Eric Vogel
School of Materials Science and Engineering
Georgia Institute of Technology

Dr. Matthew McDowell
School of Materials Science and Engineering
Woodruff School of Mechanical Engineering
Georgia Institute of Technology

Dr. Angus Wilkinson
School of Chemistry and Biochemistry
Georgia Institute of Technology

Dr. Mark Losego
School of Materials Science and Engineering
Georgia Institute of Technology

Date Approved: March 8, 2014

To Ralph and Henry

ACKNOWLEDGEMENTS

I would like to thank Dr. Meilin Liu for his guidance in all the work included in this dissertation. He has fostered a rich research environment in his laboratory at Georgia Tech and I am very thankful for the opportunity to have worked under his direction. I would also like to thank several mentors that supported my work in many ways. Their experience in research was invaluable to me as I planned experiments, collected data, and analyzed the results. Dr. Nenad Velisavljevic of Los Alamos National Lab greatly encouraged and supported my high pressure sciences work, joined me at Argonne National Lab for my experiments and helped to guide me into new areas of research. His mentorship greatly expanded my understanding of the technical and non-technical components of research. Dr. Changyong Park at Argonne National Lab APS HPCAT has been a diligent proponent of my work and a great encouragement to try new experimental techniques. I am greatly appreciative for Dr. Yogesh Vohra and Dr. Georgiy Tsoi of the University of Alabama Birmingham who provided high pressure experiment resources and helped me measure several samples in their lab. I am thankful for the research assistance provided by Dr. Chris Rouleau, Dr. Karren More, and Dr. Jong Keum of Oak Ridge National Lab which made the work of Chapter 4 possible. Dr. Yong Ding of Georgia Tech provided invaluable microscopy data and analysis useful for the nanoionics work. I wish to thank Dr. Saiful Islam and Dr. Benjamin Morgan from the University of Bath, UK for the computer calculation and simulation support.

I would like to give a special thanks to the group members of Dr. Liu's lab at Georgia Tech. Dr. Gordon Waller was involved in every step of the research presented in

this dissertation. His discussion and suggestions provided constructive criticism for my experimental work and interpretation of the data. Haibin Sun helped greatly with sample preparation and data collection for the experiments presented in Chapter 3. Jilai Ding provided important cleanroom assistance for electrical measurement of the thin film samples. Lei Zhang provided fruitful discussion of the fundamental concepts of the studied phenomena and computational support for the work.

I would like to thank my parents and siblings for their constant listening ear and their practical advice.

My wife, Abigail, joined me in the middle of this work and I am thankful for her love, constant support and encouragement in this endeavor.

I would like to thank the National Science Foundation for their generous support. The research was supported by the National Science Foundation Graduate Research Fellowship under Grant No. DGE-1148903.

Ben Rainwater
March 2016, Atlanta, GA, USA

TABLE OF CONTENTS

LIST OF TABLES

LIST OF FIGURES

LIST OF ABBREVIATIONS

AFC	Alkaline fuel cell
AFM	Atomic force microscopy
BF-STEM	Bright-field scanning transmission electron microscope
BOP	Balance of plant
BZCY	$BaZr_{1-x-y}Ce_xY_y O_3$
BZCYYb	$BaZr_{0.1}Ce_{0.7} Y_{0.1}Yb_{0.1}O_3$
BZY15	$BaZr_{0.85}Y_{0.15}O_3$
CHP	Combined heat and power
CNMS	Center for Nanophase Materials Science
CPE	Constant Phase Element
CVD	Combustion vapor deposition
DAC	Diamond anvil cell
DDAC	Designer diamond anvil cell (electrode equipped DAC)
DFT	Density Functional Theory
DG	Distributed generation
EDS	Energy-dispersive X-ray spectroscopy
EELS	Electron energy loss spectroscopy
EIA	Energy Information Agency
EMF	Electromotive force
FFT	Fast Fourier Transformation
FRA	Frequency Response Analyzer
FWHM	Full width half maximum
GDC20	$Gd_{0.2}Ce_{0.8}O_{1.9}$
HAADF	High-angle annular dark field
HPCAT	High Pressure Collaborative Access Team
HRTEM	High resolution TEM

IS	Impedance spectroscopy
IT-SOFC	Intermediate temperature solid oxide fuel cell
LiB	Lithium ion battery
LLZO	$Li_7La_3Zr_2O_{12}$
LLZTaO	$Li_{6.7}La_3Zr_{1.7}Ta_{0.3}O_{12}$
LSCF	$La_{1-x}Sr_xCo_{1-y}Fe_yO_3$
LSGM	$La_{1-x}Sr_xGa_{1-y}Mg_yO_3$
MD	Molecular Dynamics
MIEC	Mixed ion-electronic conductor
MSD	Mean Square Displacement
O&M	Operation and Maintenance
OCV	Open circuit voltage
ORNL	Oak Ridge National Laboratory
PEMFC	Proton exchange membrane fuel cell
PLD	Pulsed laser deposition
PTM	Pressure transmission medium
REG	Reciprocating engine generator
RHEED	Reflection high-energy electron diffraction
ScSZ	Scandium stabilized zirconia
SDC20	$Sm_{0.2}Ce_{0.8}O_{1.9}$
SEM	Scanning Electron Microscope
SOFC	Solid oxide fuel cell
STEM	Scanning transmission electron microscope
TSS	Two-step sintering
XRD	X-ray diffraction
μ-XRD	Micro X-ray diffraction

SUMMARY

High-performance solid-state energy storage and conversion devices are a vital technology component of the U.S. Department of Energy's clean and renewable energy implementation strategy. Solid-state fuel cells are important technologies for efficient conversion of a wide variety of fuels to electricity, and solid-state batteries are critical for safe storage of electricity generated by clean technologies. Solid-state devices are pursued due to their inherent mechanical and chemical stability at high temperatures and under harsh conditions; ensuring long-lifetime, fuel flexibility and safe operation. However, ionic conductivities of the available solid-state electrolytes are much lower than those of liquid electrolytes. In order to take advantage of the beneficial properties of solid state devices, novel solid state electrolytes with higher ionic conductivity must be developed.

In this work, ionic transport properties at interfaces of solid-state electrolytes have been investigated as a route for developing fast ion conducting solid-state electrolytes. Interfacial effects including the space-charge effect, the strain effect, and the curvature effect alter ionic charge carrier mobility and/or concentration at interfaces in solid-state electrolytes, leading to dramatic changes in ionic conductivity. By harnessing these energetically-favorable effects at solid-state electrolyte interfaces and fabricating interface-rich electrolytes, the total conductivity of solid electrolytes and performance of solid-state electrochemical devices can be greatly enhanced.

The curvature effect on oxygen anion conductivity in $Sm_{0.2}Ce_{0.8}O_{1.9}$ (SDC20) has been investigated by fabrication of nanocrystalline SDC20 electrolytes. Advanced sintering techniques suppressed grain growth of the SDC20 phase, leading to samples with ~165nm grains and greater than 95% density. When compared to microcrystalline samples, with significantly lower interface to bulk volume ratio, electrical measurements reveal enhanced total conductivity of the nanocrystalline samples and ionic transference number, t_{ion}, of unity. In comparison, electrical measurements of SDC20 samples fabricated with varying interface to bulk volume ratio by pulsed laser deposition revealed no difference in the conductivity of the samples. The enhancement of electrical properties at interfaces in the nanocrystalline sample is attributed to the curvature effect on oxygen vacancy, $O_{\ddot{V}}$, concentration at the interfaces of nano-grains. It is recommended that all effort be made to reduce the grain size of SDC20 electrolytes in solid state fuel cells by alternative sintering techniques in order to dramatically enhance device performance.

The strain effect on proton, H^+, and oxygen anion, O^{2-}, conductivity in $BaZr_{0.85}Y_{0.15}O_{3-\delta}$ (BZY15) and $Sm_{0.2}Ce_{0.8}O_{1.9}$ (SDC20) has been investigated by fabrication of heterostructure BZY15/SDC20 samples by pulsed laser deposition at Oak Ridge National Lab. The interface to bulk volume ratio of the heterostructure samples was systematically varied across three samples by modification of component layer thickness while maintaining a total thickness of 125nm for all samples. Structural and electrical characterization of the heterostructure samples revealed unique growth mechanisms of the thin films and varying electrical properties based on heterostructure morphology. STEM and FFT analysis of the crystalline phases reveals the growth orientations of the SDC20 phase and BZY15 phase and s dilatative strain in the SDC20

phase of as much as ~8%. The optimized BZY15/SDC20 heterostructure sample exhibits electrical conductivities more than one order of magnitude higher than those of bulk BZY15 and approximately two orders of magnitude greater than those of bulk SDC20. The synergistic effect on electrical properties between these two important solid-state electrolytes is an exciting breakthrough in solid-state electrolyte development and a strong foundation for further composite BZY15/SDC20 electrolyte development.

In order to measure the strain effect on charge carrier transport directly, the electrode-equipped diamond anvil cell technique was used to measure the solid-state Li^+ electrolyte $Li_{6.7}La_3Zr_{1.7}Ta_{0.3}O_{12}$(LLZTaO) up to 20GPa. High pressure structural characterization was completed at the Advanced Photon Source at Argonne National Lab. Electrical characterization reveals the resistive effect of volumetric compression on electrical transport in ionic conductors. At volumetric strain greater than 8vol% the resistance of LLZTaO increases by one order of magnitude. High pressure measurements were also used to determine the bulk modulus of LLZTaO and SDC20 and a relationship between the elastic properties, dopant concentration, and the strain effect was developed.

In summary, the work provides important insight into interfacial effects on ionic conductivity in solid-state electrolytes relevant to current solid-state fuel cell and battery development. The fundamental understanding of interfacial effects on ionic conductivity has been widened and several conclusions from the work can be applied directly to enhance performance of solid state energy conversion and storage devices.

CHAPTER I

INTRODUCTION

In the global effort to reduce carbon emissions and limit dependence on natural hydrocarbon resources for electricity generation, alternative energy technologies with high efficiencies, low emissions, long lifetime, and excellent safety are under development. The development of new electricity generation and storage technologies is a critical challenge for the development of a clean energy economy. The clean energy economy has been described and supported consistently by President Obama throughout the 44th US presidency as a change in US electricity generation that will cut carbon emissions, reduce dependence on limited hydrocarbon natural resources, and provide a strong energy foundation for future economic growth.[1] Fuel cells and lithium ion batteries are two important technologies in the clean energy economy development strategy. Solid oxide fuel cells generate distributed electricity at efficiencies greater than conversion efficiencies of current centralized coal or natural gas power plants and Li-ion batteries are high energy density storage devices capable of delivering clean energy for mobile applications including for use in electric vehicles.

Solid state fuel cells and solid state Li-ion batteries are characterized by a solid electrolyte which enhances the long term stability and safety of the device when compared to devices with liquid electrolytes. The most common limiting factor for high performance and efficiency in solid-state electrochemical devices is high resistance to charge carrier flow through the solid state electrolyte. Although catalysts may be added to electrodes to increase reaction rates and overall device performance, ionic conduction in

the electrolyte is limited by the fundamental materials properties of the solid state electrolyte itself.

After many years of research and development of new electrolyte materials for solid state fuel cells and Li-ion batteries, the pursuit of new electrolyte materials discovery has yielded few new materials. In fact, the only commercially available solid oxide fuel cells today use an oxygen anion solid state conductor that was discovered more than 100 years ago. Although more electrolyte materials have been developed the total number of possible electrolytes for solid state fuel cells and batteries are limited and newly developed materials often face significant technical hurdles for full compatibility in the solid state device.

In light of the need for a clean energy economy, the work of this dissertation focuses on the development of new electrolytes for high performance solid state energy devices. Specifically, the new advances in the understanding of electrolyte technology, put forward in this dissertation, result from modification of existing solid state electrolytes by interfacial and nano-size effects. These effects have been investigated for their ability to reduce resistance to charge carrier transport and enhance the performance of solid state electrochemical devices, specifically, solid state fuel cells and solid state Li-ion batteries.

1.1 Solid state ionic conductivity

Solid state ionics is the study of mobile ions in the solid state. Ironically, disorder, or defects, in the solid state provide mechanisms for ion transport which is vital for the use of solids as electrolytes in solid state fuel cells and other solid state electrochemical

systems.[2] Engineering advantageous disorder in the solid state can lead to high technology materials with valuable electrical properties.

Michael Faraday first discovered the motion of mobile ions in solid and liquid electrolytes in 1831 – 1834.[2] He built on the foundation of Volta's electric pile in 1800, which was later used by Nicholson and Carlisle for the separation of water into H_2 and O_2 by electrolysis. Faraday used the terms cation and anion and identified their interaction with electrodes at the electrode/electrolyte interface to gain or donate electrons and form elements or molecules. By 1834 Faraday observed Ag^+ and Pb^{2+} ionic conductivity, for the first time, in Ag_2S and PbF_2 materials through experimentation with electrochemical cells. In the subsequent decades, solid state ionic conductivity of O^{2-}, H^+, Na^+, Li^+ and other mobile defects were discovered, expanding the application of solid state ionic conductors. Oxygen anion conductors are the most commonly applied solid state conductors due to their effectiveness for transporting oxygen from the air. The most widely applied solid state ionic conductor is the oxygen sensor which is used to measure oxygen concentration in the exhaust stream of automobile internal combustion engines.

Solid State Ionics has its foundation in the principles of electrical conductivity and mass transport, as well as the structure of crystals and the formation of defects in those crystals according to laws of thermodynamics. Discoveries over the 19^{th} and 20^{th} centuries developed the foundation of each of these principles and paved the way for understanding and controlling solid state ionics for use in electrochemical applications.[2]

1.2 Application of solid state ionic conductors in electrochemical devices

The development of solid state ionic conductors for electrical and electrochemical devices can be divided into categories based on the types of mobile defects present in the solid. Electroceramics are divided into the categories of *ionic conductors*, *electronic conductors* and *mixed ionic-electronic conductors*.

Although electronic defects are not the focus of this work, the semiconductor device revolution which has led to the development of integrated circuits, miniaturization of electronics, and the digital world that we live in today, was spurred by the discovery of intrinsic electronic defects in silicon and the effect of heterovalent cations for creation of extrinsic electronic defects. Photolithography processing allows precise control of donor and acceptor doping as well as electrode and current collector positioning in and on silicon. By photolithography, solid state electronic conductors can be used to produce billions of individual devices on a small footprint. The discovery, understanding and control of electronic point defects in silicon based semiconductors and other semiconducting materials cannot be overstated due to its worldwide impact on 21st Century technology, communication and behavior.

Ionic conductors and mixed ionic-electronic conductors (MIECs) are unique due to the thermodynamically required presence of ionic defects in these materials systems. Devices based on ionic conductors and MIECs primarily include solid state sensors, electrolyzers, separation membranes, solid state batteries and solid state fuel cells. Pure ionic conduction allows for the transport of charge without electron or electron hole transport. Ionic conduction becomes important specifically in solid electrochemical devices where a non-electronically conducting material, an electrolyte, is necessary for

the electronic separation of electrodes. MIECs are used primarily as catalysts and as electrode materials of solid state electrochemical devices to extend reaction sites (and ion carriers) from the electrolyte material into the electrode. MIECs are particularly important for extending the length of triple phase boundaries in solid oxide fuel cells.

Solids with fast conduction of Na^{+} [3], Li^{+} [4], H^{+} [5], O^{2-} [6], and Ag^{+} [7] ions have been discovered and are applied in solid state devices. Solid state batteries have been developed based on Na^{+}, Li^{+} and Ag^{+} ion conductors. Fuel cells, separation membranes, and electrolyzers have been developed based on H^{+} and O^{2-} conductors. Electrochromic windows have been developed based on Li^{+} ion conductors. The variation in size of ionic charge carrier is related to the activation energy for charge transport in the material system. For example, H^{+} is much smaller than O^{2-} and can move through materials with less activation energy than the O^{2-} ion. However, as we will see, the relationship between size of charge carrier and conductivity is not always straightforward and can vary based on other factors. The transport of Na^{+}, Li^{+}, and Ag^{+} conductors is generally accomplished by interstitial defects in the solid, while oxygen anion and proton conductivity generally requires oxygen vacancies for fast transport.

1.3 Solid oxide fuel cell electrolyte review

Solid oxide fuel cell electrolytes can be divided into two categories; *oxygen anion conducting electrolytes, O^{2-}*, and *proton conducting electrolytes, H^{+}*. Solid oxide fuel cells based on the two types of ion conducting electrolytes are represented in Figure 1. The proton conducting cell in Figure 1A oxidizes fuel at the anode side, transports protons through the electrolyte, and finally combines with oxygen at the cathode and electrons from the external circuit to form the fuel cell byproduct, water. Fuel cell

reactions for the proton conducting SOFC, fueled by pure hydrogen and oxygen are given in equations 1, and 2.

Anode: $$H_2 = 2H^{\cdot} + 2e^{'} \quad (1)$$

Cathode: $$\frac{1}{2}O_2 + 2H^{\cdot} + 2e' = H_2O \quad (2)$$

Alternatively, the oxygen anion conducting cell in Figure 1B reduces oxygen at the cathode, transports oxygen anions through the electrolyte which combine with hydrogen at the anode and releases electrons to form water at the anode. The oxygen anion conducting fuel cell reactions, when fueled by pure hydrogen and oxygen, are given by equations 3, and 4.

Anode: $$H_2 + O_O^X = H_2O + V_{\ddot{O}} + 2e^{'} \quad (3)$$

Cathode: $$\frac{1}{2}O_2 + V_{\ddot{O}} + 2e' = O_O^x \quad (4)$$

The overall hydrogen fuel cell reaction is given by equation 5 and is consistent independent of the charge carrier in the solid state electrolyte.

$$H_2 + \frac{1}{2}O_2 = H_2O \quad (5)$$

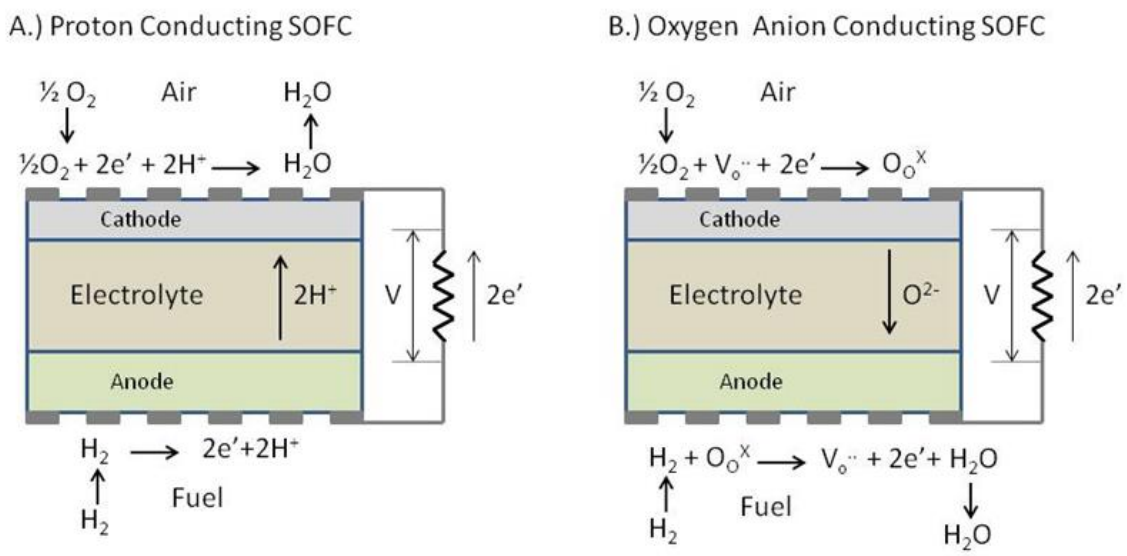

Figure 1 Schematic of the (A) Proton Conducting SOFC and (B) Oxygen Anion Conducting SOFC[8]

1.3.1 Oxygen anion conducting electrolyte

Oxygen anion conducting electrolytes are the most mature SOFC electrolyte technology and are the only type of electrolyte in commercially available SOFCs (Bloom Energy Inc.; ~$7000/kW). Charge is carried through the electrolyte not by electrons or electron holes, but by oxygen vacancies which carry a charge of +2. Intrinsic oxygen vacancy defects are present in common SOFC electrolyte materials and the concentration is primarily dependent on the oxygen partial pressure. However, intrinsic defects in the solid state ionic conductors are insufficient for high conductivity. Oxygen vacancies can be created by aliovalent doping of cations in the crystal structure which causes a charge imbalance in the crystal structure. The charge is balanced in the crystal by formation of oxygen vacancies. Aliovalent cations, up to ~20 mole% are useful for creation of oxygen vacancies for fast ionic conductivity in the electrolyte. The common oxygen anion conducting electrolytes for SOFCs are briefly reviewed below.

ZrO_2

Zirconium dioxide , ZrO_2, doped with Yttrium (Y^{3+}) or Scandium, Sc^{3+}, is the most widely used SOFC electrolyte due to its excellent chemical stability in oxidizing and reducing atmospheres at elevated temperatures, ease of thin film membrane fabrication and fast ionic conductivity at elevated temperatures (800^{o}C – 1000^{o}C).

The defect reaction for oxygen vacancy creation in ZrO_2 by doping with Y_2O_3 is given in Kröger-Vink notation in Equation 6.

$$Y_2O_3 \xrightarrow{ZrO_2} 2Y'_{Zr} + V_o^{\cdot\cdot} + 3O_o^x \quad (6)$$

The conductivity of yttria-doped zirconia (YSZ) increases up to 8 mole% addition of Y^{3+} to zirconia.[9] Compatibility with all SOFC components is critical for long-term operation of the SOFC. YSZ is known to react with the $La_{1-x}Sr_xMnO_3$ (LSM) cathode material.[9] The reaction layer can block charge carrier transport and reduce fuel cell performance. $La_{1-x}Sr_xCo_{1-y}Fe_yO_3$ (LSCF) is currently used as a compatible, high performance cathode with YSZ electrolyte, although some mild reactions still occur and long term stability of the YSZ/LSCF interface is problematic.

CeO_2

Cerium dioxide, CeO_2, doped with Samarium (Sm^{3+}) or Gadolinium (Gd^{3+}) is a commonly studied oxygen anion conducting electrolyte especially for intermediate temperature SOFCs (IT-SOFCs). The ionic conductivity of doped-ceria is ~1 order of magnitude higher than YSZ ionic conductivity at 500^{o}C. Although research on doped-ceria electrolytes has proceeded for >20 years the electrolyte is not available in a fully

commercial SOFC system to date. This is primarily due to partial electronic conductivity in doped-ceria due to reduction of Ce^{4+} to Ce^{3+} and creation of electronic defects in reducing atmospheres. Leaking electronic conductivity in the electrolyte lowers the Nernst Potential of the cell and significantly reduces the power density at the common operation voltage of 0.7V. Doped-ceria has excellent stability with SOFC cathodes and can be used as an interlayer at the YSZ/cathode interface to prevent performance-reducing reactions.[9]

$LaGaO_3$

Lanthanum gallate, $LaGaO_3$, co-doped with Strontium (Sr) and Magnesium (Mg) on the A- and B-sites of the perovskite (LSGM), respectively, has high ionic conductivity at low temperatures and is promising for use in IT-SOFCs.[9] The ionic conductivity of LSGM is similar to doped-ceria but does not form electronic defects in reducing atmosphere. The major drawbacks to the promising, but non-commercialized LSGM electrolyte are reaction with the common nickel SOFC anodes and multicomponent fabrication difficulties. An ionically insulating phase forms at the LSGM/Ni interface during fabrication which reduces fuel cell performance. Additionally, fabrication of the pure, stoichiometric co-doped perovskite phase is challenging.

1.3.2 Proton conducting electrolyte

Proton conducting electrolytes based on the $BaCeO_3$ and $BaZrO_3$ perovskite structures have been discovered[10] and developed for application in IT-SOFCs due to low activation energy for oxygen vacancy mediated proton transport in the doped structures. Proton conducting electrolytes are also beneficial for moving formation of the fuel cell product, H_2O, to the cathode side to limit fuel dilution. Water at the SOFC anode side

reduces cell voltage and efficiency due to dilution of the fuel. When hydrogen is used as fuel, the fuel utilization rate is given by equation 7.

$$U_{fH_2} = 1 - \frac{y_{H_2,O}}{y_{H_2,I}} \tag{7}$$

Where $y_{H_2,I}$ is the molar concentration of the total molar flow at the anode inlet, I, and $y_{H_2,O}$ is the molar concentration of the total molar flow at the outlet, O. The ratio of fuel utilized to water formed is 1:1, (8).

$$\dot{n}_{H_2,Utilized} = \dot{n}_{H_2O,O} \tag{8}$$

For an oxygen anion conducting electrolyte, the partial pressure of fuel at the anode is reduced when water is present which affects the Nernst voltage. As fuel utilization increases and the concentration of water at the anode increases, the Nernst potential decreases. The SOFC with a proton conducting electrolyte produces water at the cathode, leaving the anode side gases free of H_2O. The absence of H_2O at the anode increases the voltage of the proton-conducting cell when compared to the oxygen anion conducting cell and increases the performance of the device.

If the SOFC electrolyte is a mixed-ion conductor or a composite of two ion conducting materials, the fuel cell water will form at both sides of the cell. Formation of a portion of the water at the anode side is beneficial for carbon coking tolerance[11] and from our experience is expected to be necessary for SOFCs fueled with hydrocarbon fuels.

$BaCeO_3$

Barium Cerate, $BaCeO_3$, doped with Zirconium (Zr^{4+}) and Yttrium (Y^{3+}), BZCY and related compounds are proton conducting SOFC electrolytes with high conductivity at intermediate temperatures and are under development for use with IT-SOFCs. Barium zirconate ($BaZrO_3$) demonstrates high chemical stability in fuel cell conditions and barium cerate ($BaCeO_3$) has high ionic conductivity. BZCY and BZCYYb take advantage of the high conductivity and stability and form a fast ion conducting IT-SOFC electrolyte material. The electrical conductivities of BZCY and BZCYYb are shown in Figure 2A[12] in comparison to the other electrolytes presented in this section. The slope of the conductivity versus temperature plot is smaller for BZCY and BZCYYb when compared to doped-ceria and YSZ due to the low activation energy for proton transport. A representative SEM cross-section image of a BZCYYb electrolyte SOFC is shown in Figure 2B. A large limitation of the BZCY and the BZCYYb electrolyte materials is the number of components in the structure and the difficulty to prepare the pure phase perovskite with optimal properties. Further work to improve the processing and fabrication techniques are necessary before the $BaCeO_3$-based proton conducting electrolytes will be commercialized. However, development of commercial SOFCs based on these electrolytes is currently in progress in the Membrane Sciences Group at Coorstek in Golden, CO.

The common SOFC oxygen anion and proton conducting electrolytes are listed in Table 1.

Table 1 Comparison of common SOFC oxygen anion and proton conducting electrolytes

Electrolyte	Charge Carrier	Operation Temperature (^{o}C)	Strengths/Weaknesses
Doped-ZrO_2	O^{2-}	800-1000	Ease of fabrication; Excellent chemical stability; high temperature necessary for fast ionic conductivity
Doped-CeO_2	O^{2-}	600-800	Fast ionic conductivity; Partial electronic conductivity which lowers the Nernst Potential of the cell
Doped-$LaGaO_3$	O^{2-}	600-800	Fast ionic conductivity at intermediate temperature; Detrimental chemical reaction with Ni-containing anodes
Doped-$BaCeO_3$	Mixed O^{2-}/H^{+}; primarily H^{+} below 600^{o}C	500-800	High conductivity at intermediate temperatures; pure phase processing/fabrication difficulties

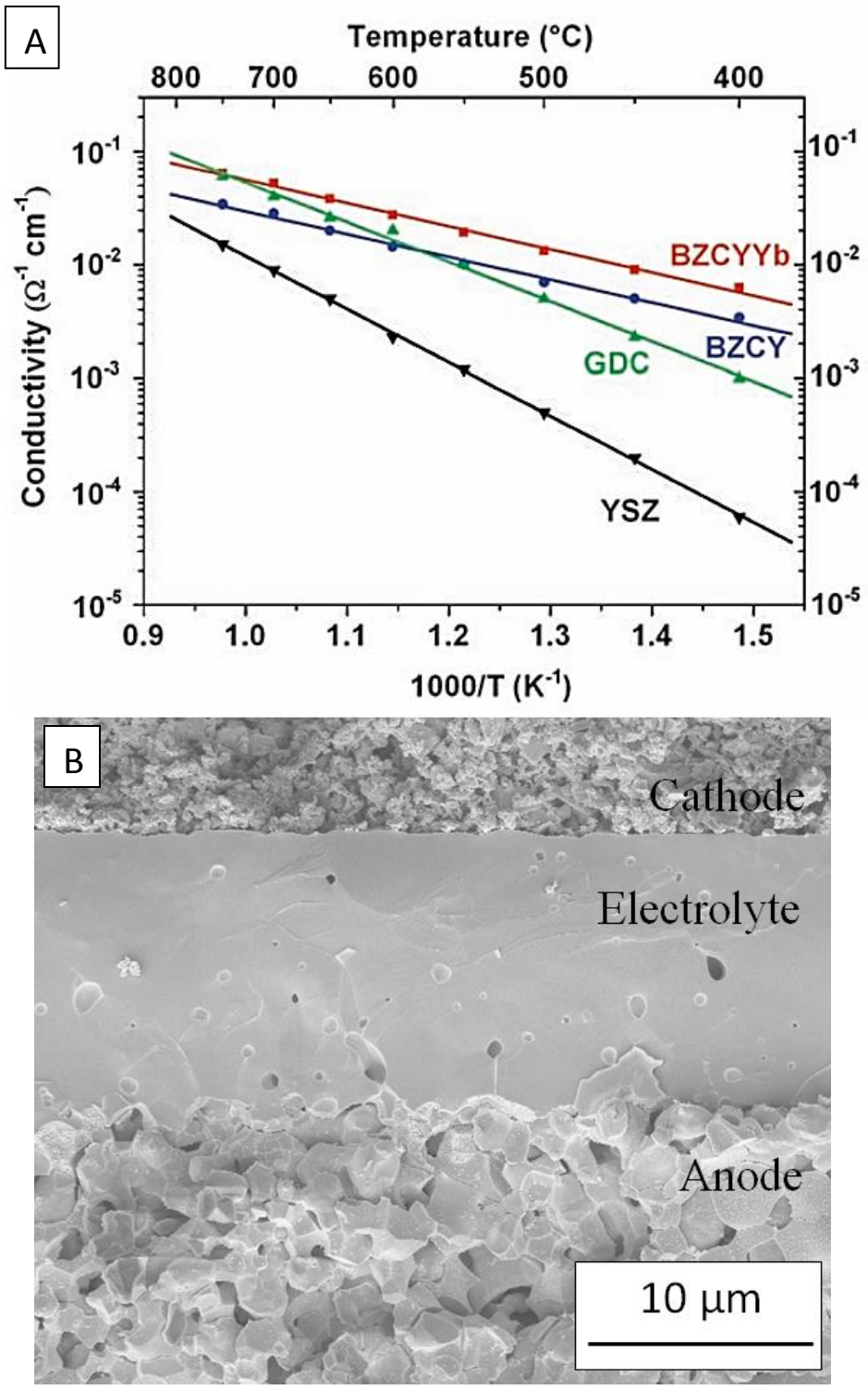

Figure 2 (A) Comparison of ionic conductivity of common oxygen anion and proton conducting SOFC electrolytes from 800°C to 400°C[12]; (B) A typical thin film BZCYYb electrolyte SOFC microstructure cross-section[8]

1.4 Solid state Li-ion battery electrolyte review

Solid state lithium ion conductors with high ionic conductivity at ambient temperature are of great interest for application in Li-ion batteries (LIB). Advantages of solid state electrolytes in LIBs when compared to liquid/polymer electrolytes include thermal stability, electrochemical stability with electrodes, and ease of on-chip miniaturized fabrication using standard semiconductor processing techniques[13],[14]. A solid electrolyte must have high Li-ion conductivity at near-room temperature to limit ohmic polarization and negligible electronic conductivity to limit self-discharge of the energy stored in the device.

The pursuit to discover new materials with high Li-ion conductivity at room temperature has led to many new materials families, including $Li_7La_3Zr_2O_{12}$ (LLZO, Garnet-type)[15], $Li_{3x}La_{(2/3)-x}A_{(1/3)-2x}TiO_3$ (LLTO, Perovskite)[16], NASICON-type[17],[18], sulfide glasses[19], LiPON[20] and others[14]. From 1975 – 2005, eight new Li-ion solid state conductor material families, with high conductivity, were reported as seen in Figure 3. The new material innovation rate during this period was ~1 new material per 4 years of worldwide research, due to the difficulty and inherent slowness of new material discovery.

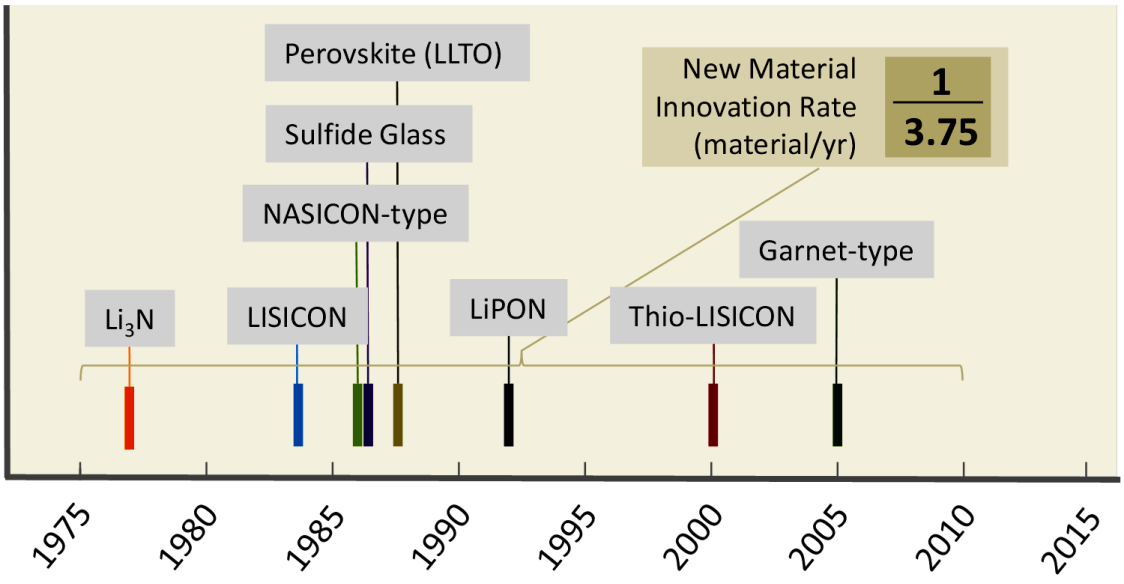

Figure 3 Important solid state lithium ion conductor families reported from 1975-2005; calculated materials innovation rate

$Li_7La_3Zr_2O_{12}$

A new family of fast garnet-type Li-ion conductors with typical compositions $Li_5La_3M_2O_{12}$ (M = Nb, Ta)[21] and $Li_7La_3Zr_2O_{12}$[22] were recently discovered and have been developed intensively for application as high performance electrolytes in solid state lithium ion batteries.[22-28] This garnet-type li-ion solid electrolyte has high chemical stability in oxygen and water containing atmospheres,[29] with lithium metal[30] and with common lithium ion battery electrode materials,[31] making it the most promising solid electrolyte material for Li-ion batteries. The optimized structure, $Li_{6.7}La_3Zr_{1.7}Ta_{0.3}O_{12}$[32], has fast ionic conductivity of 0.96 mS cm^{-1} at 25°C[32]. The Li ions can be considered a Frenkel defect, with Li ion vacancies at some sites along the migration pathway and Li^+ ions at other sites. The time of the interstitial in its lattice site and the time spent between lattice sites is comparable.[7]

1.5 Low-cost, low-temperature solid oxide fuel cells

Solid oxide fuel cells (SOFCs) are high technology energy conversion devices which convert chemical energy to electrical energy by electrochemical conversion instead of combustion. Waste heat from SOFCs can be used in a combined heat and power (CHP) configuration to achieve ~90% total fuel efficiency. A variety of fuels, including pure hydrogen, methane (natural gas), biogas, coal gas, and other hydrocarbon fuels, can be used to fuel SOFCs making them a fuel flexible energy conversion technology. Ambient air is readily available as oxidant for the fuel cell reaction. The high conversion efficiency of SOFCs reduces greenhouse gas generation per kWh of electricity produced making it an alternative energy conversion technology.

SOFCs are comprised of all solid state components including anode, cathode, electrolyte, interconnect, and sealant. Significant research has been conducted on materials for fast oxygen reduction at the SOFC cathode, anodes that are tolerant to contaminants in the fuel stream (especially carbon coking on the Ni anode), interconnects that are stable in oxidizing and reducing atmospheres, and sealant materials that remain hermetic through thermal cycling. As in all types of fuel cells, SOFCs are defined by the type of electrolyte membrane that is used. Fuel cells based on proton conducting solid state electrolytes and oxygen anion conducting solid state electrolytes were discussed in the previous sections and are illustrated in Figure 1.

In current commercially available SOFCs, the operation temperature is required to be greater than 800^{o}C. The high operation temperature is necessary for fast ion transport through the YSZ electrolyte. However the extreme temperature makes long term chemical and mechanical stability an important topic of continued research for durable

SOFC systems. Stability of all five major SOFC components is necessary to ensure the target SOFC system lifetime of 10 years and long term stability is a key factor for commercialization of an SOFC system. One strategy to improve long term stability of SOFCs is to reduce the operating temperature from greater than 800^{o}C to the temperature range of 400^{o}C - 600^{o}C. At lower operating conditions, thermal cycling is less severe and chemical reaction energy between SOFC components is reduced. Conveniently, this strategy is compatible with an attempt to reduce SOFC capital cost by reducing operating temperature.

Reduction of the SOFC operating temperature can reduce SOFC system capital cost by 20% - 40% (See Appendix A) by reduction of the cost of expensive interconnect materials, sealants and high temperature balance of plant (BOP) components. Cost reduction is attainable at operation temperatures near 500^{o}C because less expensive materials such as stainless steel and traditional sealants can be used. However, in order to see a paradigm shift in SOFC operation temperatures and to realize low capital costs, SOFC performance at low temperatures must be enhanced. Currently, SOFC performance is dramatically reduced when operated at 500^{o}C. Although savings in cost from low temperature materials is possible at 500^{o}C the total cost will not be reduced due to extra stack area required to meet the output power requirement. While all reactions become more sluggish at low temperature and add to the reduced performance, ohmic polarization in the solid state electrolyte is dramatically increased and cannot be enhanced by the addition of high performance catalysts which can enhance electrode reactions. The conventional oxygen anion conducting electrolyte material, YSZ, is not suitable for low temperature operation due to low ionic conductivity. The proton

conducting solid state ionic conductor, doped-$BaCeO_3$, has higher ionic conductivity at low temperatures than YSZ but is still insufficient for achieving sufficient performance at less than 500^oC to meet cost goals for commercially viable SOFCs. Fast-ion conducting solid state electrolyte materials are needed to increase fuel cell performance at low temperature and realize commercial SOFCs.

1.6 Ohmic polarization in SOFCs – A barrier to low temperature SOFC operation

The overall reaction for a fuel cell operating on hydrogen as fuel and oxygen as oxidant is given by equation 9.

$$H_2 + \frac{1}{2} O_2 \rightarrow H_2O \tag{9}$$

The potential of a fuel cell at open circuit voltage (OCV) can be calculated using Equation 10 which is better known as the Nernst Equation. The activity of the products and reactants can be approximated by the partial pressure of the gases in the fuel cell.

$$E_N = E^\theta + \frac{RT}{2F} ln \frac{a_{H_2} a_{O_2}^{0.5}}{a_{H_2O}} \cong E^\theta + \frac{RT}{2F} ln \frac{P_{H_2} P_{O_2}^{0.5}}{P_{H_2O}} \tag{10}$$

The standard potential of the SOFC at given temperature, pressure and gas activity does not depend on fuel cell type or cell materials but on the thermodynamic properties used in Equation 10 and the gas species involved in the cell. The measured and theoretical OCV of an SOFC with Ni-BZCYYb/BZCYYb/LSCF-BZCYYb architecture at given conditions is shown in Figure 4. The measured value of the SOFC OCV deviates from the theoretical value due to leaking electronic conductivity in the electrolyte or due to gas transport from the anode to cathode sides by pinholes or sealing leaks.

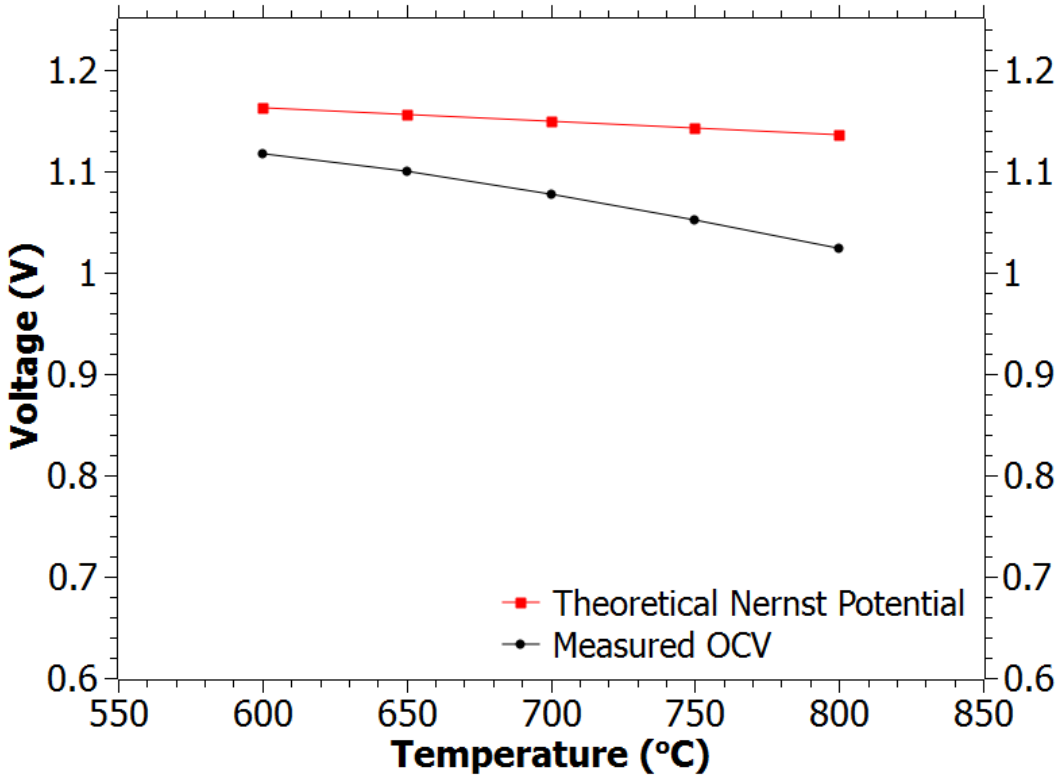

Figure 4 Measured and theoretical OCV of Ni-BZCYYB/BZCYYb/LSCF-BZCYYb SOFC with 3%H_2O/H_2 fuel and 3%H_2O/O_2 oxidant from 600°C – 800°C[8]

When the cell is closed, and no longer at OCV, the voltage of the cell is reduced from the Nernst Potential. In order to experimentally determine the current-voltage relationship of the fuel cell, the current density, i (A/cm^2) is increased from zero current, at OCV, to a current density that fully suppresses the cell voltage. An example of polarization curves formed by this technique for an SOFC, an alkaline fuel cell (AFC), and a proton exchange membrane fuel cell (PEMFC) are reproduced in Figure 5. In general the cell voltage at a given current density is described by Equation 11 which includes the overpotential of the cell due to each of the SOFC components.

$$E = E^{\theta} + \frac{RT}{2F} ln \frac{P_{H_2} P_{O_2}^{0.5}}{P_{H_2O}} - |n_{cathode}| - |n_{anode}| - |n_{electrolyte}| \qquad (11)$$

In Figure 5, polarization due to slow kinetics at low current densities are dramatic in the PEMFC and AFC cells, ohmic polarization at moderate current densities is significant in the SOFC due to electrolyte resistance and mass transfer polarization is observed at high current density in the PEMFC. The cell voltage is reduced from the Nernst potential due to polarization at the electrodes and in the electrolyte of the fuel cell.

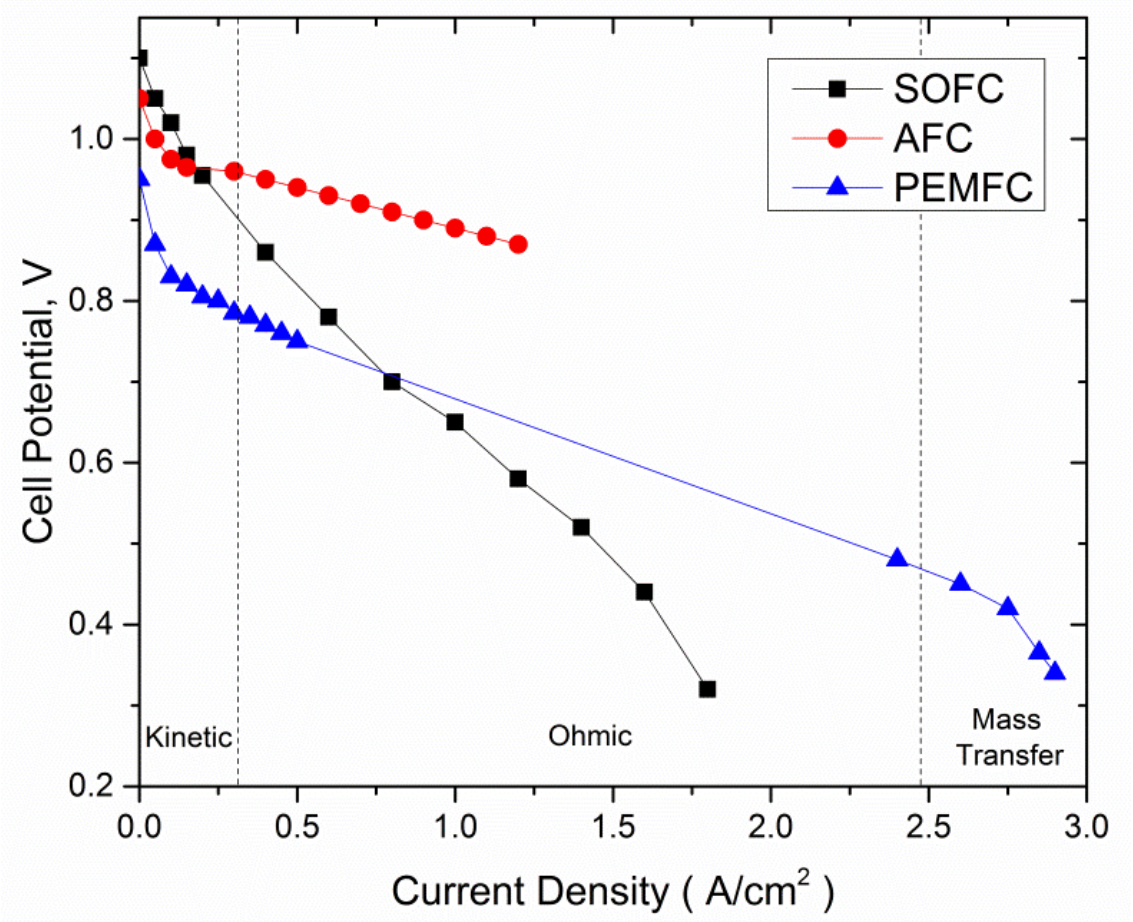

Figure 5 Typical polarization curves for Proton Exchange Membrane Fuel Cell (PEMFC), Alkaline Fuel Cell (AFC), and Solid Oxide Fuel Cell (SOFC) (reproduced from Fuller and Harb, 2015)[33]

The ohmic polarization, iR_{Ω} , dramatically decreases the potential of the SOFC due to high bulk resistivity in the solid electrolyte. Conductivity in the solid electrolyte is

expressed by the Arrhenius type Equation 12 which exponentially depends on temperature and activation energy.

$$\sigma = \sigma_o exp\left(\frac{-E_{a,\sigma}}{RT}\right) \tag{12}$$

As seen in Figure 6, the ohmic polarization increases at low SOFC temperatures due to large activation energy for ionic conductivity in the solid state electrolyte. The large overpotential due to ohmic polarization decreases the current density of the cell at a given voltage.

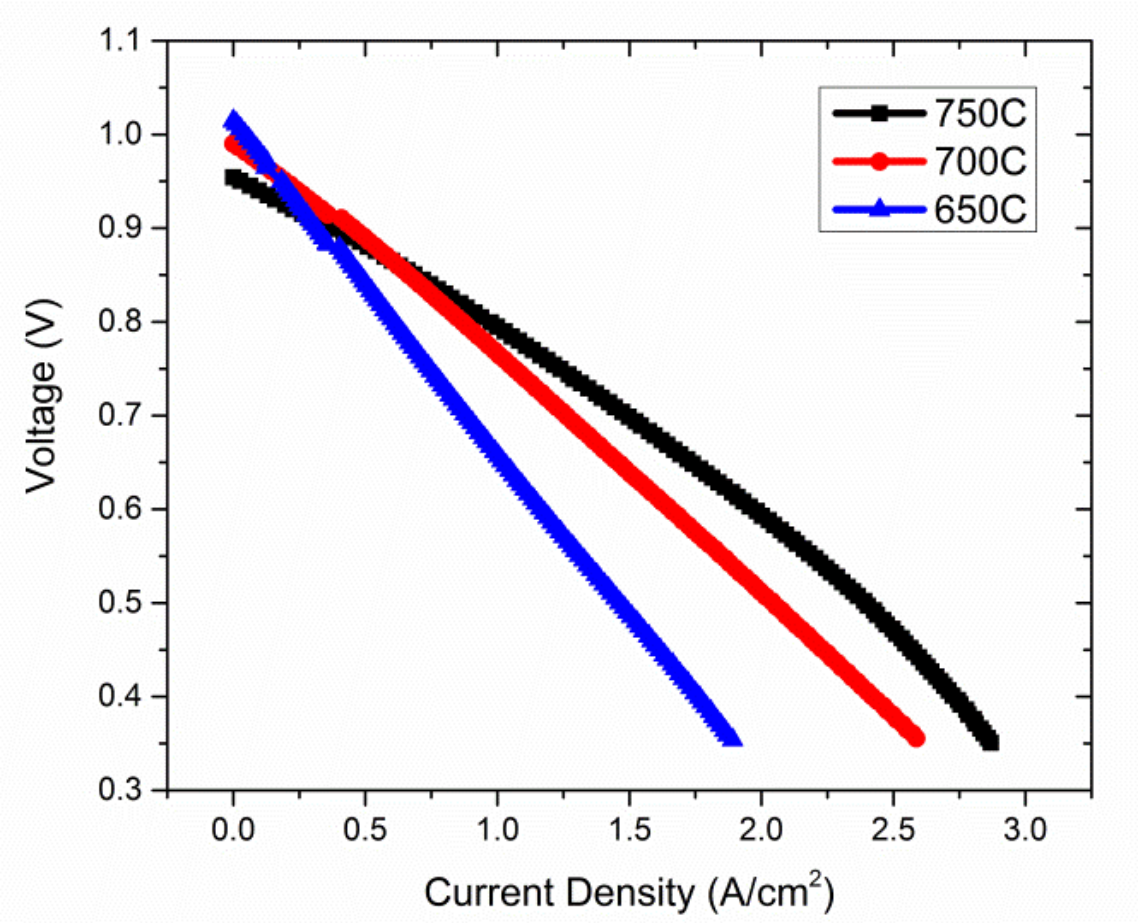

Figure 6 Polarization curves for Ni-BZCYYB/BZCYYb/LSCF-BZCYYb SOFC at 750^{o}C, 700^{o}C, and 650^{o}C

In order to relate overpotential to fuel cell cost, Figure 7 (top) shows the I-V curve for a low and high resistance SOFC. In Figure 7 (bottom) the current density of the cell

versus SOFC stack cost is plotted for a hypothetical SOFC system of 100kW, $\$0.873/cm^2$ at 0.7V. As overpotential increases, the cell current density drops and SOFC stack cost increases. As system overpotential, or ohmic polarization of the solid state electrolyte, is decreased the fuel cell cost decreases. Dramatic increases in solid state electrolyte ionic conductivity can dramatically reduce SOFC costs and speed commercialization of SOFCs for low cost, clean electricity generation.

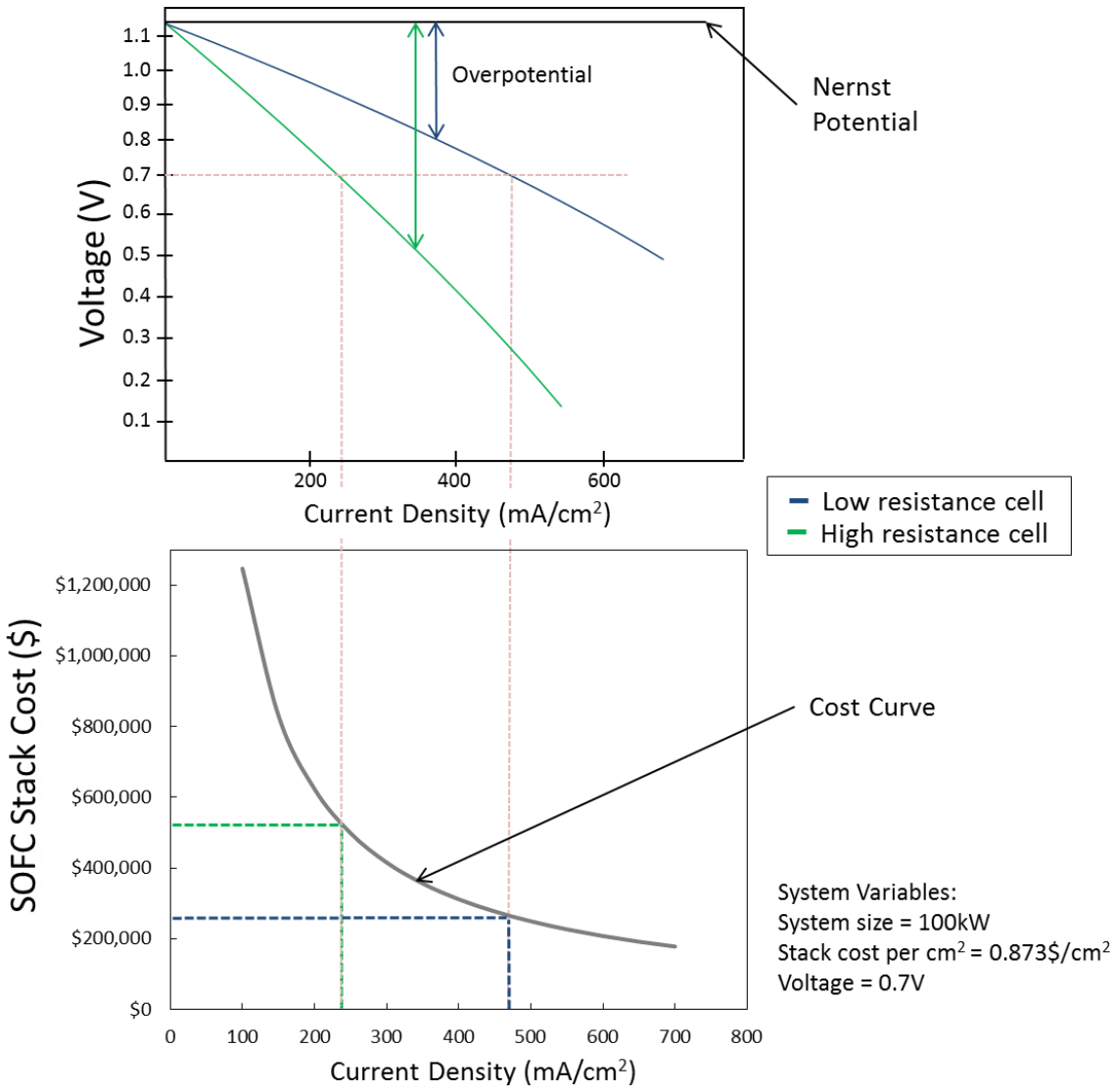

Figure 7 Illustration of the impact of cell overpotential/resistance on SOFC cost; (Top) Voltage-Current Density curve for a high resistance (green) and low resistance (blue) SOFC with predominately ohmic polarization; (Bottom) Stack cost – Current Density curve

The voltage efficiency of a fuel cell is expressed by equation 13[33] which makes the effect of polarization on cell performance straightforward.

$$\eta_v = \frac{electrical\ work\ from\ cell}{maximum\ work\ from\ cell} = \frac{Cell\ Voltage}{Nernst\ Potential} \tag{13}$$

Engineering SOFCs with ultra-thin electrolyte membranes is a way to reduce ohmic polarization in SOFCs. However, electrolytes for SOFCs can only be reduced to a minimum thickness (~10um) due to challenges with long term cell stability. Developing new solid state electrolytes with fast ionic conductivity is the best approach to lowering SOFC electrolyte polarization, enhancing SOFC performance, and reducing SOFC cost.

1.7 Enhancing solid state fuel cell and battery electrolyte ionic conductivity by interfacial and nanoscale effects

In the pursuit to develop fast ion conducting electrolytes, a concentrated focus towards interfacial effects on transport has evolved over the previous two decades. Effects at grain boundaries and heterogeneous interfaces, where structure and electrochemical potential deviate significantly from the bulk, are being studied intensively as possible opportunities for dramatically enhancing ionic conductivity in solid state fuel cell and battery electrolytes.[34-43]

In order to increase the ionic conductivity of solid state electrochemical device electrolytes, effects that have been observed to modify conductivity at electrolyte interfaces and in nanostructured electrolyte materials have been explored. If the transport property deviation at the interface is beneficial for enhancing ionic conductivity a large number of interfaces can be engineered into the bulk of the ionic conductor so that the interfacial properties dominate the total properties of the material. Figure 8 graphically represents the impact of interfacial volume on total conductivity when interfacial conductivity is much higher, much lower, or equal to the bulk conductivity.

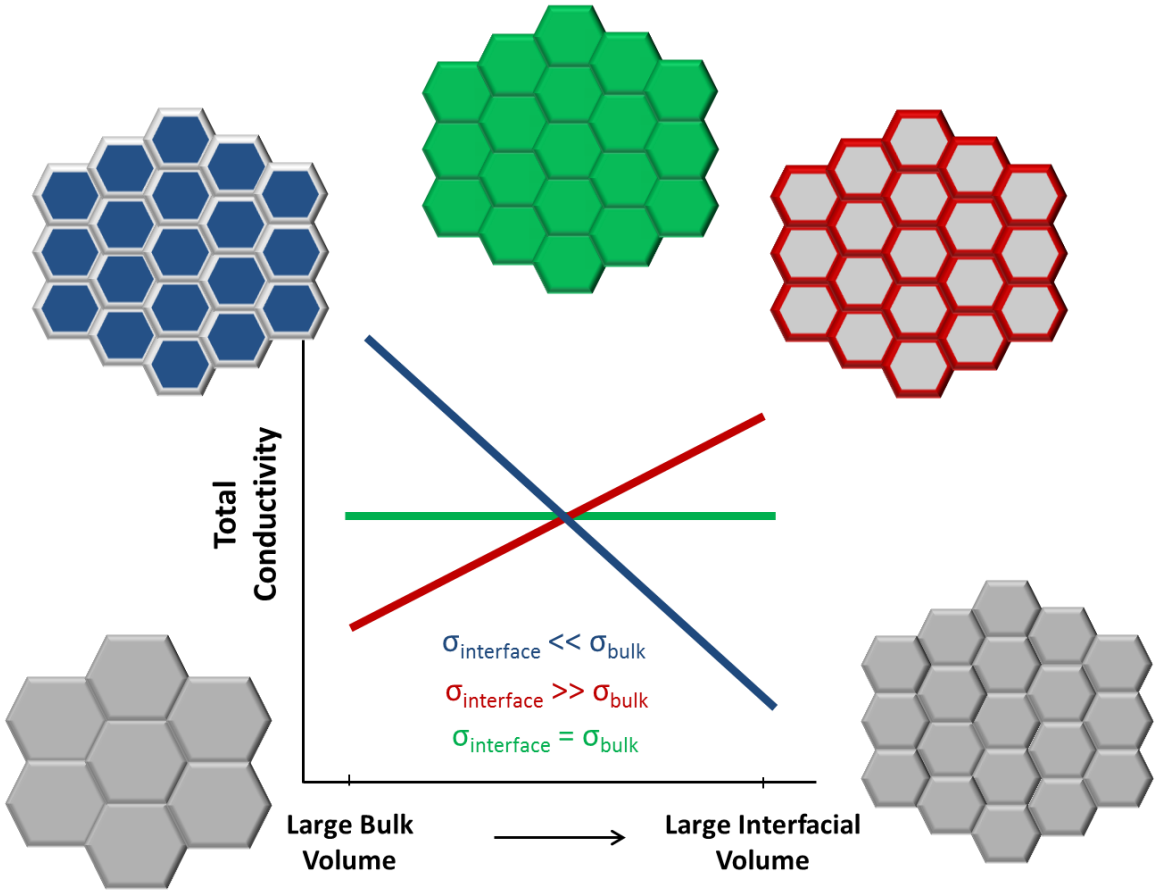

Figure 8 Visualization of interfacial effect and total conductivity dependence on interfacial volume; As the interfacial volume increases (moving from large grain sample to nano-grain sample the total conductivity will increase if the interfacial effects enhance

A more detailed review of interfacial and nano-size effects will be given in Chapter 2.

1.8 Contributions of this work

The contents of this dissertation describe, in detail, experimental investigations of effects on ionic charge carrier transport due to large strains and interfacial effects for the purpose of increasing ionic conductivity in fuel cell and battery solid state electrolytes. Structure-transport property relations are investigated in bulk samples, thin films and nanostructured samples. The work is motivated by literature reports of significant

deviations from bulk transport properties in O^{2-}, H^{+}, and Li^{+} conductors due to interfacial effects including the strain effect, the space charge effect, and the curvature effect. In order to determine if reported interfacial effects are significant and if they can be applied to electrochemical devices, three multi-component studies have been conducted.

The role of interfacial effects in $Sm_{0.2}Ce_{0.8}O_{1.9}$ (SDC20) has been widely debated in the literature, with experimental reports supporting both enhancement and diminishment of electrical properties. The results of the study presented in Chapter 3 shed new light on the understanding of interfacial effects on SDC20. Through the investigation of a series of three carefully controlled experiments, interfacial effects in SDC20 have been shown to depend heavily on sample geometry and fabrication. Nanostructured SDC20 electrolytes fabricated by two-step sintering show dramatic enhancement in ionic conductivity due to the curvature effect. Nanostructured SDC20 electrolytes are recommended for dramatic enhancement in solid-state fuel cell performance at low temperatures without increased cost.

In the pursuit to lower operating temperatures of SOFCs and reduce capital costs associated with fuel cell systems, a composite H^{+} and O^{2-} conducting electrolyte has demonstrated more than one order of magnitude enhancement in ionic conductivity over the BZY15 bulk property and approximately two orders of magnitude over the SDC20 bulk property in the $300^{o}C$ to $450^{o}C$ temperature range. FFT analysis of HAADF STEM characterization of the BZY15/SDC20 heterostructure sample reveals the enhancement in conductivity is due to the strain effect on the SDC20 phase. The work provides a new foundation for the pursuit of mixed H^{+} and O^{2-} conducting electrolytes for efficient, high performance solid oxide fuel cells

Finally, the high-pressure diamond anvil cell technique has been applied to the study of interfacial effects in solid state ionic conductors for the first time. The structural stability of SDC20 and LLZTaO has been measured with respect to pressure, the bulk modulus of both materials has been calculated from high pressure data, the electrical resistance of LLZTaO with respect to pressure has been measured and a new understanding of optimal doping concentration in SDC20 to optimize interfacial effects has been proposed.

The dissertation provides a leap forward in the understanding of interfacial effects on electrical properties of three ionic conductors, SDC20, BZY15 and LLZTaO, which are vitally important materials for high performance, low cost, reliable and safe solid oxide fuel cells and solid-state batteries. New techniques have been applied to the study and new effects in and "in-between" these important materials have been elucidated through the work presented here. The work is directly applicable in solid state energy storage and conversion technology to increase performance and drive device commercialization efforts. Commercialization of these important solid-state energy devices will be an important step towards the clean energy economy of our future.

CHAPTER II

Interfacial and nano-scale effects on ionic conductivity in solid state ionic conductors

Electrical, mechanical and optical properties of nano-scale materials can vary drastically when compared to micro-sized and larger objects due to the significant surface area to bulk volume ratio of nanomaterials. With the development of tools to fabricate, manipulate and characterize materials at the nanoscale, nanotechnology has increasingly become a high-technology focus and a new research frontier. Controlled nucleation and growth techniques, Atomic Layer Deposition (ALD), Molecular Beam Epitaxy (MBE), Pulsed Laser Deposition (PLD) and other techniques can be used to fabricate nanomaterials from the bottom-up. Instruments including scanning probe devices can be used to characterize and control atoms to create nanostructured materials and architectures from the top-down. The applications of the unique properties of nanomaterials in the health, energy, environment, and electronics sectors have been well documented.[44; 45] The need to pursue new understanding and control of materials at the nanoscale cannot be overstated due to the wide-ranging benefits of new properties unlocked at the nanoscale. Interfacial and nano-scale effects on ionic conductivity in solid state ionic conductors offer new properties which can be used to improve the performance of solid state electrochemical devices.

This chapter will begin with a brief discussion of interfacial and nanoscale effects on transport phenomena including heat transfer and electronic transport. After the first section, the specific effects of interfaces and nano-sized grains on transport of ionic charge carriers will be discussed at length. The following chapters of the dissertation will

describe extensive experiments probing the effect of interfaces and nano-size grains on ionic conductivity in which the principles presented in this chapter have been applied for discussion of the phenomena observed.

2.1 Interfacial and nanoscale effects on transport phenomena

The current investigation of interfacial and nanoscale effects on ionic conductivity comes after several years of study of other interesting transport phenomena at interfaces and on the nanoscale. With advances in nanoscale fabrication and characterization technologies, heat and mass transport phenomena at the nanoscale has been increasingly studied. Advances in the understanding and deviations of heat transport at the nanoscale when compared to the bulk have been made in thin films and nanostructured materials. For example, in thin film monocrystalline silicon, interfaces cause phonon scattering and decrease the heat conduction of the thin film at a given temperature.[46] The heat conduction plotted versus monocrystalline film thickness is shown in Figure 9A. As film thickness decreases below 100nm the thermal conductivity of the film decreases at constant temperature. The effect of dislocations and other defects on phonon scattering have also been studied. A similar effect in Cu thin films is shown in Figure 9B taken from Nath and Chopra.[47] As the Cu film thickness decreases and approaches the nanoscale, significant changes in thermal conductivity have been measured and attributed to interfacial effect-dominated heat transfer mechanisms in the thin film. Heterostructured GaAs/AlAs films with 70nm layer thickness each and 71 repeated layer pairs were fabricated by molecular beam epitaxy (MBE) by Yu and Chen.[48] The heterostructure was tested for thermal diffusivity and compared to the bulk values of thermal diffusivity in GaAs and AlAs, as seen in Figure 9C. The thermal diffusivity of

the heterostructured sample at room temperature was 0.249 cm^2/s compared to the corresponding bulk value of 0.39 cm^2/s which is a decrease in diffusivity by >30%. The decrease in thermal diffusivity is attributed mainly to interface scattering of phonons. Quantum size effects are mentioned as a possible factors in the decreased transport properties in the heterostructure. However, the phonon mean free path in GaAs and AlAs is smaller than the layer thickness fabricated in this sample, indicating low contribution of the quantum confinement effect to the reduced transport properties.[48]

Interface physics of the $LaAlO_3/SrTiO_3$ heterostructured system have been studied for more than ten years due to superconductivity measured at the $LaAlO_3/SrTiO_3$ interface. The perovskite $AO\text{-}BO_2$ stacking sequence creates $Sr^{2+}O^{2-}$ and $Ti^{4+}O_2^{2-}$ layers in the $SrTiO_3$ oxide and $La^{3+}O^{2-}$ and $Al^{3+}O_2^{2-}$ layers in the $LaAlO_3$ oxide. The interface between the perovskite materials continues the $AO\text{-}BO_2$ stacking sequence which creates a polar/nonpolar interface and redistribution and/or formation of mobile electronic defects at the interface.[49] The large electronic charge carrier mobility at the interface, as measured by the Hall Effect, is shown in Figure 9D& 9E from Ohtomo and Hwang[50] along with the schematic representation of the layered structure.

The 2-dimensional material, graphene has been studied extensively for its unique thermal and electrical properties. Extremely high electronic mobility has been measured in suspended graphene nanosheets after cleaning of the graphene to eliminate impurities and prevent extrinsic scattering. The technique used by Bolotin et. al.[51] to suspend a single, monolayer graphene sheet allowed the graphene to be cleaned extensively and prevent extrinsic scattering common in graphene samples tested on a substrate due to impurities at the interface between the graphene and the substrate. The six probe

configuration with graphene suspended in the middle of the metal contacts is shown in Figure 9F & 9G[51] along with the electron mobility measurements.

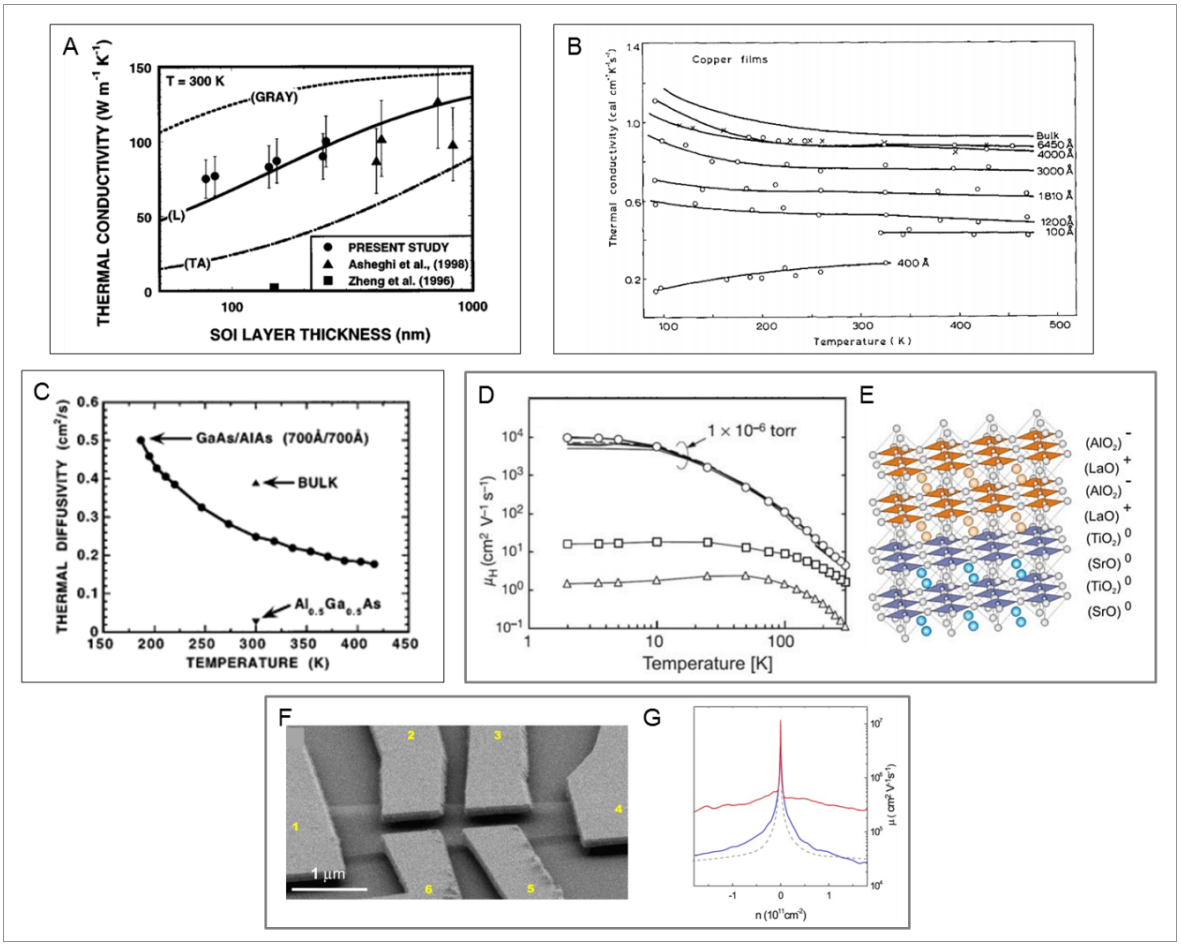

Figure 9 (A) Measured (filled circles, triangles, squares) and calculated (dotted lines) thermal conductivity of monocrystalline thin film silicon on silicon dioxide as a function of silicon film thickness; [46] (B) Thermal conductivity of Cu thin films as a function of temperature for films ranging in thickness from 10nm to bulk;[47] (C) Thermal diffusivity of GaAs/AlAs heterostructured thin film (70nm layers, 71 total layer pairs) as a function of temperature with comparison to bulk properties at room temperature;[48] (D&E) Hall electronic mobility of $LaAlO_3/SrTiO_3$ heterostructured oxide as function of temperature, at three PLD fabrication deposition pressures (circles) 1e-6 torr, (squares) 1e-5 torr, and (triangles) 1e-4 torr determining the quality of the polar/nonpolar interface;[49] (F&G) Suspended graphene with six electrodes and measured electron mobility as a function of charge carrier concentration.[51]

The study of ionic transport at interfaces and in nanostructured materials is a continuation of the thermal and electronic transport studies presented in this section.

Ionic transport study has direct application in solid state electrochemical systems including solid state batteries and fuel cells to reduce ohmic polarization and enhance device performance. The exciting work on interfacial effects in heat and mass transport outlined in this section emphasize this unique research area and the possible discoveries waiting to be uncovered at interfaces in solid state ionic conductors.

2.2 Enhancing ionic conductivity of solid state electrolytes by interfacial effects

In the field of solid state ionics, pioneering studies of the effects on ionic conductivity at interfaces and at the nanoscale have been completed by Despotuli[52], Maier[53-55], Tuller[56], and Kosachi[36; 37]. The study of phenomena involving fast ion transport at interfaces and the nano-scale has been termed “nanoionics”.

In polycrystalline solid state ionic conductors, individual grains are sintered to form a dense body. Sintering parameters can be adjusted to increase grain or grain boundary volume to maximize beneficial properties or limit detrimental properties. When grain size is large, as shown in Figure 10A the grain bulk properties of the material dominate the properties of the sample. When grain size is reduced to the nanoscale, as shown in Figure 10C, the large surface area of the grains leads to significant grain boundary volume in the dense body. As the size of the grains decreases further, the bulk properties of the solid state ionic conductor become insignificant and the grain boundary (interfacial) properties dominate the total materials properties.

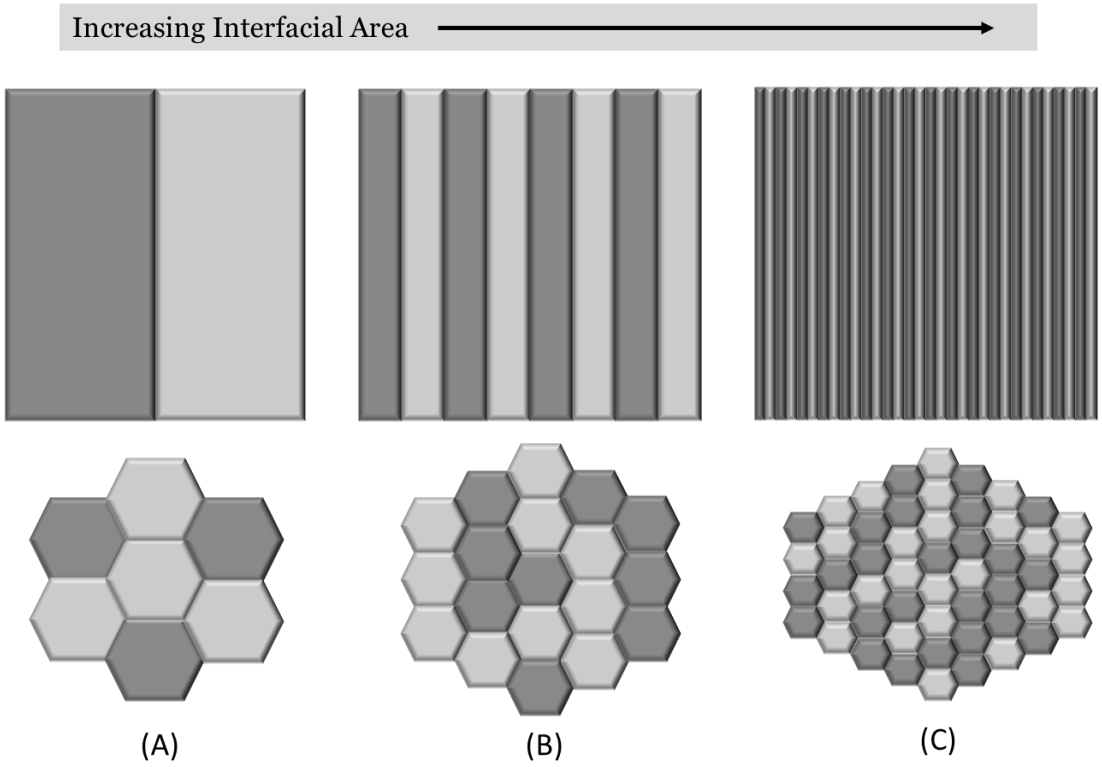

Figure 10 Schematic of the effect of reduced grain size on interfacial area in a polycrystalline material

In the field of nanoionics, positive effects on ionic transport at interfaces are pursued and samples with maximum interfacial volume are fabricated to enhance total ionic transport. The ideal case for optimization of interfacial effects in ionic conductors is shown in Figure 11. When the interface volume is maximized the total conductivity of the sample is much larger than the conductivity of either constituent phase.

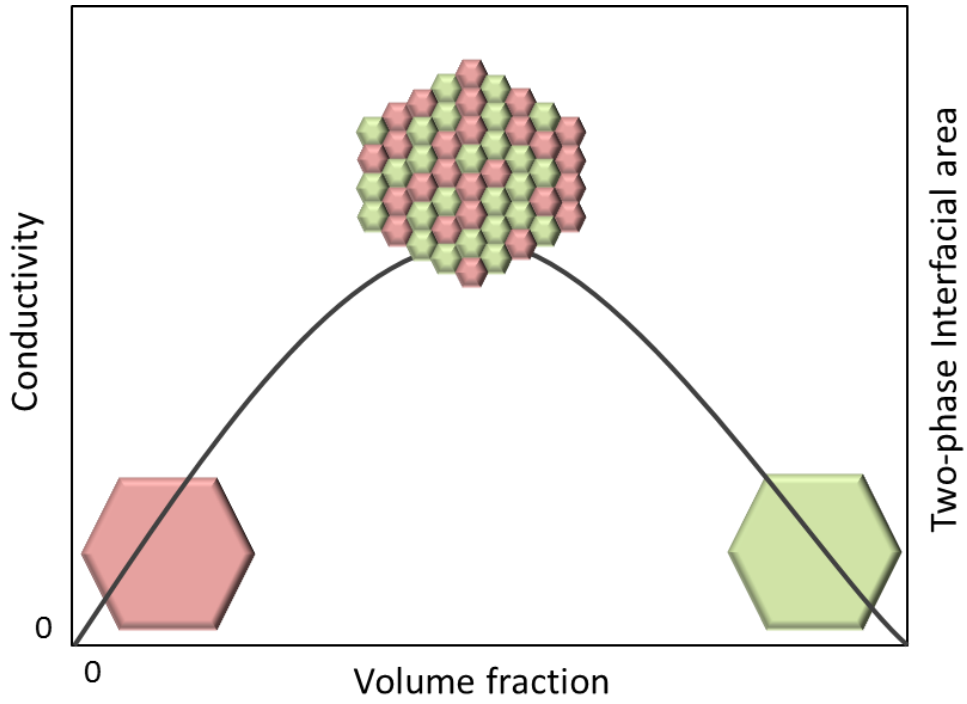

Figure 11 Representation of synergistic, two-phase interfacial area effect on ionic conductivity. Modified based on Maier (2014). [57]

For ionic transport, the interface can become a trap to mobile charge carriers or a superconductive transport highway. The interface is capable of increasing or decreasing the ion concentration depending on the nature of the interface. It is necessary to characterize the interfacial properties of each nanostructured solid state ionics system to understand the effects on charge carrier concentration and mobility. Fundamental studies of ionic transport in bulk materials are possible with density functional theory (DFT) and molecular dynamics (MD) techniques, however, fundamental study of ionic transport at the interface has been limited and is not easily studied by computational methods. Although new computational approaches are being pursued, experimental techniques are valuable for understanding the real ionic transport properties of interfaces.

Interfacial effects that will be studied in this work include the **space charge effect**, the **strain effect**, and the **curvature effect**. The space charge effect is caused by redistribution of charge carriers at the interface due to a charged grain boundary core. The strain effect is caused by crystal lattice rearrangement at the interface. The curvature effect is caused by the surface energy of nano-sized grains.

The ionic conductivity, σ, is the product of charge carrier concentration (*n* or *c*), charge of the carrier (q), and the mobility of the charge carrier (μ), as shown in Equation 14. All interfacial effects on ionic conductivity, studied in this work will result from changes in number of charge carriers or mobility of charge carriers at the interface.

$$\sigma = n \cdot q \cdot u \tag{14}$$

We will come to the physical limitations of achieving dense solid state ionic conductors while maintaining nano-size grains and ways to experimentally verify the interfacial phenomena in the following chapters. However, we will first look in depth at the space charge, strain and curvature effects reported in the literature.

2.3 Discovery of interfacial effects in solid state ionic conductors

Studies of the LiI-Al_2O_3[58] composite material system, an ionic conductor/insulator composite, were the first experiments to unravel interfacial effects on ionic conductivity. The volume fraction of Al_2O_3 in LiI was systematically increased from 0 mol% to 60 mol% and conductivity measurements were collected. The ionic conductivity of the system increased by one order of magnitude with 40 mol% Al_2O_3 at 25^{o}C and the OCV of a Li/LiI-Al_2O_3/PbI_2,Pb galvanic cell confirmed the lack of electronic conductivity. When considering no interfacial effects on transport, the addition

of Al_2O_3 to LiI should slightly decrease ionic conductivity due to blocking effects. However, interfacial effects between the Al_2O_3 and LiI phases explain the anomalous behavior. Conduction by Li^+ vacancies in LiI-Al_2O_3 was assumed due to lack of change in the activation energy of the transport process for the composite sample.

After discovery of the anomalous enhancement of ionic conductivity in the LiI-Al_2O_3 system, the mechanism for the dramatic enhancement was debated by Wagner of Arizona State University[59; 60], Maier of the Max-Planck-Institut für Festkörperforschung[61-68], Dudney of Oak Ridge National Lab[69-71], and Goodenough of the University of Texas at Austin[72; 73]. Maier's publications on interfacial effects on ionic transport have continue to the present day[57] and have expanded research on the topic of solid state ionic conductors.

2.3.1 Space charge effect on ionic conductivity in solid state ionic conductors

In polycrystalline ionic conductors, charged interfaces create "space-charge regions" which drastically alter the concentration and/or mobility of ions. The space charge effect has been attributed as the cause of drastic changes in ion transport in ionic conductors with low extrinsic doping concentration. The explanation of enhanced Li^+ transport in the LiI-Al_2O_3 composite system has been explained by a space charge argument. By adding γ-Al_2O_3, high concentrations of Li vacancies, V'_{Li}, are formed due to adsorption of Li^+ on the surface of the γ-Al_2O_3 particles. In this way, no other charge compensating defects are necessarily formed and the increased concentration of Li vacancies increases the ionic transport.[74] The space charge effect in LiI-Al_2O_3 is represented schematically in Figure 12. In the space charge region around the Al_2O_3 particle, shown in Figure 12A, the concentration of Li^+ is dramatically decreased and the

concentration of V'_{Li} is enhanced, as seen in Figure 12B. The high concentration of V'_{Li} enhances transport in those regions. As the concentration of Al_2O_3 increases to 40 mol% the ionic conductivity of the sample increases dramatically due to increased space charge regions in the sample. However, above 40 mol% the Al_2O_3 concentration has a blocking effect on ionic conductivity and the ionic transport of the system is decreased. This effect is shown in Figure 12C & 12D.

The space-charge argument used to explain ionic conductivity in the LiI-Al_2O_3 system has been used in similar composite systems demonstrating enhanced ion transport properties including β-AgI/Al_2O_3, AgCl/Al_2O_3, CuCl/Al_2O_3, HgI_2/Al_2O_3, LiBr-H_2O/Al_2O_3 and LiCl/Al_2O_3 (with alternate insulating phases including SiO_2, fly ash, and αFe_2O_3).[69]

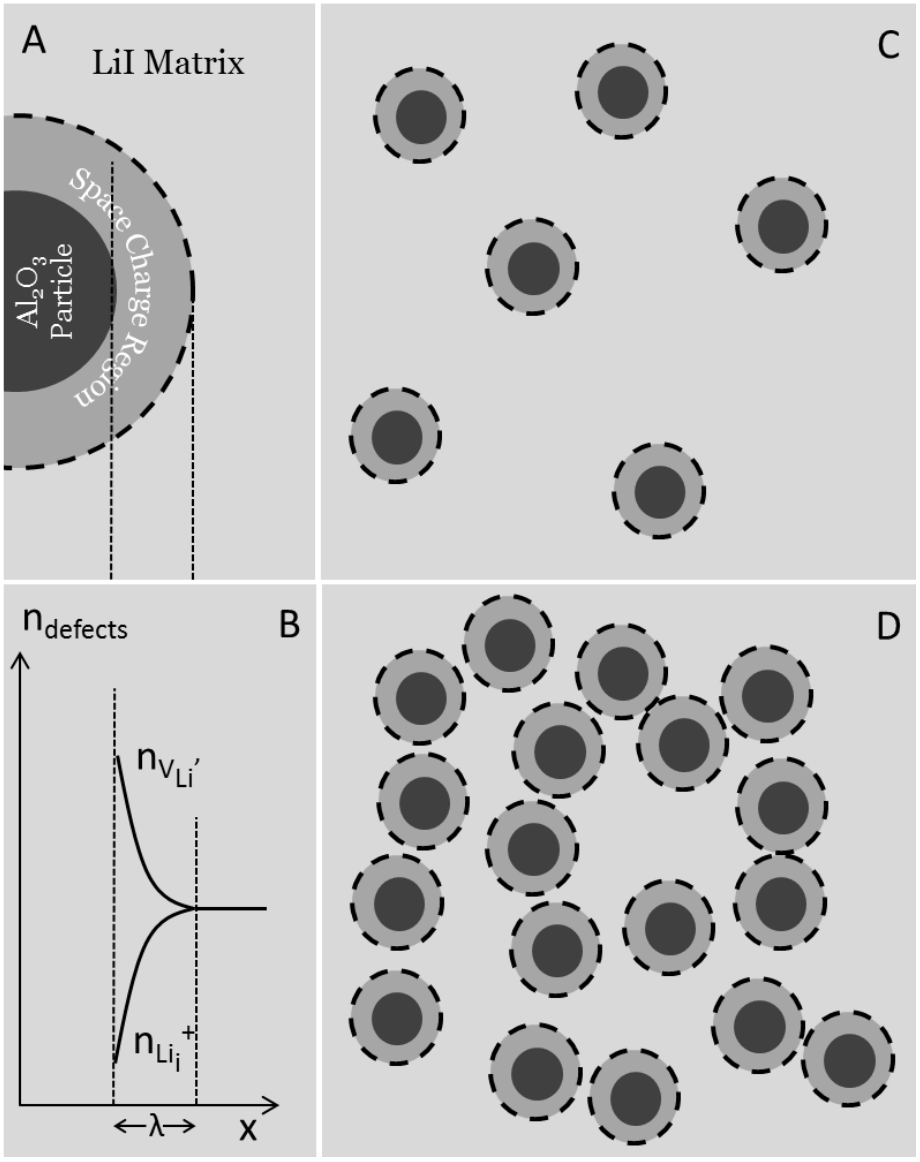

Figure 12 Schematic representation of (A) space-charge effect at a single Al_2O_3-LiI interface, (B) defect concentration changes at interface, (C) Al_2O_3 dispersed particles below maximum conductivity threshold, and (D) Al_2O_3 dispersed particles above maximum conductivity threshold causing blocking of transportation pathways.

In another highly cited example of interfacial effects on ionic conductivity, a nanostructured CaF_2/BaF_2 composite was fabricated by pulsed laser deposition (PLD) and the electrical properties were measured as a function of individual layer thickness while total thickness was constant. As seen in Figure 13, the total conductivity of the composite structure increased as the number of CaF_2/BaF_2 interfaces increases. The total

conductivity of the composite structure is higher than the bulk conductivity of either of the individual components.

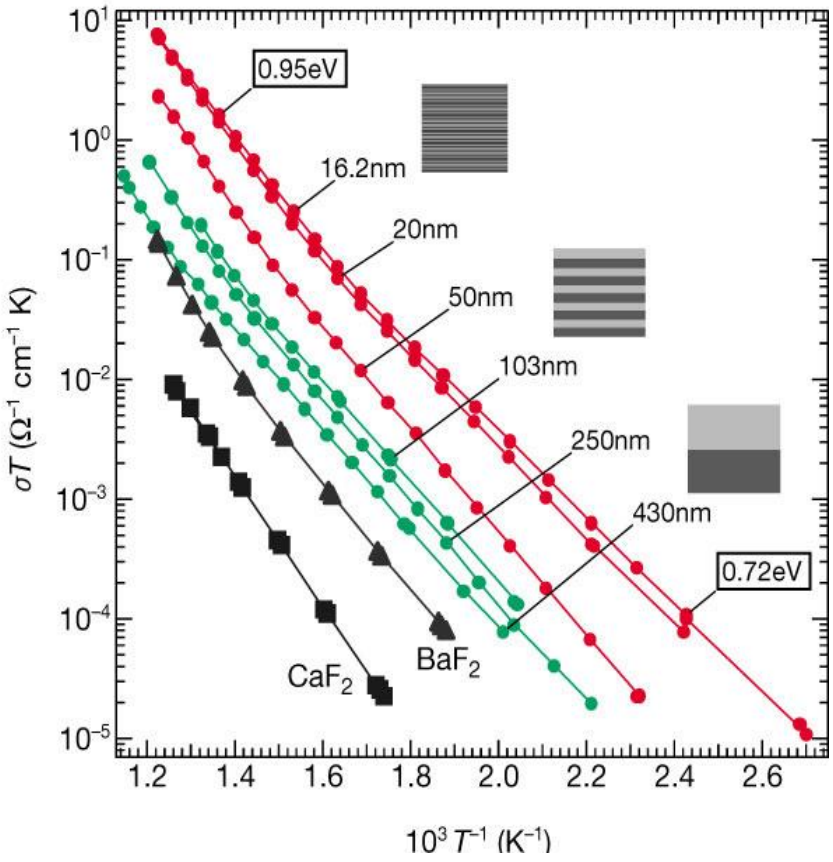

Figure 13 Conductivity as a function of temperature for CaF_2 BaF_2 heterostructure; interfacial effects contribute to significant electrical conductivity enhancement

The space charge region at the CaF_2/BaF_2 interface leads to enhanced charge carrier density of F^- in the CaF_2 phase. The origin of the space charge region, formed at interfaces in ionic conductors is the space charge potential[75] or "core charge" formed at the interface. The excess charge at the grain boundary/interface will lead to a development of a *space charge region* which extends into the bulk phase. The space charge region is proportional to the Debye length, λ, which is given by Equation 15. The Debye length is inversely proportional to the concentration of charge carriers in the bulk

phase, *C*. The space charge region will lead to a depletion or enrichment of charge carriers which will have obvious effects on the ion conductivity of the material.

$$\lambda = \sqrt{\frac{\varepsilon RT}{2Z_1^2 F^2 C_{1\infty}}} \tag{15}$$

Electroneutrality of the bulk is disrupted at the interface due to the charged interface/grain boundary core. The development and quantification of the core charge, however, is not straightforward and depends on the material system in consideration. The core charge (space charge potential) has been indirectly calculated in $SrTiO_3$ at high and low symmetry grain boundaries from diffusion experiments[75] but is not easily measured directly.

A core charge can be formed at heterogeneous interfaces, leading to a space charge region and space charge effects. In the LiI-Al_2O_3 composite electrolyte example from Liang,[58] the presence of OH^- groups on the interface of Al_2O_3, which are used in the atomic layer deposition technique and also effect the catalytic properties of well-known oxides including alumina and silica,[63] form a negative core charge at the LiI-Al_2O_3 interface. The negative core charge attracts Li^+, creating excess V'_{Li} and enhancing transport in the space charge region. Although an in-depth discussion of the surface effects at particular oxides studied in this dissertation will be discussed in the experimental results sections, generally, core charges at interfaces and grain boundaries will tend to stabilize defect formation at the interface or destabilize the surface defect. If the interaction with the second phase repels the defects the defects will be driven into the bulk and possibly into interstitial sites in the matrix. If the second phase interaction is

attractive, ions and defects will be drawn out of the bulk to the interface. These core charges will undoubtedly affect the transport properties in the material in the space charge region at the interface.

A core charge can be formed at homogeneous interfaces due to low formation energy for defect formation at the interface. Sayle[76] reports that the formation of oxygen vacancies at the surface or interface of CeO_2 is more thermodynamically favorable than formation of vacancies in the bulk. The defect reaction is written in Equation 16 where *S* represents a surface site and *M* is a bulk site. This preference for vacancies at the interface leads to a positive core charge which can significantly alter the transport properties of the system.

$$M_s + V_{\ddot{M}} \leftrightarrow M_M + V_{\ddot{s}} \tag{16}$$

Additionally, the defect formation energy is dependent on the crystallography of the surface at the interface. Based on calculations,[76] the relative stability of CeO_2 surfaces is (111) > (110) > (310). A schematic of the (310) surface of CeO_2 is shown in Figure 14. The surface features, including steps, flats and corner sites can be visualized as important features which impact the energy for defect formation.

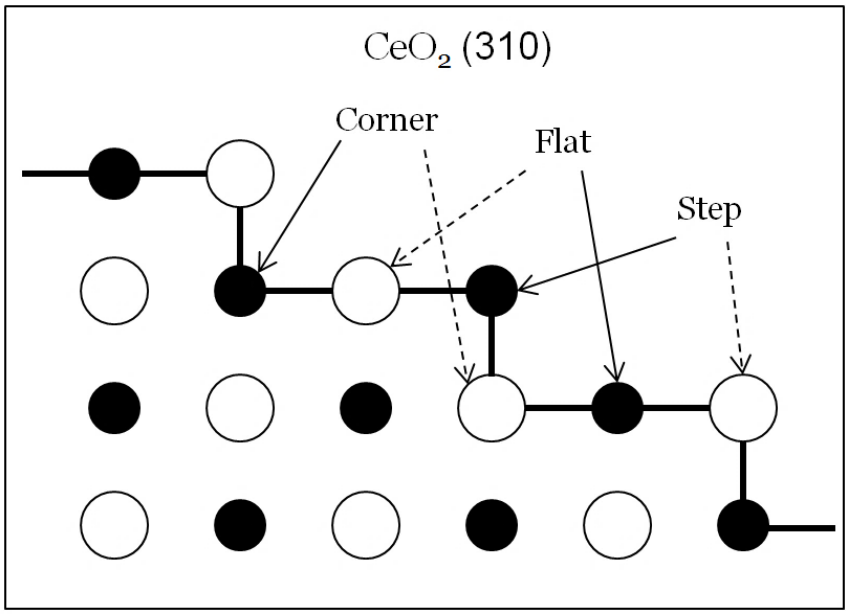

Figure 14 Schematic of CeO_2 (310) surface with step, flat, and corner sites representing the variation in surface chemistry that effects the formation energy for defects at the surface. (Reproduced from Sayle[76])

To understand the effect of core charge on the defect concentration of a solid state ionic conductor, an example is given. For B-site doping of Yttrium in $BaZrO_3$ the defect reaction is written in Kroger-Vink notation in Equation 17. Positively charged oxygen vacancies, $V_o^{\cdot\cdot}$, are created by acceptor doping. In low pO_2 atmospheres additional oxygen vacancies and charge compensating electronic defects are formed in the material system, according to Equation 18.

$$Y_2O_3 \xrightarrow{BaZrO_3} Y'_{Zr} + V_o^{\cdot\cdot} + 2O_o^x \tag{17}$$

$$O_O^x \leftrightarrow V_o^{\cdot\cdot} + \frac{1}{2}O_2 + 2e' \tag{18}$$

If a hypothetical positive core charge is present at grain boundaries, oxygen vacancies will be repelled from the grain boundaries, electrons will be attracted to the grain boundaries and dopant atoms will remain constant in the material. Therefore the

grain boundaries will block ionic transport in the system and the electronic conductivity will be enhanced.

In summary, a space charge region develops due to the core charge (space charge potential) which leads to non-intuitive effects on ionic transport in the system. Systems with high interfacial volume, such as nanocrystalline electroceramics and heterostructured thin films of solid state ionic conductors, must be fabricated and tested to determine if space charge effects contribute significantly to transport properties. If a significant effect is measured, a detailed study of the interface is necessary to determine the mechanism for the core charge and the space charge effect in the system.

2.3.2 Strain effect on ionic conductivity in solid state ionic conductors

The effect of strain on ionic transport has been studied extensively by Korte, C., Janek, J. et al[77-79] in Germany and by additional researchers in the United States over the past decade. Primarily, thin film samples with coherent, semi-coherent or incoherent heterophase boundaries have been studied. These samples include heterostructure samples and single film samples with up to 8% lattice mismatch and significant strain at the interface.[36; 37; 78-80] Remarkable enhancements in ionic transport in the systems have been reported.[80] The most succinct experimental results of the strain effect on ionic conductivity are shown in Figure 15.[79; 81] A series of well-defined heterostructure ionic conductor (YSZ)/ insulator samples with defined lattice mismatch were fabricated. The ionic conductivity of the samples was measured and plotted as a function of interface mismatch. As seen in Figure 15, the transport properties of the heterostructure samples are linearly correlated to the interface mismatch of the systems. When compressive strain

is imposed on the lattice the transport properties are suppressed. Conversely, when a dilatative strain is imposed on the lattice the transport properties are enhanced.

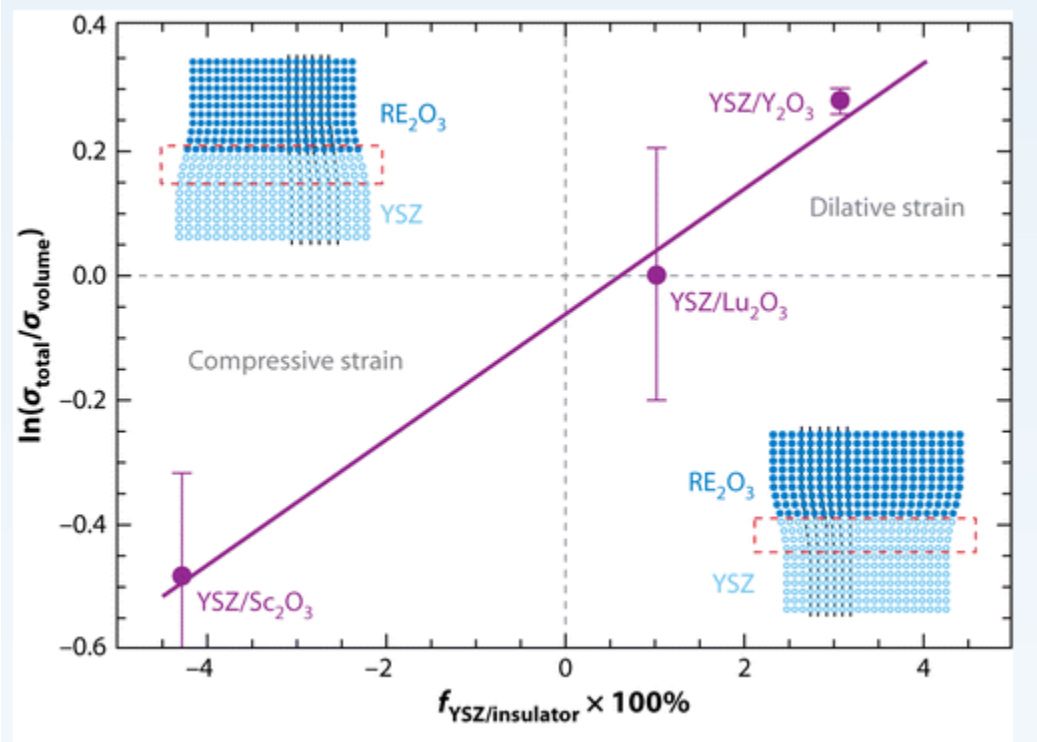

Figure 15 Plot of the logarithm of the total heterostructure sample conductivity relative to the bulk conductivity versus the lattice mismatch factor, $f_{YSZ/ins}$. (Taken directly from Tuller Bishop 2011 Review – Point defects in oxides.[81] Originally from Schichtel N, Korte C, Hesse D, Janek J. 2009.[79])

Lattice mismatch imposes strain on the lattice which changes the volume of the crystal structure unit cell. In general, the volume of the lattice is closely related to the energy required for ion transport. As the ion moves from one stable site to another, in the crystal lattice, it passes along pathways that are crowded by other ions in the crystal. The pathway is composed of sites of higher energy that are not stable sites for the mobile ion. The critical radius, r_{crit}, is the high-energy point between stable lattice positions and is primarily responsible for the energy required for charge carrier transport. As the lattice is strained, the volume changes which changes the energy necessary for transport. In

general, as the lattice expands the energy required for ion transport is reduced. As the lattice is compressed the energy required for ion transport is enhanced. A simple graphic showing the effect of strain on the saddle point for oxygen vacancy transport is shown in Figure 16. In models that are more complicated, the effect of ion vibration in the lattice on the critical radius and transport energy is considered.

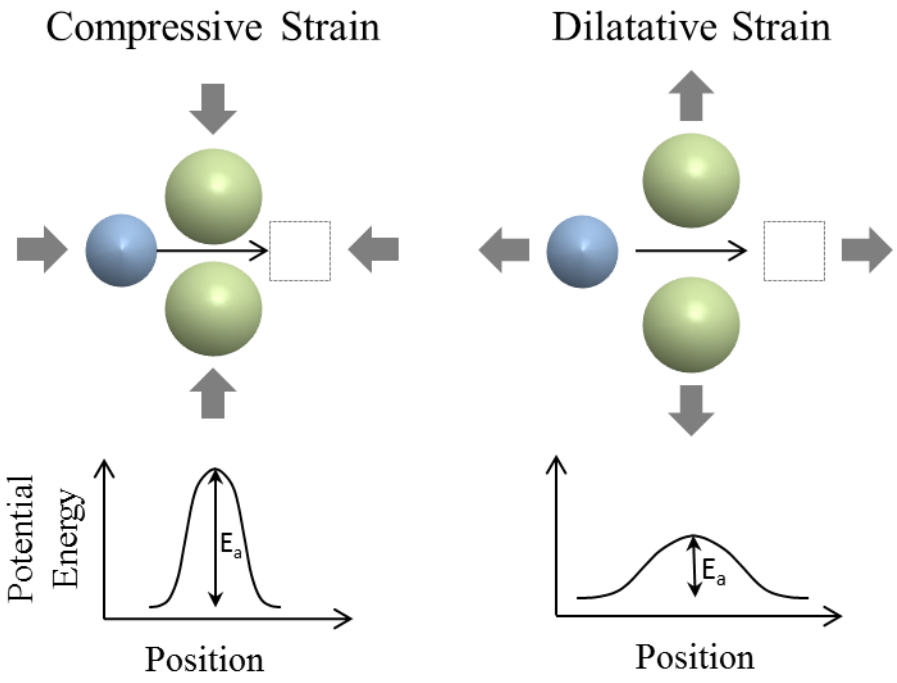

Figure 16 The effect of compressive (left) and dilatative (right) strain on the critical radius of the saddle point along the vacancy transport pathway and corresponding changes to migration energy in response to lattice strain

The change in volume of the lattice during migration to accommodate the transporting ion is the migration volume, ΔV_{mig}, which is related to the lattice volume, V_{latt}, bulk modulus, B, and migration energy, ΔE_{mig}, by Equation 19.[82]

$$\Delta V_{mig} \approx -\frac{V_{latt}}{B}\left(\frac{\partial \Delta E_{mig}}{\partial V_{latt}}\right)_T \tag{19}$$

When considering oxygen vacancy transport along the <100> direction in cubic, fluorite-structured CeO_2, the variation of migration energy, ΔE_{mig}, for the oxygen vacancy as a function of isotropic strain has been calculated by DeSouza, R. et al. and is plotted in Figure 17.[82] Compressive strain increases the energy required for oxygen vacancy migration while dilative strain decreases the energy required for migration.

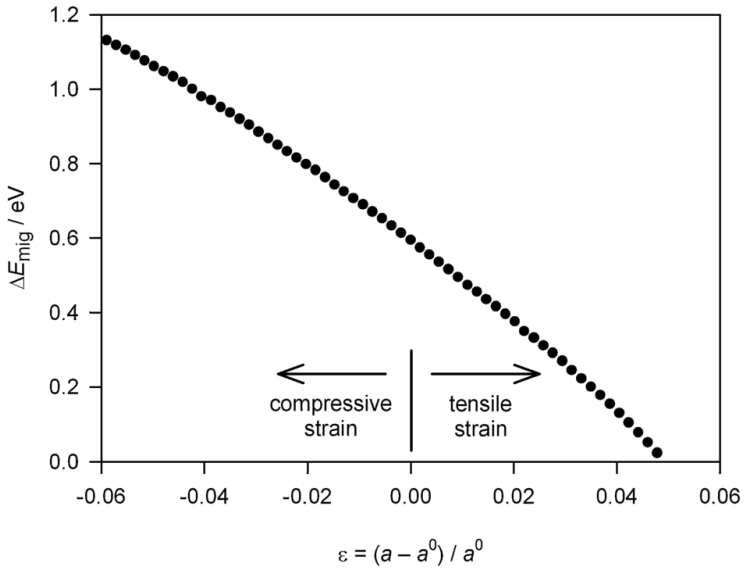

Figure 17 Activation energy of oxygen-vacancy migration, ΔE_{mig}, in CeO_2 as a function of isotropic strain, where a^o is the ambient pressure lattice constant of CeO_2.(Taken directly from DeSouza et al.)[82]

Although the effect of strain is straightforward, lattice mismatch is often accommodated by defect formation at the "strained interface" as well as significant crystal structure changes. These effects are hard to model and real interfaces with lattice mismatch must be carefully characterized to determine the strain effect on ionic conductivity. The strain effect is a promising interfacial and nano-scale effect which can dramatically effect ion transport properties of doped solid state electrolytes.

2.3.3 Curvature effect on ionic conductivity in solid state ionic conductors

For nano-grain systems, surface tension effects on the energy of the system are important and can lead to excess charge at the interface. For a large particle, the surface tension component of the chemical potential is insignificant, however, as the curvature of the particle increases (radius decreases) the surface tension component of the chemical potential must be considered. The effect of curvature on surface energy and defect concentration and/or mobility at the nano-particle interface is called the curvature effect.

The chemical potential, $\mu(\bar{r})$, of a Wulff crystal with average radius, $\bar{r}$, is given by Equation 20 where, γ is the surface potential, r is the radius of the crystal, V is the volume of the crystal, and $\mu\ (\infty)$ is the chemical potential of the crystal with infinite bulk to surface ratio.[54] As the radius of the crystal (grain, particle, etc.) decreases the chemical potential increases.

$$\mu(\bar{r}) = \mu\ (\infty) + 2\frac{\bar{\gamma}}{\bar{r}}V_m \tag{20}$$

The effect of surface tension on the thermodynamic properties of materials is evident in the systems of nanoparticle Au or Pt. The melting point of nanoparticles of Au and Pt are depressed by hundreds of degrees Celsius due to the effect of surface tension on the chemical potential of the material.[83]

The surface tension effect on chemical potential of a metal has been measured as an excess EMF, ΔE^{ex}, between a microcrystalline silver electrode and a nanocrystalline silver electrode with an appropriate ionic conductor as electrolyte between the electrodes.[84] Similar measurements that quantify the excess Gibbs energy of the nanocrystalline structure in comparison to the microcrystalline structure have been

published for nano-sized Cu electrodes[85]. The described cell is represented in Equation 21 and the EMF of the cell is represented by Equation 22.

$$M_{nanocrystalline}/M^{z+}\ electrolyte\ /\ M_{microcrystalline} \tag{21}$$

$$\Delta E^{ex} = E_{mc} - E_{nc} \tag{22}$$

The curvature effect will be considered in nanocrystalline systems where the particle size is significantly reduced. The curvature effect is especially significant when distinguishing effects between thin film samples, possessing no curvature, and nanocrystalline samples. The curvature effect will be applied in this way in Chapter III.

2.3.4 Undesired interphase formation effect on ionic conductivity in solid state ionic conductors

Interphases, phases formed by chemical reaction at heterogeneous interface or by segregation of impurities from precursor materials, can form at grain boundaries/interfaces and block conduction pathways. Special care must be taken to reduce impurities in the matrix and to ensure chemical stability of both phases to prevent the interface blocking effect. Gerhardt and coworkers measured suppressed transport properties at grain boundaries in trivalent-doped CeO_2. [86; 87] Although the blocking effect was first investigated as related to dopant segregation at the interface, the authors determined that the blocking effect was due completely to the formation of a Si-rich phase at the interface which physically blocked the conduction pathway in the material. After eliminating Si impurities from the precursor materials the blocking effect was eliminated.

Careful interpretation of effects at grain boundaries and interfaces on charge transport must be completed before conclusions are reached. Many effects, including low concentration blocking phases, can be responsible for dramatic changes in electrical properties of solid state ionic conductors at interfaces and grain boundaries.

2.4 Conclusion

Unique effects on transport mechanisms occur in materials at nanometer length scales. Interfacial and nanoscale effects on heat and electronic transport properties have been briefly reviewed. Interfacial and nanoscale effects on ionic transport have been dealt with in more detail. The first ionic conducting system which exhibited enhanced ionic conductivity due to interfacial effects, LiI-Al_2O_3, and the explanation for the enhancement have been introduced. Current work on the strain effect has also been reviewed. The possible interfacial effects at interphase boundaries in solid state ionic conductors, presented in this chapter, are summarized in Figure 18. These effects will be considered for interpretation of the electrical properties measured in the following chapters.

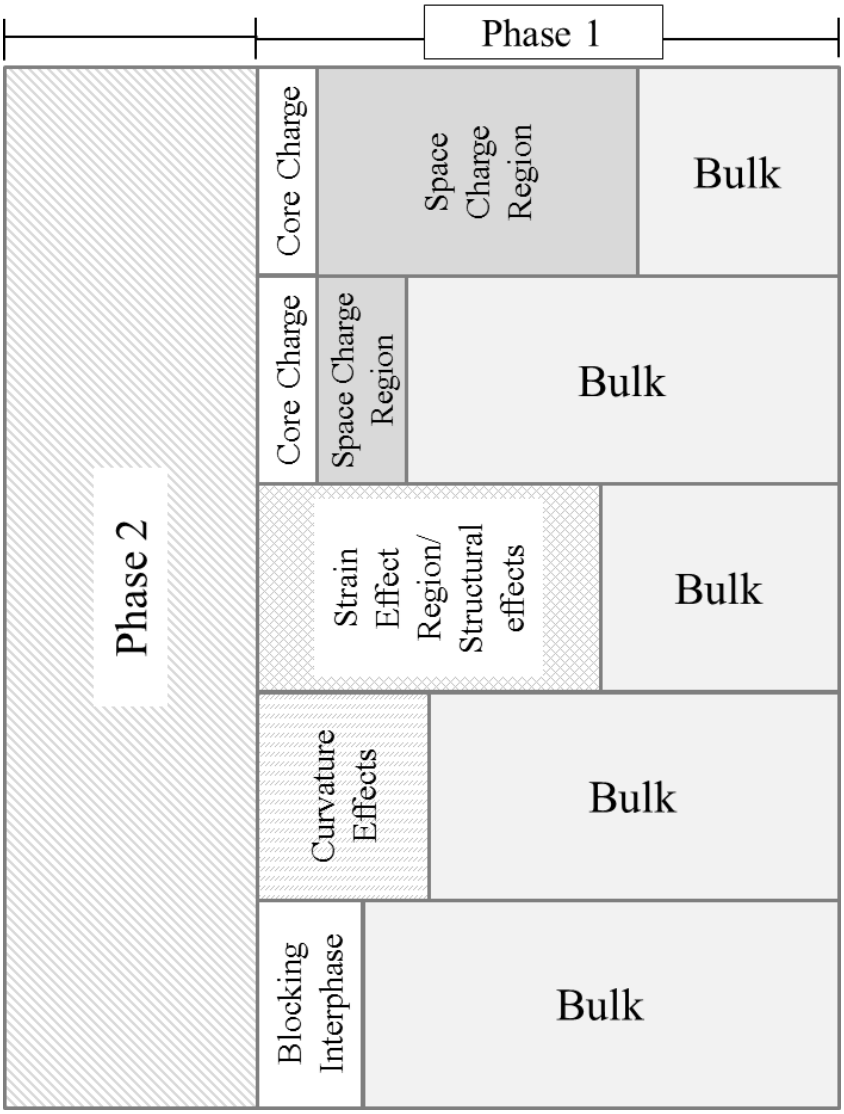

Figure 18 Possible effects on ionic conductivity at the heterophase interface as presented in this chapter including space charge effects, strain effects, curvature effects, and blocking interphase effects.

CHAPTER III

Interfacial effects on electrical conductivity in nanocrystalline and thin film doped-CeO_2

3.1 Introduction

While it is known that the electrical conductivity of a solid electrolyte is often sensitive to its nanostructure, the detailed mechanisms of ionic and electronic transport in nanostructured electrolytes are yet to be established. The main objective of the studies described in this chapter is to investigate the interfacial and nanoscale effects on ionic conductivity in $Sm_{0.2}Ce_{0.8}O_{1.9}$ (SDC20), a promising intermediate-temperature fuel cell electrolyte. Chapter II outlined the known effects on charge carriers at interfaces and on the nanoscale. These effects modify either the concentration or the mobility of the mobile charge carriers in ionic conductors, as listed in Table 2. Depending on the type of conductivity (ionic or electronic) and the magnitude of conductivity desired, these effects can be used to dramatically enhance ionic conductivity of existing ionic conductors for application as solid state electrolytes. As the grain size of a dense solid electrolyte is reduced, the interfacial volume to bulk volume increases and interfacial effects begin to play a role in the total transport properties of the material. In this section alternative sintering and consolidation techniques have been used to create dense, nanocrystalline Sm^{3+} doped CeO_2 samples, which are difficult to fabricate using conventional sintering, and their electrical properties have been tested. Additionally, SDC20 thin films with high interface to bulk volume ratio have been fabricated and their electrical properties have been studied. A new insight into the effects that occur at the interfaces and grain

boundaries of doped CeO_2 has been gained through the study of these nanocrystalline and thin film samples. A deeper understanding of the effects and the fabrication techniques, which enable beneficial interfacial effects to occur, will allow further development of solid state electrolytes for high performance, low operation temperature fuel cells.

Table 2 Potential interfacial effects on charge carrier concentration and mobility in doped CeO_2 that would enhance ionic transport in the solid state electrolyte

Potential uses of interfacial effects in doped CeO_2 for SOFC electrolyte application
1. Increased oxygen vacancy concentration, $\uparrow C_{V_o^{\cdot\cdot}}$
2. Increased oxygen vacancy mobility, $\uparrow \mu_{V_o^{\cdot\cdot}}$
3. Decreased electronic defect concentration, $\downarrow C_{e'}$
4. Trapped/Blocked e^- defects, $\downarrow \mu_{e'}$

3.2 Background

CeO_2 is a mixed ionic and electronic conductor with oxygen vacancy, $Vo^{\cdot\cdot}$ and excess electronic defects, e', as verified by Tuller[88], Huang and Goodenough[89], et al.[90] To increase the concentration of oxygen vacancies, $Vo^{\cdot\cdot}$, CeO_2 is doped by acceptors such as Gd^{3+}, Sm^{3+}, or Y^{3+}. Oxygen vacancies are formed according to equation (23).

$$Sm_2O_3 + 2Ce_{Ce}^{X} + O_o^{X} \rightarrow 2Sm_{Ce}^{'} + V_o^{\cdot\cdot} + 2CeO_2 \quad (23)$$

Maximum ionic conductivity has been measured in 20mol% doped-CeO_2, $Ce_{0.8}Sm_{0.2}O_{1.9}$, presumably due to the minimum distortion by Sm^{3+} on the cubic fluorite crystal lattice of ceria; however, the exact explanation for the optimal dopant ion is not in agreement among researchers[91]. Classic solid state electrolyte data from a well-

constructed experiment of the dopant concentration effect on Sm^{3+} doped CeO_2 is shown in Figure 19.[92]

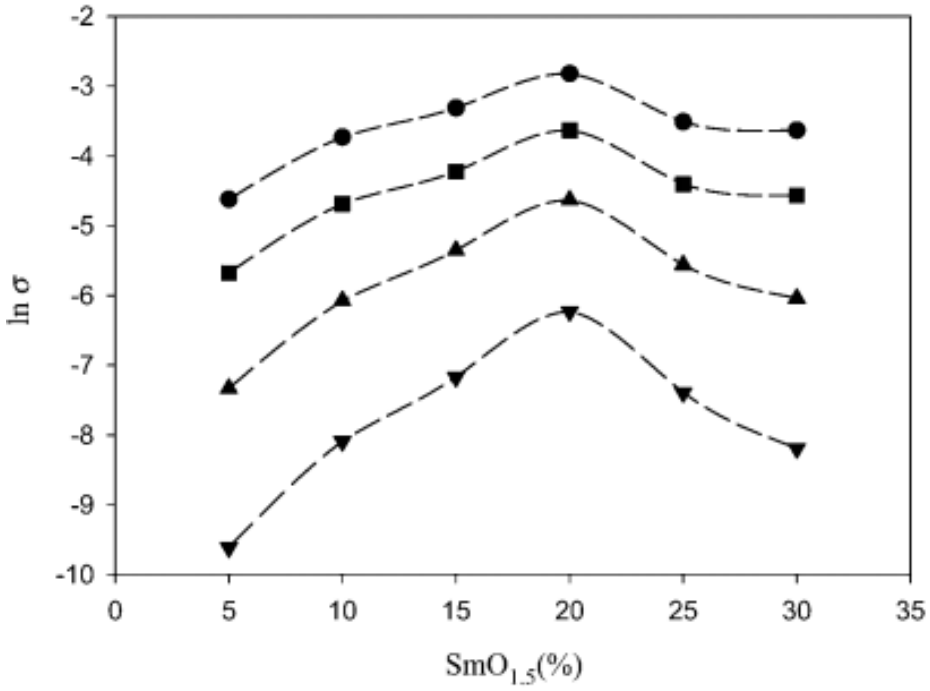

Figure 19 Electrical conductivity of Sm3+ doped CeO2 as a function of dopant concentration at 500oC (down triangles), 600oC (up triangles), 700oC (squares), 800oC (circles). Taken directly from Jung et al.[92]

In atmospheres with low oxygen partial pressure, P_{O_2}, oxygen vacancies and excess electrons form, leading to mixed electronic and ionic conductivity. The formation of oxygen vacancies and excess electrons at low $_PO_2$ occurs by equation (24). Additionally, at low $_PO_2$, Ce^{4+} can be reduced to Ce^{3+} also requiring the formation of charge compensating electronic defects.

$$O_o^X \leftrightarrow 2e^{'} + V_o^{\cdot\cdot} + 1/2O_2 \qquad (24)$$

Doped CeO_2 has high total ionic conductivity at intermediate temperatures (<600^oC) and is considered one of the most promising solid oxide fuel cell electrolytes

for intermediate temperature operation. The ionic conductivity of doped-CeO_2 is shown in comparison to other electrolytes in Figure 2A in Chapter 1. However, the electronic charge carriers present in doped-CeO_2 at low P_{O_2} conditions are detrimental for SOFC device efficiency. The anode side of the solid state electrolyte in the fuel cell configuration is exposed to reducing atmosphere (H_2) which creates electronic defects in the electrolyte and increases the electronic portion of the mixed conductivity. The increase in electronic conductivity reduces the Nernst potential of the cell and reduces the efficiency of the device. In actual devices an electronically blocking layer (such as YSZ) is used to block electronic conductivity but the layer also increases the total resistance of of the electrolyte, diminishing the benefit of the electronically blocking layer.

In order to understand the charge carrier concentrations and charge carrier mobility in un-doped and doped-CeO_2, other researchers have previously studied effects at interfaces in CeO_2.[54; 76; 93] At the interface surface of CeO_2, the formation energy for oxygen vacancy defect formation, according to Equation 24, has been calculated by Sayle[76] and reported by Maier[54]. Oxygen vacancy formation is thermodynamically more favorable at the interfaces than in the bulk, which increases the number of vacancies at the interface and encourages oxygen vacancy migration to the interfaces. Excess oxygen vacancy concentration at the CeO_2 grain boundaries is visualized in Figure 20. As related in equation 24 the formation of vacancies is accompanied by charge compensating electronic defects. Therefore, in nanostructured, un-doped CeO_2 it is expected that the electronic defect concentration and oxygen vacancy concentration will increase as the grain boundaries volume of the sample increases. The increased

concentration of both defects is expected to enhance total mixed grain boundary conductivity.

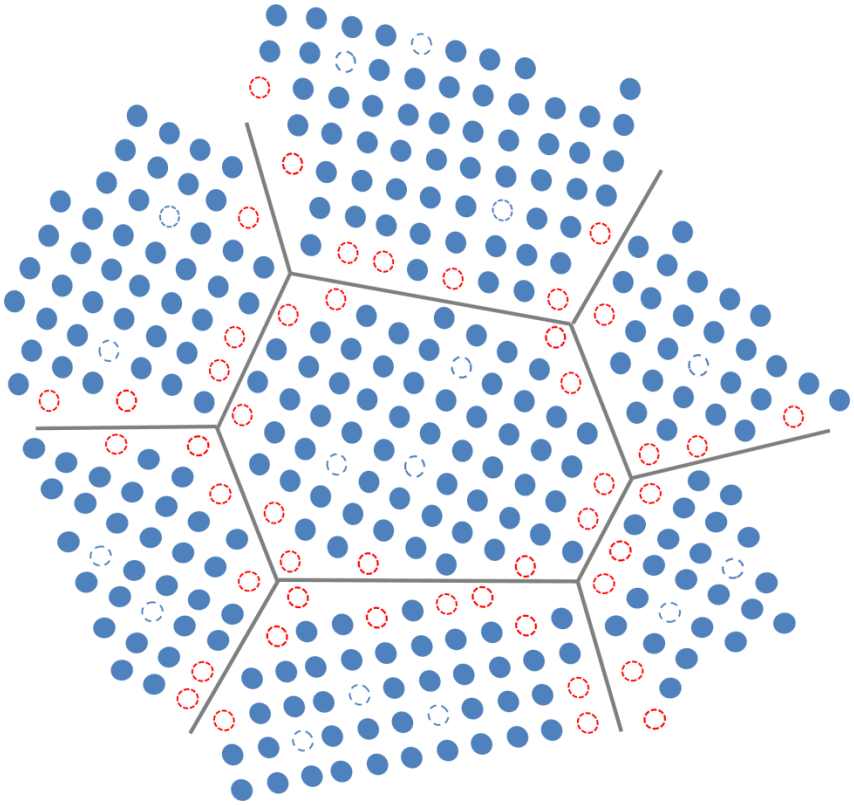

Figure 20 Sketch of CeO_2 grain boundaries (grey) with high oxygen vacancy concentration at the grain boundary/interface (red) and lower distribution of intrinsic oxygen vacancies in the bulk grains (dashed blue)

Because oxygen vacancy and electron defect concentration at the interface is expected to deviate from the concentration in the bulk, it is hypothesized that the ionic conductivity of an interface-dominated sample would have unique electrical properties. However, there is not a consensus in the literature on the effect of nanoscale grains on ionic conductivity of doped-CeO_2. Conflicting reports have been published. To summarize the contradiction in the literature over the effect of nanocrystalline doped CeO_2 on ionic conductivity, data[94] from Prof. Sossina Haile's group (Northwestern, Cal Tech) published in the Journal of the Electrochemical Society and data[95] from Anselmi-

Tamburini et al. (UC Davis) published in Advanced Functional Materials are plotted in Figure 21. In one data set the conductivity decreases with decreasing grain size. In the other the conductivity increases with decreasing grain size. With such contradiction the detailed effects of processing and testing from one laboratory to another, and the effect on reported results, are emphasized. One important distinction to note is that the density of the samples that show decreasing conductivity with decreasing grain size also decreases. In the work of Haile et al. the density of the sample with smallest grain size is only 92% which can have a significant impact on ionic conductivity of the sample. Additionally, recent low temperature measurements (<200^{o}C) of nanocrystalline CeO_2 have revealed the existence of proton conduction which may affect the data reported at such low measurement temperatures.[96] Another important work by Bellino et al. which reports a one order of magnitude increase in conductivity for nanocrystalline SDC10 compared to microcrystalline SDC10 is cited.[97]

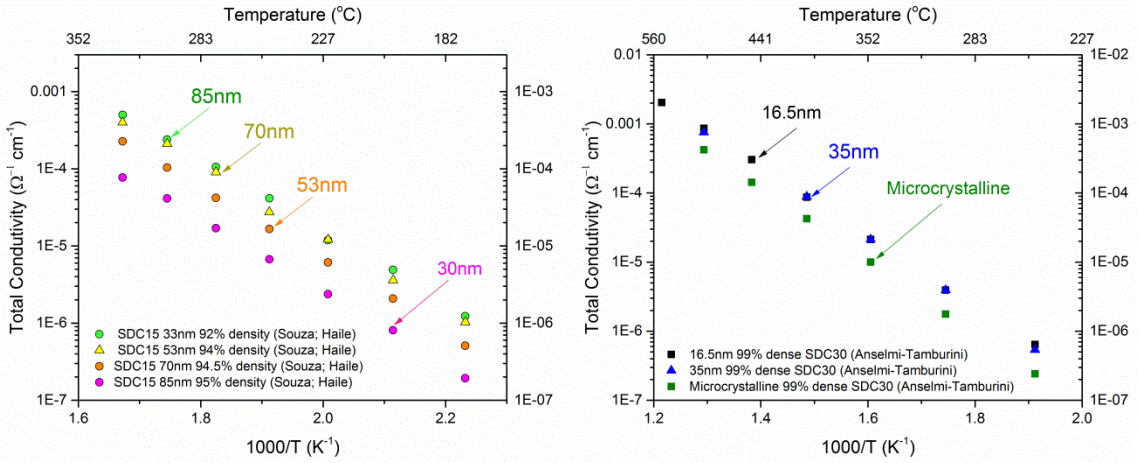

Figure 21 Ionic conductivity of Sm^{3+} doped-CeO_2 as a function of grain size from Haile et al.[94] (left) and Anselmi-Tamburini et al. [95] (right). The contradiction in the literature is highlighted due to increased total conductivity with grain size increase (left) and increased total conductivity with grain size decrease (right)

The space charge effect is another important effect that has been well documented in undoped-CeO_2 and should be considered when studying interfacial effects in these materials. Dr. Sangtae Kim and Dr. Joachim Maier have spent considerable time studying the space charge effect in un-doped and doped CeO_2.[98; 99] In CeO_2, it is hypothesized that a positive core charge (observed by trivalent dopant, Gd_{Ce}', segregation to grain boundaries in Gd-doped CeO_2 [100]) attracts negatively charged electronic defects and creates a space charge zone (SCZ) which blocks positively charged oxygen vacancies but attracts and provides a transport highway for electronic defects. This explanation is used to justify the low grain boundary conductivity measured in doped- and undoped-CeO_2 in the reported work of Guo, Maier et al.[101], Figure 23. However, several inconsistencies with the given hypothesis are immediately clear. First, the space charge zone in the heavily doped-CeO_2 sample will be much smaller than the space charge zone in the un-doped sample. The space charge zone is estimated by the Debye length where Debye length is proportional to $\sqrt{\frac{1}{C_i}}$ and C_i is charge carrier density .

$$\delta \approx \sqrt{\frac{D\varepsilon}{\sigma}} \approx \sqrt{\frac{kT\varepsilon}{z^2 i q^2 c_i}} \tag{25}$$

This is illustrated in Figure 22, which is a common graphical representation of the Debye length in aqueous electrolytes. The figure shows the effect of the Sm^{3+} dopants on the length of the space charge zone.

Therefore, the effect of the space charge zone on electrical properties will be minimized in the doped-CeO_2 sample.

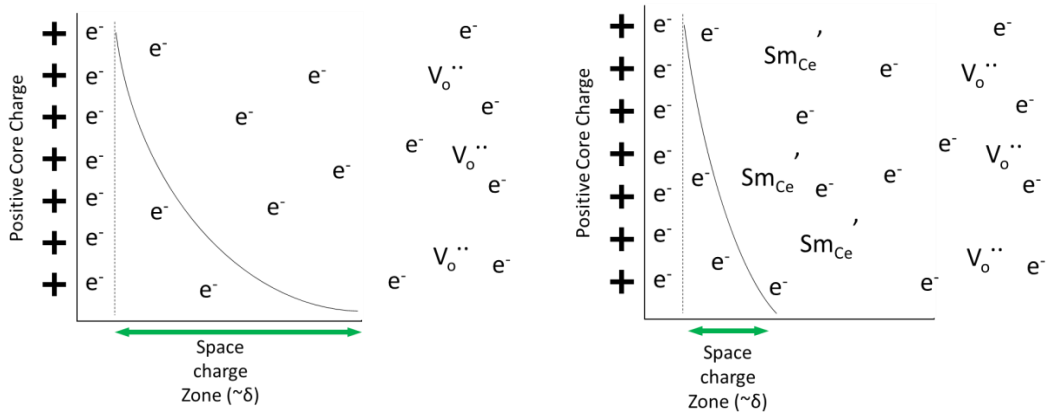

Figure 22 Schematic depicting the effect of number of charge carriers on space charge zone length in CeO_2 before (left) and after 20mol% doping of Sm^{3+} cations in the Ce^{4+} site (right).

Second, the electronic conductivity of nanostructured, doped-CeO_2 does not respond to changes in $_PO_2$ but undoped-CeO_2 does as verified by three experiments of Kim et al.[98], Tschöpe[93] and Guo, Maier et al. The data from Guo, Maier et al. is shown in Figure 23.

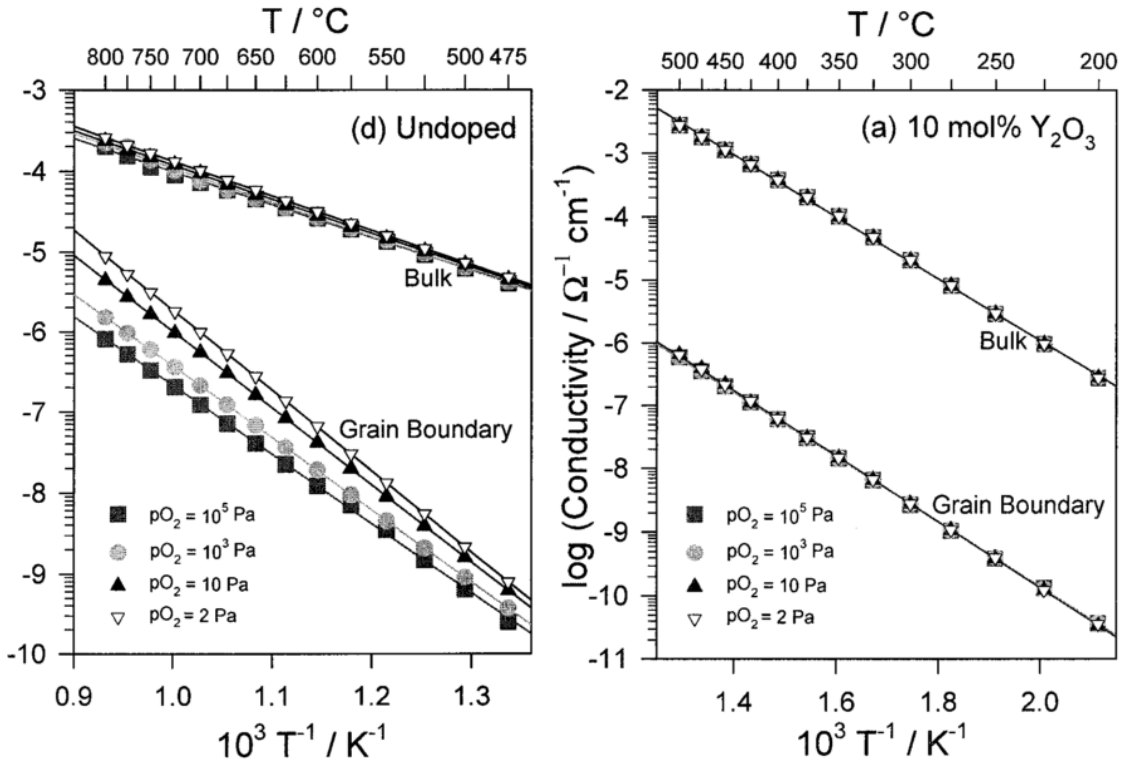

Figure 23 Temperature dependent grain boundary and bulk conductivities of undoped (left) and 10% Y_2O_3 doped microcrystalline CeO_2. Taken directly from Guo, Maier et al.[101]

As PO_2 decreases, the concentration of oxygen vacancies and electronic defects is expected to increase dramatically and the space charge effect, as proposed by Kim, should block ionic conductivity in both samples and further increase electronic conductivity in both samples. We do not see a change in electrical properties of nanostructured, doped-CeO_2 with changes in PO_2, therefore, it is suspected that the space charge effect does not play a large role in the electrical properties of the nanostructured, heavily doped-CeO_2 material. It is suspected that the change in PO_2 does not affect the conductivity of heavily doped-CeO_2 because the total change in charge carrier concentration is relatively small compared to the charge carriers present by extrinsic

doping of Sm^{3+} which creates a very large number of defects, far greater than the number of defects induced by the change in pO_2.

3.3 Theory

The theories of the interfacial effects that are expected to occur in SDC20 are covered in detail in Chapter 2. In this section we will look at the unique techniques used to fabricate the samples and then the next section will provide detailed information about the experimental procedures. To study the interfacial and nanoscale effects in Sm^{3+}-doped CeO_2, three types of samples were studied – nanocrystalline samples, thin film samples, and samples with a minority secondary phase. To form the samples, we used the conventional sintering technique, two-step sintering technique, dynamic shock consolidation technique, and pulsed laser deposition technique. Two-step sintering and dynamic shock consolidation are less utilized techniques in materials science and will be discussed here. The thin film sample series used to investigate the SDC20 interfacial effects will also be discussed.

3.3.1 Two-step sintering of nanocrystalline ceramics

Sintering is a critical industrial process for the manufacture of technical ceramics. At elevated temperatures and for extended time periods, the porosity between ceramic particles in a green body compact is eliminated due to atomic diffusion driven by the reduction of interfacial energy. Conventional sintering is carried out by heating the compacted powders to a certain temperature and holding at the temperature until the ceramic body is fully dense. During this process, grain growth accompanies the reduction of porosity due to the effort to reduce grain boundary area.

Due to the expected, advantageous variations in mechanical and electrical properties of nanocrystalline materials, researchers have attempted non-conventional sintering methods to reduce the grain size of dense body ceramics. These non-conventional methods include two-step sintering[102], spark plasma sintering[103], high pressure sintering[104], and microwave sintering[105]. Of each of the methods listed, two-step sintering (TSS) is the most likely to be adopted as an industrial process. For this reason, TSS, was used to prepare nanocrystalline SDC20 dense compacts for characterization of electrical properties.

TSS uses a two-step heating schedule for the sintering of compacted nano-grained ceramic particles to limit grain growth. An initial sintering temperature is reached to achieve >70% density. The initial temperature is held for a short time and then rapidly decreased to a lower, second sintering temperature. At the second temperature, grain boundary diffusion fills in the remaining open porosity while the particle network remains constant and grain growth is suppressed. The second temperature is maintained for an extended time (~20 hours) due to slower kinetics. A classic example of the effect of TSS on the densification and grain growth of Y_2O_3, taken from Chen and Wang (Nature, 404, 2000)[102] is displayed in Figure 24.

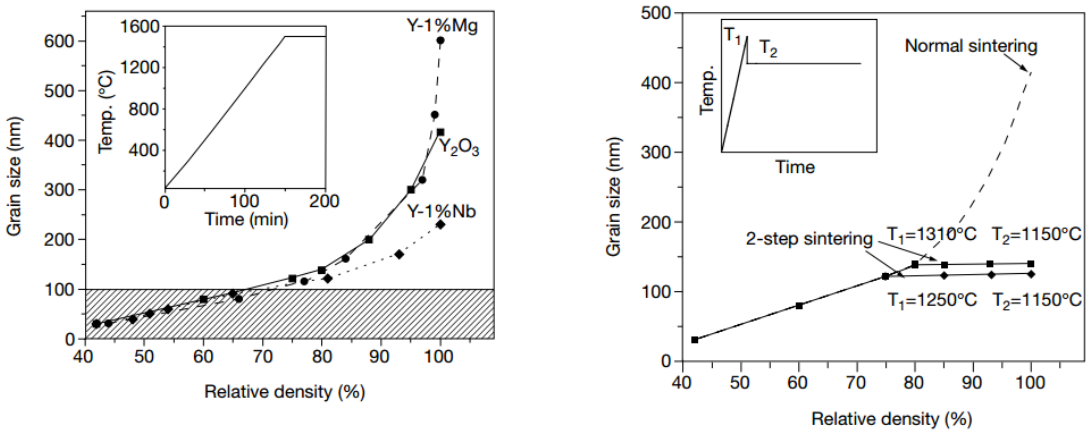

Figure 24 Example of the effect of conventional (left) and two-step sintering (right) on the grain growth and relative density of Y_2O_3. Taken directly from Chen and Wang.[102]

TSS is an industrially relevant technique for the production of dense, nanocrystalline ceramics and will be used in this work to fabricated dense, nanocrystalline SDC20 for the study of grain boundary effects on ionic conductivity.

3.3.2 Dynamic shock consolidation of nanocrystalline ceramic powders

Dynamic shock consolidation is an alternative method for fabrication of high density, nanocrystalline ceramic materials and a technique that Dr. Naresh Thadhani at Georgia Tech has a career of experience working with. Dynamic shock consolidation is achieved by impacting the green-body sample with a flyer plate accelerated by a projectile with velocity of ~1000m/s.[106] Dynamic consolidation occurs when the high-pressure shock wave generated by the impact of the flyer plate with the target sample imparts energy sufficient for interparticle fusion of the green body. As the shock wave propagates through the nanopowder, pore collapse occurs and friction between the nano-powder grains instigates localized heating at the grain surfaces.[107] Particle velocity obtained by the shock wave is very high, leading to plastic deformation and fracture of

the particles. A summary of the dynamic shock consolidation technique is shown in Figure 25.

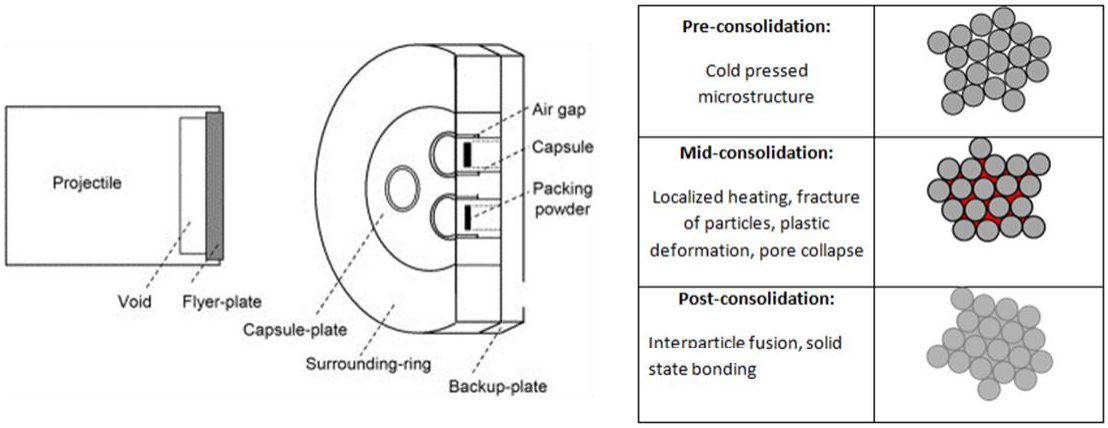

Figure 25 (Left) Schematic of dynamic shock consolidation projectile and impact zone including the sample capsule; (right) Visual representation of consolidation process in dynamic shock consolidation process.

Dynamic shock consolidation has been used to compact a variety of ceramic samples, including undoped and gadolinium-doped ceria,[106; 108; 109] Fe_3O_4[110], SiO_2[111], although most of the dynamic shock consolidation literature is focused on metals. In dynamic shock consolidation experiments of ceramic materials, two problems can interfere with achieving dense, high quality samples for electrical measurements. First, the wave propagation in the sample and sample capsule can cause the compacted sample to fracture. A consolidated sample with enough surface area to attach electrical contacts is necessary for measuring the electrical conductivity of the sample after consolidation. Second, a non-uniform microstructure could inadvertently be attained due to changes in pressure in the nanocrystalline sample as a function of time of the experiment. A non-uniform microstructure will lead to averaged electrical properties of the sample and difficulty in correlating the microstructure (grain size, grain boundary density) to the electrical properties.

Because of the short duration of the shock wave propagation during dynamic shock consolidation, a green-body of ceramic nanopowders is densified with minimum grain growth. Preserving the precursor particle size during densification is not possible with conventional sintering techniques due to unwanted grain growth during necessary holding times at high temperature. Dynamic shock consolidation prevents grain growth and can be used to fabricate nanostructured, dense ceramics that are not possible to fabricate by any other technique.

3.3.3 Systematic variation of interface to bulk volume ratio by variable thickness thin film series

Thin film fabrication techniques offer precise control of sample geometry and crystallinity which makes them a popular technique for determining the effect of interfacial properties on electrical transport in ionic conductors.[34; 35; 40; 77; 112-114] By systematically varying the thickness of SDC20 thin films on single crystal substrates, the interface-property-dominated film volume can be altered and the electrical property trends of the sample can be correlated to the interfacial properties. This concept is illustrated in Figure 26 where the series includes samples with 50%, 25% and 12.5% interface-dominated sample properties. In this work, a series of SDC20 films with varying thickness will be grown on MgO substrates to investigate the interfacial effects in SDC20.

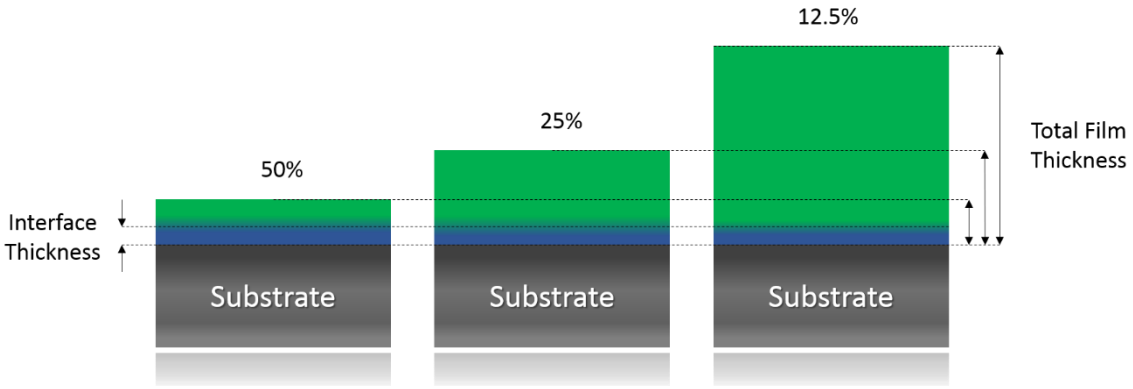

Figure 26 Theoretical thin film test series with 50% (left), 25% (middle) and 12.5% (right) interface-dominated sample properties.

3.4 Experimental

$Sm_{0.2}Ce_{0.8}O_{1.9}$ nanopowders, used for this work, were fabricated by a co-precipitation method. Cerium nitrate hexahydrate ($Ce(NO_3)_3 \cdot 6H_2O$, Alfa Aesar, 99.5%) and samarium nitrate hexahydrate ($Sm(NO_3)_3 \cdot 6H_2O$, Alfa Aesar, 99.9%) aqueous solution was prepared with cation concentration of 0.1 mol/L and molar ratio of Ce^{3+}:Sm^{3+} equal to 4:1. Ammonia dicarbonate (NH_4HCO_3, Fluka, 99. 9%) aqueous solution with concentration of 0.1mol/L was prepared with molar ratio of ammonium bicarbonate to cation equal to 2. The metal nitrate solution was added to the ammonia bicarbonate solution slowly (10mL/min) while stirring. White precipitates were collected and rinsed with distilled water (2x) and ethanol (2x) then dried and calcined at 600^{o}C for 2h.

Crystal structure characterization was completed by XRD analysis using a Panalytical X'Pert Powder X-ray diffractometer with Cu K-alpha radiation (λ = 0.15418nm). The powder XRD pattern in Figure 27A confirmed the fluorite phase and no

significant impurity phases. The morphology of the agglomerated SDC20 nanopowders is was characterized by SEM in Figure 27B.

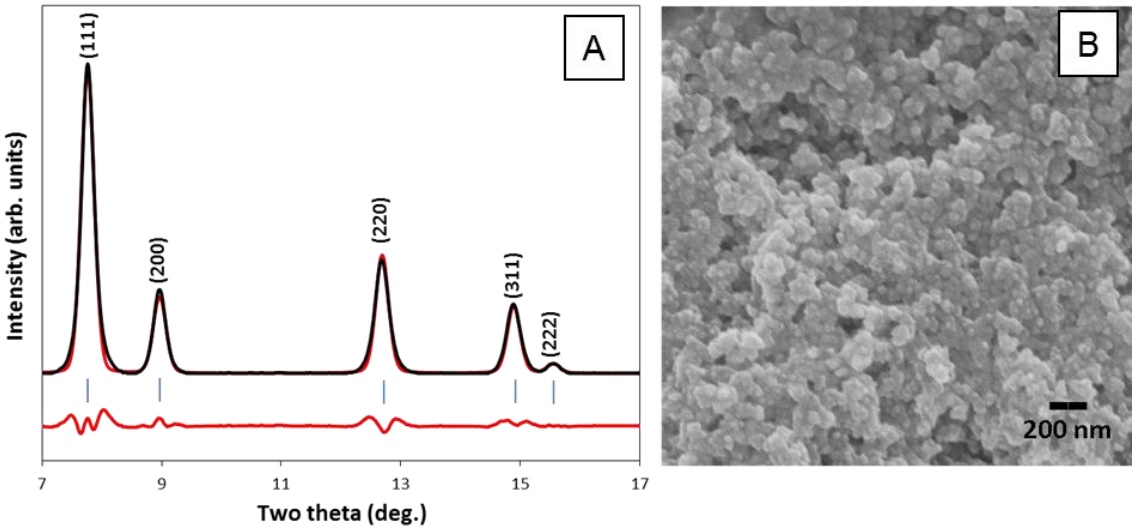

Figure 27 (A) Low pressure XRD pattern of SDC20 powder (P=0.25 GPa, a = 5.433Å, V = 160.35Å^3). (B) Scanning electron microscope (SEM) image of ~35nm nanocrystalline SDC20 used in all experiments

3.4.1 Two-step sintering

In order to fabricate ultrafine-grained SDC electrolytes to observe interfacial effects on the ionic conductivity, the two-step sintering (TSS) technique has been used. The nanocrystalline powders were mixed with 0.5% polyvinyl butyral (PVB) binder and dry-pressed into pellets (d=13mm, t=1mm) under uniaxial pressure of 400MPa. The pellets were first heated to 600^{o}C at 3^{o}C/min and held for 1 hour to remove organic binders. The pellets were then subjected to TSS with parameters as follows; T_1 = 1200^{o}C, R_1 = 5^{o}C/min, H_1=5 min, T_2 = 1050^{o}C, R_2 = 15^{o}C/min, H_2 = 20 hours where T is temperature, R is rate, and H is hold time. For comparison of nanocrystalline SDC20 to microcrystalline SDC20, pellets were prepared as described above however the pellets were sintered using a conventional sintering schedule as follows, T_1 = 1500^{o}C, R_1 = 3^{o}C/min, and H_1 = 5 hours.

The microstructure of the sintered nanocrystalline and microcrystalline SDC20 pellets were characterized using a thermally assisted field emission scanning electron microscope (SEM, LEO 1530). Pellets were fractured and profile and top view images were collected as shown in Figure 28. The grain size was determined by analysis of multiple locations on the dense pellet. There was no significant grain size variation across the pellet. Pellet density was measured using the Archimedes method. The average grain size of the nanocrystalline sample is reported to be ~165nm and the relative density was measured as 96.5% of theoretical density. The microcrystalline SDC20 pellet grain size is ~1.5 μm with >96.5% of theoretical density.

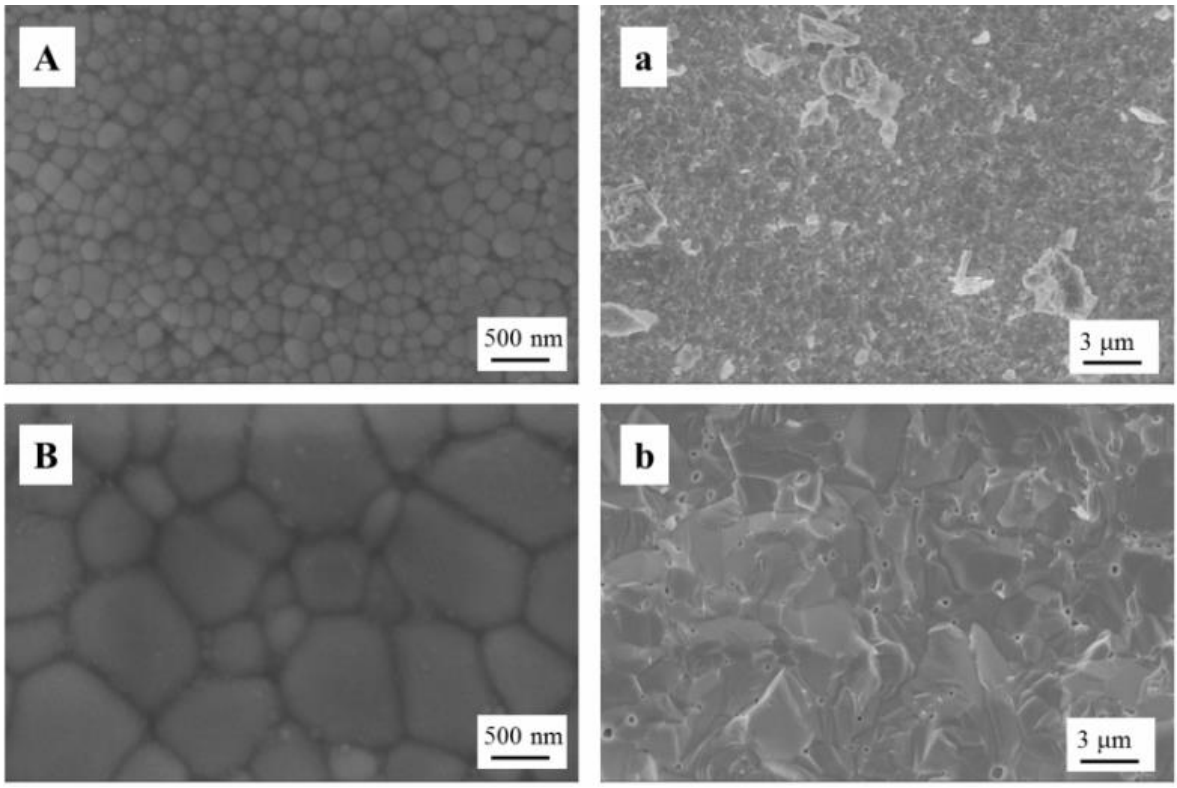

Figure 28 SEM images of SDC electrolyte sintered by (A, a) two-step sintering and (B, b) conventional sintering. Left: surface morphologies; right: cross-sectional morphologies. (Samples prepared by Haibin Sun)

3.4.2 Dynamic shock consolidation of SDC20 powders

SDC nanoparticles with particle size of ~35nm were pressed by uniaxial pressure (Carver Press) into the sample capsule (~1mm thick disk; ~12mm diameter; stainless steel) with a green body density of ~60% of theoretical density as seen in Figure 29 (left). At pressures higher than 60% theoretical density, plastic deformation of the sample capsule occurred. High green body density is expected to improve consolidation of the sample and mitigate crack formation. In the work cited from the literature, gadolinium doped ceria nanopowders were pressed to only 48% of theoretical density.[106] Figure 29 (right) shows the nanocrystalline SDC20 powders with high density after uniaxial pressing but before dynamic shock consolidation.

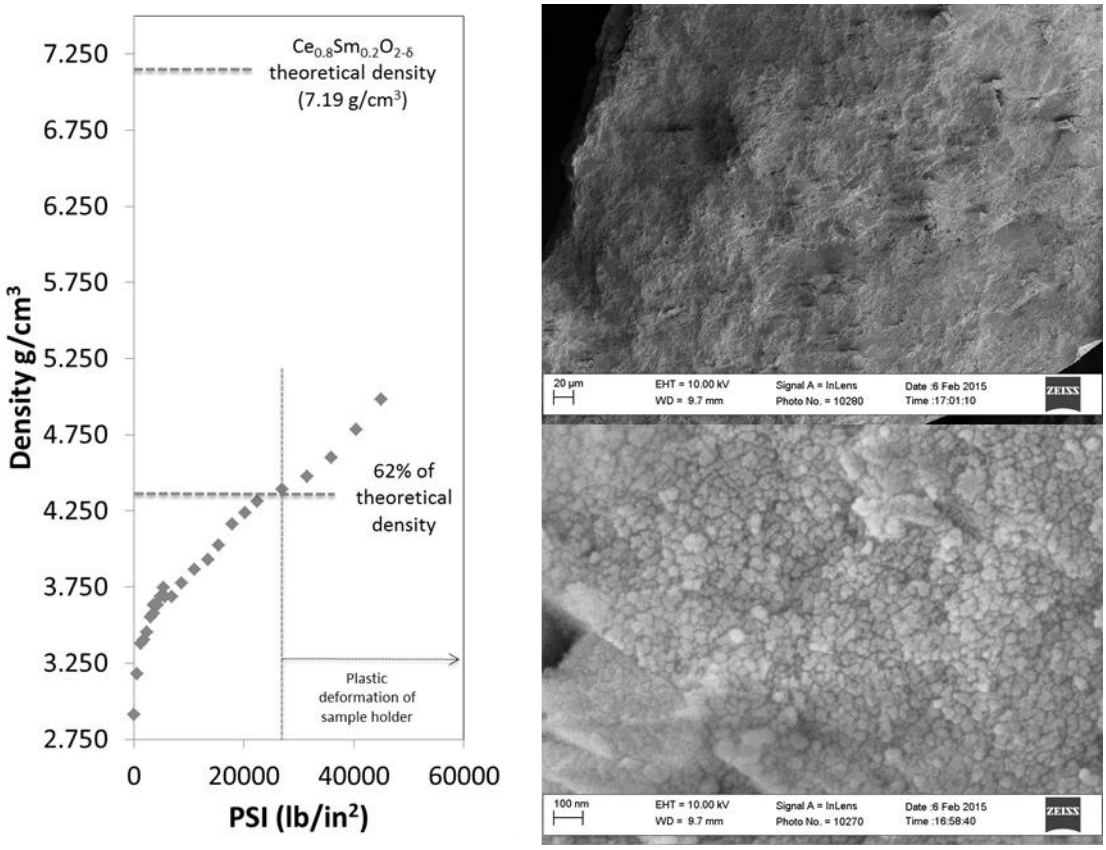

Figure 29 Pressure-density curve of SDC green body by uniaxial pressing (left); low magnification SEM of SDC pellet cross section after uniaxial pressing (top right); high magnification SEM of SDC pellet cross section after uniaxial pressing (bottom right)

After dynamic shock consolidation of the SDC20 green body samples, the sample capsules were removed and opened by machining the top of the capsule from the sample. As seen in Figure 30, the samples were not fully consolidated and were found to still have powder-like consistency. The pellet seen at the bottom of Figure 30B is completely fractured and not useful for electrical testing.

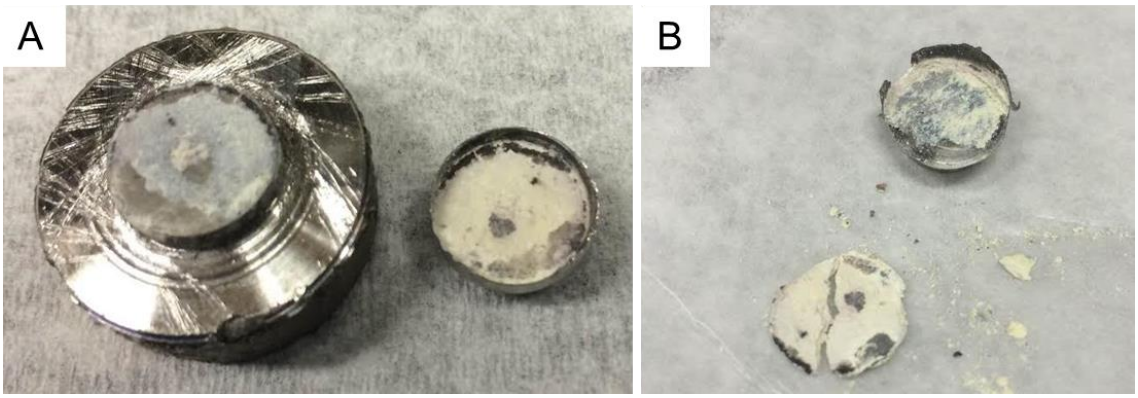

Figure 30 Digital photographs of SDC20 powders machined from stainless steel sample canisters after dynamic shock consolidation

SEM analysis of the SDC20 pellets after dynamic shock consolidation, shown in Figure 31, revealed no significant particle plastic deformation or nanoparticle consolidation but severe microcracking of the sample. It is clear that the initial or reflected shock wave was not optimized for sample geometry and acoustic properties which fractured the green body sample. As seen from the images, the sample density after dynamic shock consolidation was considerably lower than the necessary 95% density for electrical measurements.

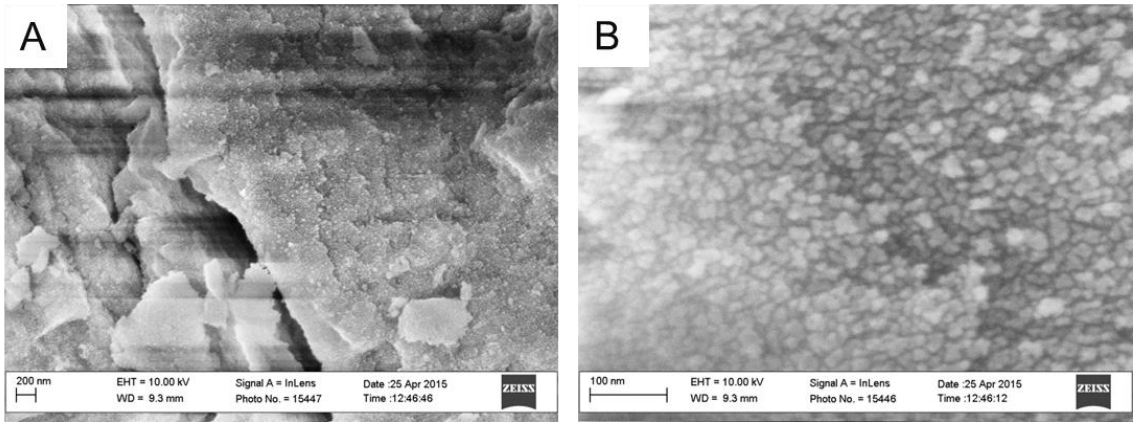

Figure 31 SEM images of SDC pellet cross section after dynamic shock consolidation revealing significant microcracking and no significant particle consolidation

After three initial tests of SDC20 nanopowders, barium zirconate ($BaZrO_3$) powder and composite SDC20/$BaZrO_3$ powders, some particle deformation and consolidation was observed, however not to the extent necessary for electrical testing. Green bodies with ~50nm nanoparticles were consolidated to a larger extent than the ~35nm SDC20 particles presented here. No further optimization of dynamic shock consolidation of the SDC20 35nm samples was completed and electrical measurements were focused on the nanocrystalline samples fabricated by two-step sintering.

3.4.3 Pulsed layer deposition of SDC20 thin films

SDC20 thin films were fabricated by pulsed laser deposition (PLD) at Oak Ridge National Lab (ORNL) in the Center for Nanophase Materials Science (CNMS). Detailed information about the SDC20 target preparation and PLD setup is listed in Chapter 5 where further thin film studies are reported.

In these measurements, SDC thin films with thickness of 250nm and 500nm were fabricated on MgO (001) single crystal substrates. The MgO substrates were submerged in buffered oxide etch (BOE) for 30 seconds, rinsed with DI water and annealed at 1100^{o}C for 6 hours before SDC20 deposition. PLD fabrication parameters were as follows; 100mtorr PO_2, 700^{o}C, 0.065cm^2 spot size, 10Hz, 2.86J/cm^2. Electrical connection to the SDC20 thin films was made with silver paste and silver wires. The spacing between the current collection pads on the films was 4mm. Impedance spectroscopy measurements were completed using the Solartron 1255 Frequency Response Analyzer and a Solartron 1296 Dielectric Interface in the frequency range of 5MHz to 10mHz with a 2.6V AC bias. A large bias voltage was used to reduce the noise of the impedance data. A schematic of thin film impedance measurements as a function

of bias voltage is shown in Figure 32 which shows the data noise reduction without a change in the measured data values. We believe that the large bias voltage used for the measurements only served to reduce data noise and did not otherwise skew the data.

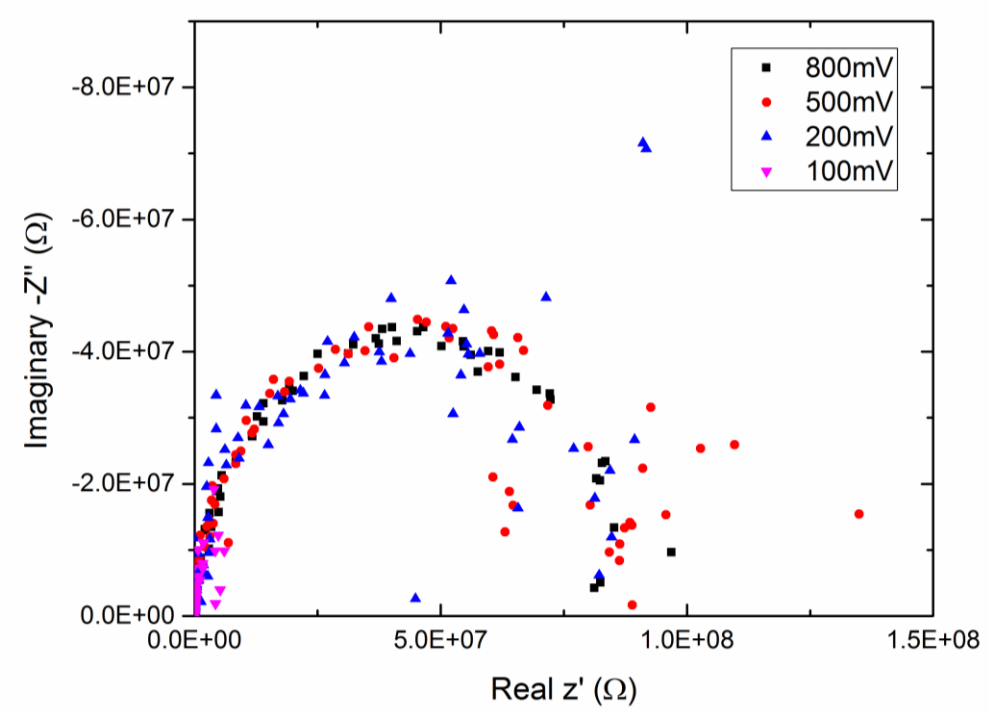

Figure 32 Impedance spectroscopy data as a function of bias voltage for thin film SDC20 measurements. As bias voltage increases the data is not changed but the noise ratio is decreased. High bias voltage is critical for 'low-noise' impedance data for SDC20 thin film samples

3.4.4 Electrical measurements of SDC20 pellets

The electrical properties of the SDC20 pellet were tested using impedance spectroscopy with a Solartron 1255 frequency response analyzer and EG&G 273A potentiostat with 10mV AC amplitude and from 1 MHz to 0.1 Hz. SDC20 pellets were prepared with Ag electrodes and Ag wires for electrical connection. The Ag paste was treated at 650^{o}C before electrical testing to remove solvents and binders and to sinter the Ag particles in the paste (Heraeus). The pellets were tested in ambient air. The bulk

resistance of the SDC20 pellets was recorded from the high frequency intercept of the real impedance axis when the imaginary impedance is equal to zero. The bulk conductivity was calculated according to Equation 26 where L is the thickness of the pellet, A is the superficial area of the pellet and R_b is the high frequency intercept of the real impedance axis. The grain boundary and total resistance was determined by fitting of the impedance data. The activation energy was determined from the plot of conductivity versus temperature using Equation 27 where E_a is activation energy, σ is conductivity, and k is the Boltzmann Constant.

$$\sigma = \frac{1}{R_b} \cdot \frac{L}{A} \tag{26}$$

$$\sigma = \left(\frac{\sigma_o}{T}\right) \exp\left(\frac{-E_a}{kT}\right) \tag{27}$$

3.4.5 Concentration cell measurements

In order to determine the ionic (t_{ionic}) and electronic ($t_{electronic}$) transference numbers of the nanocrystalline and microcrystalline SDC20 samples, concentration cell measurements were collected. The total conductivity of the solid electrolyte , σ_{total}, is composed of the ionic and electronic contributions by Equation 28. Because electronic conductivity is highly undesirable in solid electrolytes, it is important to determine what portion of the total current is carried by electronic defects. The impedance measurements presented in the previous section do not differentiate between ionic and electronic contributions to total conductivity. Therefore, it is necessary to complete concentration cell measurements to determine the contributions.

$$\sigma_{total} = \sigma_{ionic} + \sigma_{electronic} \quad (28)$$

Concentration cell measurements were conducted using a two-sided, atmosphere-controlled testing configuration as shown in Figure 33. SDC20 cells were measured using a cell configuration of

$$air(O_2), Pt/\ SDC20\ /Pt, pO_2 \quad (29)$$

where air(O_2) represents ambient air and pO_2 were changed from pure oxygen to a mixture of 15 ppm O_2 with argon.

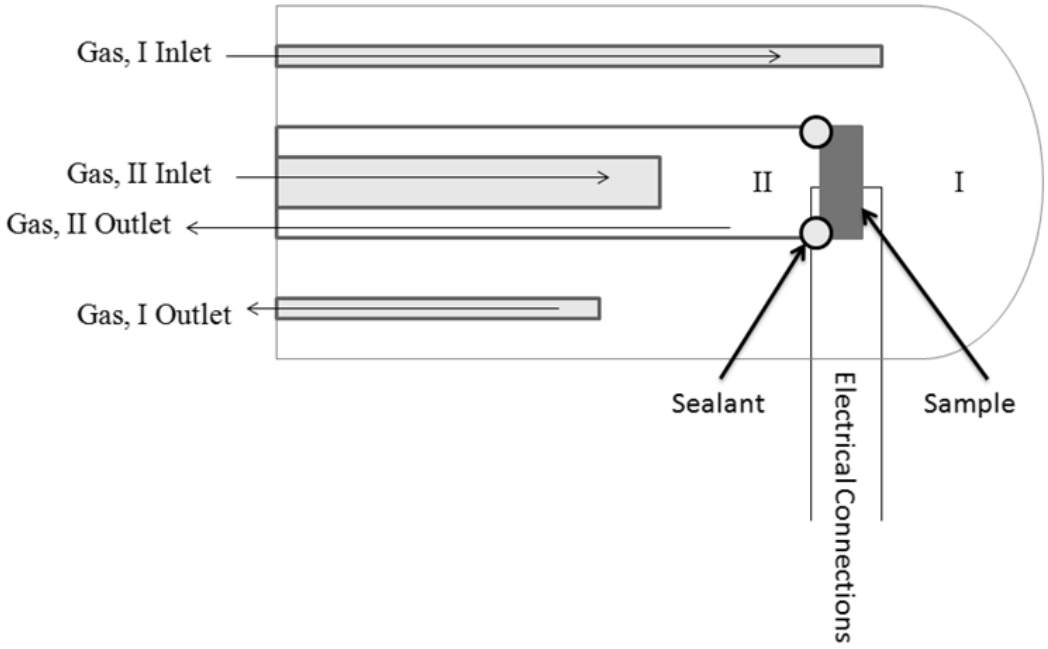

Figure 33 Schematic of configuration used for concentration cell testing of nanocrystalline SDC20 to determine the ionic and electronic transference numbers of the material.

Complete sealing of the concentration cell is important to ensure known concentrations of gases on the anode and cathode side and accurate transference number measurements. The SDC20 pellets were sealed on the testing fixtures using Schott

GM31107 sealing glass. The glass was mixed with acetone and Duco Cement (5.0g glass : 0.5g Duco Cement : 10mL acetone) to create a paste. The paste was applied to the fixture as shown in Figure 34A & 34D. As seen in Figure 34 an alumina tube section was added to the top of the pellet to aid in the glass seal application. The glass seal was heated to 600^{o}C for 2h and reduced to 500^{o}C for testing. As seen in Figure 34, the glass seal fired with a long tube atop the pellet formed a large gap at the pellet that prevented its use. In Figure 34C & 34D the top tube length was shortened which confined the glass seal to remain around the pellet and form a complete seal which was used for the measurements. Gas leakage was tested by flowing He through Chamber I while using Mass Spectrometry to detect He in the Chamber II gas stream. Gas leakage was determined to be less than 0.3%.

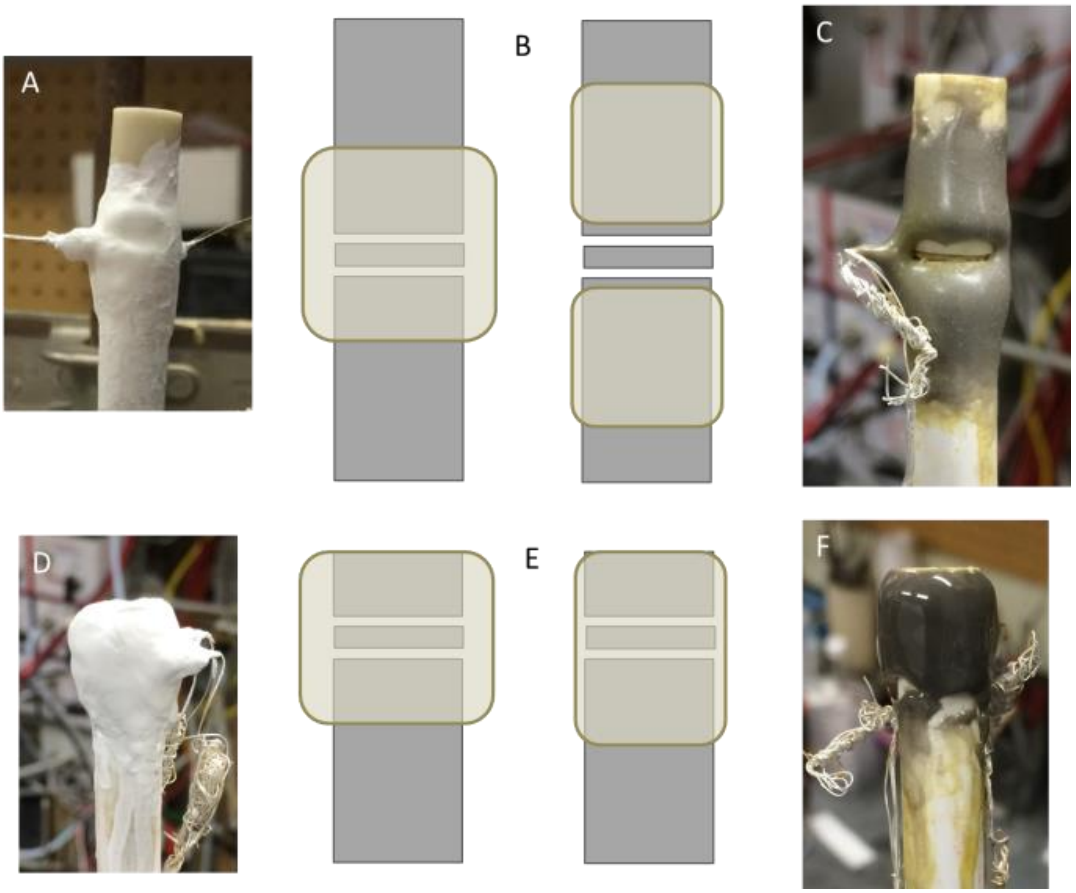

Figure 34 Glass sealing schematic displaying surface tension effect on sealing of concentration cell. The figure shows images after application of glass sealant slurry (A & D), diagrams of sealant shrinkage after firing for long configuration (B) and short configuration (E), and images of sealed concentration cells after firing (C & F)

3.4.6 Fabrication of Pt nanoparticle loaded SDC20 microcrystalline samples

Pt (4 vol%) nanoparticle-loaded SDC20 microcrystalline samples were fabricated by the combustion method. Stoichiometric amounts of Cerium (III) Nitrate Hexahydrate, Samarium (III) Nitrate Hexahydrate and Chloroplatinic Acid Hexahydrate were mixed in DI water until dissolved. Citric acid and ethylenediaminetetraacetic acid (EDTA) were added in proportion of total metal ions to citric acid to EDTA as 1:1.5:1 ratio. EDTA was used as a chelating agent and citric acid was used for both chelating agent and to support combustion. After combustion the SDC20-Pt4vol% powders were collected, pressed into

pellets (thickness = 600μm, diameter = 13mm) by uniaxial pressing, and fired at 1400^{o}C for 5h for electrical testing.

3.5 Results and Discussion

3.5.1 Electrical conductivity measurements of nano- and microcrystalline SDC20 electrolyte

Figure 35 displays the impedance spectra for the microcrystalline (left) and nanocrystalline (right) SDC20 samples. The ZView™ program (Version 2.1b, Scribner Associates, Inc.) was used for spectra fitting. For all impedance measurements two arcs were observed in the impedance spectra. The equivalent circuit used to fit the impedance data is shown in the inset and consists of one resistor (R) and two RQ circuits in series (where Q is the symbol used to denote a constant phase element, CPE). R_1 represents the grain bulk resistance, R_G; R_2 represents the grain boundary resistance, R_{GB}; and R_3 represents the electrode resistance associated with charge transfer, R_E. CPE1 and CPE2 are constant phase elements from which the capacitances can be calculated. The effective resistance of the electrolyte includes both the grain boundary resistance and the grain bulk resistance. The electrolyte resistance, $R_{electrolyte}$, is equal to the sum of R_G and R_{GB}. The impedance arc corresponding to the electrode (silver paste) processes will be discussed at the end of this section.

The collected impedance data of Figure 35 shows that the bulk resistance of the microcrystalline pellet (~750 ohms, electrode diameter = 0.77cm, pellet thickness = 0.79mm) is higher than the bulk resistance of the nanocrystalline pellet (~400 ohms, electrode diameter = 0.79cm, pellet thickness = 0.85mm)), although both samples have

similar geometry (diameter and thickness). Additionally, the fitted grain boundary impedance is much lower in the nanocrystalline sample.

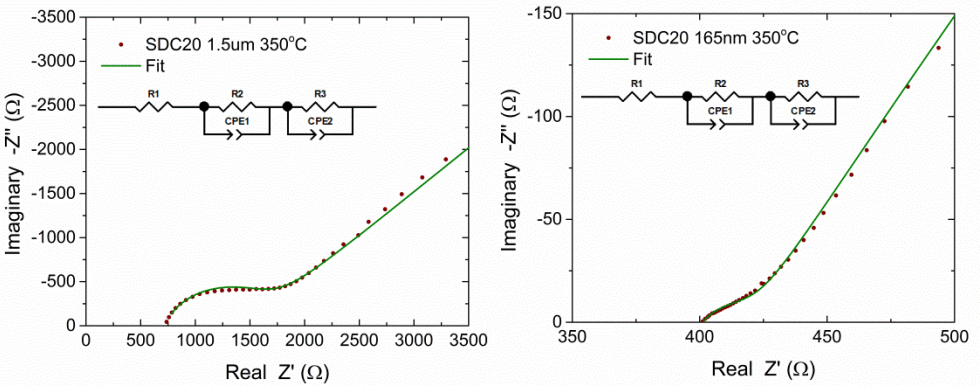

Figure 35 Impedance spectra measured at 350°C for microcrystalline (left) and nanocrystalline (right) SDC20 electrolytes. (Data collected by Haibin Sun, fitted by BHR)

The impedance spectra for nanocrystalline SDC20 at 300°C, 400°C, and 500°C is shown in Figure 36. As the impedance spectra evolves over temperature the bulk resistance value decreases from ~400Ω at 350°C to ~45Ω at 450°C and ~11Ω at 550°C. The fit of the data also shows that the grain boundary impedance intersection with the real axis cannot be adequately fit at high temperature due to the overlap of the grain bulk and grain boundary impedance arcs.

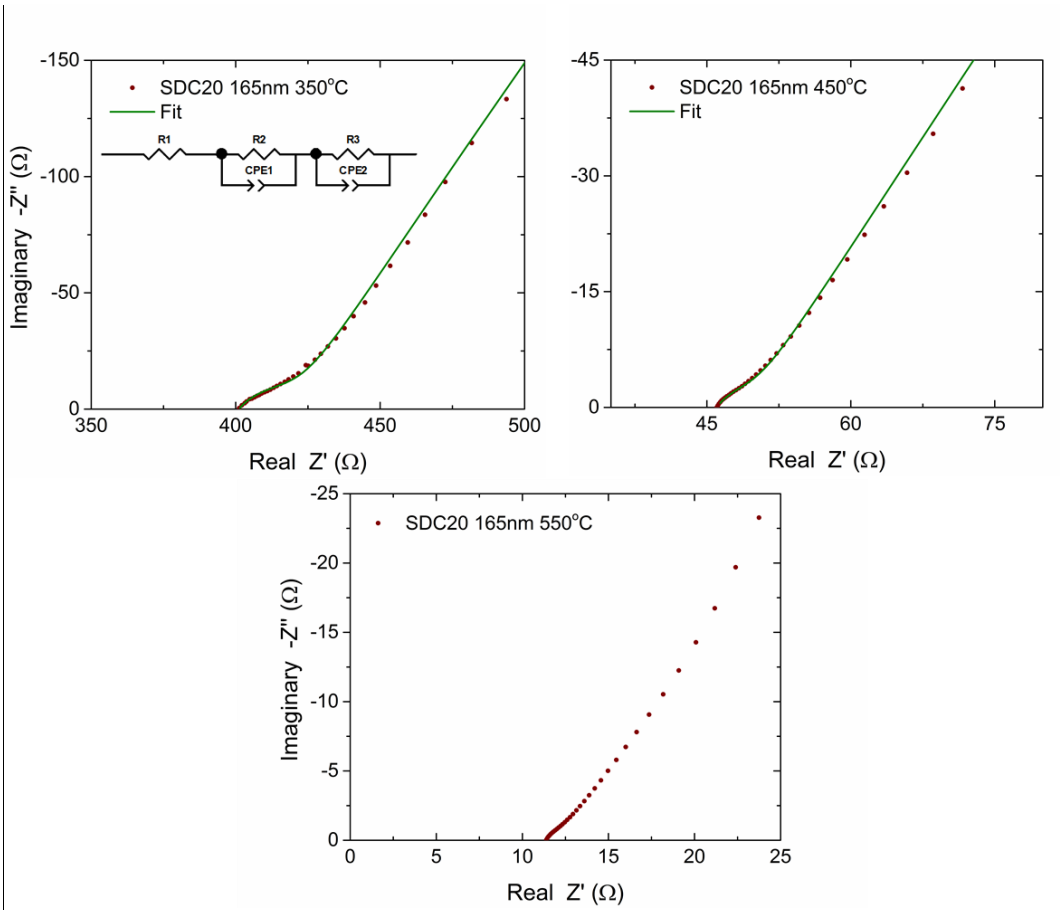

Figure 36 Impedance spectra measured at different temperatures (a) 350°C, (b) 450°C, (c) 550°C for nanocrystalline SDC20 electrolyte fabricated by TSS. (Data collected by Haibin Sun, fitted by BHR)

In Figure 37, the grain bulk resistance, grain boundary resistance and total conductivity of both the microcrystalline and nanocrystalline SDC20 samples are plotted. The grain bulk and grain boundary resistances of the nanocrystalline sample are both less than the resistances of the microcrystalline sample. The change in grain resistance is ~2x and the change in grain boundary resistance is ~1 order of magnitude. This is consistent with the hypothesis that in the nanostructured SDC20 sample the changes in conductivity will be primarily associated with the grain boundary because the total grain boundary volume is increased significantly. The total conductivity of the nanocrystalline SDC20 sample is ~2-3x great than the total conductivity of the microcrystalline SDC20 sample.

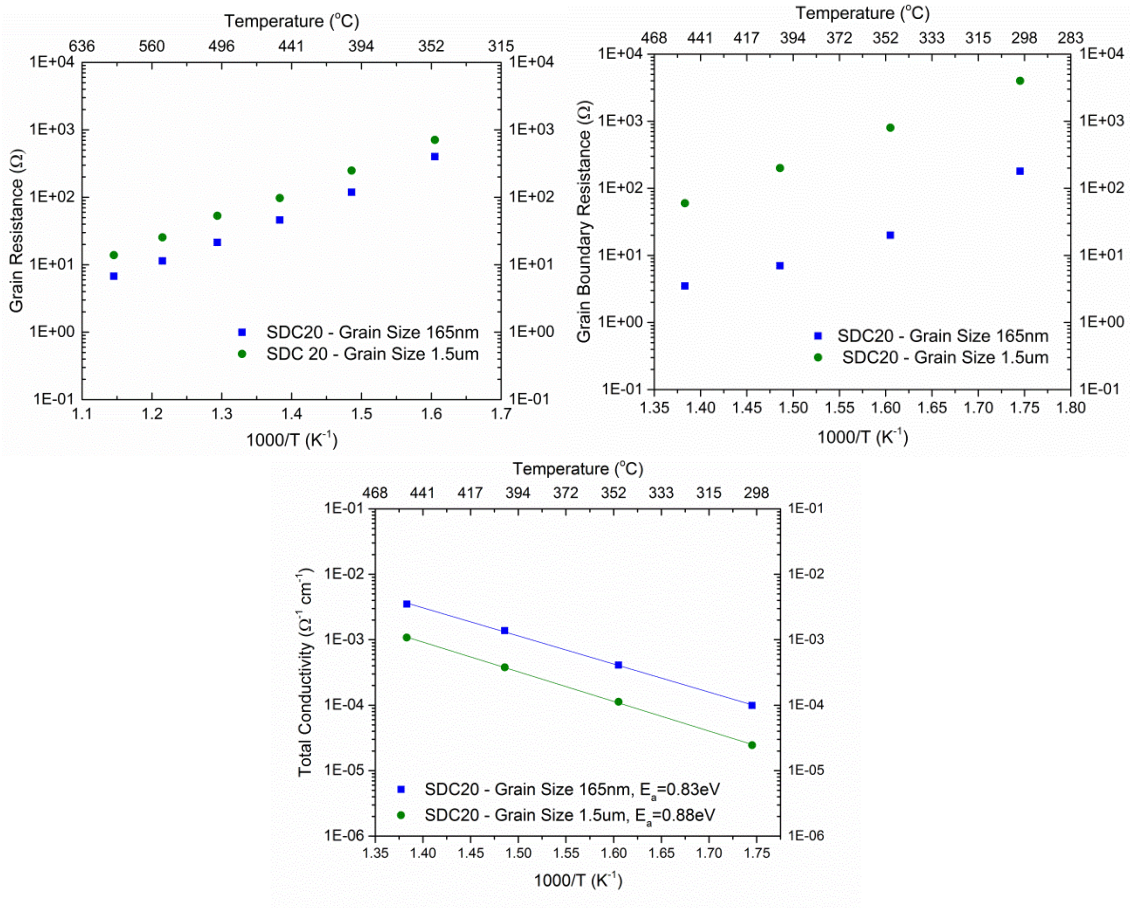

Figure 37 Grain resistance (a), grain boundary resistance (b) and total conductivity (c) for nanocrystalline and microcrystalline SDC20 electrolytes. (Data collected by Haibin Sun)

In order to confirm that the second arc observed in the impedance measurements of nano- and microcrystalline SDC20 is due to the silver electrodes used for current collection of the pellet sample, impedance measurements were collected as a DC bias was applied. The data collected for 0.1V DC bias and 0.3V DC bias, as well as after the bias is removed, is shown in Figure 38. It is apparent that the arc attributed to the electrode charge transfer is dependent on the DC bias. The polarization effect on the impedance spectra indicates that the second arc is due to charge transfer processes in the electrode.

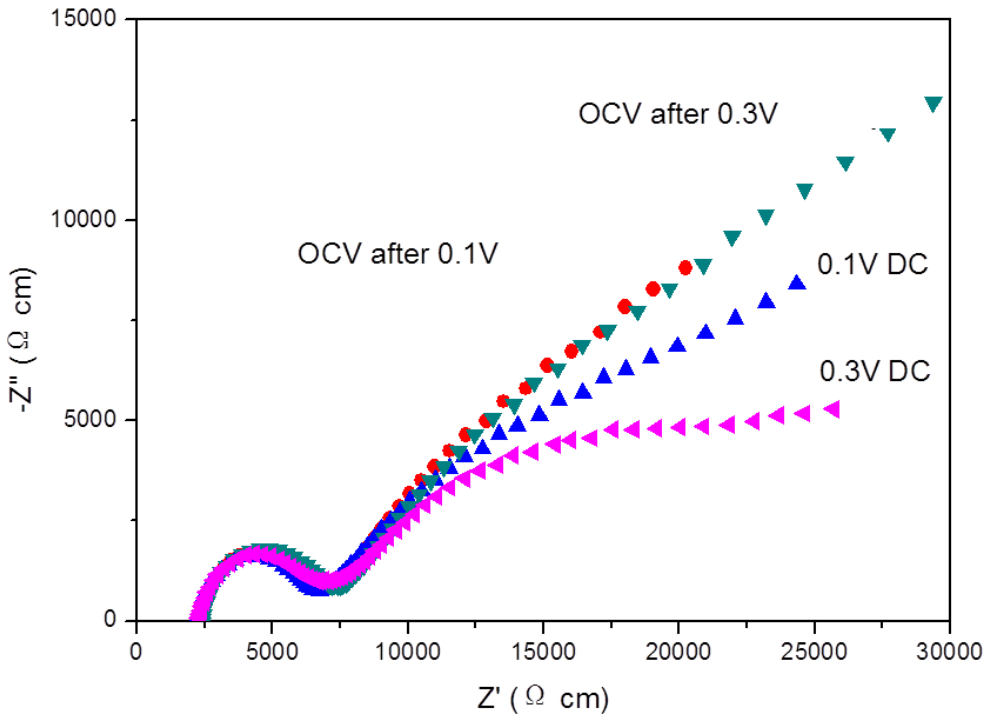

Figure 38 Impedance data of microcrystalline SDC20 pellet at 0.1V and 0.3V DC bias condition and at OCV after DC bias condition. The data was measured at 300^{o}C in ambient air. (Data collected by Haibin Sun)

3.5.2 Transference number testing of nano- and microcrystalline SDC20 electrolyte

In order to determine if the conductivity enhancement in nanocrystalline SDC20 is due to electronic or ionic conductivity at the grain boundaries of nanocrystalline SDC20, ionic transference number was determined using the concentration cell measurement. Two concentration cells with varying PO_2 on each side of the SDC20 electrolyte were constructed for testing and Pt electrodes were attached to measure the OCV of the cell under each condition. To calibrate the exact partial pressure of O_2 at each electrode in both concentration cells, a concentration cell based on YSZ pellet was constructed and measured under both conditions. The OCV measurements of the YSZ cell were used as the reference for the SDC20 electrolytes due to the purely ionic

conduction of YSZ in both oxidizing and reducing atmospheres. The OCV of the cells was measured from 500^{o}C to 600^{o}C.

The first concentration cell is represented in the inset of Figure 39. The electrode atmospheres are ambient air and 15ppm O_2 balanced by Ar, from a bottle. The OCV measurements for nanocrystalline SDC20, microcrystalline SDC20 and YSZ electrolyte pellets are shown in Figure 39. Under this low PO_2 atmosphere condition, a significant deviation from the YSZ OCV was measured at 600^{o}C for both the nano- and microcrystalline SDC20 samples, as expected. This means that a significant portion of the conductivity at that temperature is electronic. The ionic transport number, t_{ion}, for both nano- and microcrystalline SDC is ~0.87 at 600^{o}C. The creation of electronic defects at low pO_2 is expected as described earlier in this chapter by Equation 24. However, interestingly there is very little electronic conductivity at 500^{o}C under these conditions. It is important to note that the transference numbers for nano- and microcrystalline SDC are nearly identical under these concentration cell conditions. Therefore, there is no additional electronic conductivity due to the large interface volume present in the nanocrystalline SDC20 structure. The electronic portion of the total conductivity in both micro- and nanocrystalline SDC20 is due to the reduction of Ce^{4+} to Ce^{3+}, not the grain size or interface volume.

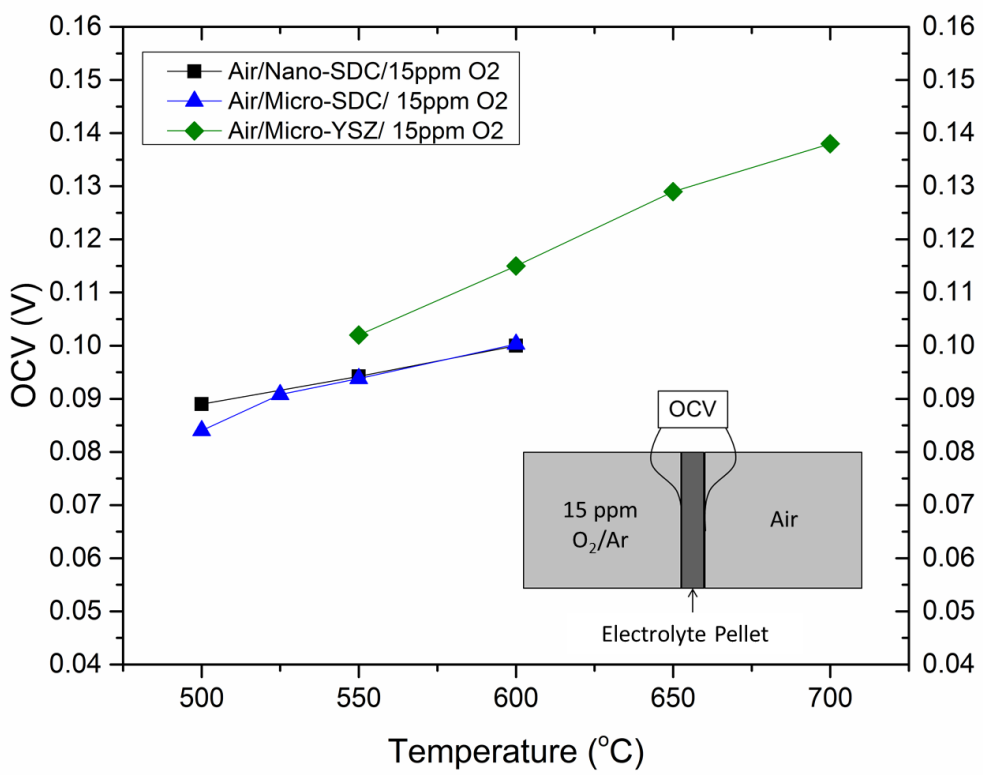

Figure 39 OCV measurements of Nano-grain SDC, Micro-grain SDC, and Micro-grain YSZ in 15ppm O_2 – Air concentration cell

The second concentration cell is represented in the inset of Figure 40. The electrode atmospheres are ambient air and pure O_2 from a bottle. This concentration cell most closely represents the conditions in which the electrical conductivity of nanocrystalline SDC20 was measured by impedance spectroscopy in the preceding section. The OCV measurements for nanocrystalline SDC20, microcrystalline SDC20 and YSZ electrolyte pellets are shown in Figure 40. In this atmospheric and high oxygen concentration condition, no significant deviation from the YSZ OCV was measured in either nanocrystalline or microcrystalline SDC20 from 500°C to 600°C. This data suggest that the ionic transference number, t_{ion}, for nanocrystalline SDC under these high P_{O2} conditions is close to 1.

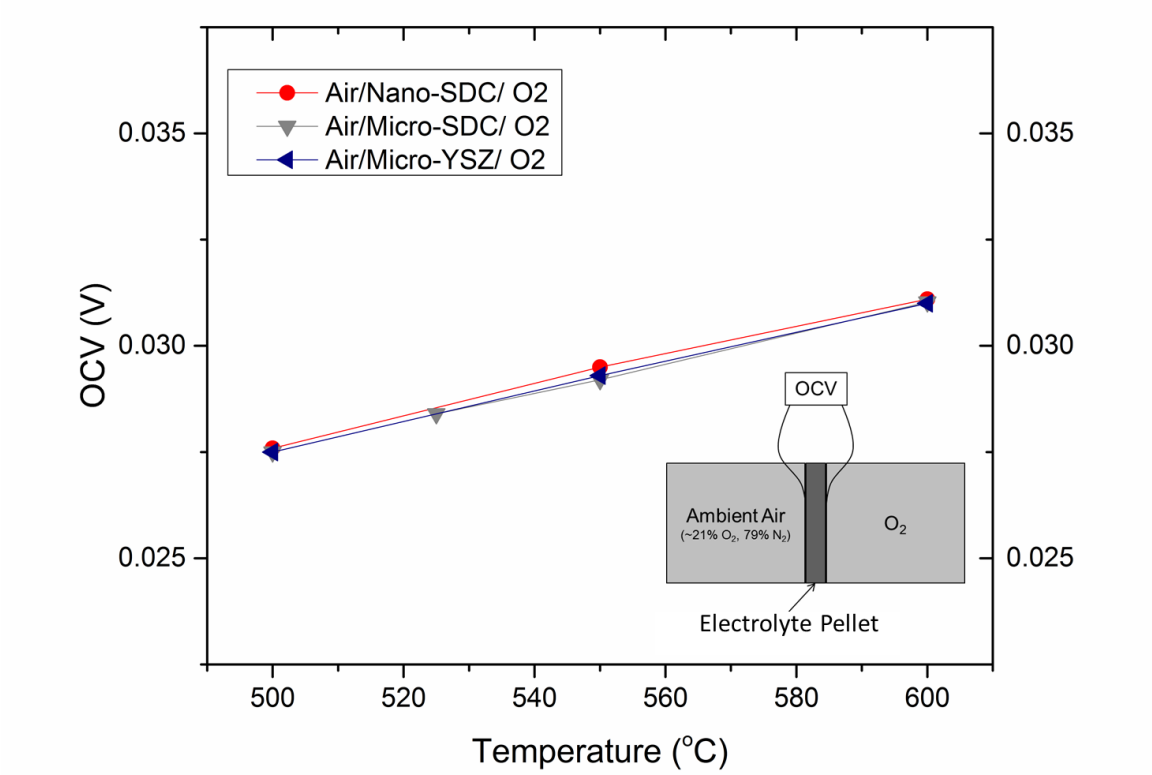

Figure 40 OCV measurements of Nano-grain SDC20, Micro-grain SDC20, and Micro-grain YSZ in Air-O_2 concentration cell

The results of the concentration cell tests are summarized in Table 3 and 4. It is apparent that no significant deviation in OCV in the nanocrystalline concentration cells when compared to the microcrystalline concentration cells under both conditions, confirming that the nanocrystalline nature of the SDC20 sample does not introduce electronic conductivity into the sample as some suspect. The nano- and microcrystalline samples behave similarly when compared to YSZ under the same concentration cells. Under low pO_2 conditions both SDC20 samples have an ionic transference number of t_{ion}= ~0.87 and in ambient pO_2 conditions both SDC20 samples have an ionic transference number of t_{ion}= ~1.0.

Table 3 OCV values of Nano-SDC20 and Micro-SDC20 concentration cells at 600°C in Air/electrolyte/O_2 and 15ppm O_2/electrolyte/Air conditions

Sample	Temperature (°C)	Concentration Cell	OCV	OCV drop (%)
Micro-SDC	600	Air/Micro-SDC/O2	0.031	
Nano-SDC	600	Air/Nano-SDC/O2	0.031	0%
Micro-SDC	600	15ppm O2/Micro-SDC/Air	0.1003	
Nano-SDC	600	15ppm O2/Nano-SDC/Air	0.1	0%

Table 4 OCV values of Nano-SDC20 and YSZ concentration cells at 600°C in Air/electrolyte/O_2 and 15ppm O_2/electrolyte/Air conditions. Transference numbers of nanocrystalline SDC20 calculated from deviation from YSZ OCV.

Sample	Temperature (°C)	Concentration Cell	OCV	OCV drop (%)	Transference Number
Micro-YSZ	600	Air/Micro-YSZ/O2	0.031		
Nano-SDC	600	Air/Nano-SDC/O2	0.031	0%	$t_{ion} = 1$
Micro-YSZ	600	15ppm O2/Micro-YSZ/Air	0.115		
Nano-SDC	600	15ppm O2/Nano-SDC/Air	0.1	13%	$t_{ion} = 0.87$

The OCV data proves that the enhancement of total conductivity in the nanocrystalline SDC20 sample is purely ionic; accordingly, nanostructured SDC20 electrolytes in solid oxide fuel cells are expected to enhance cell performance and energy conversion efficiency.

The enhanced ionic conductivity in the nanocrystalline sample is most accurately explained by a curvature effect on charge carrier concentration at the nanocrystalline SDC20 grain boundaries. As discussed in Chapter 2, as particle size decreases the chemical potential of the nanocrystalline phase changes due to excess surface energy. It is

known that oxygen vacancy formation at CeO_2 interfaces is energetically favorable. Therefore, we conclude that oxygen vacancies, formed by extrinsic doping of Sm^{3+}, migrate to the grain boundaries as particle size decreases in order to reduce the curvature effect excess surface energy. The large number of charge carriers at the interface dramatically reduces grain boundary resistance and enhances the ionic conductivity of the system. This conclusion is consistent with experimental data that verifies t_{ion}=~1 for the nanocrystalline SDC20.

3.5.3 Thin film testing of SDC20 on MgO (001) with varying interface volume fraction

SDC20 thin films with thickness of 250nm and 500nm were fabricated on MgO substrates by PLD at ORNL CNMS. The electrical conductivity data was collected from 300^{o}C to 550^{o}C and is presented in Figure 41. It is apparent that the conductivity of both films is identical, although the interface-dominated volume of the 250nm film is two times the 500nm film. Because the resistance of the thin film samples is very large, the resistance of the sample holder was measured to verify the absence of leakage current. Figure 42 shows the resistance of the sample holder and the thin film samples. The resistance of the samples is approximately one order of magnitude lower than the resistance of the sample holder; therefore, it was concluded that leakage current did not have an effect on these measurements. The overlapping conductivity data of both 250nm and 500nm SDC20 thin films reveals that the SDC20/MgO interface has no effect on the mobile charge carriers in the film. Although the concentration of misfit dislocations and strain fields associated with the dislocations are expected to be significantly larger in the 250nm film the total electrical properties remain unchanged.

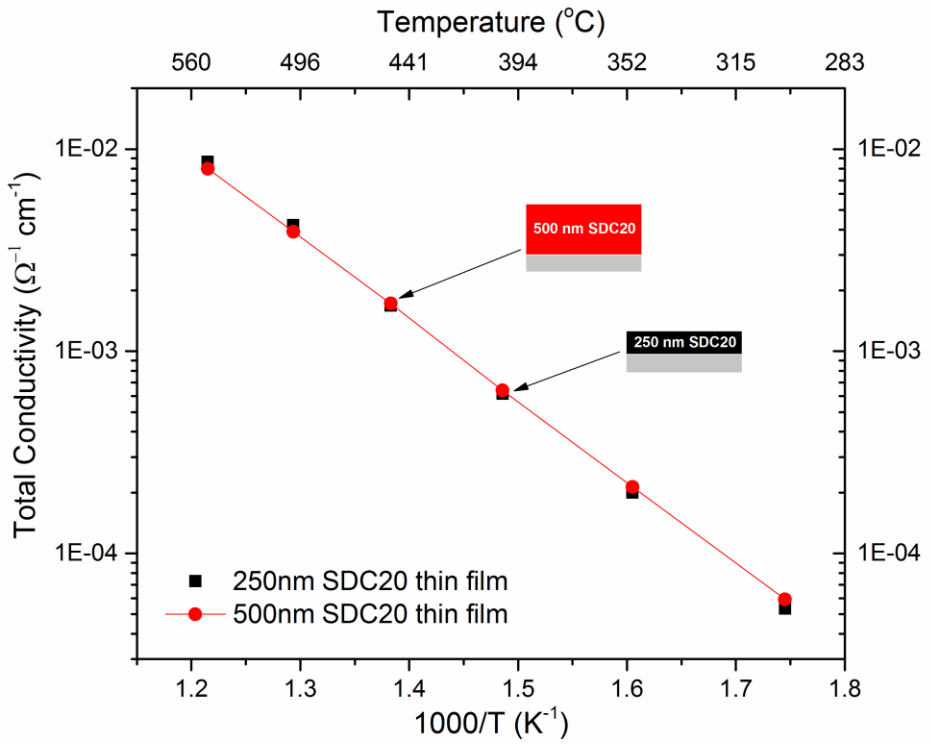

Figure 41 Total conductivity of SDC20 thin films fabricated by PLD with 250nm and 500nm thickness

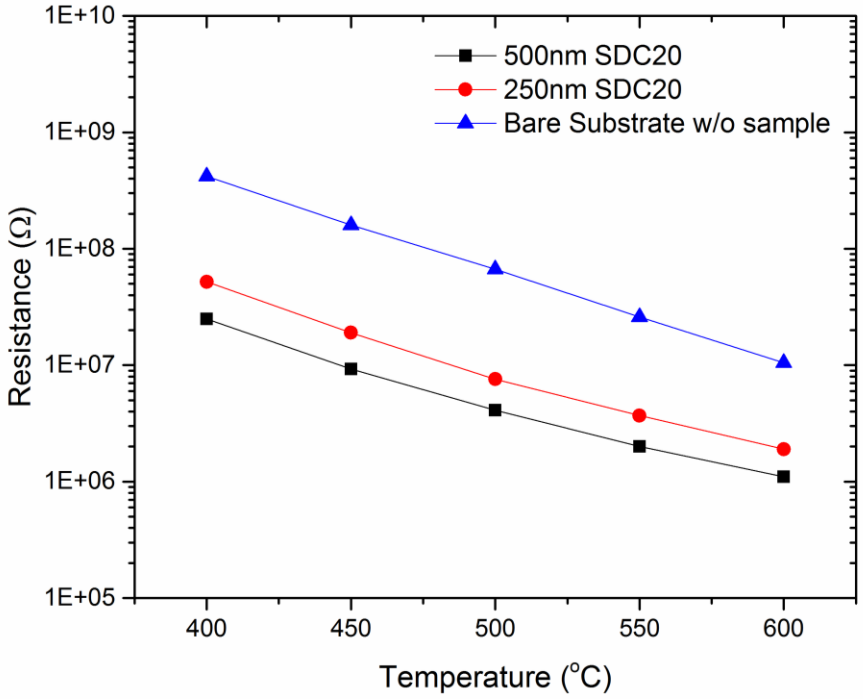

Figure 42 Resistance of sample holder without sample (blue), with 250nm SDC20 sample (red), and with 500nm SDC20 thin film sample (black)

Figure 43 compares the conductivity of SDC20 thin films to the nanocrystalline and microcrystalline samples measured in the previous section. Although TEM analysis of the SDC20 thin films was not completed to determine the thin film grain size, the results show that the conductivity of the SDC20 thin films is between the conductivity of the pellet samples. In this comparison, it is interesting that the SDC20 thin film samples show no change in conductivity based on interface volume, however, a large difference is measured in the pellet samples with nano- and micro-grains. Several conclusions can be drawn from this helpful comparison. First, the measurement of the thin film samples is valid and a true measurement of the SDC20 material. The activation energy of all samples is equivalent and the conductivity is convincing. Second, the interfacial effects in the thin film samples are not the same as the nano- and microcrystalline samples. The change in interfacial effects can be attributed to changes in processing conditions, because the two sample types were fabricated with very different techniques. Additionally, the difference can be attributed to the curvature of the grains of the nanocrystalline SDC20 pellet samples which are not present in the flat SDC20 thin film samples. The excess surface energy of the curved surfaces is expected to have a significant impact on charge transport in nanocrystalline SDC20. The data for nanocrystalline and thin film SDC20 verifies that interfacial effects occur in SDC20 but only at certain interfaces, in this case the nanocrystalline grain boundaries.

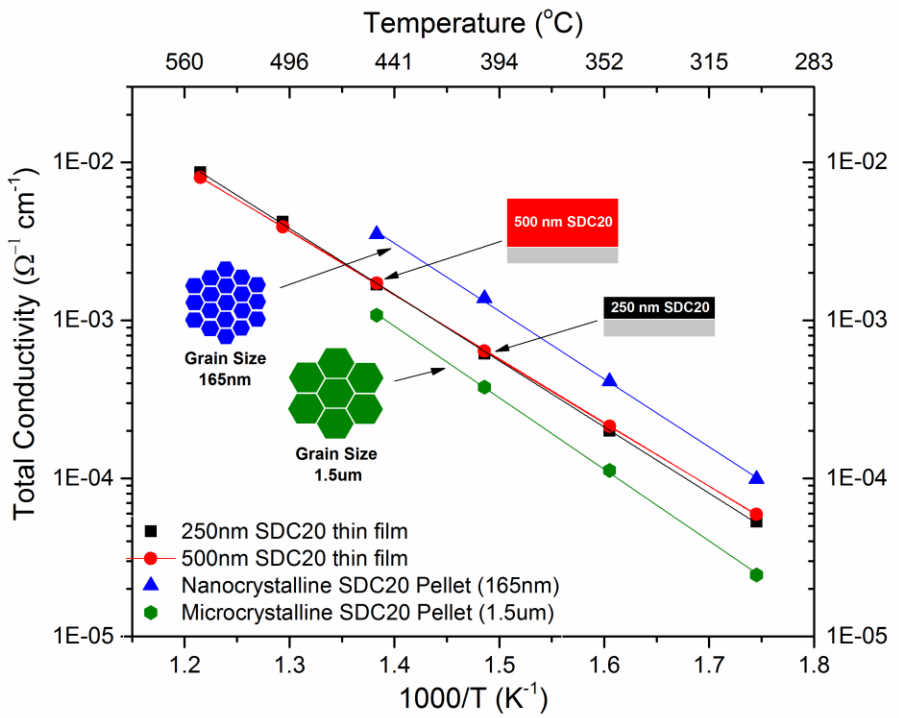

Figure 43 Conductivity comparison graph of SDC20 thin film samples and SDC20 nano- and microcrystalline samples

3.5.4 Interfacial effects in Pt particle loaded Sm-doped CeO_2

In order to determine secondary phase interfacial effects with SDC20, in continuation of the work of the previous section on the SDC20/MgO thin film interface, SDC20 pellets were loaded with 4vol% platinum and the electrical properties of the pellets were measured. The composite, as-prepared powders, shown in the SEM image of Figure 44, are characteristic of the combustion fabrication technique. The crystallites are on the nanoscale and connected into a porous foam-like structure. Energy-dispersive X-ray spectroscopy (EDS) was used to determine the chemical nature of the Pt particles found in the as-prepared SDC20 powders. Although few large particles could be found, one microcrystalline particle is imaged in Figure 44 with the EDS data revealing that it is a platinum particle. While most of the Pt particles formed from solution during the

combustion process were nanoparticles, some microcrystalline particles, such as this one, were found.

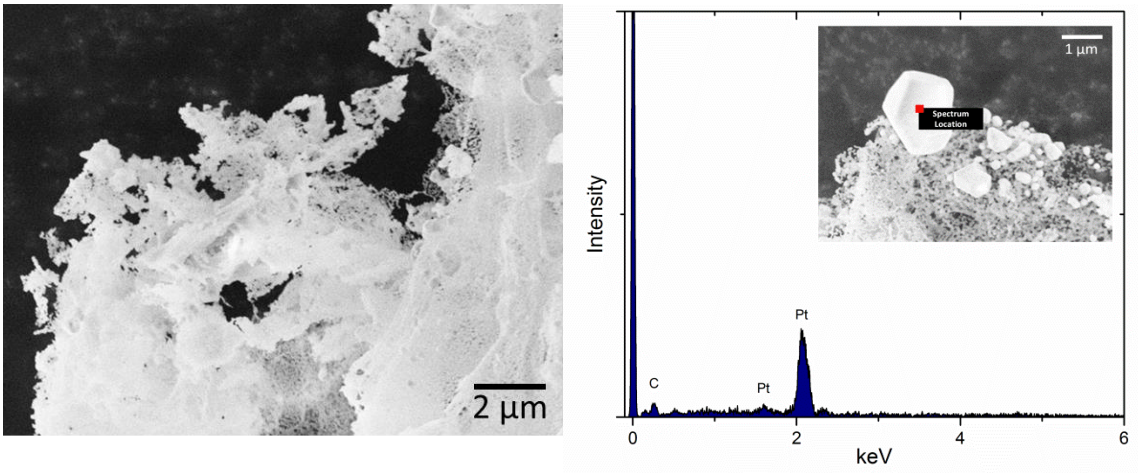

Figure 44 (Left) SEM image of 4vol% Pt – SDC20 powders fabricated by the combustion process, (Right) EDS analysis of Pt particles in SDC20 powders

After firing, the 4vol% Pt – SDC20 pellets were analyzed by SEM and XRD. The SEM analysis of the pellet cross section is displayed in Figure 45 (Left). The sintering was incomplete and the sample maintained a small amount of porosity. XRD analysis of the pellet is presented in Figure 45 (Right). The XRD data confirms the fluorite SDC20 crystal structure and the presence of Pt metal in the sample.

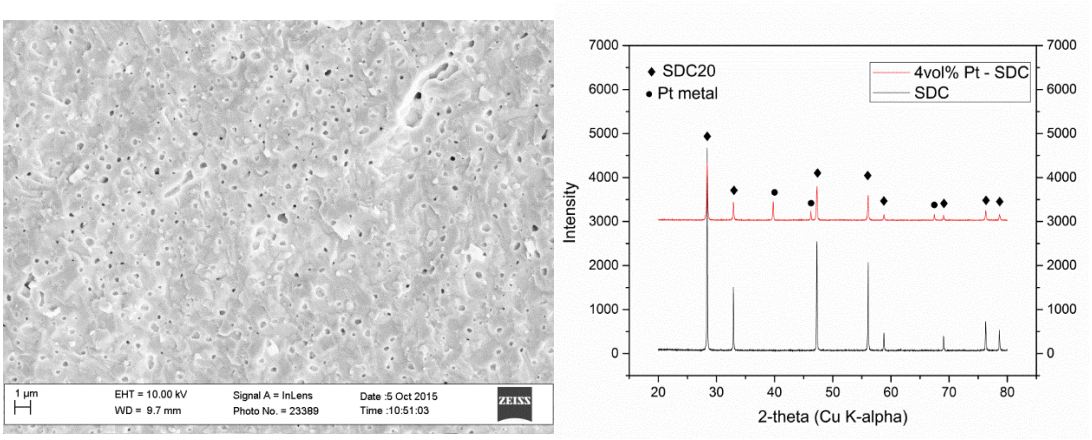

Figure 45 (Left) SEM image of 4vol% Pt loaded SDC 20 pellet cross section after sintering at 1400oC/ 5h in air; (Right) XRD of SDC20 powder fabricated by the citric acid method and 4 vol% Pt – SDC20 nanocomposite powder

Electrical measurements of the 4vol% Pt-SDC20 sample (electrode diameter = 0.635cm, pellet thickness = 0.62mm), collected by impedance spectroscopy in ambient air, are shown in Figure 46. The fitted impedance data for 4vol% Pt SDC20 microcrystalline sample is shown in Figure 46 (left-top). The impedance data is well-fitted to the same equivalent circuit as the SDC20 microcrystalline sample of the previous section. The grain and grain boundary resistances, from the fitting data, are plotted as a function of temperature in Figure 46 (right-top & left-bottom) in comparison to both the nano- and microcrystalline samples from the previous section. It is apparent that the grain boundary resistance of the 4vol% Pt SDC20 microcrystalline sample is approximately equivalent to the SDC20 1.5 µm sample. The grain resistance of the 4vol% Pt sample is lower than the nanocrystalline SDC20 sample at low temperatures, and higher than the microcrystalline SDC20 sample at high temperatures. The grain boundary resistance of the 4vol% Pt sample is heavily dependent on temperature. The total conductivity of the 4vol% Pt sample is compared to the total conductivity of the other samples. The

conductivity of 4vol% Pt is higher than the microcrystalline SDC20 sample but lower than the nanocrystalline SDC20 sample.

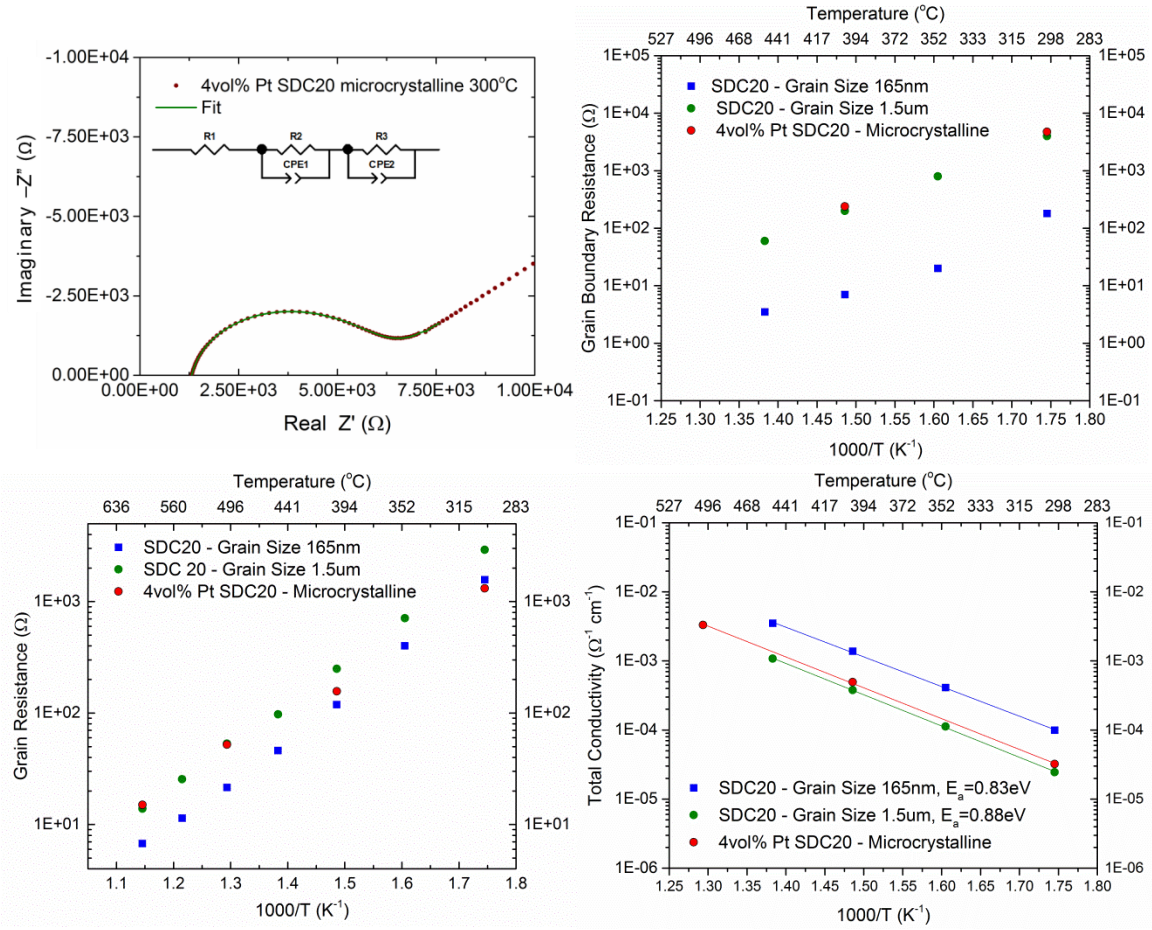

Figure 46 (left-top) Impedance spectra of 4vol%Pt SDC20 microcrystalline pellet at 300°C, (right-top) Grain boundary resistance of 4vol%Pt SDC20 microcrystalline pellet, (left-bottom) Grain resistance of 4vol%Pt SDC20 microcrystalline pellet, (right-bottom) Total conductivity of 4vol%Pt SDC20 microcrystalline pellet compared to microcrystalline SDC20 and nanocrystalline SDC20 (165nm grain size) pellet

To determine the nature of the charge carriers in the 4vol%Pt SDC20 microcrystalline sample, concentration cell measurements were completed. The results of the air(O_2), Pt// 4vol% Pt SDC20 //Pt, 15ppm O_2 – Ar concentration cell test are shown in Figure 47. The low voltage of ~0.077V measured by the concentration cell technique at 600°C reveals that the ionic transference number, t_{ionic}, of 4vol% Pt SDC20 pellet in the

given atmosphere is approximately 0.65 and the electronic conductivity transference number, $t_{electronic}$, is 0.35. Although the Pt volume concentration is low and a percolation pathway is unlikely to have been formed, enhanced electronic conductivity is measured in the 4vol% Pt SDC20 sample. It is highly likely that the concentration or mobility of electronic defects at the SDC20-Pt metal interface was increased and altered the electrical properties of the pellet.

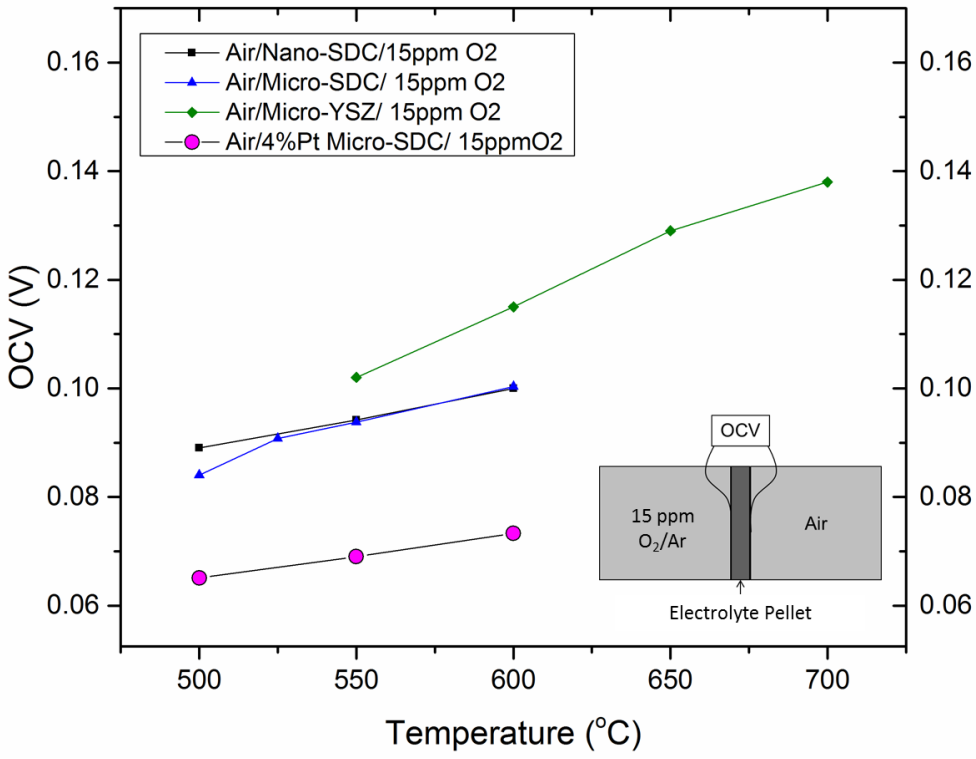

Figure 47 OCV measurements of 4vol% Pt SDC microcrystalline, Nano-grain SDC, Micro-grain SDC, and Micro-grain YSZ in 15ppm O_2 – Air concentration cell

3.6 Conclusions

In this investigation the role of interfacial effects on electrical conductivity in Sm^{3+} doped-CeO_2 has been clearly demonstrated. By using two-step sintering to fabricate nanocrystalline SDC20 samples, the effect of grain boundary concentration on transport properties has been measured. The grain boundary resistance of nanocrystalline SDC20

samples is significantly lower that the grain boundary resistance of microcrystalline SDC20. Total conductivity of nanocrystalline SDC20 is approximately one order of magnitude higher than that of microcrystalline SDC20 and concentration cell measurements have been conducted to prove the ionic nature of the enhanced electrical conductivity. Thin film SDC20 samples were fabricated by PLD with varying interface volume percentages to determine the effect of the MgO- SDC20 interface on electrical properties. The data presented shows that no significant variation in conductivity was measured when interface-dominated volume of the sample was changed. Comparing the nanocrystalline SDC20 results to the thin film results it is clear that the electrical properties are dependent on the exact nature of as-prepared sample and the interface. A curvature effect at the interfaces of the nanocrystalline SDC20 pellet is suspected to increase oxygen vacancy concentration at the interface. The enhanced oxygen vacancy concentration dramatically reduced grain boundary resistance and increased the total ionic conductivity of the sample. 4vol% Pt-SDC20 samples were fabricated to determine the interfacial effects of a secondary phase dispersed in the SDC20 sample. Concentration cell measurements indicate that the interfacial effect at the Pt/SDC20 interface enhanced electronic conductivity in the sample by increasing electronic charge carrier concentration or mobility.

Chapter IV

Interfacial effects on electrical conductivity in $Sm_{0.2}Ce_{0.8}O_{1.9}$ and $BaZr_{0.85}Y_{0.15}O_{3-\delta}$ thin film heterostructure samples

4.1 Introduction

In the previous chapter, dense, nanostructured Samarium-doped CeO_2 pellets were studied to explore interfacial and nano-scale effects on ionic conductivity. Although it would be beneficial to study SDC20 pellets with higher interfacial volume fraction (smaller grains), unavoidable grain growth during sintering limits the sample interface volume fraction, as discussed in the chapter. In this study, we explore the high aspect ratio of thin films and create ion conducting samples with interface volume dominated properties. Thin film thickness is easily controlled due to the slow growth process of pulsed laser deposition. By adjusting the thickness of the film, the interface volume to bulk volume ratio is easily controlled (as seen in Figure 26). Thin film studies of interfacial and nano-scale effects on ionic conductivity are a valuable tool for exploring new electrical properties of ionic conductors.

Recent studies of interfacial effects at thin film/substrate and thin film heterostructure interfaces have shown significant enhancement of ionic conductivity. The most cited example from the literature of colossal enhancement of electrical properties in thin film ionic conductors due to interfacial effects is from the work of Garcia-Barriocanal et al. from the Universidad Complutense de Madrid and Oak Ridge National Laboratory.[80] In this work, the ionic conductivity of Yttria-stabilized Zirconia (YSZ) is enhanced by approximately eight orders of magnitude when the heterostructure

is composed of YSZ layers of 1nm and $SrTiO_3$ layers of 10nm thickness. The significant enhancement of ionic conductivity is attributed to a 7% dilative strain in the YSZ layer at the YSZ/STO interface. Although the results of the YSZ/STO heterostructure work have been debated[114], the significant enhancement in electrical properties in the solid state electrolyte excite the desire to pursue interfacial effects further.

In this section we will investigate the interfacial effects between $BaZr_{0.85}Y_{0.15}O_{3-\delta}$, a proton conducting oxide, and $Sm_{0.2}Ce_{0.8}O_{1.9}$, the oxygen vacancy conducting oxide studied in Chapter III, and discuss the mixed-ion conducting electrolyte's use in internal reforming, intermediate temperature fuel cell systems.

4.2 Theory

4.2.1 Computer calculations of transport properties at BZY15/SDC20 interface

The BZY15/SDC20 interface is similar to the YSZ/STO interface studied by Garcia-Barriocanal et al.[80] Both heterostructures area composed of one perovskite crystal and one fluorite crystal and the lattice mismatch is approximately equal (BZY15/SDC20 ~9%; YSZ/STO ~7%). Preliminary DFT calculations and MD simulations (performed in our group by Lei Zhang) show the effect of 8% bi-axial strain on CeO_2 at 1000K. The changes in crystal structure, due to biaxial strain and temperature, are shown in Figure 48. The degree of disorder in the CeO_2 crystal structure increases from the stable condition as biaxial strain (7%) is applied and the disorder increases further as the temperature approaches 2500K.

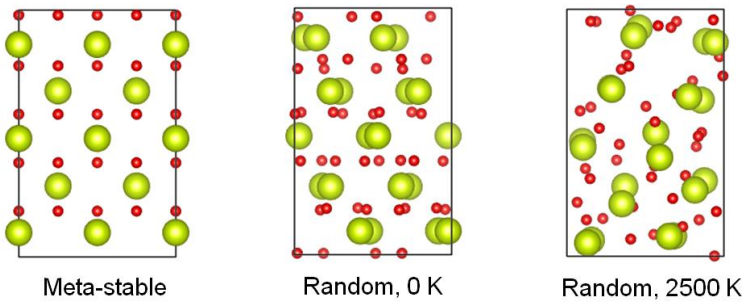

Figure 48 DFT-generated atomic structure of ceria in three scenarios: left, metastable fluorite CeO_2 structure; middle, disordered CeO_2 structure due to a-b bi-axial strain; right, fully disordered structure under both strain and thermo-activation at 2500K (yellow = Cerium; red = Oxygen)

The SDC20/$BaZrO_3$ interface has been modelled by DFT and is shown in Figure 49. A slightly different atomic configuration has been found depending on the termination of the BaZrO3 layer with BaO or ZrO_2.

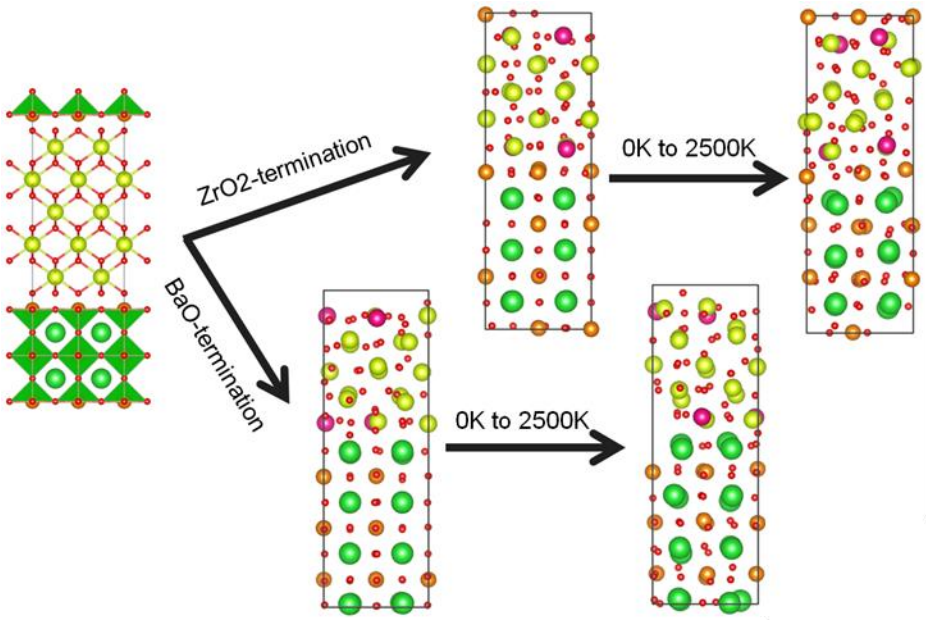

Figure 49 Graphical representation of simple add-on model of fluorite and perovskite structures (left), and rearrangement of atomic structure due to 7% a-b biaxial strain and temperature increase from 0K to 2500K. (yellow = Ce, plum = Sm, green = Ba, bronze = Zr, red = O)

The mean-square-displacement (MSD) of oxygen anions in strained CeO_2 has been generated by ab-initio molecular dynamics. The diffusion coefficient for each case has been calculated from the MSD data for comparison to diffusion in unstrained, bulk $Sm_{0.2}Ce_{0.8}O_{1.9}$. The migration barrier, E_k, of SDC20 has been set at 0.65eV and the vibration frequency for oxygen vacancy hoping is set to 5 THz. The diffusion coefficient data as a function of temperature (1000K – 2500K) is plotted in Figure 50 for oxygen vacancy diffusion in $Sm_{0.2}Ce_{0.8}O_{1.9}$ and oxygen anion diffusion in 7% strained, ZrO_2-terminated CeO_2. At 1000K (727^{o}C), a relevant temperature for solid oxide fuel cell electrolyte operation, the diffusion coefficient of oxygen anions in 7% strained, ZrO_2-terminated CeO_2 is three orders of magnitude higher than the diffusion coefficient of $Sm_{0.2}Ce_{0.8}O_{1.9}$. Although the exact interface structure of experimental samples may differ slightly from the DFT modeled ZrO_2-terminated $CeO_2/BaZrO_3$ interface, the significant enhancement in diffusion in the interface-dominated, strained structure motivates the work to experimentally verify the interfacial effect in SDC20/BZY15 and seek to apply the composite as an electrolyte for SOFCs.

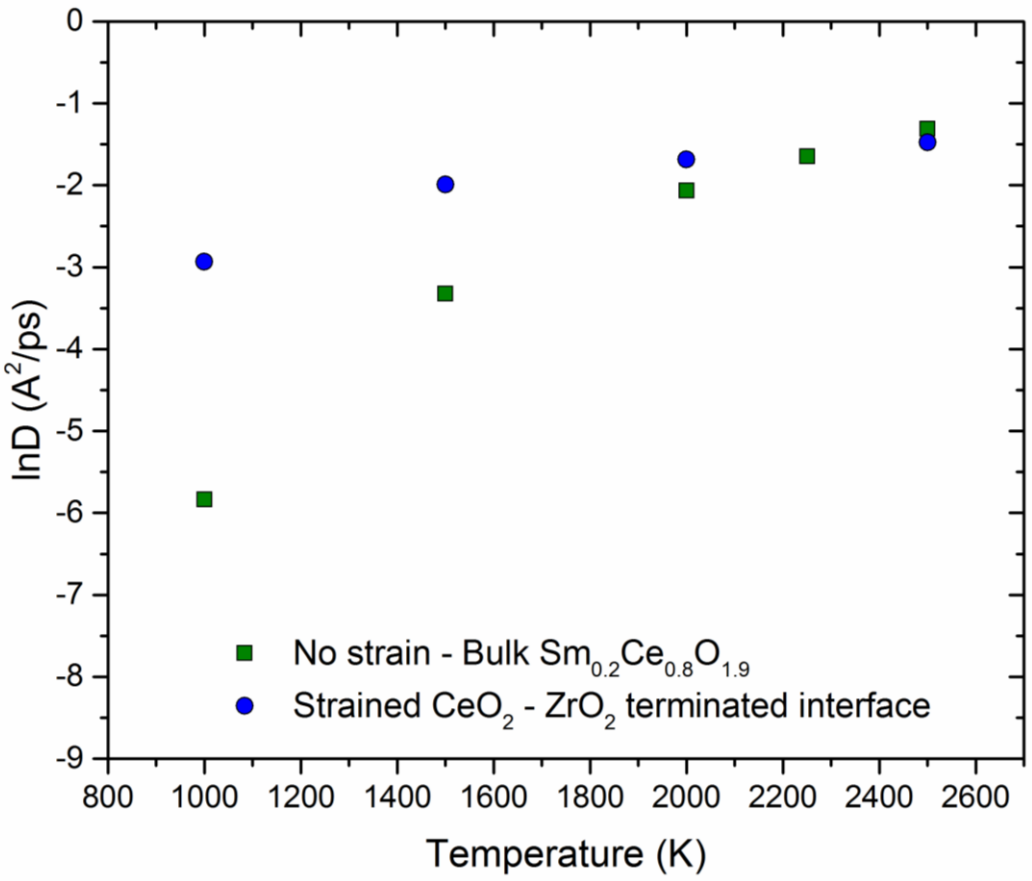

Figure 50 Diffusion coefficient of un-strained, bulk SDC20 (green) and strained CeO_2 with ZrO_2 terminated interface (blue) as a function of temperature

4.2.2 $BaZr_{0.85}Y_{0.15}O_{3-\delta}$, $Sm_{0.2}Ce_{0.8}O_{1.9}$, and MgO crystal structure and lattice mismatch calculations

Lattice mismatch between a thin film and single crystal substrate or another thin film can be quantified by Equation 30 where *f* is the lattice mismatch, and $d_{hkl,1}$ and $d_{hkl,2}$ are the lattice constants for the film and substrate respectively.

$$f_{1/2} = \frac{d_{hkl,2} - d_{hkl,1}}{d_{hkl,1}} \tag{30}$$

Interfaces with lattice mismatch are defined as coherent, semicoherent, or incoherent which corresponds to a mismatch percentage as represented in Table 5. The lattice coherency of the interface depends on film thickness, the material's elastic properties as

well as interface mismatch[115; 116]; therefore, the lattice mismatch range correlation to interface quality is an estimation.

Table 5 Thin film interface quality listed by ranges of lattice misfit calculated for a given system by Equation 30

Thin film Interface Quality	Lattice Mismatch Range
Coherent	<3%
Semicoherent	~3-5%
Incoherent	>5%

The model crystal structures for each of the materials studied in this work are shown in Figure 51. The crystal symmetry, lattice parameter and basal diagonal parameter of the systems are listed in Table 6.

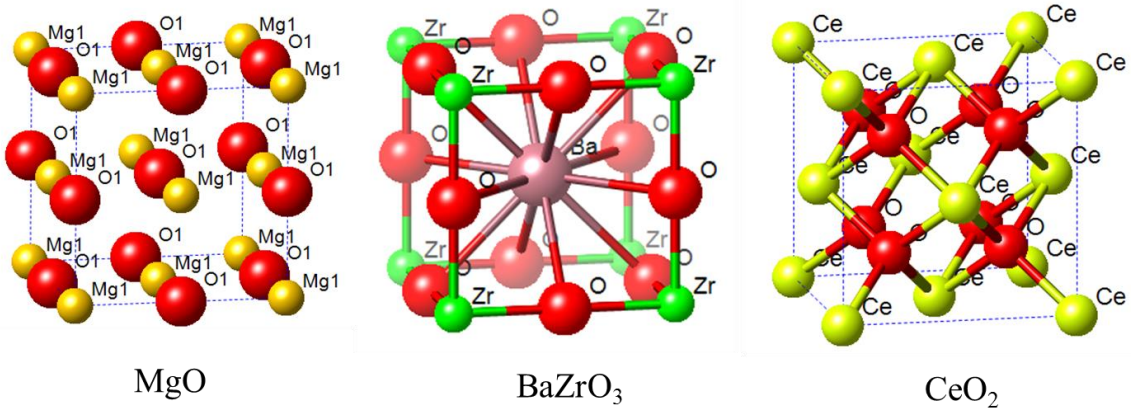

Figure 51 Unit cell representations of MgO, $BaZrO_3$, and CeO_2 crystal structures

Table 6 MgO, $BaZrO_3$, and CeO_2 crystal structure symmetry, lattice parameter, basal diagonal parameter and lattice mismatch between systems

System	Symmetry	Lattice Parameter	Basal Diagonal Parameter
$Ce_{0.8}Sm_{0.2}O_2$ (SDC)	cubic	a=~5.44Å	basal diagonal = 7.70 Å
$BaZr_{0.85}Y_{0.15}O_{3-\delta}$ (BZY)	cubic	a=~4.21Å	basal diagonal = 5.95 Å
MgO (100)	cubic	a=~4.21Å	basal diagonal = 5.95 Å

While the lattice mismatch factor for a given orientation between two materials can be calculated, the exact orientation of the crystals cannot be determined until after growth and the strain at the interface is complicated by a number of factors. These factors include the presence of misfit dislocations, segregation of mobile ions or defects, grain boundaries, ion deficiencies, or other defects. The lattice mismatch calculation between given orientations provides an estimation of the disorder expected at the interface. Experimental studies are used to determine if the disorder at the interface is beneficial or detrimental for ionic transport. In general, we expect a large lattice mismatch between the BZY15 and SDC20 phases which will induce a significant amount of disorder at the BZY15/SDC20 interface and cause significant deviations of the electrical properties at the interface when compared to the bulk properties. However, because the SDC20 layer thickness will be 2nm or less, it is expected that the SDC20 will accommodate a large amount of strain, as shown in the work of Garcia-Barriocanal et al. for ultra-thin layers of YSZ.[80]

4.2.3 Heterostructure thin films studies of interfacial effects in ionic conductors

Heterostructure thin film studies have been employed successfully in the literature by Maier et al.[113] to test the interfacial effects of the BaF_2/CaF_2 heterostructure system. The results of Maier's seminal work are shown in Figure 52 (left). By systematically varying the thickness of the heterostructure layers the electrical properties are related to the interfacial volume of the sample. As the number of interfaces in the sample decreases the conductivity of the sample approaches the bulk properties of the materials of the heterostructure. When the heterostructure layers are 16.2nm thick, the interface concentration is at the maximum for the sample series and the conductivity is the highest.

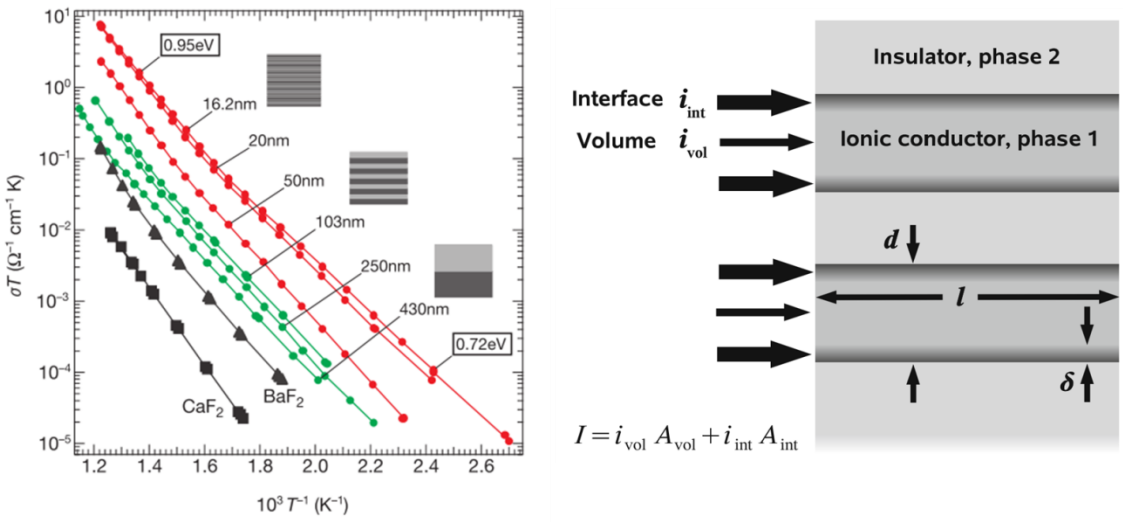

Figure 52 (Left) Ionic conductivity of the CaF_2/BaF_2 heterostructure series (layer thickness = 430nm, 250nm, 103nm, 50nm, 20nm, 16.2nm) studied by Maier et al. with significant enhancement due to interfacial effects[113], (Right) Schematic of current pathways in heterostructure sample with given layer thickness and interface dominated thickness[79]

Figure 52 (right) shows the ion conduction pathways in an insulator/ionic conductor heterostructure sample, from the work of Korte et al.[79] The thickness of the ionic conducting layers, *d*, thickness of the interface dominated region, *δ*, interface

current density, i_{int}, and volume current density, i_{vol}, are marked. The total current density is equal to the interfacial current density and the volume current density. For a heterostructure system of two ionic conductors, the total current density is given by equation 31.

$$I = i_{ion\ 1,bulk}A_{ion\ 1,bulk} + i_{ion\ 2,bulk}A_{ion\ 2,bulk} + i_{interface}A_{interface} \quad (31)$$

Additional works on heterostructure film series investigations of interfacial effects in YSZ and Calcium-stabilized Zirconia (CSZ) are cited.[78; 117]

In order to test and determine the interfacial effects at the BZY15/SDC20 interface a series of heterostructure thin films have been fabricated by PLD. As shown in Figure 53, the heterostructure sample series is a systematic study of changes in electrical properties of the heterostructure in relation to interface concentration, while maintaining constant film thickness to reduce error associated with geometric factors involved in the electrical conductivity calculations.

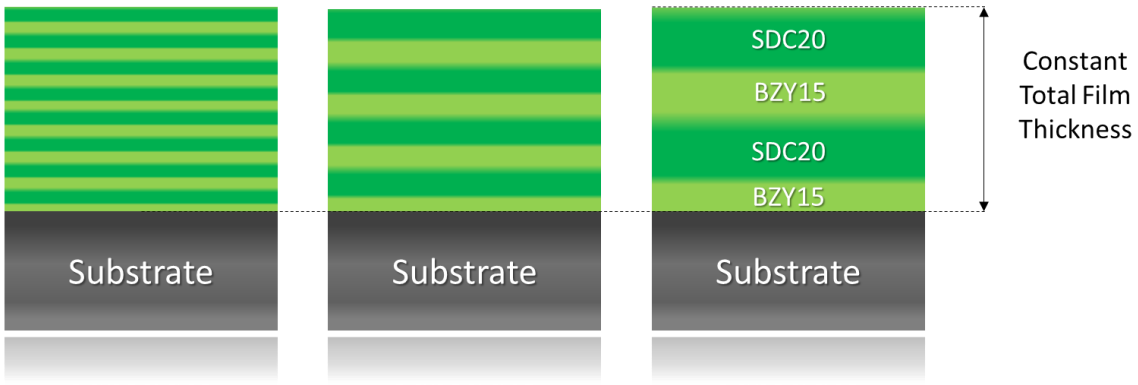

Figure 53 Heterostructure BZY15/SDC20 film series with constant film thickness but varying interface concentration

The total current density of these samples includes BZY15/SDC20 interface current pathways as well as pathways at the BZY15/Substrate (MgO) interface and the

SDC20/Air interface. For the samples measured in this study the total current density is given by Equation 32. Because the total number of BZY15/SDC20 interfaces greatly exceeds the two SDC20/Air and BZY15/MgO interfaces the effects measured in the sample will be primarily attributed to the BZY15/SDC20 interfaces.

$$I = i_{BZY15,b}A_{BZY15,b} + i_{SDC20,b}A_{SDC20,b} + i_{BZY15/SDC20,i}A_{BZY15/SDC20,i} + i_{BZY15/MgO,i}A_{BZY15/MgO,i} + i_{BSDC20/Air,i}A_{SDC20/Air,i} \quad (32)$$

4.2.4 Mixed proton and oxygen anion conducting fuel cell electrolyte

It is beneficial to use a mixed-ion conducting electrolyte in intermediate temperature fuel cells to enhance fuel cell efficiency and reduce carbon deposition from the internal reforming process. A proton conducting electrolyte (e.g. BZY15) membrane shuttles hydrogen to the cathode side of the cell to form water and increase the fuel partial pressure at the anode side (reducing fuel dilution). An oxygen anion conducting electrolyte (e.g. SDC20) passes oxygen to the anode side providing excess oxygen to bond with carbon and remove coking deposits which block anode reaction sites and degrade the anode mechanical properties. A composite, mixed-ion electrolyte of SDC20 and BZY15 can be tailored to deliver the optimal amount of oxygen to the anode for fuel reforming and carbon removal while forming excess water at the cathode to reduce fuel dilution and enhance fuel cell efficiency. The SDC20/BZY15 composite electrolyte proposed in this work is represented in Figure 54.

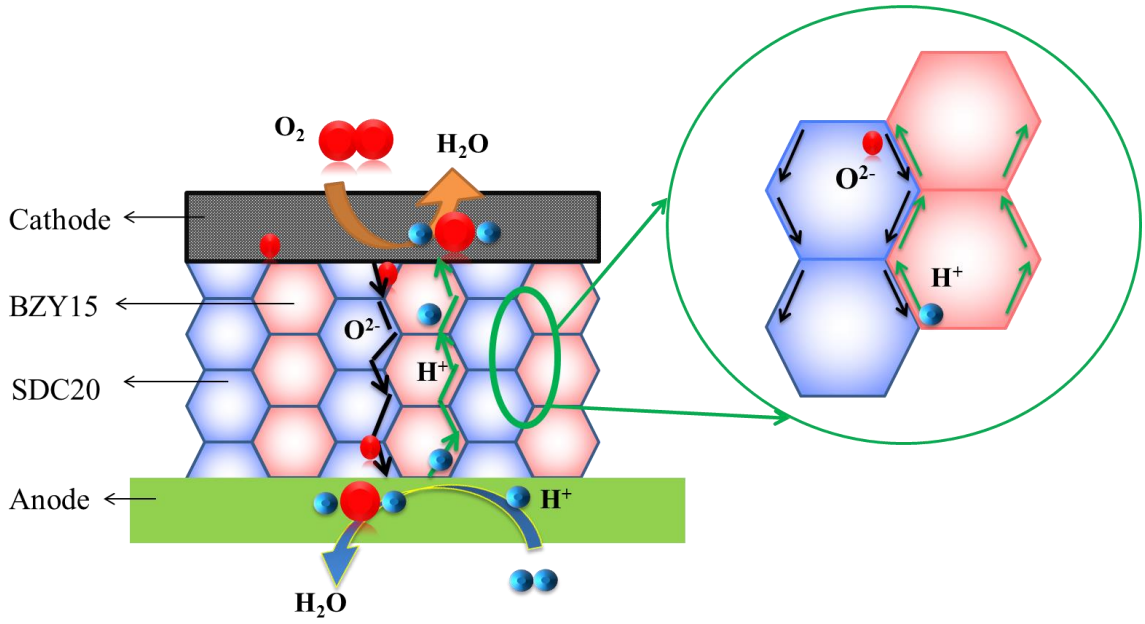

Figure 54 Composite, mixed oxygen vacancy and proton conducting solid state electrolyte which forms water at both the anode and cathode sides of the cell for high fuel cell efficiency, internal reforming assistance and carbon coke removal

Additionally, and importantly for this investigation, the interfaces of the mixed-ion electrolyte are capable of providing low resistance charge carrier pathways due to interfacial effects. Interfacial effects between BZY15 and SDC20 electrolytes have been investigated by DFT modeling and will be investigated by thin film testing of the heterostructure materials.

Although composite electrolytes for SOFCs have been fabricated and tested in our lab, chemical compatibility between the composite electrolyte components is a chronic issue due to the required high sintering temperature (>1400^{o}C) for fuel cell electrolytes. In general, chemical compatibility is a significant technical hurdle for composite electrolytes. It has been confirmed that an electronically blocking phase forms at the NiO-$BaZr_{0.1}Ce_{0.7}Y_{0.1}Yb_{0.1}O_{3-\delta}$(anode)/SDC20(electrolyte) interface after sintering.[118] Although a blocking layer between SDC20 and anode is beneficial for reducing

electronic conductivity and increasing fuel cell OCV, the blocking layer has also been confirmed to reduce ionic transport. In order to bypass this common difficulty in composite electrolyte development, heterostructure electrolytes can be fabricated at 700^{o}C by PLD. Because the temperature is much lower than the typical sintering temperature of fuel cell electrolytes, there is no secondary phase formation and the true interfacial properties can be tested.

4.2.5 Fabrication techniques for vertical alignment of heterogeneous interfaces

Recently, a PLD technique has been reported which enables the fabrication of vertically-aligned composite films with out-of-plane interfaces.[119-124] The out-of-plane characteristic of the interfaces is designed to increase ionic transport in direction of charge transport (O^{2-}) for each film, is made in Figure 55.

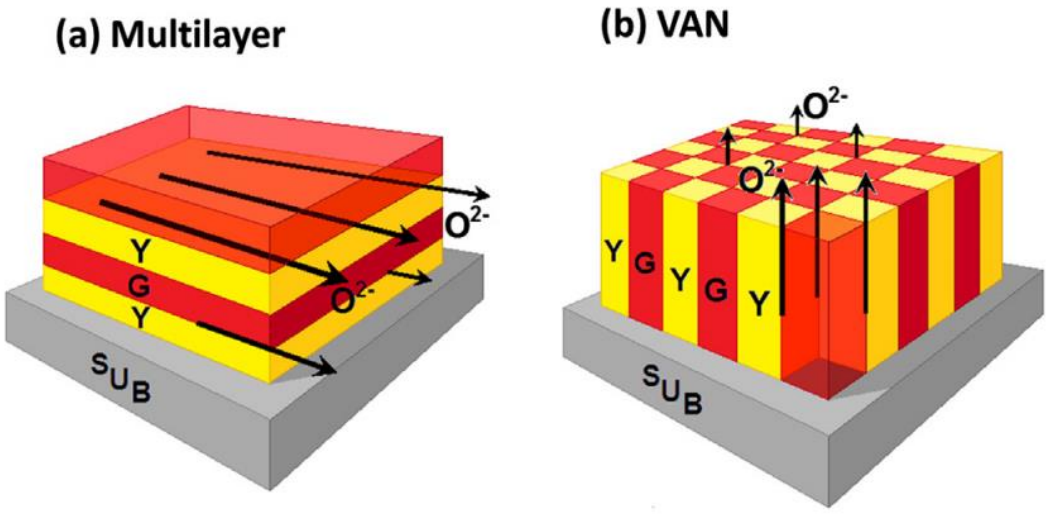

Figure 55 (A) Illustration of traditional heterostructure thin film sample and (B) a self-assembled vertically-aligned composite film designed to increase out of plane ionic transport (Image taken directly from Su, Q., Wang, H., et al.[120])

Vertically-aligned composite films are fabricated by PLD using a sintered, composite target. During deposition of the film onto the substrate, PLD parameters are controlled to promote segregation of each phase, forming a nanocolumnar structure with two-phase, uniform composition. The spontaneous formation of vertically-aligned composite films is dependent on chemical stability of the constituent phases and structural compatibility of each phase with the substrate. This technique is considered a unique possibility for transferring our investigation of interfacial effects in heterostructure films to real electrolytes in micro-SOFCs. The transfer process pursued in this work is illustrated in Figure 56. We will investigate thin film heterostructure model systems and begin translation of the interfacial effects to fuel cell electrolytes by the fabrication of BZY15/SDC20 vertically-aligned composite films.

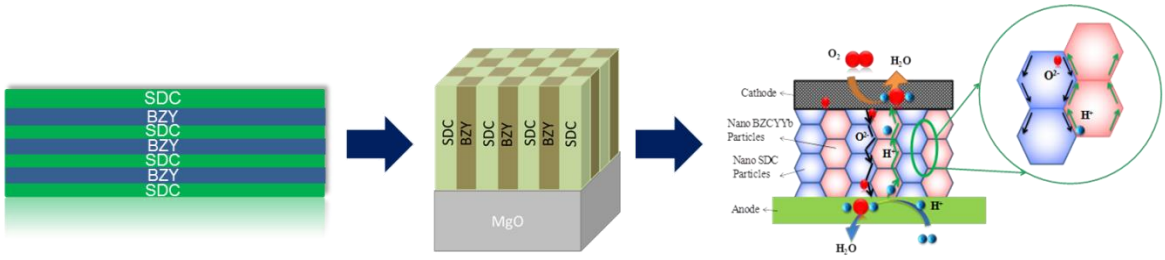

Figure 56 Schematics depicting translation of interfacial studies on thin film heterostructure model systems (left) to vertically-aligned composite BZY15/SDC20 films (middle) and implementation into a solid state electrochemical device with BZY15/SDC20 vertically-aligned composite electrolyte (right)

4.3 Experimental

4.3.1 Characterization of thin film quality by X-ray diffraction

Films grown by PLD can vary in their quality, ranging from perfect epitaxy to ideal polycrystalline random orientation. Perfect epitaxial films are defined as single crystal films with perfect registry with the substrate and the absence of defects. While many films are claimed to be “epitaxial” the actual quality may be better described as

nearly perfect epitaxial, textured epitaxial, strongly textured polycrystalline or textured polycrystalline according to Speakman's nomenclature.[125] High resolution X-Ray diffraction of PLD fabricated films is essential for characterizing the quality of thin films grown on single crystal substrates. Particularly, for this work HRXRD has been used to determine the composition, orientation, and mosaic spread of films fabricated by PLD.

All thin film X-ray diffraction measurements were collected using a PANalytical MRD four-circle diffractometer with Cu-Kα radiation. The incident beam optics consisted of a 4-bounce hybrid monochromator to filter X-rays other than Cu-$K\alpha_1$ (1.54056 Å) output. The beam was collimated to ~20 arc sec in the plane of scattering. A 1/2° slit was placed at the end of the incident optics, before the sample.

Omega-2Theta Scan

Omega-2theta scans have been used in this work to determine the Bragg diffraction peaks of the thin films fabricated by PLD for one specific tilt. The scan of a thin film sample measured using this method is shown in Figure 66. For a polycrystalline or powder sample, all Bragg diffraction peaks will be present in the omega-2theta scan due to random crystallite orientation which satisfies all possible Bragg diffractions. However for epitaxial or strongly textured films, all unit cells or crystallites are oriented with respect to the substrate and so only produce one family of Bragg peaks. The omega-2theta scan is valuable for phase identification of the film and for confirmation of the highly textured quality of the film.

Omega Scan – Rocking Curve

In this work, rocking curve measurements have been used to determine the mosaicity and defected nature of the thin films fabricated by PLD, as well as the quality of the MgO substrates used for fabrication. Rocking curve measurements are carried out by moving the X-ray detector to a desired Bragg diffraction angle and then collecting a scan over a range of omega. As omega is scanned, the range of tilt of the grains in the highly textured film (or substrate) is measured. For a perfect epitaxial film the Bragg peak will appear as a sharp peak over a low range of omega. As the mosaicity or defected nature of the film increases, the Bragg peak will broaden as a reflection of the film quality.

Omega-2Theta vs. Omega - Reciprocal Space Map

Omega-2Theta vs. Omega(tilt) measurements have been used to construct reciprocal space maps of the (100) Bragg peak of the BZY15 thin films fabricated by PLD. In this scan, omega-2theta measurements are collected over a range of omega to map the degree of tilt of the highly textured films. From the scan data a contour plot is constructed which includes the intensity of the Bragg reflection at all points in omega and omega-2theta. The map provides a useful visualization of the thin film and easily distinguishes films of higher quality from films with high mosaicity and large numbers of defects.

A schematic of thin films with varying quality is shown in Figure 57. The films in this work will be most closely associated with the film qualities illustrated here.

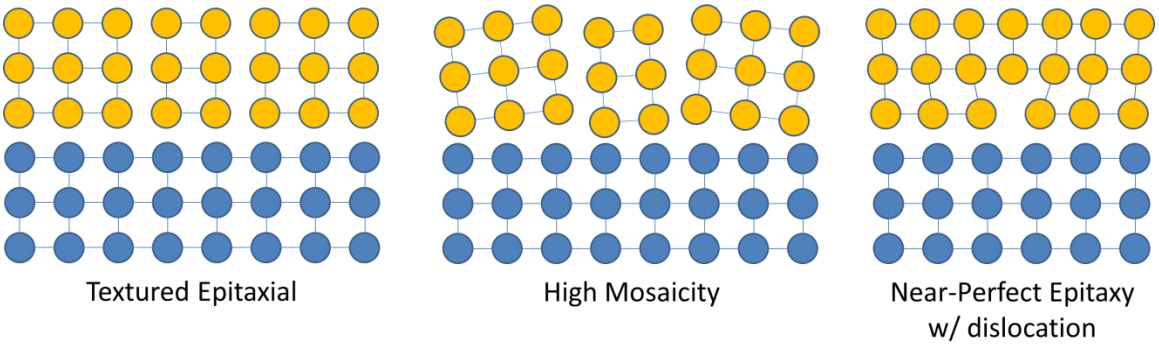

Figure 57 Illustrations of thin film qualities including textured epitaxial (left), high mosaicity (middle) and near-perfect epitaxy with dislocation (right)

4.3.2 Reflection high-energy electron diffraction (RHEED)

Reflection high-energy electron diffraction (RHEED) has been used in the work for *in-situ* characterization of thin film fabrication by PLD. RHEED is a surface sensitive electron diffraction technique which is useful for characterization of the structure of crystalline materials. An electron beam at low incident angle interacts with the sample and diffracts according to the crystal structure of the top surface of the film producing a characteristic streaking pattern that is detected and imaged. At ORNL CNMS the RHEED system is fixed at 40mm above the target surface which requires all PLD film deposition to be made at 40mm if RHEED analysis is desired. The RHEED pattern (both (100) and (110)) of the surface of the MgO substrate was imaged before deposition. Within ~5 PLD laser pulses the characteristic film streaks became visible, demonstrating the surface sensitivity of the technique. RHEED is especially beneficial for thin film heterostructure growth because it can be used to monitor the completion of a full layer of film and signal the fabrication to switch to the next layer material.

4.3.3 Electron Microscopy

In this work, visualization and chemical analysis of thin films fabricated by PLD were characterized by electron microscopy at Oak Ridge National Laboratory and at Georgia Tech. Transmission Electron Diffraction (TEM) and Scanning Transmission Electron Microscope (STEM) techniques are invaluable for characterization of materials at the length scale required in this work. Visualization of film interfaces at the atomic scale enable grain size analysis, atomic distribution, dislocation identification, and degree of angle between grains in textured epitaxial and polycrystalline films.

All images and composition data completed at ORNL was collected on an aberration-corrected JEOL 2200FS instrument. All images and composition data completed at Georgia Tech were collected on an FEI Tecnai F30 super-twin field-emmision-gun TEM. High resolution TEM (HRTEM) has been used to study the atomic structure and defects of thin film samples. STEM images were collected with a bright field detector and the images are comparable to the HRTEM images. STEM High-angle annular dark-field imaging (HAADF) was performed simultaneously with Electron Energy Loss Spectroscopy (EELS) analysis for chemical characterization of the thin films. For the HAADF technique the Bragg scattered electrons are not collected but a large number of incoherently scattered electrons are collected. These electrons are extremely sensitive to the atomic number of atoms in the sample and so can be used for chemical analysis.

4.3.4 PLD Fabrication

The PLD facility at Oak Ridge National Laboratory Center for Nanophase Materials was used for thin film fabrication. The PLD system (Figure 58) is equipped

with a KrF excimer pulsed laser (λ=248nm) source that was operated with energy density of 2.86J/cm^2, a target spot size of 0.065cm^2 – 0.005cm^2, 1-10Hz pulse rate, and approximately 700^{o}C substrate temperature. The PLD chamber was backfilled with O_2 and the deposition pressure was approximately 40 – 100mtorr. An automated target-holder oscillated the BZY15, SDC20 and BZY15/SDC20 composite PLD targets during deposition. The substrates were rotated during deposition for uniform deposition. An In-situ RHEED gun and detector was mounted in the PLD chamber for film characterization 40 mm below the substrate holder/heater.

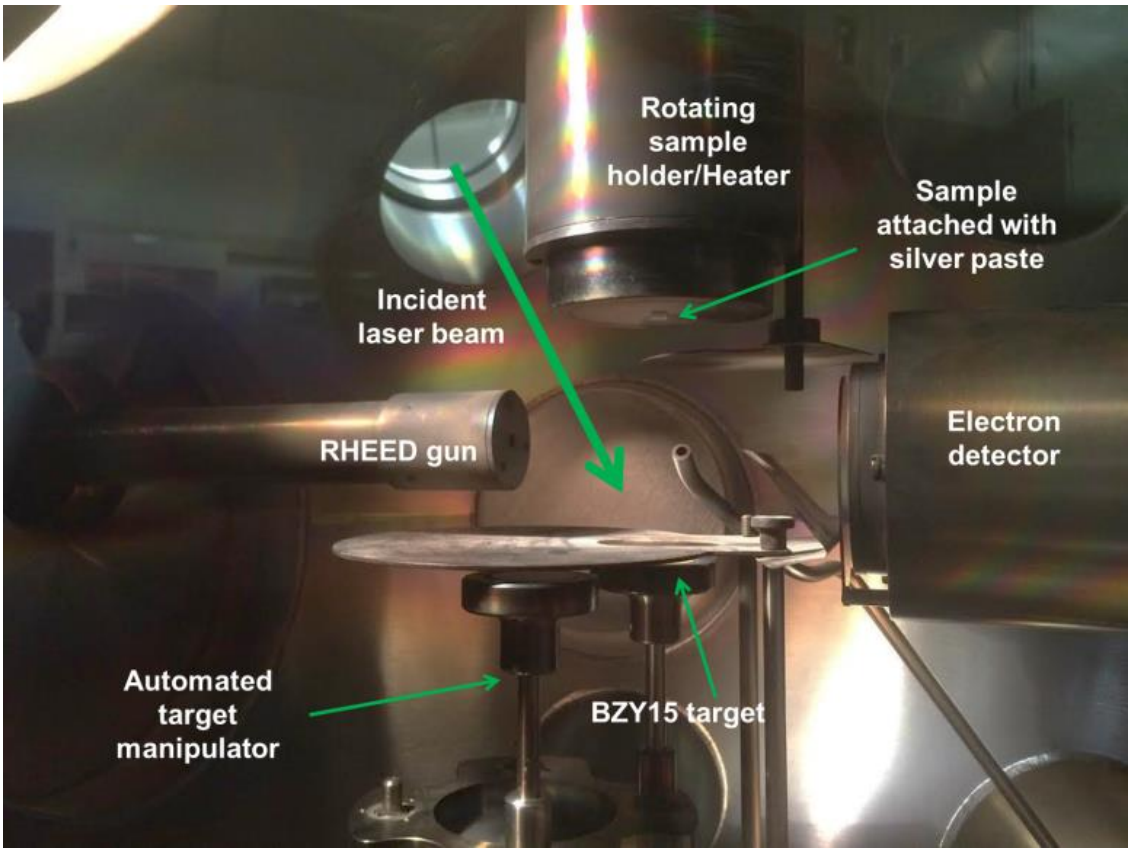

Figure 58 Pulsed Laser Deposition chamber at Oak Ridge National Laboratory Center for Nanophase materials with RHEED capability

4.3.5 Target fabrication

BZY15 was prepared by the solid-state reaction method from barium carbonate (Sigma Aldrich, ≥99% $BaCO_3$), zirconium oxide (Alfa Aesar, 99% ZrO_2), and yttrium (III) oxide (Alfa Aesar, 99.99%, Y_2O_3) precursor powders in stoichiometric ratio. The powders were mixed for 24h in ethanol, dried, and then calcined at 1100^oC for 10h. The calcining process was repeated to achieve the pure phase. To reduce the particle size and aid the sintering process, the as-prepared BZY15 powder was ball milled for 2hrs, at 800rpm in deionized water using a Fritsch planetary ball mill (Pulverisette 7). PLD targets were fabricated by uniaxial pressing (124MPa) of disks (d = 32mm) with thickness of 3mm and firing at 1500^oC for 5h with heating rate of 3^oC/min in ambient atmosphere. The SEM cross section of the PLD target fabricated with ball-milled BZY powders and with powders that were not ball milled can be seen in Figure 59.

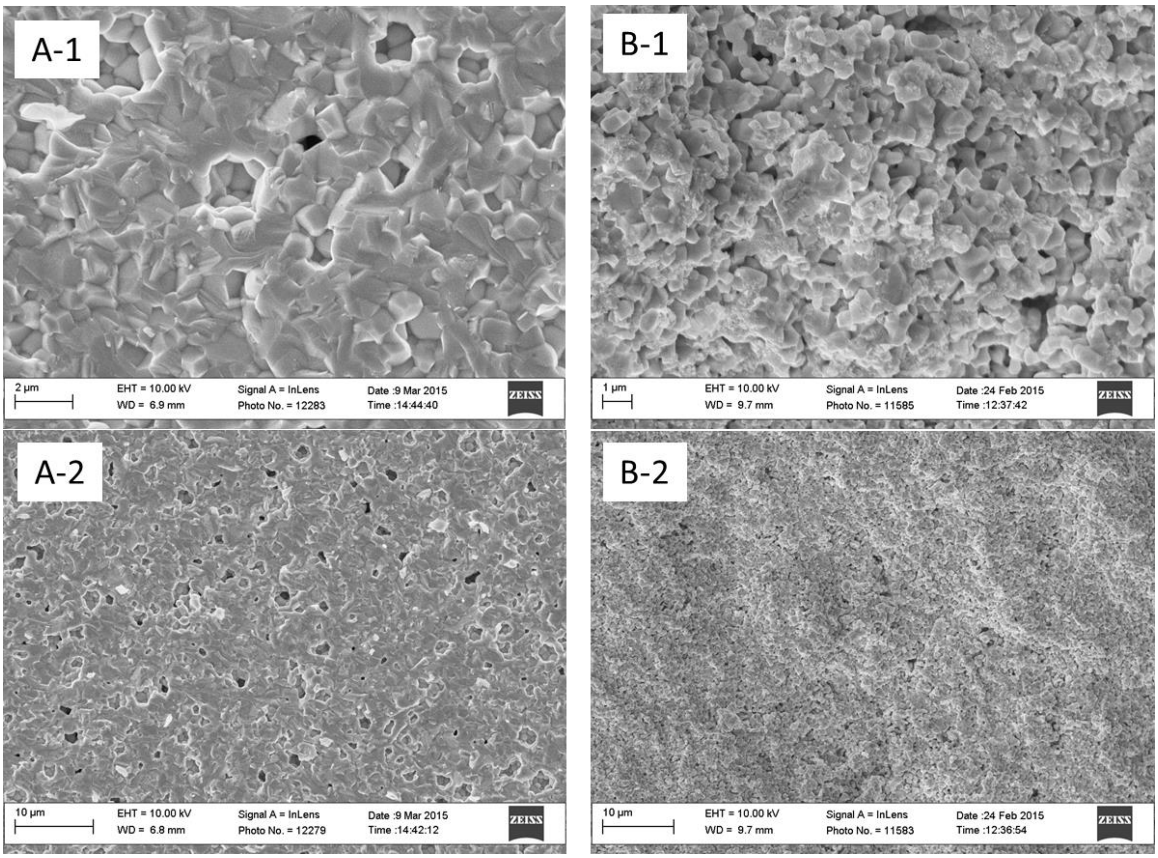

Figure 59 SEM images of (A-1, A-2) BZY15 PLD target sintered at 1500oC for 5h after 2h planetary ball-milling at 800rpm, and (B-1, B-2) BZY15 PLD target sintered at 1550oC for 10h without initial ball-milling. Reduction of particle size by ball milling significantly enhances PLD target density after sintering.

SDC20 targets were prepared from commercial SDC20 powder (Nextech Materials, mid-grade, micro-crystalline) by uniaxial pressing and firing at 1400^{o}C for 5h. The targets were easily densified with this firing procedure.

Composite BZY15 and SDC20 targets were prepared by mixing BZY15 and SDC20 in 50:50 vol% ratio in ethanol for 12 hours. The ball-milled BZY15 powders were used as precursor to enhance densification during sintering. The powders were dried, uniaxially pressed and sintered at 1500^{o}C for 5h.

4.3.6 MgO (100) substrate preparation

MgO (100) single crystal substrates (5mm x 5mm x 1mm, single side polish) were purchased from MTI Corporation and Princeton Scientific Corporation. The substrates were treated in buffered oxide etch (BOE) for 30 sec, rinsed in DI water and annealed at 1100^{o}C for 6h. Atomic Force Microscopy (AFM) was used characterize the MgO substrate surfaces. The MgO (100) substrates were affixed to the substrate holder/heater using silver paste and cured at ~100^{o}C for 30 mins before mounting in the PLD chamber.

4.3.7 Electrical measurements

Impedance spectroscopy was used to measure the impedance of the thin film samples in ambient air from 300^{o}C to 450^{o}C. The impedance was collected in the frequency range of 5MHz to 10mHz with a 100-200mV AC bias using a Solartron 1255 Frequency Response Analyzer, EG&G 273A Potentiostat and a Solartron 1296 Dielectric Interface. Platinum electrodes were applied at ORNL CNMS in the cleanroom by photolithography and Pt metal evaporation in a 6 pad arrangement as shown in Figure 60. Electrical connection to the thin films samples was made by Ag wires attached to the Pt pads by Ag paint. The samples were annealed at 550^{o}C for 2 hours to ensure proper electrical connection to the pads before electrical measurements were recorded.

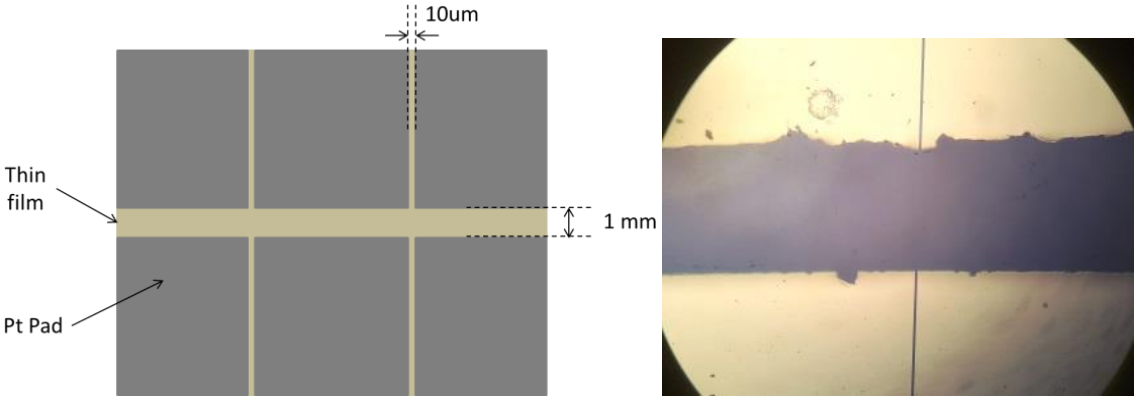

Figure 60 (Left) Schematic of Pt pad layout on thin film sample; (Right) optical microscope image of 1mm spacing between Pt pads (horizontal) and one set of 10um spaced Pt pads (vertical)

In the literature, an "illusional" interfacial effect on ionic conductivity has been discussed due to artifacts of in-plane conductivity measurements of thin film samples.[126] We found illusional thin film effects in BZY15 thin films during our preliminary testing when using the thin film testing scheme identified in Section 3.4.4. The conductivity data, calculated from thin film impedance data collected, is shown in Figure 61. Although an increase in conductivity is measured with a decrease in film thickness, it was determined that leakage current through the Al_2O_3 sample holder created the "illusional" interfacial effect. The raw resistance data for the BZY15 thin films and bare sample holder (without thin film sample present) are shown in Figure 62. The resistance of the low-purity Al_2O_3 sample holder is equivalent to the resistances measured when the thin film sample is present. Therefore, the calculated conductivity increase with decreasing film thickness (increasing interface-dominated volume) is an artifact of the conductivity calculation.

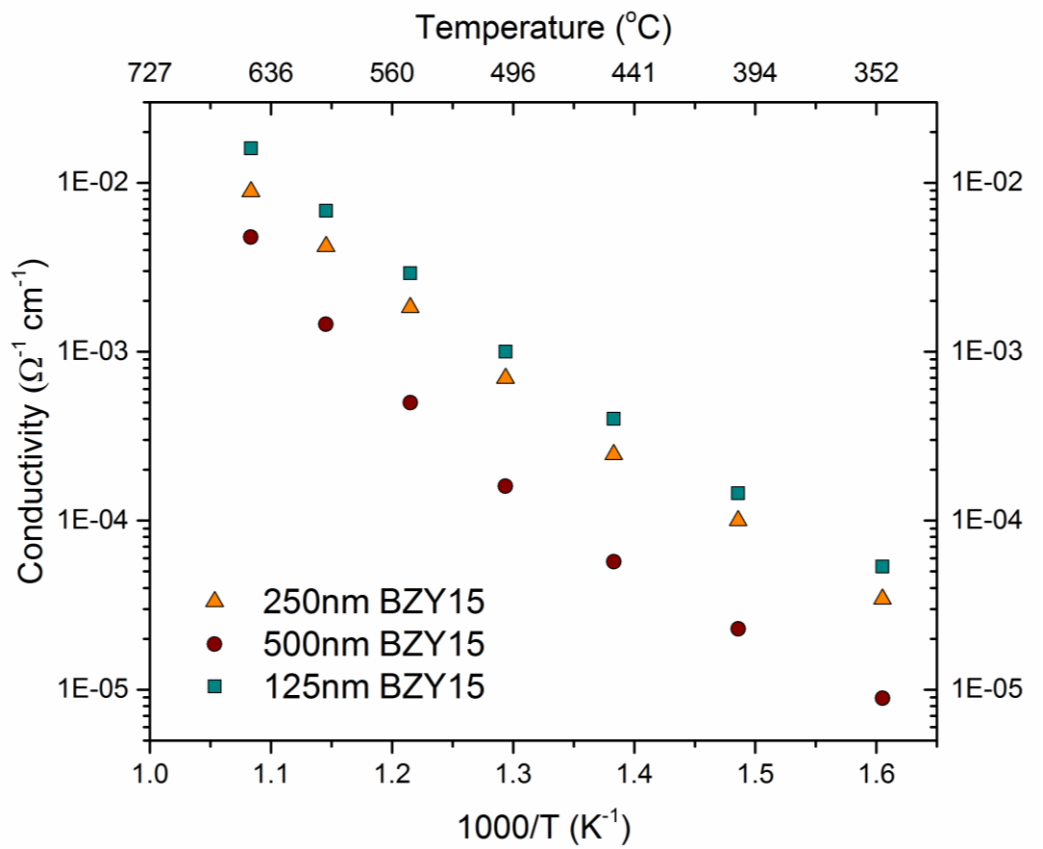

Figure 61 Total conductivity of BZY15 thin film samples exhibiting "illusional" interfacial effects due to leakage current in the Al2O3 holder of the testing setup.

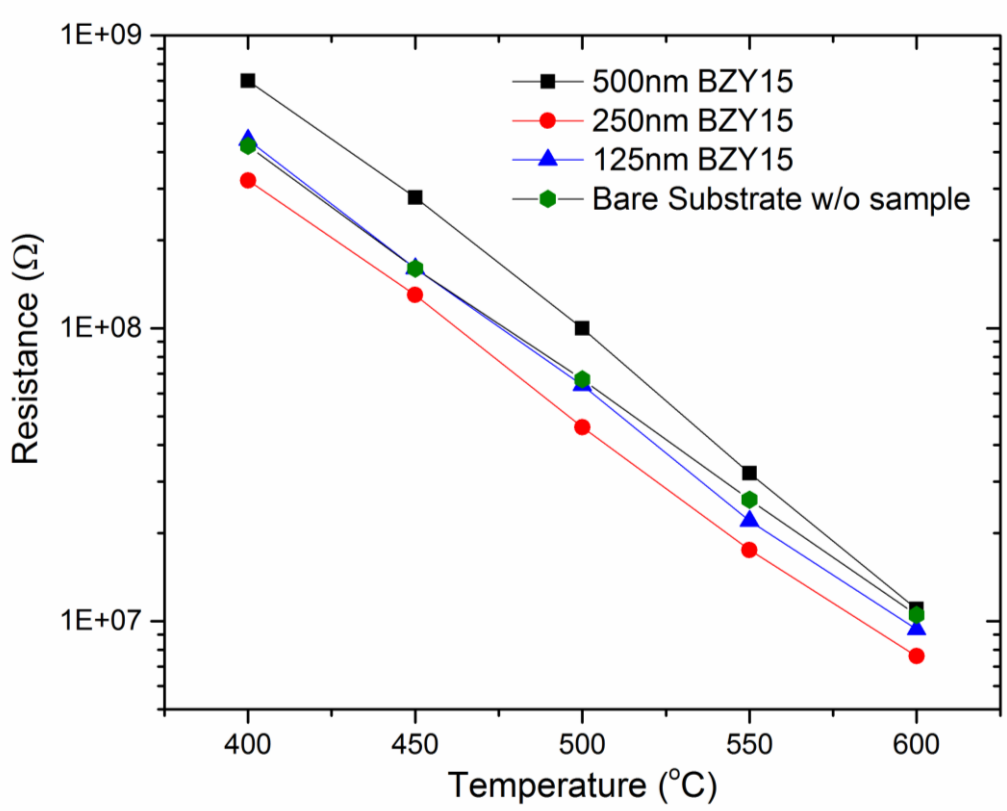

Figure 62 Total resistance of BZY15 thin films compared to total resistance of alumina substrate

To ensure that the electrical resistance measurements of the heterostructure samples was not influenced by the leakage current through the measurement fixture, resistance measurements of the fixture, fixture + substrate, and fixture + substrate + thin film were taken as shown in Figure 63. The resistance of the heterostructure film is significantly lower than the resistance of the fixture measurement and the fixture + substrate measurement. This ensures that the resistance measurement of the films is a true measurement and the interfacial effects determined from the measurements are not illusional. Additionally, the thickness of heterostructure films measured in this study was fixed so that the geometry of the samples would remain constant for all conductivity calculations from the impedance data.

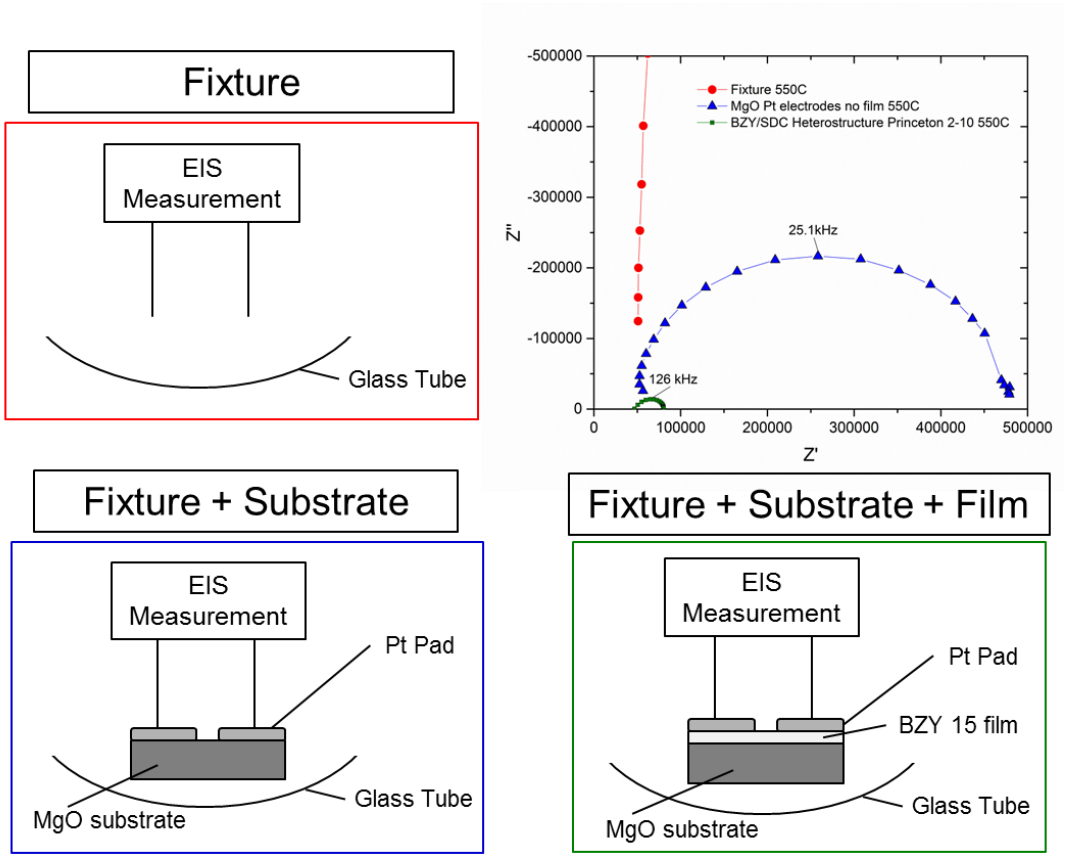

Figure 63 Comparison of impedance spectroscopy (IS) measurements for the fixture used for high temperature measurements of thin film samples (red) to check for leakage current in the fixture; IS measurements of the MgO substrate with no film (blue); and IS measurements of the BZY15 film on MgO substrate (green)

During testing of the thin films samples up to 500^{o}C it was found that the area between the Pt electrodes (connected to Ag wires by Ag paint) was coated with non-connected Ag particles. The SEM images and EDS data of the regions near the left electrode (A), between the electrodes (B), and near the right electrode (C) are shown in Figure 64.

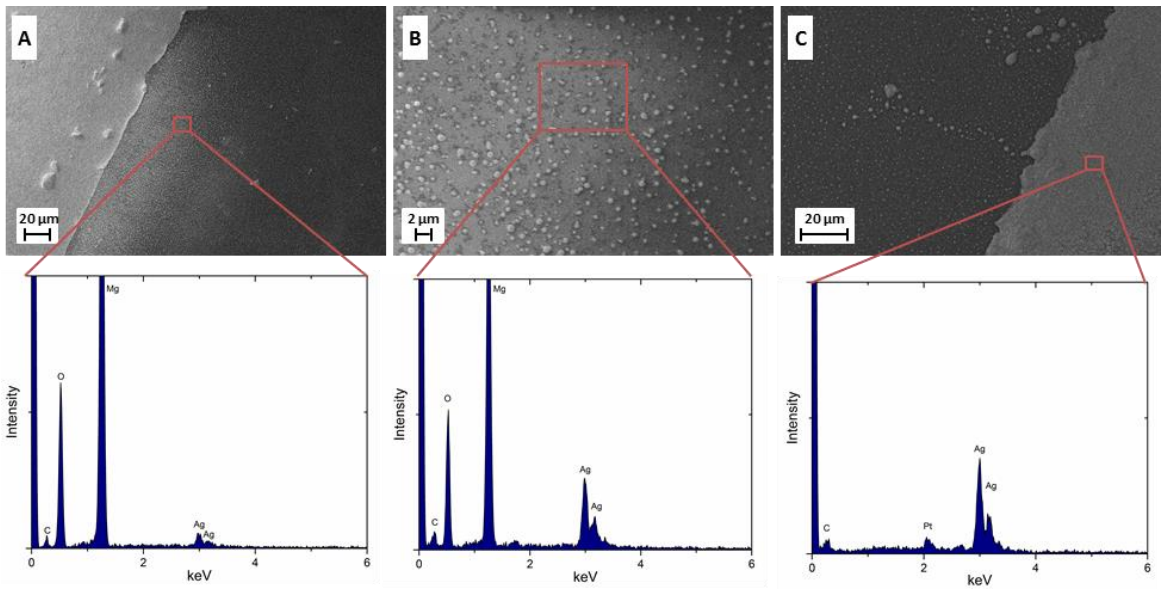

Figure 64 SEM and EDS analysis of MgO substrate with Pt electrodes after electrical testing from 400oC to 600oC. (A) & (C) represent the left and right electrodes in the testing configuration, respectively, and (B) is a high magnification of the MgO substrate wit h Ag nanosphere deposition taken halfway between the Pt electrodes. The corresponding EDS spectra reveal the chemical nature of each section of the sample after testing.

The typical impedance spectra for the thin film samples is shown in Figure 84. The impedance spectra is composed of only a single semicircle in the Nyquist plots. We fit the semicircle with a single RC circuit and take the lowest frequency intercept with the real axis to be the total resistance of the thin film sample. This approach is identical to all thin film and heterostructure ionic conductor sample studies in the literature and isfurther explained by Korte, et al.[78]

4.3.8 Heterostructure sample fabrication

In order to investigate interfacial effects, $BaZr_{0.85}Y_{0.15}O_{3-\delta}$ and $Sm_{0.2}Ce_{0.8}O_{1.9}$, heterostructure thin film samples have been fabricated by PLD. The list of heterostructure thin film samples is shown in Table 7. The total thickness of the films was fixed to

125nm but the number of layers, deposited by PLD is systematically varied. The number of BZY15/SDC20 interfaces increases as layer thickness decreases.

Table 7 BZY15/SDC20 heterostructure samples fabricated by PLD for testing of interfacial effects between the ionic conducting layers.

Sample ID	Film	Description	Calculated # of BZY15/SDC20 interfaces	Thickness
5 – 0.5	BZY15/SDC20 Heterostructure	5nm BZY15 / 0.5nm SDC20 x23 layers	**45** interfaces	125nm
10 – 1	BZY15/SDC20 Heterostructure	10nm BZY15 / 1nm SDC20 x12 layers	**23** interfaces	125nm
20 - 2	BZY15/SDC20 Heterostructure	20nm BZY15 / 2nm SDC20 x6 layers	**11** interfaces	125nm

4.4 Results and discussion

4.4.1 Structural and chemical characterization of $BaZr_{0.85}Y_{0.15}O_{3-\delta}$ and $Sm_{0.2}Ce_{0.8}O_{1.9}$ films on MgO substrate

In-situ RHEED Characterization of Thin films

In-situ RHEED was used to determine the crystallinity of the single layer films during PLD growth. The RHEED patterns for the MgO single crystal substrate, BZY15/MgO sample, and SDC20/MgO sample are shown in Figure 65. During fabrication, the samples were rotated for uniform deposition but the RHEED images were collected during the first 5 laser pulses, before the substrates began rotating. The BZY15/MgO and SDC20/MgO samples both showed highly-oriented crystalline structure with sharp diffraction streaks.

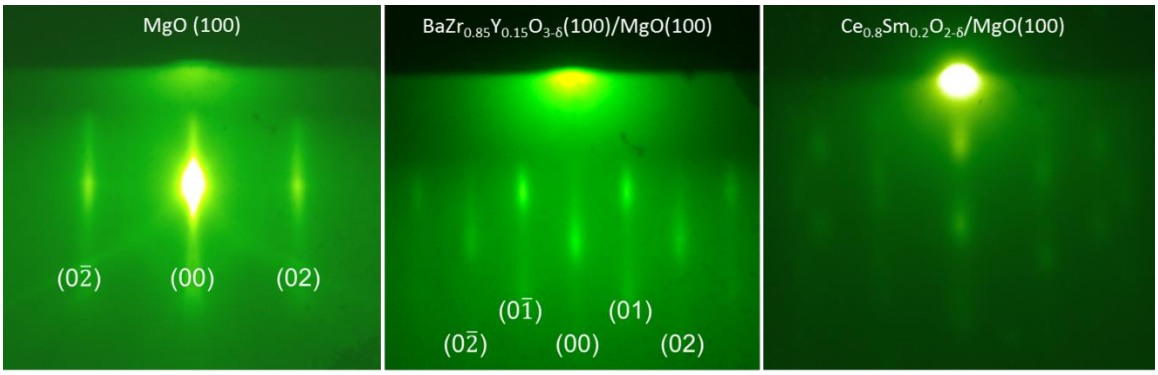

Figure 65 RHEED characterization of MgO (100) substrate before PLD deposition, BZY15 (100) on MgO (100), and SDC20 on MgO (100)

Thin film XRD Characterization

In order to optimize the PLD parameters for fabrication of BZY15 and SDC20 heterostructures, single layers of each of the films were fabricated on MgO substrates. The structure and chemical composition of the BZY15 and SDC20 thin films were characterized by thin film x-ray diffraction (XRD), TEM and STEM analysis.

The 2theta XRD scan of SDC20 on MgO(100), is displayed in Figure 66. The diffraction reveals a (111) growth direction of SDC20 on the MgO substrate which differentiates our growth results from the results of Sanna et al.[127] Sanna et al. reported PLD growth of SDC20 on MgO (100) in the (001) growth direction. The rocking curve of the (111) peak has a FWHM value of 0.2^{o}, which indicates a highly textured film. No other SDC peaks were observed except for the (111) family peaks.

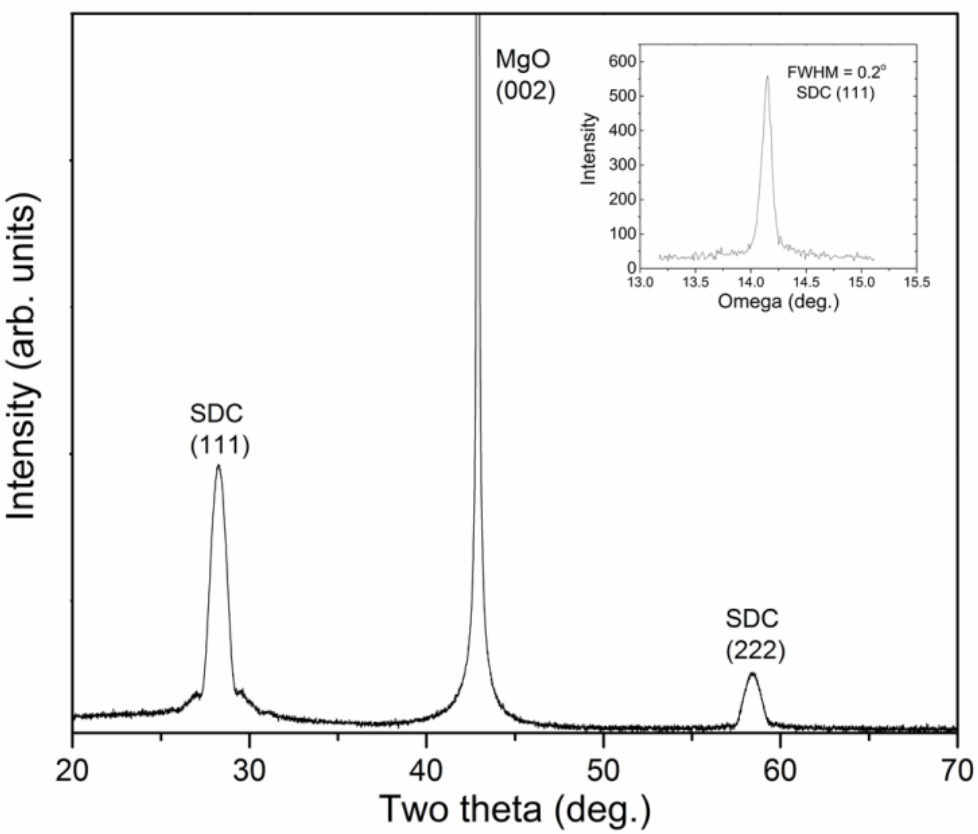

Figure 66 X-ray diffraction of SDC20 film (111) on MgO (100) substrate with rocking curve inset.

The 2theta XRD scan of BZY15 on MgO(100) is shown in Figure 67. The diffraction pattern reveals a (100) growth direction of BZY15 on the MgO substrate. The rocking curve of the (100) peak is shown in the inset of Figure 67 and the FWHM of the rocking curve is 0.1^{o}, which indicates the BZY15 film on MgO (100) is highly textured.

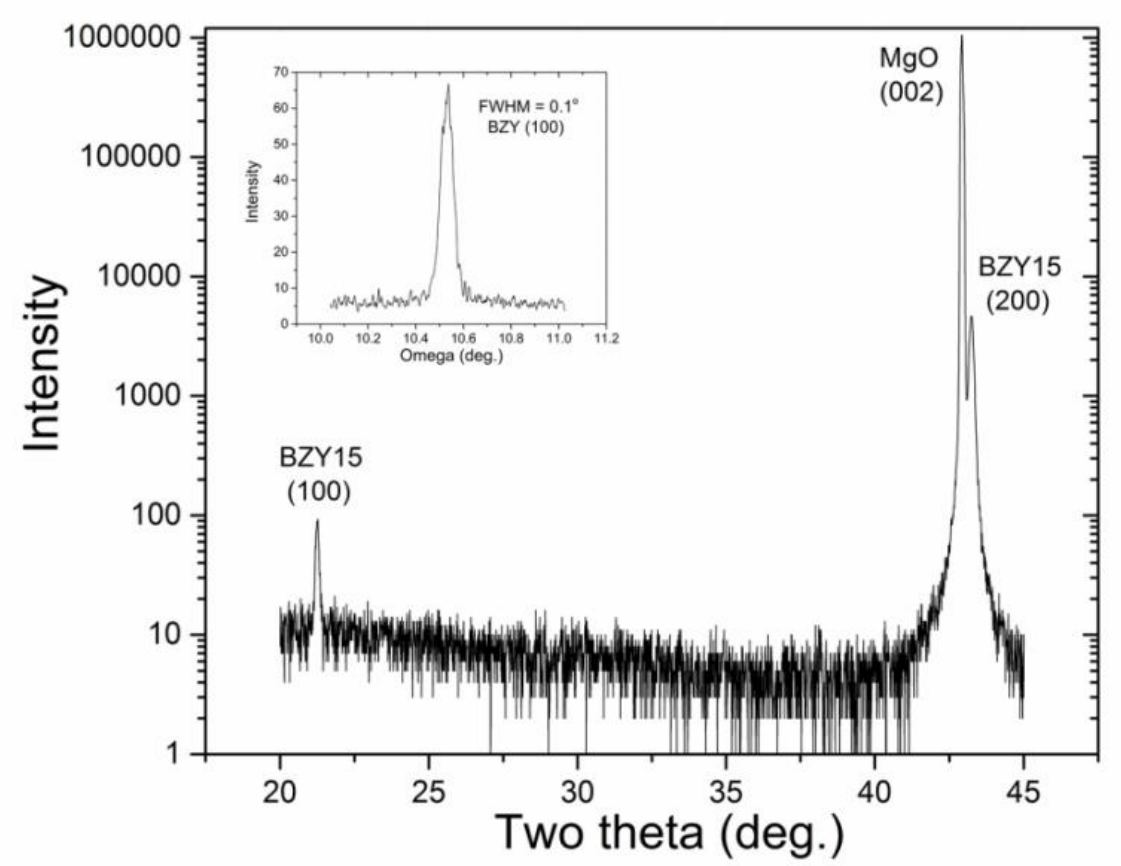

Figure 67 X-ray diffraction of BZY15 film (100) on MgO (001) substrate with rocking curve inset.

To determine the effect of PLD parameters on film quality, reciprocal space maps of two BZY15 films, fabricated by different PLD parameters, were collected. The PLD parameters used to fabricate the film measured in Figure 68A were 100mtorr PO_2, 700^oC, 0.065cm^2 spot size, 10Hz, 2.86J/cm^2. The PLD parameters of the film fabricated and measured in Figure 68B were 40mtorr PO_2, 700^oC, 0.005cm^2 spot size, 10Hz, 2.86J/cm^2. The large spread of the BZY (100) peak in the omega direction in Figure 68A reveals high mosaicity of the film (tilt in the film growth direction). After the PLD oxygen partial pressure and spot size were reduced in the fabrication of the film of Figure 68B, the omega spread of the BZY (100) peak is much smaller, indicating a higher quality film

with low mosaicity. The PLD parameters used to fabricate the BZY15 film measured in Figure 68B were used for fabrication of heterostructure samples.

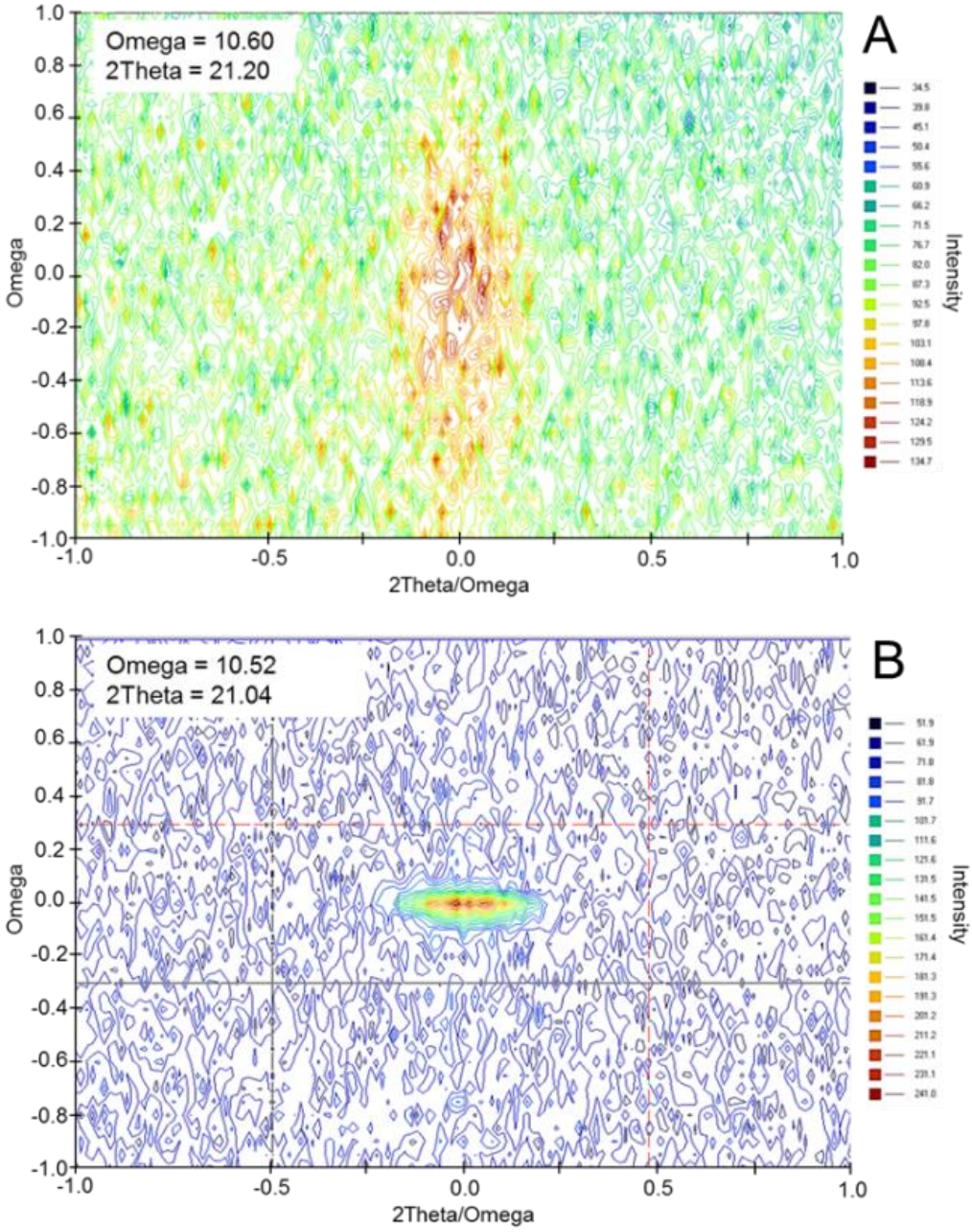

Figure 68 Two-axis rocking curve scan (Cu k-alpha) of 50nm BZY thin films around the (100) Bragg peak for PLD fabrication parameters of (A) 100mtorr $_PO_2$, 700oC, 0.065cm^2 spot size, 10Hz, 2.86J/cm^2; and (B) 40mtorr $_PO_2$, 700^{o}C, 0.005cm^2 spot size, 10Hz, 2.86J/cm^2. The XRD analysis reveals the omega tilt of BZY crystal for each condition.

A phi scan of the BZY15 film on MgO (001) substrate was collected to determine the "in-plane" crystalline structure of the film and substrate. The phi axis is perpendicular to the film substrate. The phi scan, Figure 69, was collected over 360^o while keeping the Bragg and incidence angles set at the (202) MgO reflection. In this scan, four peaks with 90^o separation and approximately the same intensity were detected, as expected for the single crystal substrate. Next the same phi scan was repeated for the (211) BZY15 reflection. Eight peaks, symmetrically aligned to the MgO (202) peaks were detected. The angle between the reflection planes can be found using Equation 33 for cubic systems. The angle between the BZY (211) and (112) reflections which contribute the eight reflections is found to be 33.56^o which is consistent with the data. The phi scan of BZY and MgO proves the cube-on-cube orientation of BZY grown on MgO.

$$cos\varphi = \frac{h_1h_2 + k_1k_2 + l_1l_2}{\sqrt{(h_1^2 + k_1^2 + l_1^2)(h_2^2 + k_2^2 + l_2^2)}} \tag{33}$$

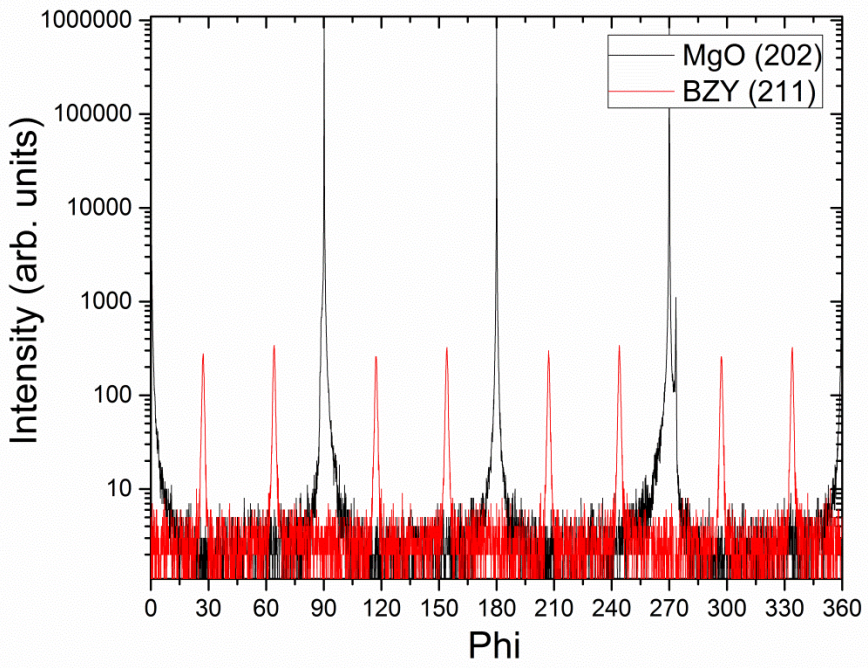

Figure 69 Phi scan XRD patterns of BZY15 grown on (001) MgO substrate, keeping the Bragg and incidence angles set at different asymmetric reflections of the materials.

The planes contributing to Bragg diffraction in the 360^{o} phi scan are illustrated in cubic unit cells in Figure 70.

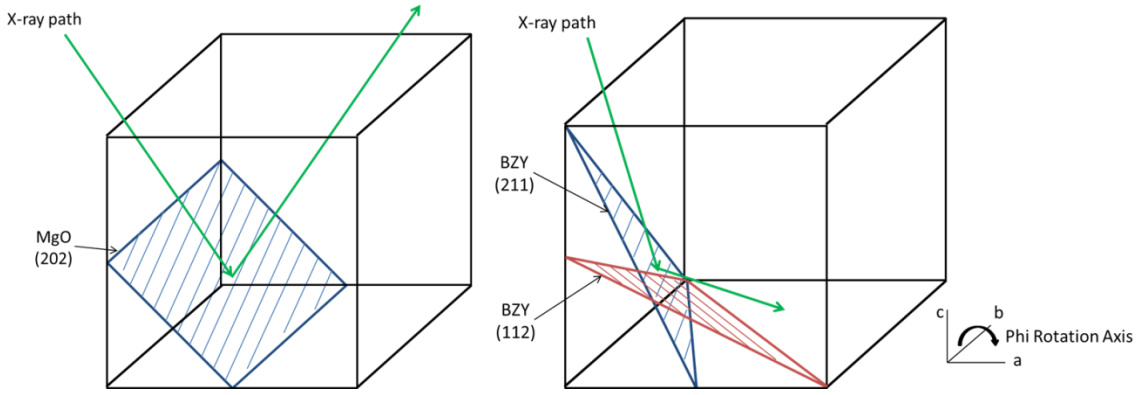

Figure 70 Representative planes satisfying Bragg diffraction in MgO (left) and BZY (right) during 360^{o} phi-scan of the BZY15 thin film on MgO substrate

TEM and STEM Characterization of BZY15 films on MgO substrates

BZY15 films fabricated on MgO substrates were characterized by TEM and STEM for microstructural and chemical analysis. TEM and STEM images of the BZY15 films fabricated by PLD and analyzed by thin film XRD in the previous section are shown in Figure 71. Figure 71A shows the film fabricated at 100mtorr PO_2 and 0.065cm^2 spot size. Figure 71B shows the BZY15 film fabricated at 40mtorr PO_2 and 0.005cm^2 spot size. The TEM images agree with the XRD analysis and verify that the low pressure and small spot size PLD parameters are best for fabricating high quality BZY15 films. HAADF STEM images reveal the difference of nanostructure between the two films. The low quality film fabricated by non-optimized PLD parameters (A) has multiple grains in the field of view with high angle grain boundaries. The film fabricated with optimized PLD parameters is uniform and does not have high angle grain boundaries.

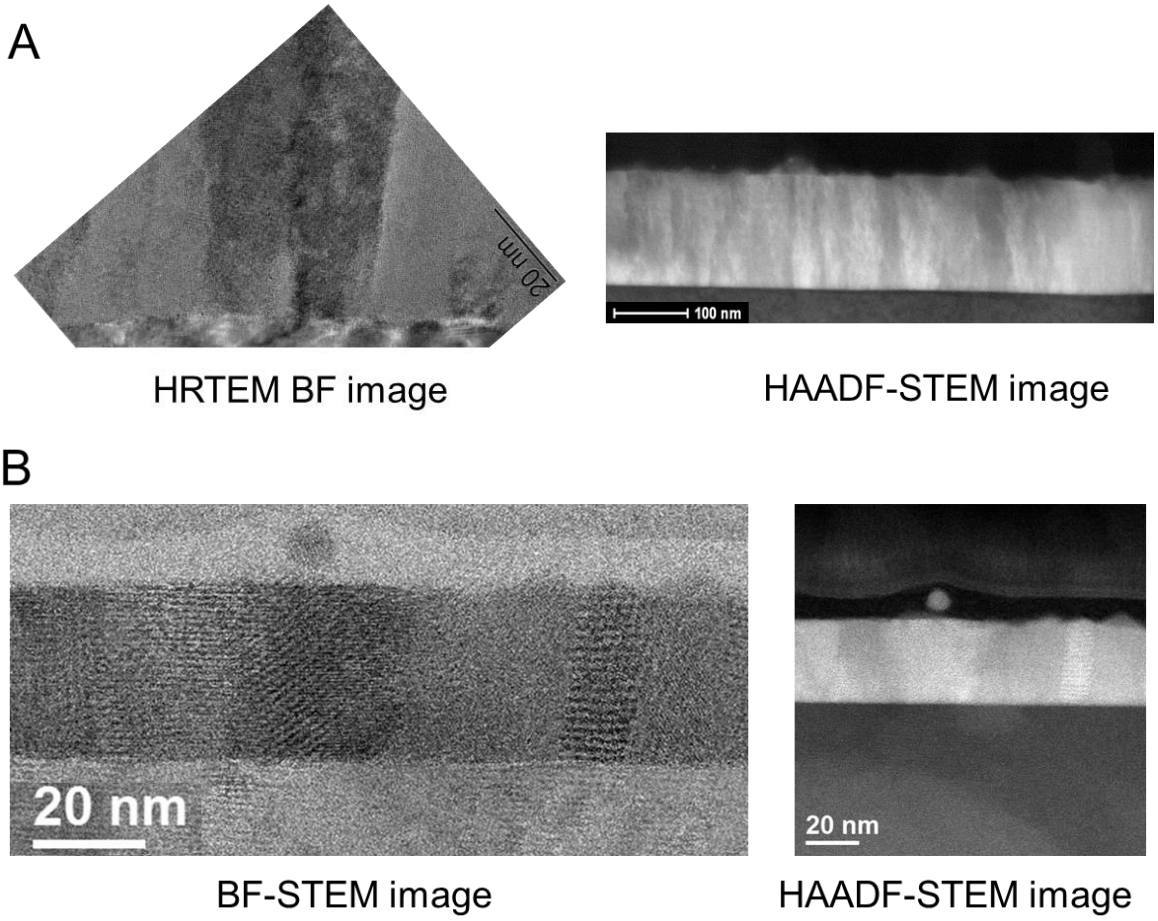

Figure 71 TEM and STEM images of BZY15 thin film with PLD fabrication parameters of (A) 100mtorr PO2, 700oC, 0.065cm2 spot size, 10Hz, 2.86J/cm2; and (B) 40mtorr PO2, 700oC, 0.005cm2 spot size, 10Hz, 2.86J/cm2 (Data collected by Dr. Karren More, ORNL and Dr. Yong, GT)

Aberration-corrected STEM analysis of the optimized BZY15 film is shown in Figure 72. The crystallinity and interface between the BZY15 layer and MgO is very sharp. However, dark contrast regions, perpendicular to the MgO substrate are noticeable. The regions are not grain boundaries, as first suspected, but they are regions that are depleted in Ba which is confirmed with EDS analysis. It is clear that crystallinity across the boundary between the light contrast and dark contrast regions is continuous with no angle between the regions, which is characteristic of a grain boundary. This continuous crystallinity was found across all similar regions viewed in this analysis.

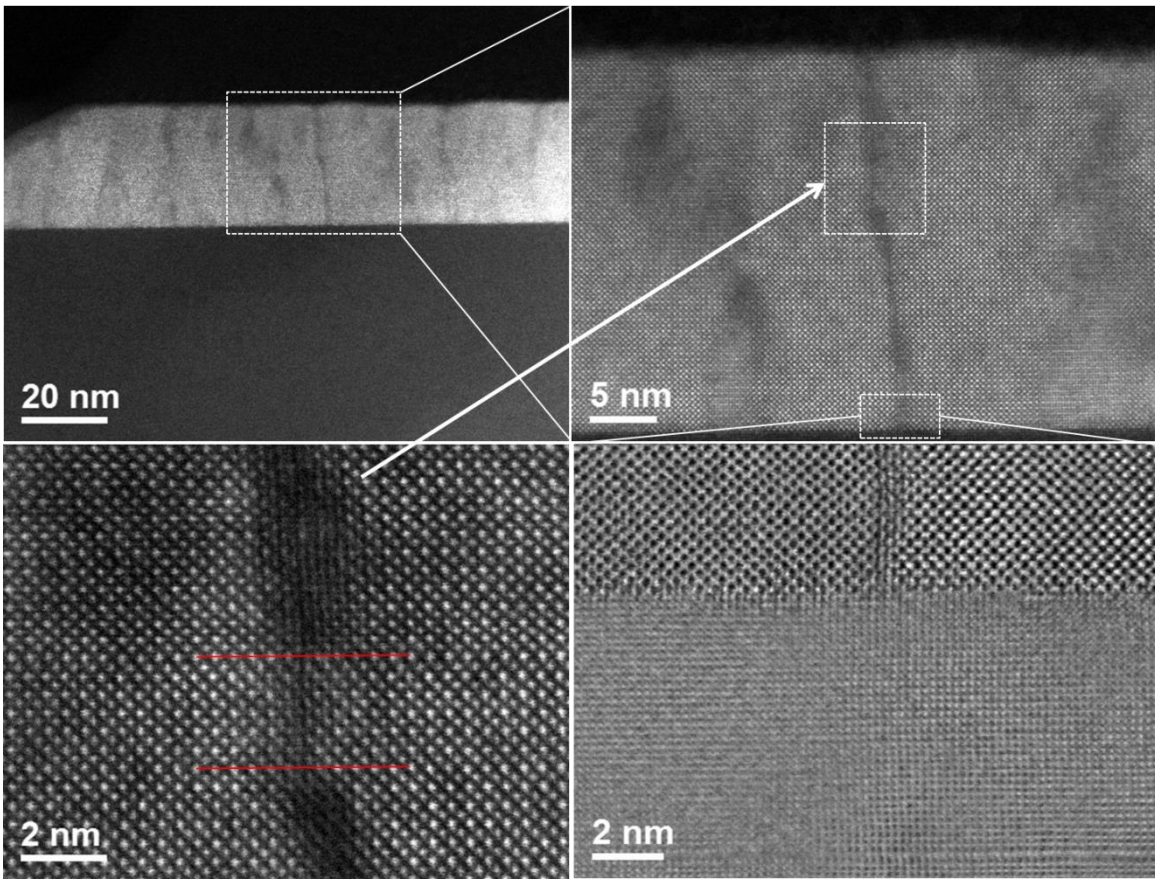

Figure 72 Abberation-corrected STEM images of BZY15 film fabricated with optimized PLD parameters; Details of dark contrast regions and BZY15/MgO interface highlighted. (Data collected by Dr. Karren More, ORNL)

Chemical analysis of BZY15 thin films fabricated by optimized PLD parameters was completed by STEM EDS measurement. The STEM image, taken from a different location on the film than Figure 72, and corresponding composition maps for Zr and Ba are shown in Figure 73. It is apparent from the Ba composition map that the dark regions are Ba deficient, however, the Zr appears to be uniform throughout the film. Ba has a low vaporization point and Ba loss in barium zirconate materials during high temperature sintering is well documented.[128] The loss of barium in the PLD fabrication process is not surprising due to the heat imposed on the target by the laser during fabrication.

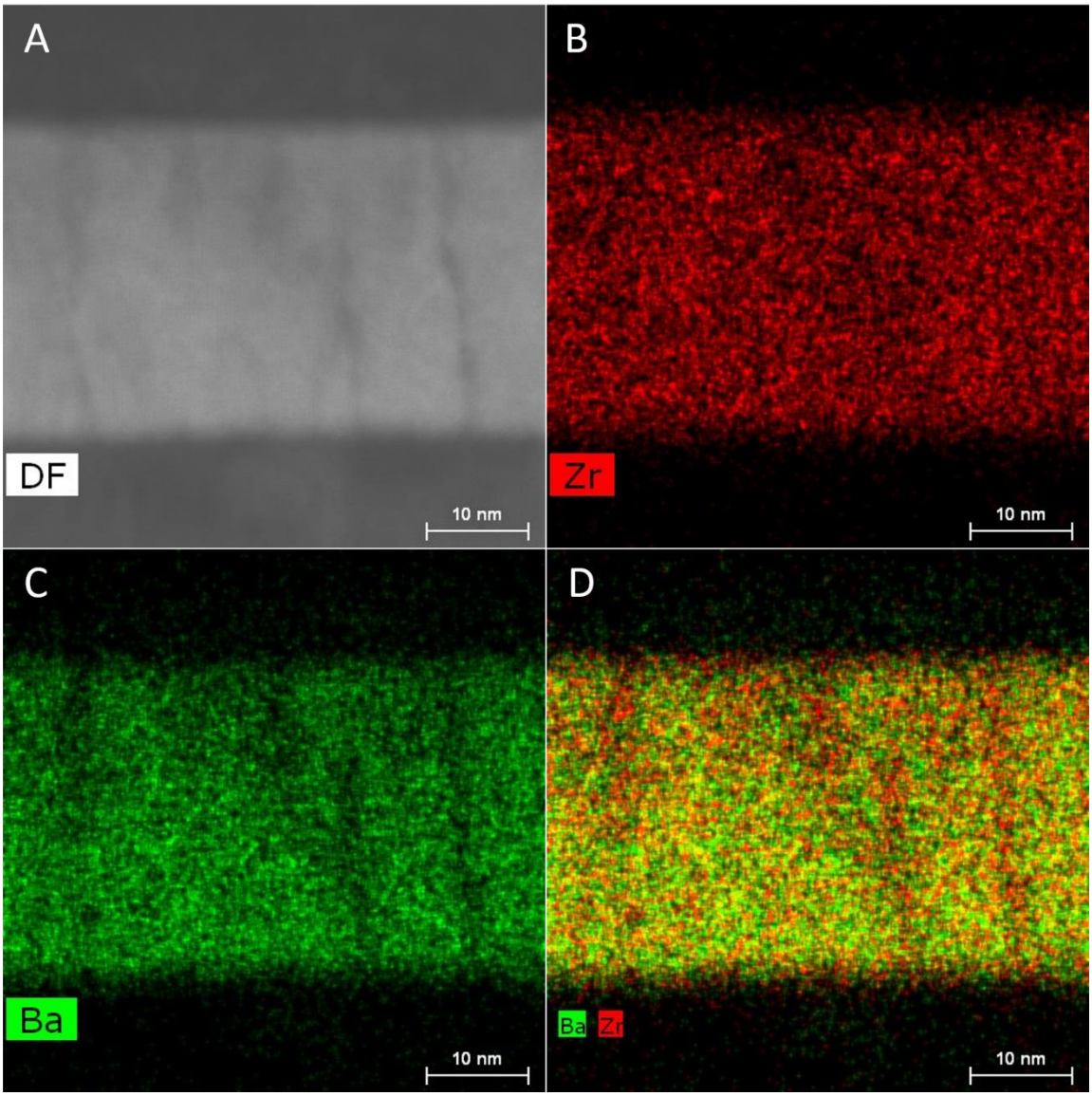

Figure 73 STEM (A) and EDS Mapping (B-D) of BZY15 film (Princeton 2-5) on MgO substrate with Ba deficient vertical regions

4.4.4 Structural and chemical characterization of $BaZr_{0.85}Y_{0.15}O_{3-\delta}/Sm_{0.2}Ce_{0.8}O_{1.9}$ heterostructure films

A sample series of three BZY15/SDC20 heterostructures were fabricated by PLD. The samples were fabricated by alternating laser pulses on BZY15 and SDC20 targets to create a layered structure on the MgO substrates. The number of pulses was systematically changed to change the layer thicknesses, while maintaining a constant film thickness of 125nm. Three samples were fabricated with an expected architecture of 5nm

BZY15/ 0.5nm SDC20, 10nm BZY15/ 1nm SDC20, and 20nm BZY15/ 2nm SDC20. These samples will be referred to as 5–0.5, 10–1, and 20-2, respectively. The structure of the heterostructure films was characterized by TEM and STEM.

5nm BZY15/ 0.5nm SDC20 heterostructure sample (45 interfaces)

STEM images of the 5nm BZY15/ 0.5nm SDC20 heterostructure sample are shown in Figure 74. Although at low magnification the layers appear to be continuous in the in-plane direction of the sample, at high magnification it is apparent that a layered-columnar structure has formed. The growth indicates non-wetting of the SDC20 phase on the BZY15 surface.

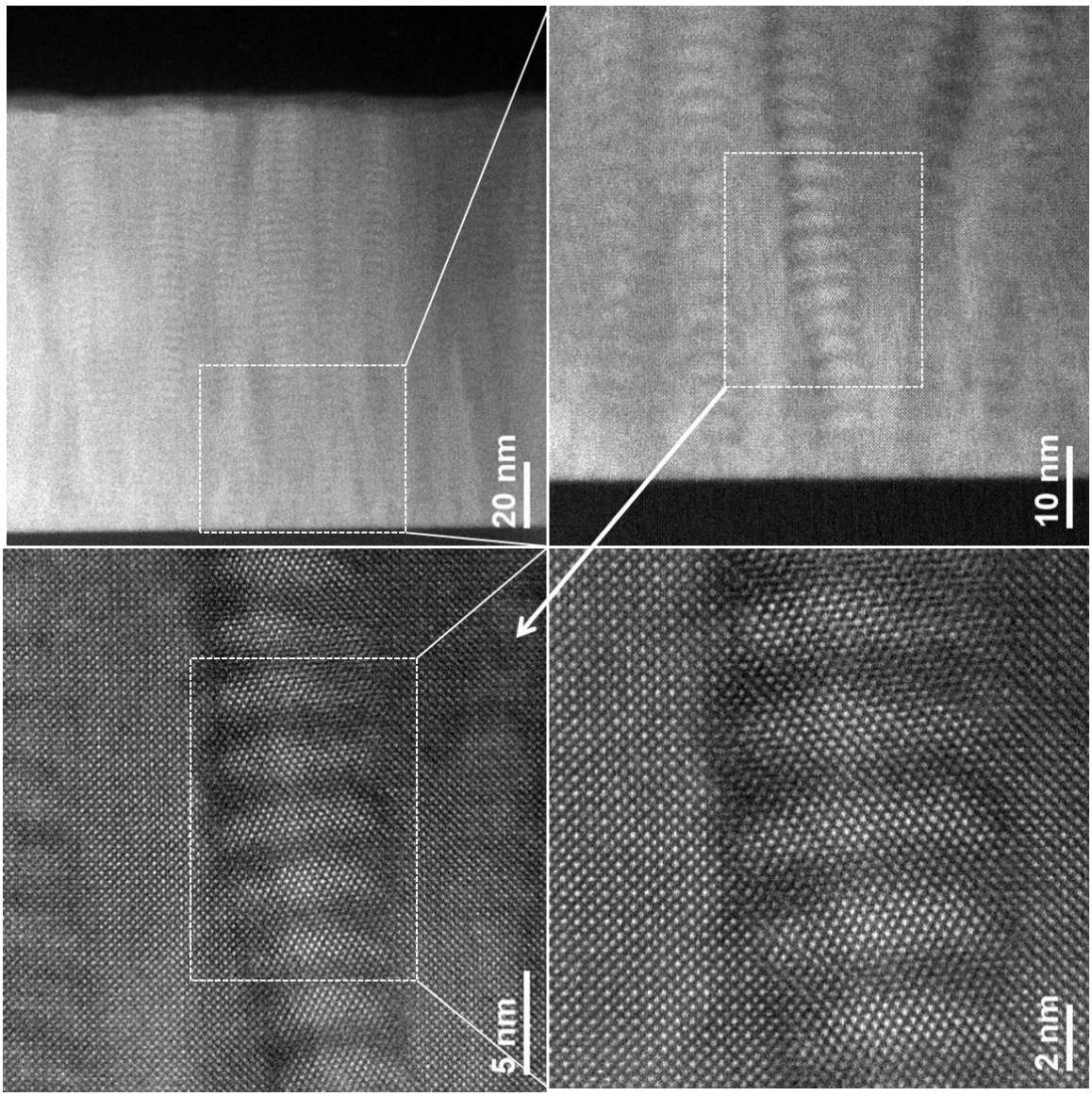

Figure 74 Aberration-corrected STEM images of 5nm BZY15/ 0.5nm SDC20 heterostructure sample with total thickness of 125nm. MgO substrate is dark region at bottom of (top-left & top-right). Layer-columned structure is shown in detail (bottom-right). PLD fabrication parameters - 40mtorr $_pO_2$, 700^oC, 0.005cm^2 spot size, 10Hz (Data collected by Dr. Karren More, ORNL)

STEM-EDS chemical analysis of the 5nm BZY15/ 0.5nm SDC20 heterostructure sample is shown in Figure 75. It is apparent that large Ba-containing regions separate BZY15/SDC20 regions.However, a large amount of element interdiffusion has occurred.

The BZY15/SDC20 layers run parallel to the MgO substrate surface and are confined to columns of ~10nm width that are perpendicular to the MgO substrate surface.

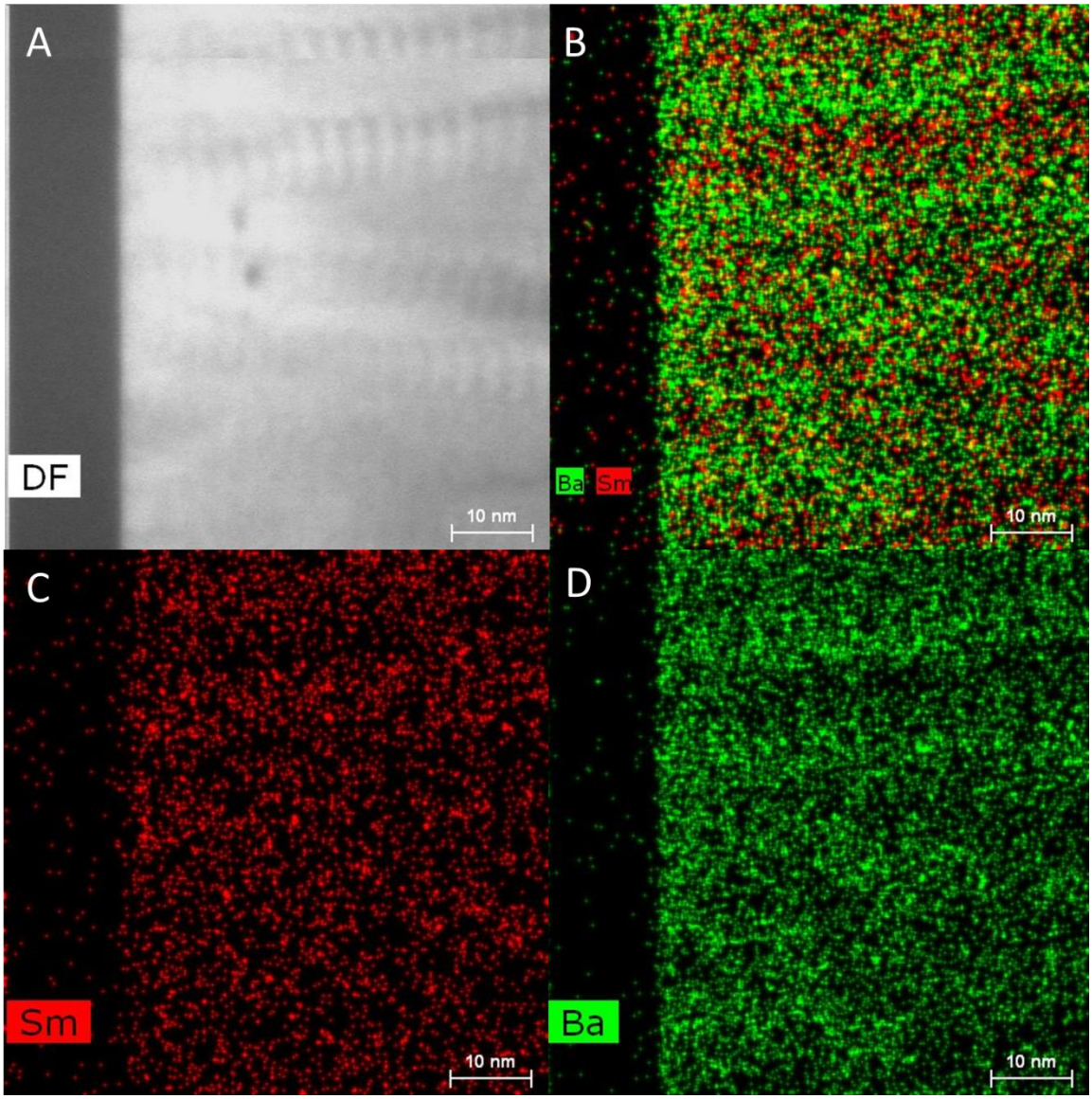

Figure 75 STEM (A) and EDS Mapping (B-D) of BZY15/SDC20 film (Princeton 2-9) on MgO substrate with Ba rich regions between heterostructured regions; MgO substrate on left side of images (Data collected by Dr. Karren More, ORNL)

A more detailed analysis of Sample 5 – 0.5 is shown in Figure 76. Figure 76A shows the high-angle annular dark-field (HAADF) STEM image of Sample 5 – 0.5 with the columnar heterostructure surrounded by a bulk phase. Figure 76C shows the FFT

pattern calculated from the STEM image. The BZY15 and SDC20 diffraction spots are visible. The zone-axis of BZY15 structure is identified as the [001] direction and the zone-axis of the SDC20 structure is identified as the [011] direction. The diffraction spots belonging to the BZY15 110 and SDC20 200 are indexed as overlapping meaning the BZY15 (110) and the SDC20 (200) planes are parallel In Figure 76B the inverse FFT image related directly to the diffraction spots from the SDC20 phase in the dotted box is shown. This analysis clearly shows that the bright, banded regions of the STEM image are SDC20 FCC phase surrounded by the perovskite BZY15 phase.

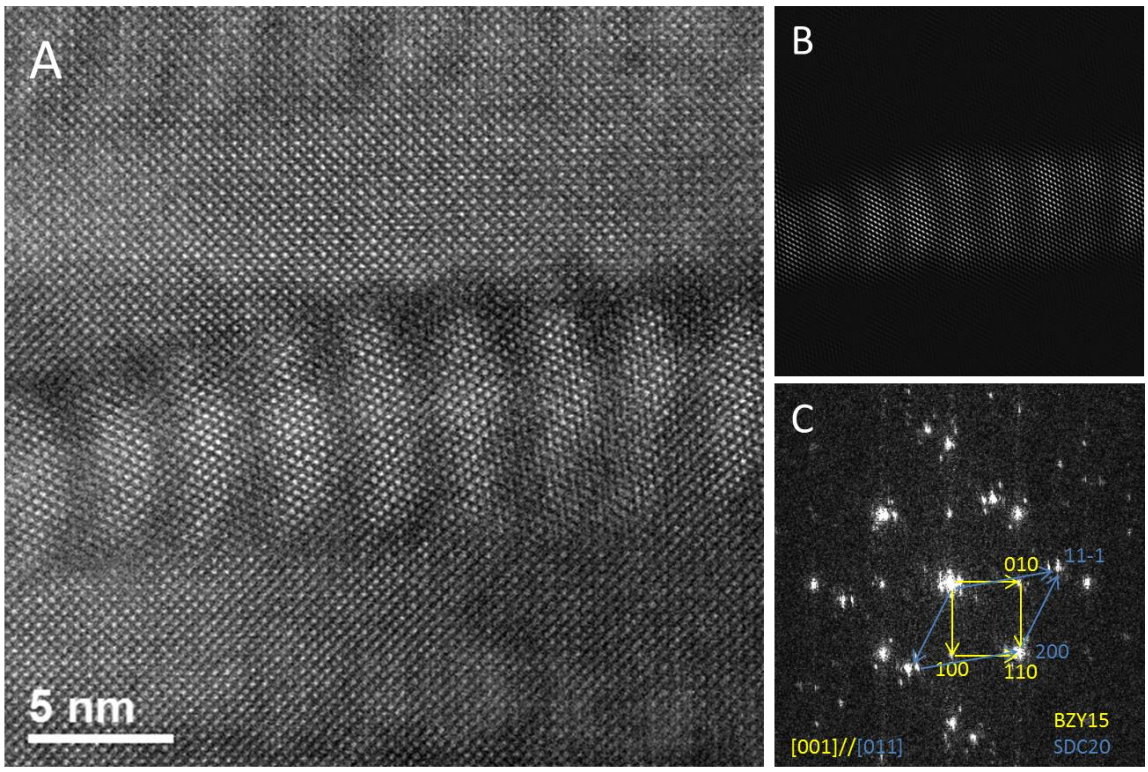

Figure 76 (A) STEM analysis of 5nm BZY15/ 0.5nm SDC20 heterostructure sample, (B) inverse FFT image to show the SDC20 crystalline regions in (A), (C) FFT pattern of image (A)

10nm BZY15/ 1nm SDC20 heterostructure sample (23 interfaces)

STEM images of the 10nm BZY15/ 1nm SDC20 heterostructure sample are shown in Figure 77. SDC20 layers are clearly distinguished from the BZY15 layers and the total number of BZY15/SDC20 interfaces is confirmed to be 23, as calculated. The 10-1 sample does not show clear segregation of the SDC20 phase, as seen in the 5-0.5 sample. However, after closer inspection, regions of higher concentration of SDC phase and more disorder from the BZY15 structure are visible, as in Figure 77C. In general, the SDC20 regions are more continuous in the 10-1 sample than the 5-0.5 sample but slight disruption to the crystal structure is found in the SDC20 layers. STEM-EDS mapping of the sample is shown in Figure 78. The Sm-containing SDC20 layers between the BZY15 layers are identified.

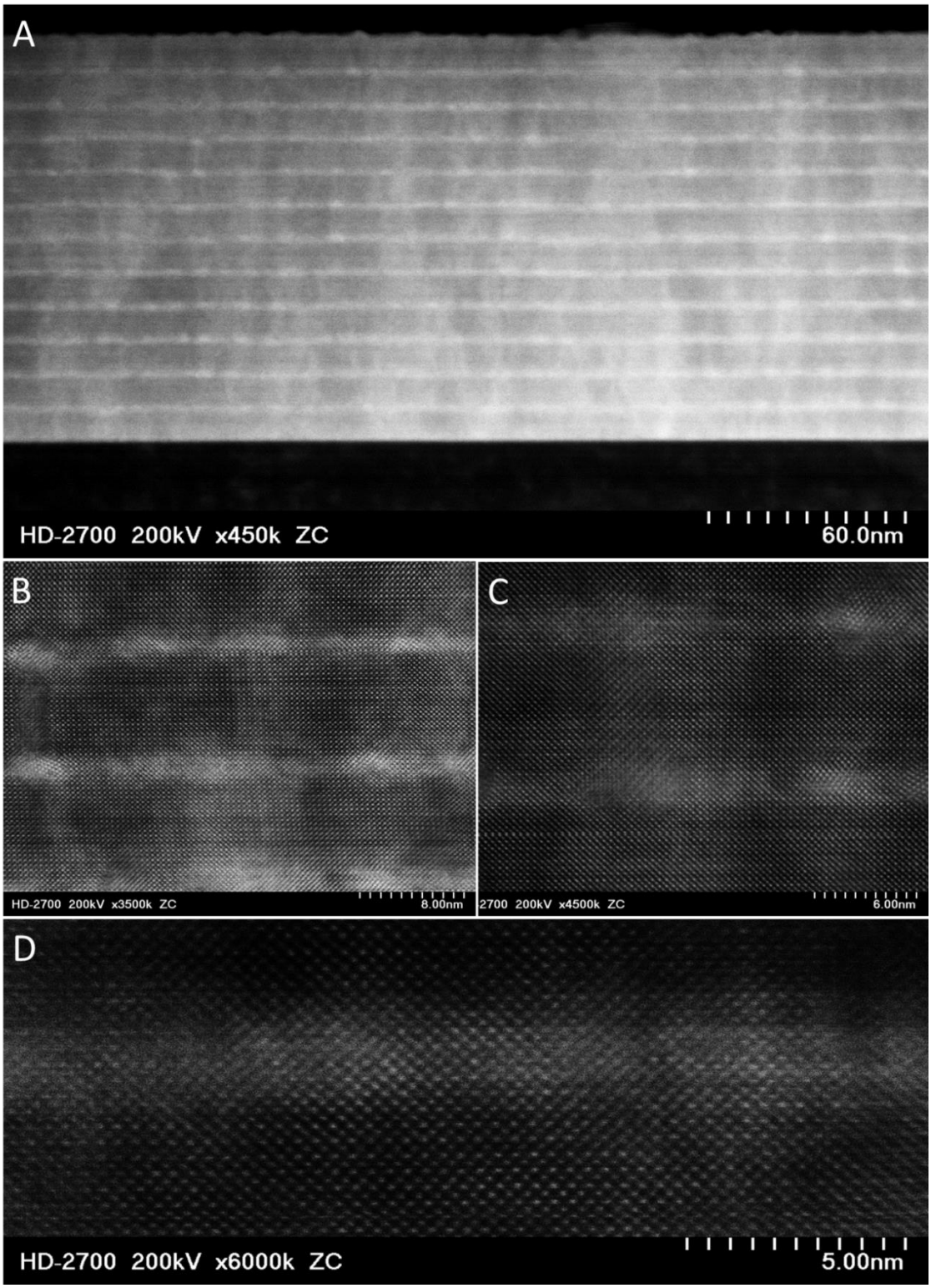

Figure 77 Aberration-corrected STEM images of 10nm BZY15 / 1nm SDC20 heterostructure sample with 23 BZY15/SDC20 interfaces; MgO substrate at bottom of images (Data collected by Dr. Yong Ding, GT)

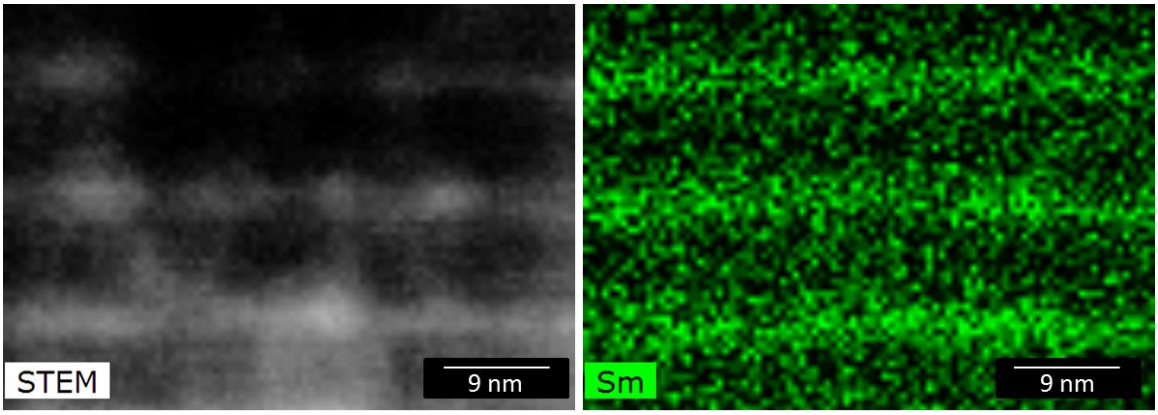

Figure 78 STEM-EDS analysis of 10nm BZY15/ 1nm SDC20 heterostructure sample with STEM image of analysis region (left) and Sm concentration map of analyzed region (right) (Data collected by Dr. Yong Ding, GT)

The crystallinity of the SDC20 regions was characterized by Fast Fourier transform (FFT) analysis from the STEM image of Sample 10-1. Figure 79A shows the high-angle annular dark-field (HAADF) STEM image with two SDC20 layers (light grey) and three BZY15 layers (dark grey). Figure 79C shows the FFT pattern calculated from the solid square region on the STEM image. The BZY15 diffraction spots are visible and the zone-axis of BZY15 structure is identified as the [001] direction. The FFT pattern calculated from the dotted box region is shown in Figure 79D. The BZY15 diffraction spots are present but the diffraction spots for the FCC SDC20 crystal appears as well. The diffraction spots belonging to the BZY15 110 and SDC20 200 are indexed as overlapping. The BZY15 (110) and the SDC20 (200) planes are epitaxial and are highlighted in red on the STEM image. In Figure 79B the inverse FFT image related directly to the diffraction spots from the SDC20 phase in the dotted box is shown. All regions circled on the STEM image are regions of SDC20.

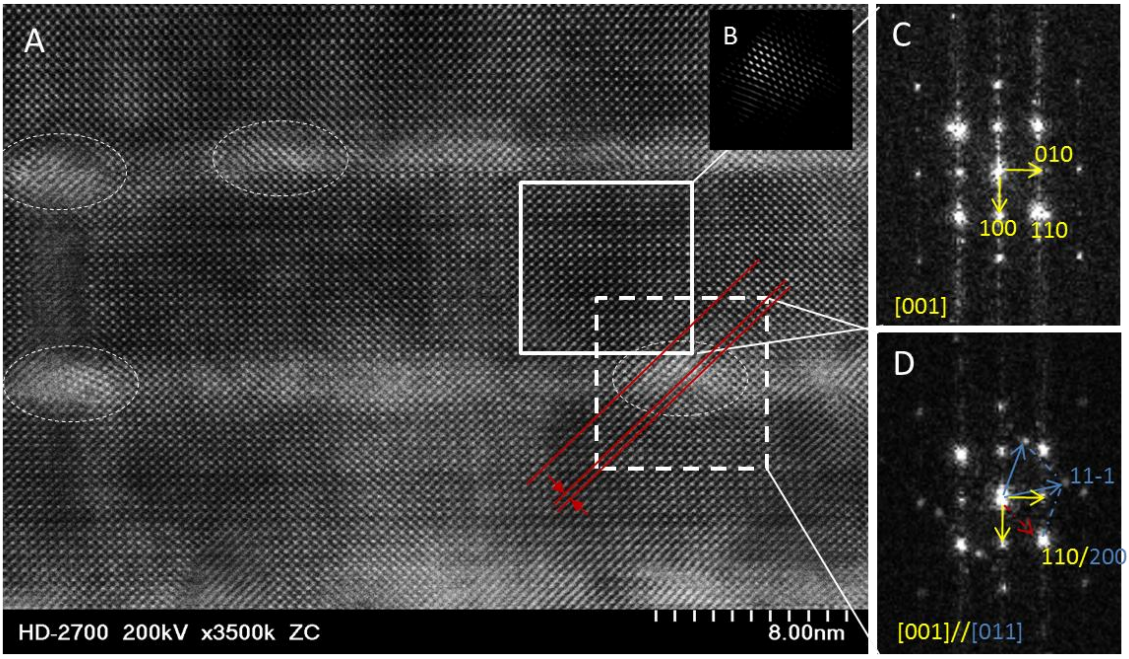

Figure 79 (A) STEM analysis of 10nm BZY15/ 1nm SDC20 heterostructure sample, (B) inverse FFT image to show the SDC20 crystalline region in dotted box, (C) FFT pattern of solid box region in BZY15 layer of sample, (D) FFT pattern of SDC20 containing region in dotted box.

The lattice orientation of the BZY15 and SDC20 phases is shown graphically in Figure 80. The BZY15 [001] and SDC20 [011] directions are parallel and the BZY15 (110) and SDC20 (200) planes are parallel. The lattice spacing for the SDC20 (200) plane is d=2.74Å and the lattice spacing for the BZY15 (110) plane is d=2.97Å. The lattice mismatch between the planes is ~8%.

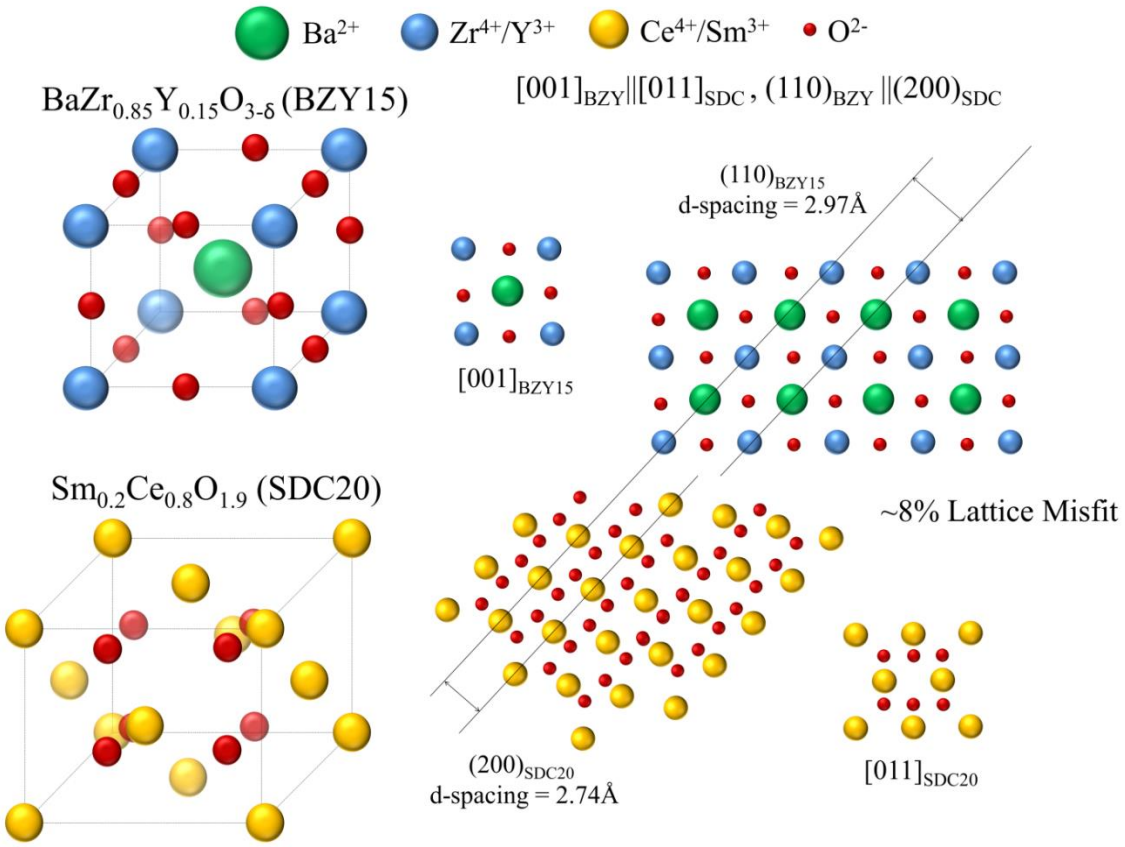

Figure 80 BZY15 and SDC20 crystal structures; 2d $[001]_{BZY15}$ and $[011]_{SDC}$ lattice planes; $[001]_{BZY}||[011]_{SDC}$, $(110)_{BZY}||(200)_{SDC}$ relationship between BZY15 and SDC20 phases in the 10-1 and 20-2 sample

20nm BZY15/ 2nm SDC20 heterostructure sample (11 interfaces)

STEM images of the 20nm BZY15/ 2nm SDC20 heterostructure sample are shown in Figure 81. SDC20 layers are clearly distinguished from the BZY15 layers and the total number of BZY15/SDC20 interfaces is confirmed to be 11, as calculated. In the high magnification STEM images, particles of SDC20 have been clearly formed at the BZY15/SDC20 interface. The particles are crystalline and are much larger as well as more defined than the crystalline SDC20 regions of Sample 10-1.

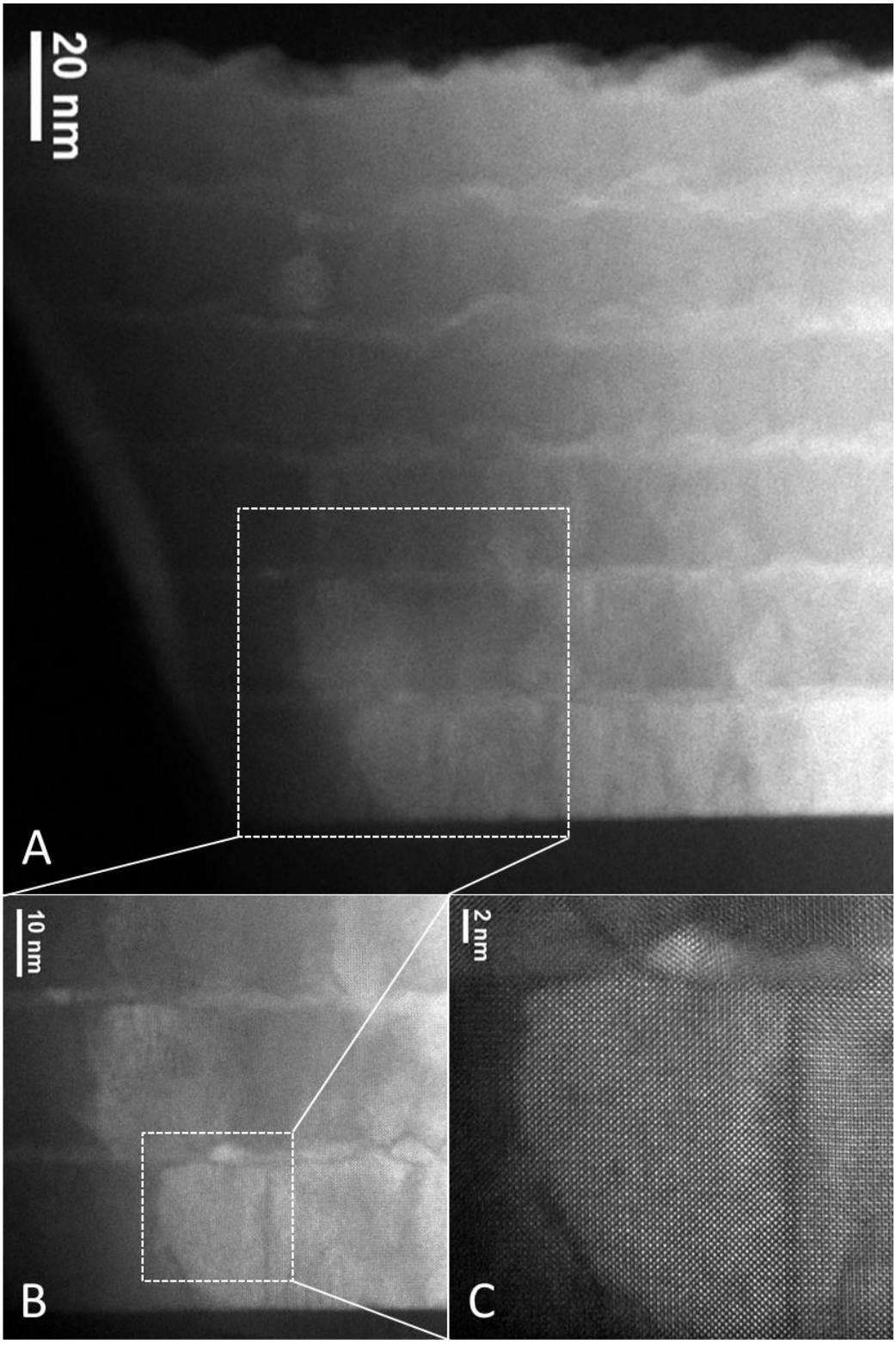

Figure 81 Abberation-corrected STEM images of 20nm BZY15 / 2nm SDC20 heterostructure sample with 11 BZY15/SDC20 interfaces; MgO substrate at bottom of images (Data collected by Dr. Karren More, ORNL)

STEM-EDS analysis of the 20-2 sample is shown in Figure 82. The Ce rich SDC20 layers are easily distinguished in the chemical maps.

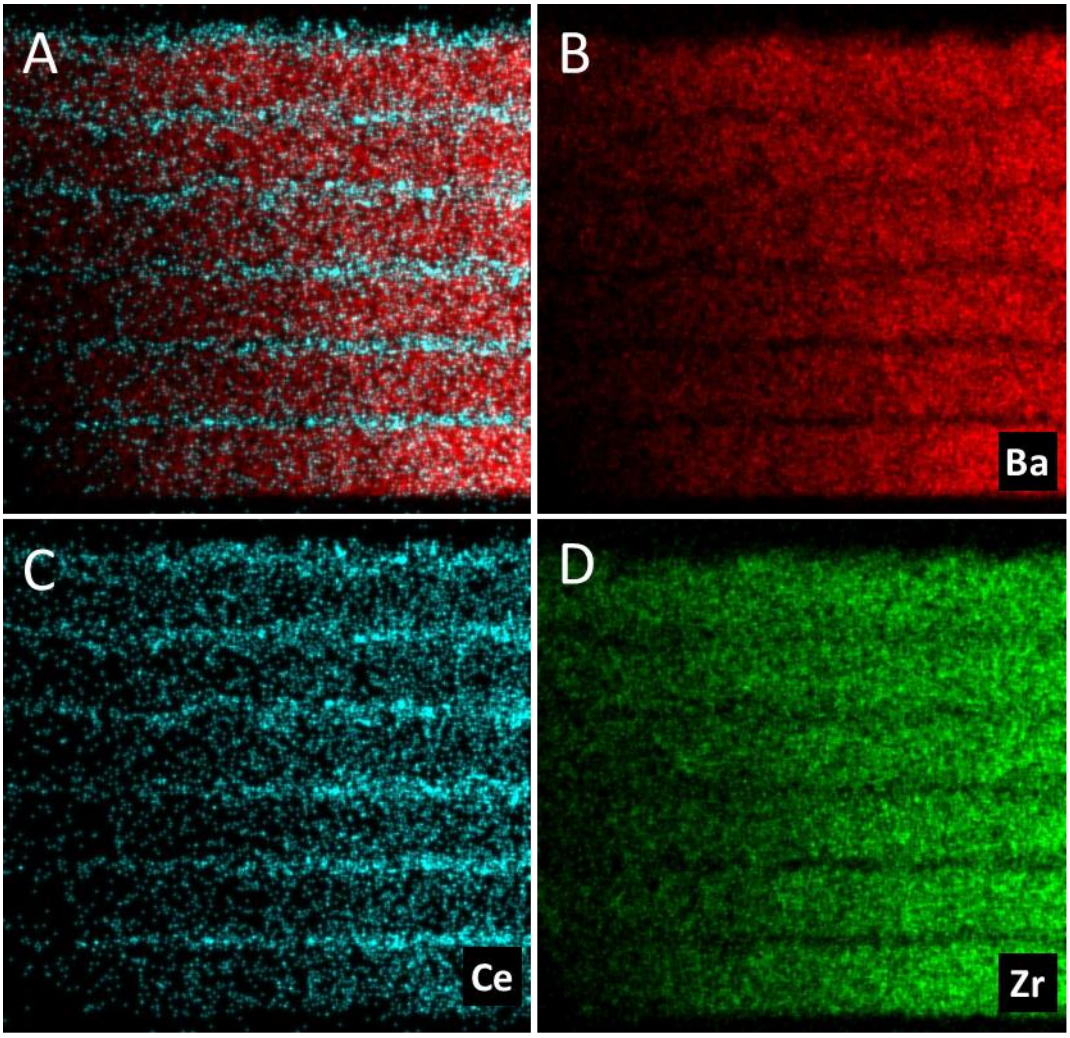

Figure 82 STEM-EDS analysis of 20nm BZY15/ 2nm SDC20 heterostructure sample with Ba, Ce and Sm concentration maps; MgO substrate at bottom of images (Data collected by Dr. Karren More, ORNL)

A comparison of the SDC20 crystalline regions in Sample 10-1 and Sample 20-2 is shown in Figure 83. In general, the crystalline SDC20 particles in Sample 20-2 are more distinct than in Sample 10-1. Larger SDC20 crystallite size allows for a greater strain relaxation in Sample 20-2 when compared to strain in the SDC20 phase of Sample 10-1. As evidenced by the STEM image and FFT patterns, the planar distances of BZY15

(110) and SDC20 (200) planes are equal and there is required to be dilatative strain in the SDC20 phase up to 8%. The thick BZY15 layers are expected to impose significant strain on the thin SDC20 regions. Significant dilative strain in the SDC20 phase will lead to deviations in ion transport in the SDC20 phase.

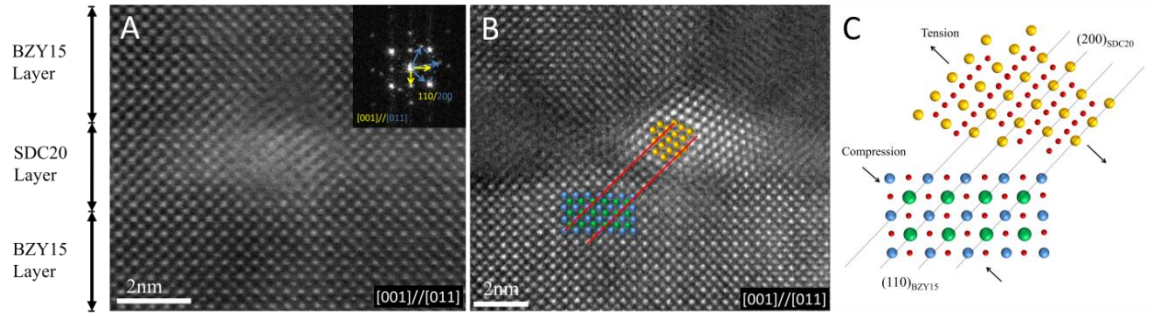

Figure 83 Comparison of SDC20 regions in heterostructure Sample 10-1 (A) and Sample 20-2 (B). The crystalline SDC20 regions in Sample 10-1 are less distinguishable than the crystalline regions in Sample 20-2 by STEM analysis although electron diffraction patterns reveal their presence. (C) BZY||SDC relationship with 8% lattice strain

4.4.3 $BaZr_{0.85}Y_{0.15}O_{3-\delta}$ and $Sm_{0.2}Ce_{0.8}O_{1.9}$ electrical testing results

Electrical measurements of the heterostructured BZY15/SDC20 thin films were collected to determine the interfacial effect on charge transport. The impedance spectroscopy data collected for the 20nm BZY15 / 2nm SDC20 sample is shown in the Nyquist plot of Figure 84. The total resistance of the sample was calculated from the low frequency intercept of the real axis. Impedance data for the 10nm BZY15 / 1nm SDC20 and the 5nm BZY15 / 0.5nm SDC20 sample were collected as well and the shape of the 20nm BZY15 / 2nm SDC20 sample is representative of all collected impedance data.

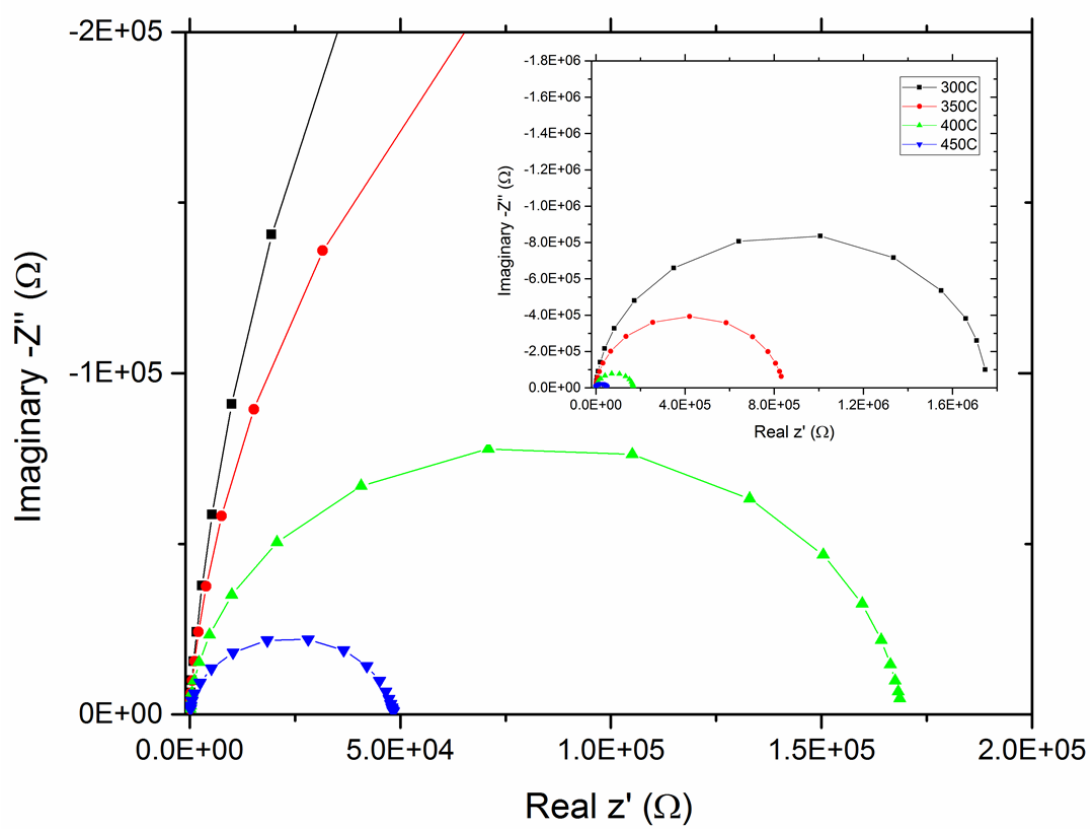

Figure 84 Impedance spectrum collected for 20nm BZY15 / 2nm SDC20 heterostructure sample with 11 continuous interfaces. This impedance data is typical for all thin film impedance data collected in this study

The conductivity of each heterostructure sample was calculated from the impedance spectroscopy data and is plotted in Figure 85 with respect to temperature. The electrical conductivity of the heterostructure 10nm BZY15 / 1nm SDC20 sample is the highest of all heterostructure samples fabricated. The 20nm BZY15 / 2nm SDC20 sample has slightly lower conductivity than 10nm BZY15 / 1nm SDC20 sample and the 5nm BZY15 / 0.5nm SDC20 has the lowest conductivity.

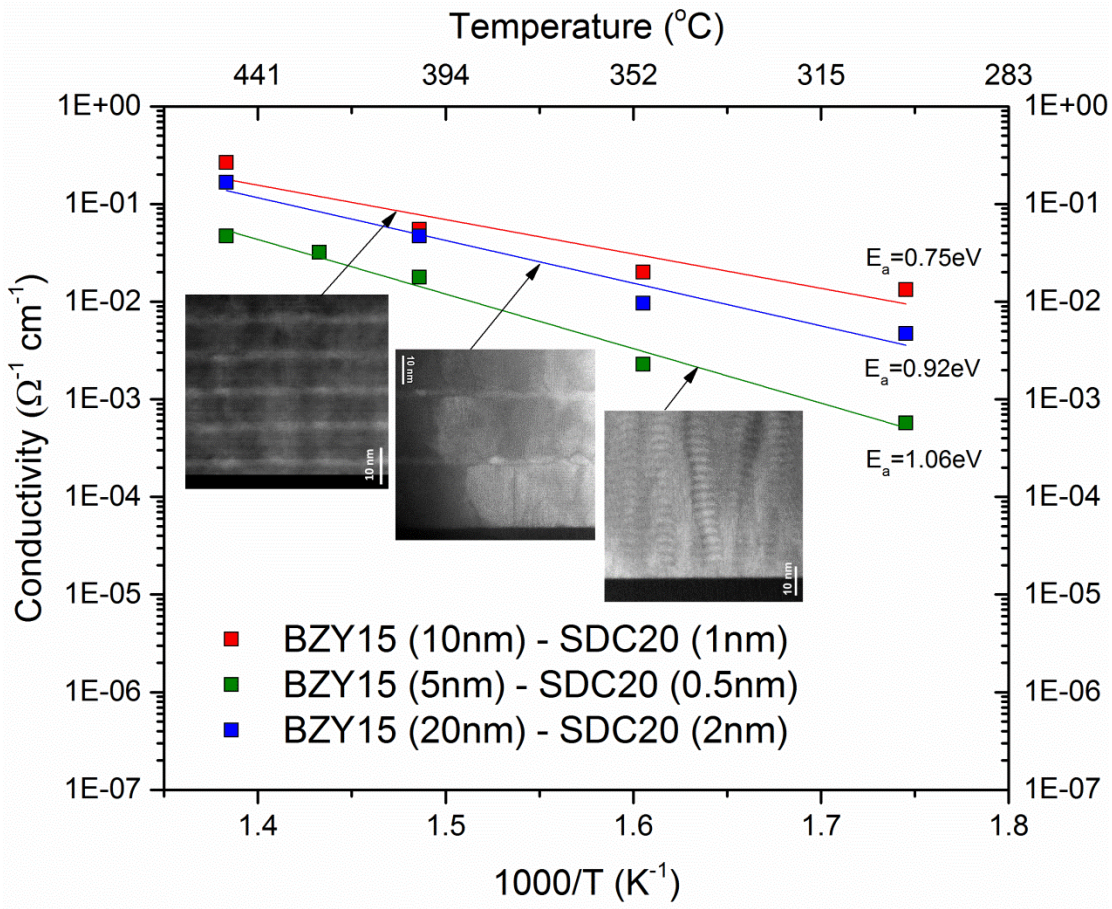

Figure 85 Electrical conductivity of BZY15/SDC20 heterostructure samples with (green) interrupted layers, (red) 10nm/1nm – 23 BZY15/SDC20 interfaces, (blue) 20nm/2nm – 11 BZY15/SDC20 interfaces

In Figure 86, the electrical conductivity data for the BZY15/SDC20 heterostructure sample is compared to the single-phase samples of BZY15 and SDC20. It is notable that the electrical conductivity of the heterostructure sample is approximately one order of magnitude higher than the bulk BZY15 sample and almost 2 orders of magnitude higher than the nanocrystalline SDC20 sample. The activation energy of the heterostructure sample is similar to the activation energy for the nanocrystalline SDC20 sample but between the activation energies of each single-phase sample. The activation energy of the heterostructure sample indicates that the charge transport mechanism is similar to the mechanism of nanocrystalline SDC20, oxygen-vacancy mediated charge

transport, which is expected based on the DFT/MD calculation and simulation of strained, ultra-thin SDC20.

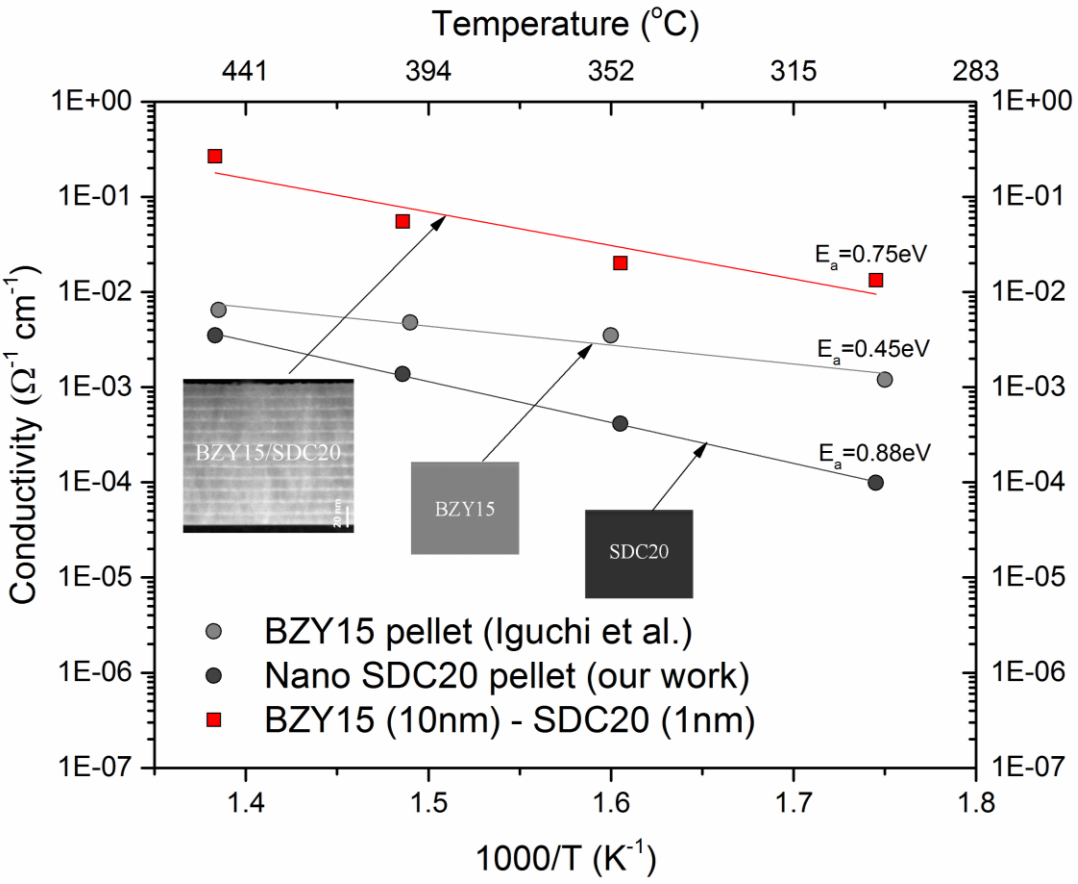

Figure 86 Total electrical conductivity of BZY15(10nm)/SDC20(1nm) in ambient atmosphere (red), nanocrystalline SDC20 pellet in ambient air (dark grey; data from Chapter 3), and BZY15 pellet in 3%H_2O-Air atmosphere (light grey; data taken from Iguchi et al.)[129]

The STEM and electron diffraction analysis of each heterostructure sample provides great insight into the unique properties of the samples which dramatically enhance the electrical properties. Schematics of the samples have been constructed based on the STEM and electron diffraction analysis and are shown in Figure 87. The left-most schematic is representative of the 5-0.5 sample. The 5-0.5 sample has very thin heterostructure layers, separated by ~10nm of the BZY phase. The SDC20 layers are very

thin and are expected to be strained significantly by the surrounding BZY15 phase. The center schematic of Figure 87 shows wider and thicker SDC20 regions between the BZY15 layers, as found in the STEM analysis of Sample 10-1. The STEM analysis shows continuous high contrast layers between the BZY15 layers, but after closer inspection, discrete regions in the high contrast layers are SDC20 while the other regions between the crystalline regions are due to diffusion of Sm^{3+} and Ce^{4+} or regions behind the field of focus in the sample, as represented in the figure. The final figure shows the largest SDC20 regions with the smallest spacing between SDC20 regions, as characterized in Sample 20-2. The strain in the SDC20 phase is expected to be lowest in this sample. The BZY15 layers grow in uniform layer by layer conditions, however, the SDC20 phase appears to prefer adatom-adatom interactions and grows by an island or cluster mechanism.

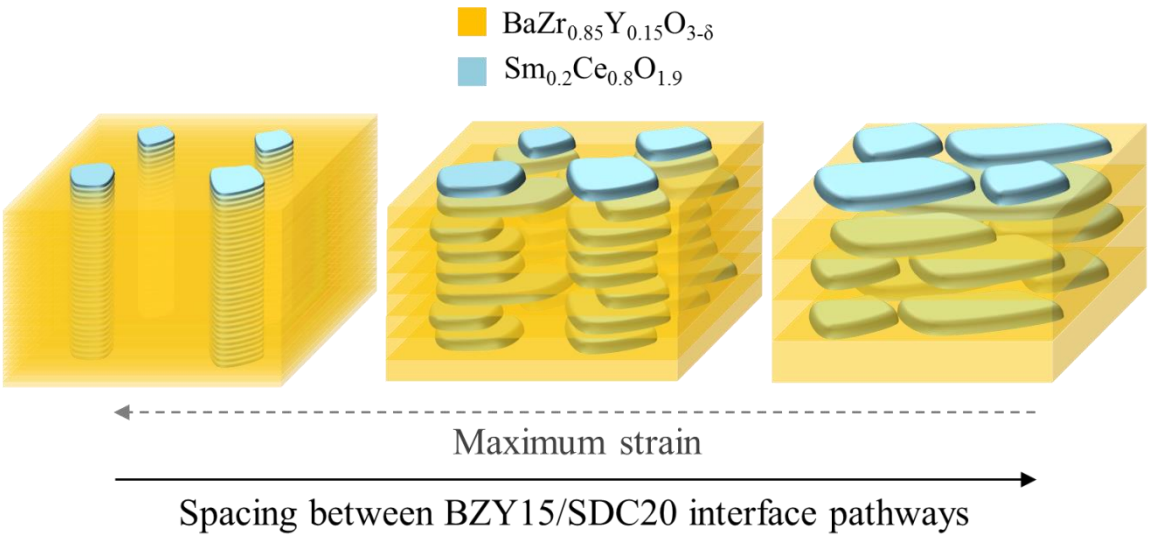

Figure 87 Schematic of BZY15/SDC20 heterostructure samples fabricated by PLD. SDC20 layer thickness, plane-to-plane orientation and region width are considered with respect to SDC20 phase strain and spacing between interface pathways

The mechanism for enhancement in electrical properties of the heterostructure SDC20 samples is interpreted as a strain effect at the BZY15/SDC20 interface. STEM and electron diffraction analysis of Sample 10-1 show that the epitaxial relationship between the BZY15 (110) and SDC20 (200) planes induces up to ~8% dilatative strain in the SDC20 lattice. The expansion of the SDC20 lattice is expected to drastically enhance transport in the SDC20 phase as reviewed in Chapter 2. Enhancement of ionic conductivity in the SDC20 phase due to dilatative strain is consistent with the activation energy measurement of the system. The activation energy measured for Sample 10-1 is slightly lower than the activation energy calculated for bulk SDC20.

The reason for faster transport in Sample 10-1 than either Sample 20-2 or Sample 5-0.5 is a balance between maximum strain and interconnectedness of the BZY15/SDC20 pathway in the sample. Although the thin layers of Sample 5-0.5 are expected to experience the most strain from the BZY15 phase, the 10nm BZY15 regions between heterostructures act as blocking columns to ionic transport. Conversely, the distance between fast interface pathways is shortest in Sample 20-2 but the strain is the lowest in the sample. It is reasoned that Sample 10-1 has the ideal mix of interface strain for high mobility of charge carrier and the short pathways for fast interface transport.

4.4.2 Characterization of vertically aligned $BaZr_{0.85}Y_{0.15}O_{3-\delta}/Sm_{0.2}Ce_{0.8}O_{1.9}$ heterostructure

An attempt to align the BZY15/SDC20 interfaces vertically was made using the composite target PLD method detailed in Section 4.2.5. A composite target of BZY15 (50 vol%) and SDC20 (50vol%) was used to prepare the composite films. PLD parameters for deposition were 100mtorr PO_2, 700^oC, 0.065cm^2 spot size, 10Hz, 2.86J/cm^2 with

rotating substrate. TEM analysis of the films is shown in Figure 88. Large, vertical grains (~30nm width) were formed during the deposition process.

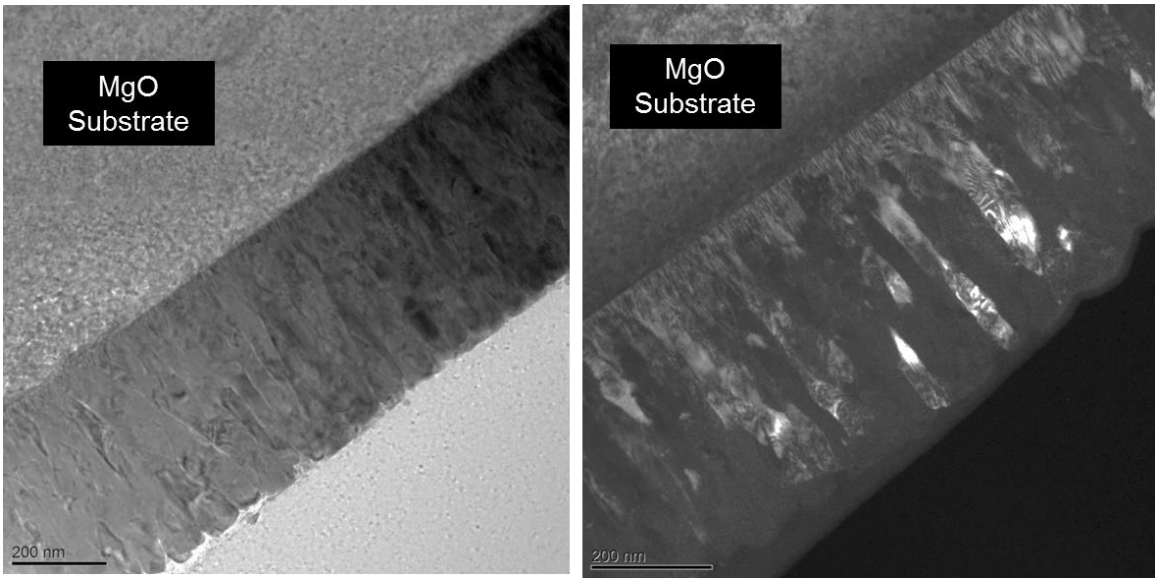

Figure 88 Bright-field and dark-field TEM analysis of composite BZY15/SDC20 films fabricated by PLD from a composite BZY15/SDC20 target with large vertical grains (Data collected by Dr. Yong Ding, GT)

STEM electron energy loss spectroscopy (EELS) was used to analyze the chemical composition of the composite BZY15/SDC20 sample. The EELS line analysis is shown in Figure 89. Distinct Ba-rich and Sm-rich regions were found in the vertical direction (perpendicular to the substrate surface) with width of ~20-30nm.

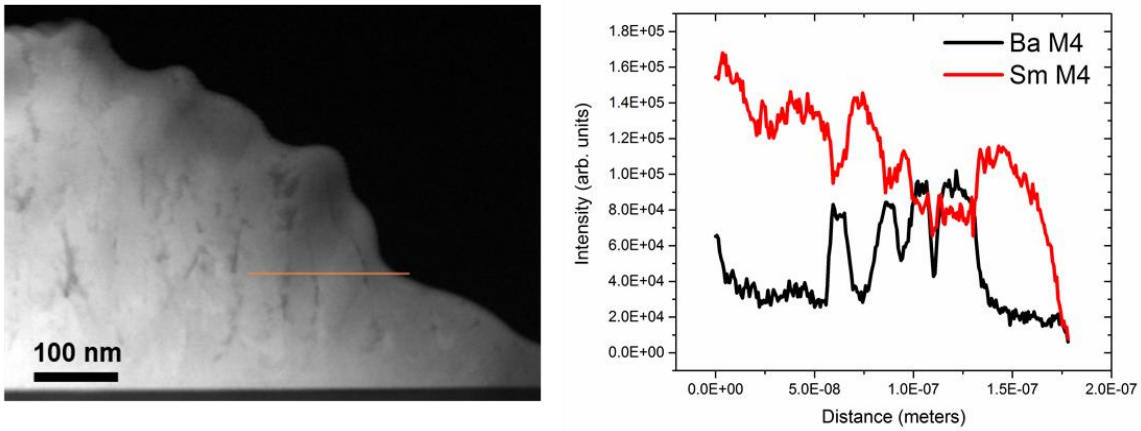

Figure 89 STEM image of BZY15/SDC20 composite sample with line analysis marker (left); intensity of the Ba M4 peak (black) and Sm M4 peak (red) as a function of distance across the composite sample (parallel to the substrate surface)

Chemical mapping of the EELS data for the composite BZY15/SDC20 sample is shown in Figure 90. Although distinct Ba-rich regions and distinct Ce- and Sm-regions are easily distinguished, the regions are not completed, vertical columns and do not span the substrate surface and air-side. Further optimization of the PLD parameters is necessary to achieve the vertically-oriented structures reported by MacManus-Driscoll, J., Wang, H. et al.[130]

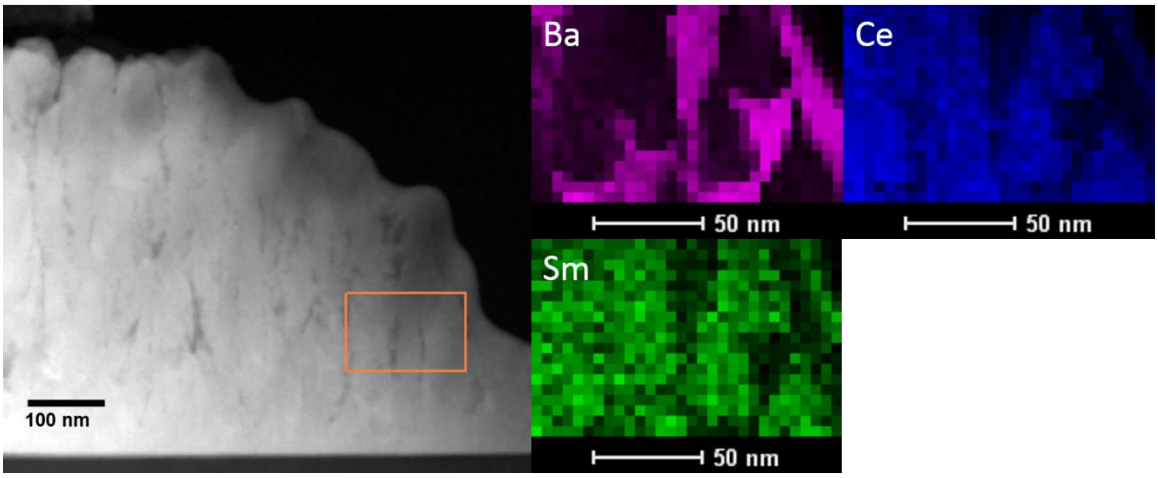

Figure 90 Chemical mapping of STEM-EELS data for Ba, Ce, and Sm in the BZY15/SDC20 composite thin film sample (Data collected by Dr. Yong Ding, GT)

4.5 Conclusion

The interfacial effects between BZY15 and SDC20 are of interest because of the usefulness of a composite proton-oxygen vacancy conducting SOFC electrolyte. Because the BZY15/SDC20 interface exhibits beneficial transport properties, the composite BZY15/SDC20 electrolyte should be eagerly pursued as a novel fuel cell electrolyte with fast ion transport and electrode water formation flexibility. In this study, DFT calculations and MD simulations of the $BaZrO_3/Sm_{0.2}Ce_{0.8}O_{1.9}$ interface indicate that diffusivity enhancement up to three orders of magnitude is possible at the interface due to the strain effect. The BZY15/SDC20 interfacial electrical properties were investigated by fabrication and characterization of thin film heterostructure samples. Thin film PLD deposition parameters were optimized by growth of single-phase films. Heterostructure samples were fabricated with varying layer thicknesses to determine the interfacial effect on electrical properties. A heterostructure sample with total thickness of 125nm and layer thickness of 10nm (BZY15) and 1nm (SDC20) was found to have electrical conductivity greater than one order of magnitude higher than either BZY15, measured in wet air, or nanocrystalline SDC20 single phase samples. It is proposed that the ~8% lattice mismatch at the BZY15/SDC20 interface causes significant disorder which contributes to fast transport and favorable electrical properties.

Chapter V

High pressure synchrotron μ-XRD study of structure-transport property relationships in Li^+ and O^{2-} solid state ionic conductors

5.1 Introduction

In the previous chapter, an enhancement in electrical conductivity of more than one order of magnitude was reported due to interfacial effects between BZY15/SDC20. Several literature reports of the interfacial effects on ionic conductivity in oxygen anion conductor/insulator thin film samples were also cited. As demonstrated, the primary method for studying interfacial effects in ionic conductors has been by fabrication of heterostructure thin film samples on single crystal substrates.[35] Careful thin film preparation using pulsed laser deposition (PLD) is required to fabricate high quality films and study the interfacial effects on electrical properties of the material. A detailed TEM analysis of the interface between ionic conductor and insulating substrate is necessary to determine the crystal structure at the interface for accurate interpretation of the transport properties measured by AC impedance spectroscopy. Often, defects at the interface, most commonly dislocations, complicate the interfacial effects on electrical properties, leading to difficulty in the fundamental interpretation of interfacial effects.[35; 131-133] The tedious nature of the current interfacial effects studies, and the limitations of the techniques used, require the introduction of new techniques to study interfacial effects in materials which can unveil the fundamental mechanisms of changes in electrical properties.

In this work, the high-pressure diamond anvil cell technique has been applied to the study of interfacial effects on ionic conductors for the first time to unveil fundamental mechanisms involved in electrical transport at interfaces in solid state ionic conductors.

The diamond anvil cell has been used widely to study structural transitions at extremely high pressures (>100GPa), found commonly in geological sciences.[134-137] Additionally, diamond anvil cells equipped with metal electrodes have been used to search for insulator, semiconductor, metallic, and superconductor high-pressure phase transitions in a variety of materials.[138-142] Here, the diamond anvil cell and synchrotron XRD will be used to impose up to 8% volumetric strain in Li^+ and O^{2-} solid state ionic conductors to probe structural transitions at high pressure, elastic properties of the materials and changes in electrical properties as a function of pressure. This approach seeks to understand interfacial effects by imposing the bulk material to the same extreme effects found at the interface. This approach is expected to greatly enhance the fundamental understating of the strain effect on the structure and transport properties of solid-state ionic conductors.

$Sm_{0.2}Ce_{0.8}O_{1.9}$ (SDC20) and $Li_{6.7}La_3Zr_{1.7}Ta_{0.3}O_{12}$ (LLZTaO), a Li^+ ion conducting solid state electrolyte, will be studied as a function of pressure to determine if structural transitions, which could significantly change transport properties, occur at high pressure (up to ~20GPa), to determine the isothermal bulk modulus of the materials and to directly measure the electrical resistance of LLZTaO at >8% volumetric strain. The results of these studies will be applied to the broader context of this dissertation to understand interfacial effects in solid state ionic conductors.

5.1.1 Diamond anvil cell technique

The diamond anvil cell (DAC) technique is widely used to probe materials properties at extreme pressures which cannot be studied by another method.[143] In general, a sample is positioned between the culets of two diamonds (anvils) and

compressed by pressure applied to the table of each diamond, as seen in Figure 91. Hundreds of gigapascals of pressure can be applied to a sample using this technique. The crystal structure of the small sample (typically diameter <200um) is probed by bright synchrotron μ-X-ray diffraction at a synchrotron source due to the small sample size. In this way, the crystal structure of a sample can be monitored as a function of pressure and structural phase transitions can be studied.[134-137]

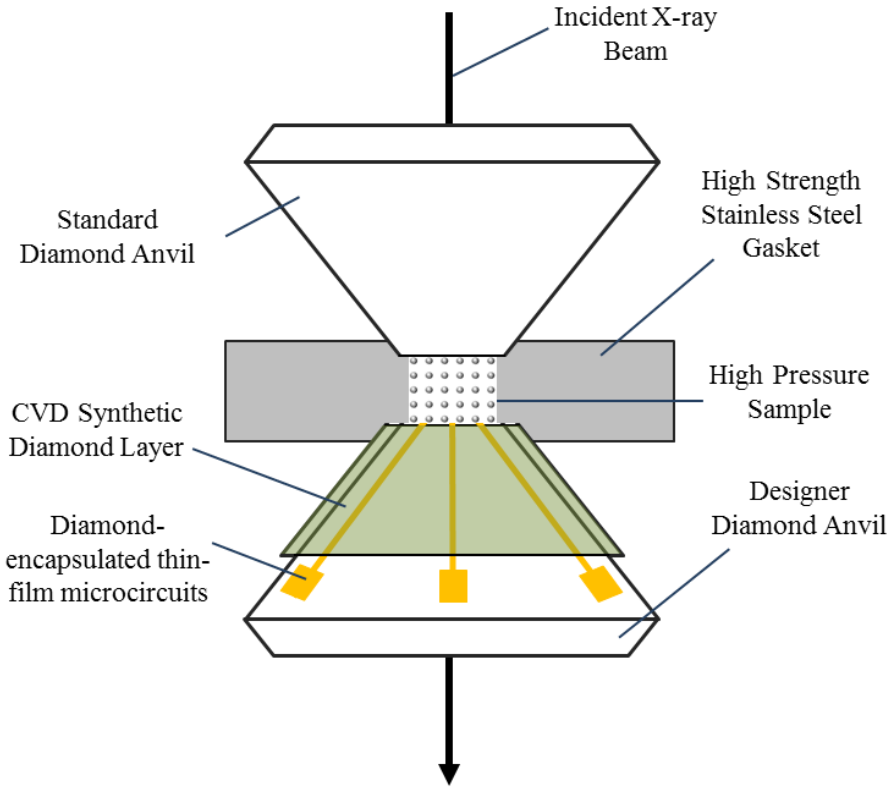

Figure 91 Designer Diamond Anvil Cell Schematic with microcircuit electrode-equipped bottom anvil

As seen in Figure 91, electrodes are added to the diamond anvils to probe the electrical properties of the sample as a function of pressure. Traditionally, thin metal probes were manually placed on top of the loaded sample before the top anvil was placed, creating contact with the sample during compression and decompression. However, as

the pressure increases, metal probe geometry changes significantly, making it difficult to determine if changes in measurement of electrical resistance were caused by probe dimension changes or changes in electrical properties of the materials.

"Designer" diamond anvil cells, developed by Vohra, et al[141] are special types of DACs equipped with diamond-encapsulated thin-film microcircuits for electrical resistance measurements at high pressure. The designer DAC diagram is shown in Figure 91. The electrodes, protected by CVD diamond, alleviate common difficulties with high pressure electrical measurements including variable electrode dimensions and shearing of electrical leads at high pressure.[141] The electrode-equipped designer DAC can be readily combined with synchrotron X-ray diffraction analysis of the sample, which provides detailed information about the evolvement of crystal structure over a large pressure range.

A typical literature example of pressure-induced structural phase change, measured with a DAC and synchrotron XRD is shown in Figure 92A.[144] The anti-fluorite phase of 1%Al-doped Mg_2Si is stable up to 10.5GPa. The Bragg diffraction peaks shift to higher 2θ as pressure increases due to shrinkage of the lattice. Above 10.5GPa a dramatic structural transition is documented with the presence of three new peaks which are highlighted. The three new peaks are assigned to the orthorhombic anti-cotunnite phase.

A typical literature example of designer DAC electrical resistance measurement is shown in Figure 92B.[141] The pressure vs resistance plot of potassium iodide (KI) shows

a dramatic decrease in resistance (enhanced transport properties) up to ~130GPa and then metallization of the material above 140GPa.

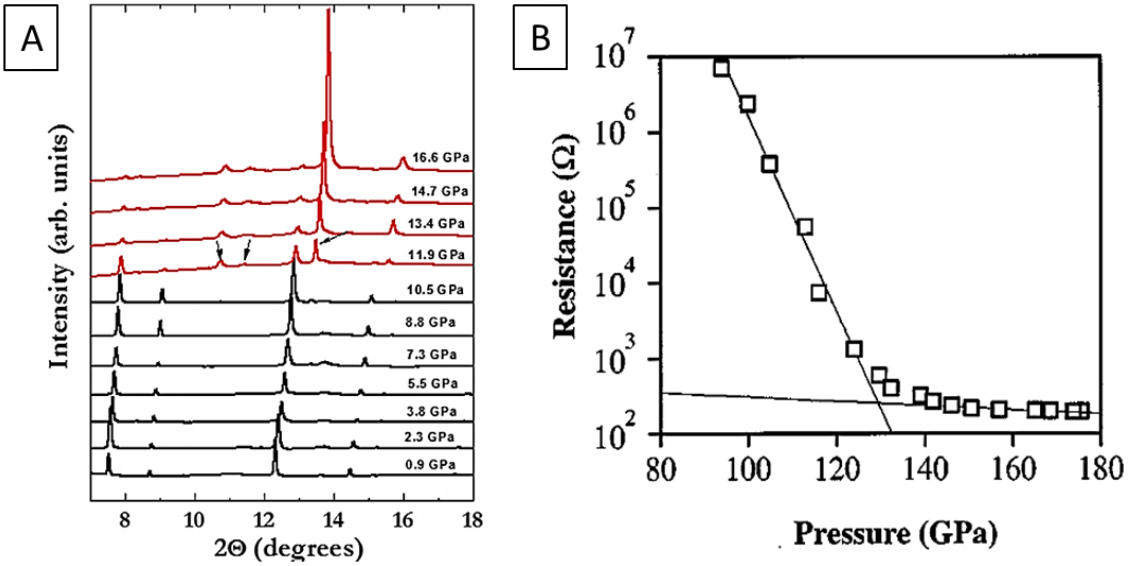

Figure 92 (A) Room temperature angle dispersive x-ray diffraction patterns of 1%Al-doped Mg2Si at selected pressures. (Taken directly from Zhao et al.)[144] (B) Resistance vs pressure plot of KI with rapid drop in resistance up to ~130GPa and leveling out above 140GPa which is interpreted as metallization of the material at high pressure[141]

The capability of in-situ measurement of structure and transport properties makes the designer DAC a unique tool for the study of the strain effect on ionic conductivity.

5.2 Theory

5.2.1 Measurement of the strain effect on ionic conductivity

The growth of coherent thin films by PLD on single crystal substrates or heterostructures generates strain at the thin film interface due to mismatch in lattice parameters of each material and the orientation of each film. When strain is released by misfit dislocations, semi- and incoherent interfaces form. The complicated strain fields around misfit dislocations and remaining strain at the interface contribute to a unique effect on charge carrier transport for the as-fabricated, thin film system.

Few studies, reported in the literature, focus on experimental measurement of changes in electrical conductivity with pressure in solid state ionic conductors. For the ideal case, no structural transition occurs in the material and the effect of pressure on transport is straightforward, as described above. The small number of publications include studies of β-Alumina[145], NaCl[146], olivine magnesium iron silicate[147], silver iodide (AgI)[7], NASICON type conductors[148], and the work was summarized by Samara[149] in 1984. However, these early studies are limited to low pressure due to the experimental technique of gas compression in a pressure vessel to reach pressures of ~0.7GPa.[7] More recently the ionic conductivity of YSZ has been measured by impedance spectroscopy under uniaxial pressure up to ~0.3GPa.[150] Although critically important for the advancement of fast ion conducting electrolytes, there has been no reported work on the effect of high pressure, where significant structural changes occur in the solid state (>2 GPa), on ionic conductivity in solid state materials. Using the DAC technique, the structural and electrical properties of solid state ionic conductors can be studied at volumetric strains of >7%.

The bulk modulus is inversely proportional to the migration energy, ΔE_{mig}, of the material, therefore, in "soft" crystals the energy required for the expansion of the lattice during transport is less than for "hard", high bulk modulus materials. The bulk elastic properties of a material are also directly related to formation of misfit dislocations at semicoherent solid-solid interfaces in thin films by the volume elastic energy of the film[151]. As the modulus of the material decreases, the volume elastic energy of the film decreases, misfit dislocation generation is suppressed and the strain field around the

dislocation is relaxed. Recent computational work by Yildiz, Marrocchelli, et al.[133] suggests that dislocations in doped-CeO_2 slow down ion transport due to defect-defect interactions. Therefore, the bulk elastic properties of SDC20 and LLZTaO are critical strain effect factors that will directly affect the transport properties of the materials at strained interfaces. However, the bulk moduli of common solid state Li^+ and O^{2-} ionic conductors have not been extensively studied. The elastic properties of these materials should be determined to provide critical information for optimizing strain at thin film interfaces for fast ionic conductivity. The Young's Modulus of Gd-doped CeO_2 and undoped CeO_2 has been studied by nanoindentation[152] and by first principles calculations[153] as a function of oxygen partial pressure. The incorporation of oxygen vacancies in the CeO_2 lattice at low oxygen partial pressure is known to increase the average bond length of the crystal and reduce the intrinsic elastic modulus of the material.[152] The bulk modulus of $Sm_{0.2}Ce_{0.8}O_{1.9}$ (SDC20) is predicted to behave similarly to Gd-doped CeO_2 at low oxygen partial pressure, indicating that the bulk modulus for SDC20 will be different from the bulk modulus of CeO_2. The elastic properties of $Li_7La_3Zr_2O_{12}$ have been calculated by resonant ultrasound spectroscopy (RUS) measurements, however, the bulk modulus has not been measured directly and the focus of the reported work was on mechanical properties (scratch resistance, stiffness) of the Li^+ ion conductor.

Although the effect of pressure on electrical transport seems straightforward, there are examples in the literature of compressive strains enhancing ion transport. In the K^+, Na^+ and Li^+ substituted β-alumina systems, hydrostatic pressure causes opposite effects on ionic resistivity due to intricate charge transport mechanisms in the

material.[145] In the case of large K^+ ions the electrical resistivity increases with increased pressure, however, in Li^+ substituted β-alumina the electrical resistivity is reduced by increased pressure. Additionally, DFT calculations and MD simulations are limited to interpretation of bulk crystal properties. The effect of pressure on charge carrier transport at interfaces is not easily described by theoretical calculations due to the unpredictable crystal structure of the interface.

Structural phase transitions could drastically affect transport pathways in solid state ionic conductors. Structural phase transitions due to strain are characterized by micro-X-ray diffraction when using the DAC technique. Additionally electrical properties of the new structures can be measured with the electrode-equipped DAC technique. Because the crystal structure at interfaces can vary drastically from the bulk, new transport pathways can form in these structures and unexpected electrical properties could be found.

5.2.2 Structure-transport property relationship in $Li_{6.7}La_3Zr_{1.7}Ta_{0.3}O_{12}$

A new family of fast garnet-type Li-ion conductors with typical compositions $Li_5La_3M_2O_{12}$ (M = Nb, Ta)[21] and $Li_7La_3Zr_2O_{12}$[22] were recently discovered and have been developed intensely for application as high performance electrolytes in solid state lithium ion batteries[22-28]. This garnet-type Li-ion solid electrolyte has high chemical stability in oxygen and water containing atmospheres[29], with lithium metal[30] and with common lithium ion battery electrode materials[31], making it the most promising solid electrolyte material for Li-ion batteries. The optimized structure, $Li_{6.7}La_3Zr_{1.7}Ta_{0.3}O_{12}$ (LLZTaO)[32], has fast ionic conductivity of 0.96 mS cm^{-1} at 25°C[32]. All Li^+ ions in the crystal are treated as interstitials with more than one available site.[7] The Li ions can be

considered as Frenkel defects, with Li ion vacancies at some sites along migration pathway and Li ions at other sites. The time of interstitial in its lattice site and the time spent between lattice sites is comparable.[7]

Cussen[154; 155] and others[156; 157] have refined the crystal structure of the Li-rich garnets (Li_x; x>3) to determine the structure-transport property relationships at atmospheric pressure. The lithium ion conductor forms in the typical $A_XB_3C_2O_{12}$ garnet structure at x=3 but addition of Li ions up to x=7 causes rearrangement of the lithium ions. Neutron diffraction experiments reveal rearrangement of lithium ions from tetrahedral sites to octahedral sites when x>3[24; 158]. Electrochemical measurements reveal a stepwise decrease in activation energy when x>3, typical of a new charge carrier migration pathway in the Li-rich compositions[159]. The structure-property relationship elucidated from these atmospheric pressure experiments is very valuable for understanding the garnet type lithium ion conductors.

The strain effect in the Li-rich garnets has not been studied by the thin film technique due to difficulty of fabrication of epitaxial thin films of the complicated composition. However, from the structure-property relationships in the garnet type li-ion conductors elucidated by neutron diffraction and electrochemical measurements, the effect of pressure on the garnet structure might not be straightforward. Pressure could make new Li+ sites energetically favorable in the LLZTaO structure and drastically change the transport mechanism of the material.

5.2.3 Structure-transport property relationship in $Sm_{0.2}Ce_{0.8}O_{1.9}$

$Sm_{0.2}Ce_{0.8}O_{1.9}$ is a well-known oxygen vacancy conductor used as an intermediate temperature electrolyte in solid oxide fuel cells (SOFCs). Structure-transport property

relationships studied in this material have focused on the effect of dopant radius on ionic conductivity. From detailed study of the doped-CeO_2 systems it has been shown that strain in the lattice critically affects the ionic conductivity. For example, in the $Ln_xCe_{1-x}O_{2-\delta}$ (where Ln = La, Gd, and Yb) system, when x=0.2 and the dopant ion is varied from Yb to Gd the lattice parameter changes from ~5.40 Å to ~5.45 Å accompanying significant changes in the oxygen vacancy diffusion coefficient.[160] The correlation between ionic conductivity and lattice strain due to varying dopant radius has also been well documented in the doped $BaCeO_3$ perovskite ionic conducting electrolytes.[161]

In this study the cell volume data calculated from XRD data will be used to determine the bulk modulus of $Sm_{0.2}Ce_{0.8}O_{1.9}$, and the result will be compared to the reported bulk modulus of undoped CeO_2. An implication will be discussed about the relationship between the change in bulk modulus of doped-CeO_2 and the oxygen vacancy transport properties at strained interfaces. The information gained from this study will enhance the understanding of the structure-transport property relationship in these important solid state ionic conductors.

5.3 Experimental

5.3.1 Fabrication of $Li_{6.7}La_3Zr_{1.7}Ta_{0.3}O_{12}$ and high pressure characterization by electrode-equipped diamond anvil cell and synchrotron μ-XRD

LLZTaO powder was prepared by the solid-state reaction method from LiOH-H_2O (Alfa Aesar), La_2O_3 (Alfa Aesar), ZrO_2 (Alfa Aesar), and Ta_2O_5 (Sigma Aldrich) precursor powders mixed in stoichiometric proportion. The precursor powders were mixed by bottle-rolling for 12 hours in 2-Propanol, pressed into a pellet and fired at 900^oC for 10h. The calcining process was repeated to achieve the pure phase.

To probe the effect of strain on electrical transport in LLZTaO a designer diamond anvil cell (DAC) [162] with CVD-diamond-protected tungsten electrodes was loaded with ~4μg of LLZTaO powder. The powder was evenly loaded in the designer DAC, as seen in Figure 93, and in contact with all electrodes. A stainless steel gasket with inner diameter of 100μm and thickness of 64μm was used between the diamond anvils and to confine the LLZTaO powder but was not in contact with the DAC electrodes. Silicone oil was used as pressure transmission medium. Four tungsten electrodes (1-4 in Fig. 2) were used for the four probe technique electrical resistance measurements. A current of 10μA was applied between electrodes 1 and 4 (~40μm spacing) and voltage was measured between electrodes 3 and 4 (~20μm spacing). The polarity of the current was alternated during the measurements and an average four-probe resistance value was calculated at each pressure. A ruby crystal was inserted into the sample for pressure calibration by spectroscopy. At 300K, the sample was compressed slowly from ambient pressure to 35 GPa and decompressed to ambient pressure while the electrical resistance was measured. The sample was pressure cycled to 35GPa two (2) times to determine the repeatability of the electrical resistance measurement.

Structural characterization of the LLZTaO powder at high pressures was conducted with high-pressure powder μ-XRD techniques at HPCAT 16-BM-D beamline[163], the Advanced Photon Source, Argonne National Laboratory. Silicone oil was used as the pressure transmission medium (PTM) and a ruby ball was used for pressure calibration. The high-pressure XRD patterns were collected up to 16.6GPa. The sample was oscillated 5 degrees during XRD collection to improve the powder statistics.

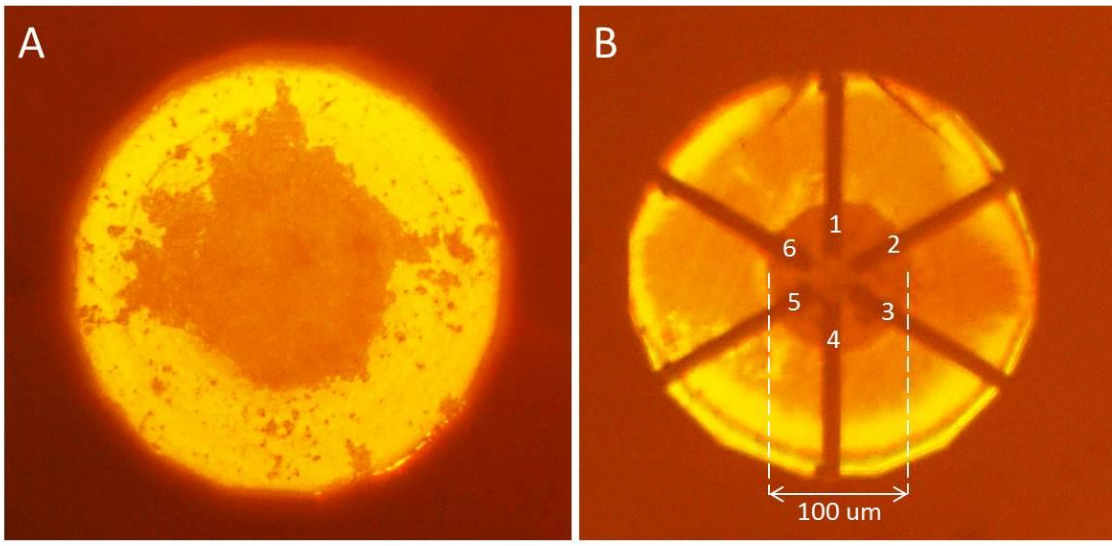

Figure 93 Optical image of LLZTaO powder loaded in Designer Diamond Anvil Cell; (A) Top-down view with power centered on the diamond anvil culet, and (B) Bottom-up view with tungsten electrodes visible.

The electrical conductivity of LLZTaO was also measured at elevated temperatures in order to compare the electrical properties – temperature relationship of the as-fabricated powder to the reported literature. LLZTaO pellets were pressed at 124MPa and sintered at 1100^{o}C for 36h in air. Lithium electrodes were pressed against each side of the pellet and AC impedance spectroscopy was collected from 55^{o}C to 115^{o}C using a Solartron 1255 Frequency Response Analyzer from 5MHz to 10mHz with a 30mV AC bias.

5.3.2 Fabrication of $Sm_{0.2}Ce_{0.8}O_{1.9}$ and high pressure characterization by diamond anvil cell and synchrotron μ-XRD

$Sm_{0.2}Ce_{0.8}O_{1.9}$ was fabricated by a co-precipitation method. Cerium nitrate hexahydrate ($Ce(NO_3)_3 \cdot 6H_2O$, Alfa Aesar, 99.5%) and samarium nitrate hexahydrate ($Sm(NO_3)_3 \cdot 6H_2O$, Alfa Aesar, 99.9%) aqueous solution was prepared with cation concentration of 0.1 mol/L and molar ratio of Ce^{3+}:Sm^{3+} equal to 4:1. Ammonia

dicarbonate (NH_4HCO_3, Fluka, 99. 9%) aqueous solution with concentration of 0.1mol/L was prepared with molar ratio of ammonium bicarbonate to cation equal to 2. The metal nitrate solution was added to the ammonia bicarbonate solution slowly (10mL/min) while stirring. White precipitates were collected and rinsed with distilled water (2x) and ethanol (2x) and then dried and calcined at 600^{o}C for 2h. The cubic fluorite phase (Fm3m) was confirmed with ambient temperature and pressure XRD. The average particle size is estimated to be 35 nm from Figure 94A, a scanning electron microscope image of the agglomerated particles collected after pre-firing at 600^{o}C. The XRD pattern (Figure 94B) shows the pure phase and the Rietveld refinement of the pattern with lattice parameter, a=5.433Å.

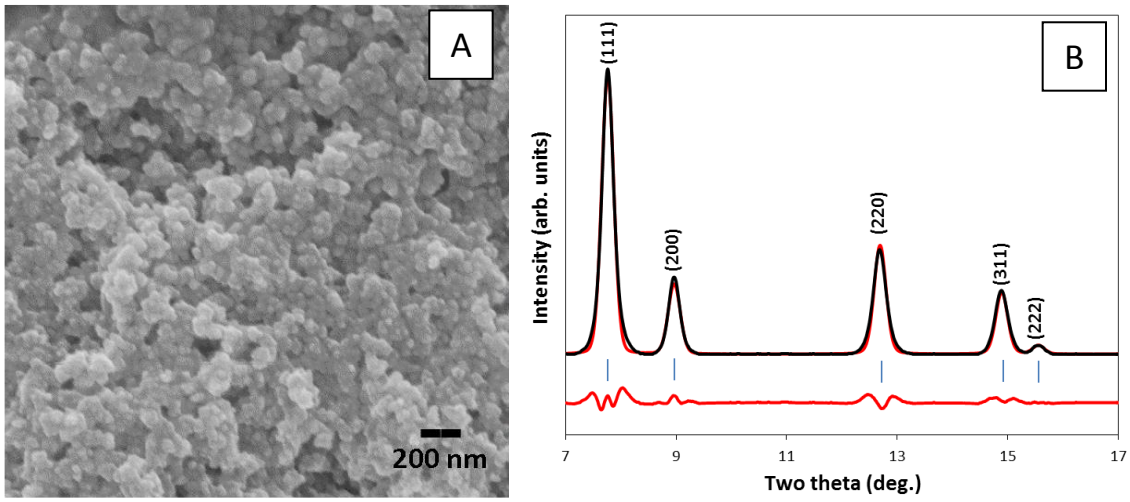

Figure 94 (A) Scanning electron microscope (SEM) image of ~35nm nanocrystalline SDC20 used in all high pressure experiments. (B) Low-pressure XRD pattern of SDC20 powder (P=0.25 GPa, λ=0.4246 Å).

High pressure was applied to the SDC20 sample using a diamond anvil cell (DAC) with a stainless steel gasket with inner diameter of 100μm. Pressure was applied to the SDC20 nanocrystalline samples in two separate runs with no pressure transmitting

medium (PTM) and with silicon oil PTM. Pressure was loaded onto the sample using a gas diaphragm in steps of ~1 GPa up to approximately 20GPa.

Structural characterization of the SDC20 powders at high pressure was conducted using high pressure μ-X-ray diffraction at HPCAT 16-BM-D beamline[163] of the Advanced Photon Source, Argonne National Laboratory. The X-ray wavelength was 0.4246 Å, and the fluorescence of a ruby ball was used for pressure calibration.

5.3.3 Synchrotron XRD at Argonne National Lab Advanced Photon Source – HPCAT 16-BM-D

16-BM-D at the Argonne National Lab Advanced Photon Source is a high-pressure-science collaborative access station. The bending magnet, monochromatic beam is primarily used for high pressure powder micro-X-ray diffraction (μ-XRD) and X-ray absorption spectroscopy (XAS). The beamline has an on-line ruby system for in-situ pressure measurement and a gas membrane delivery system for remote pressure control, allowing XRD measurements to be taken at different pressures without opening the beamline hutch. The high pressure DAC was loaded into a standard canister with gas pressure membrane. A Mar345 Image Plate detector was used for collection of the two-dimensional XRD data. The user control interface at 16-BM-D is shown in Figure 95. All alignment was completed remotely through the use of the software.

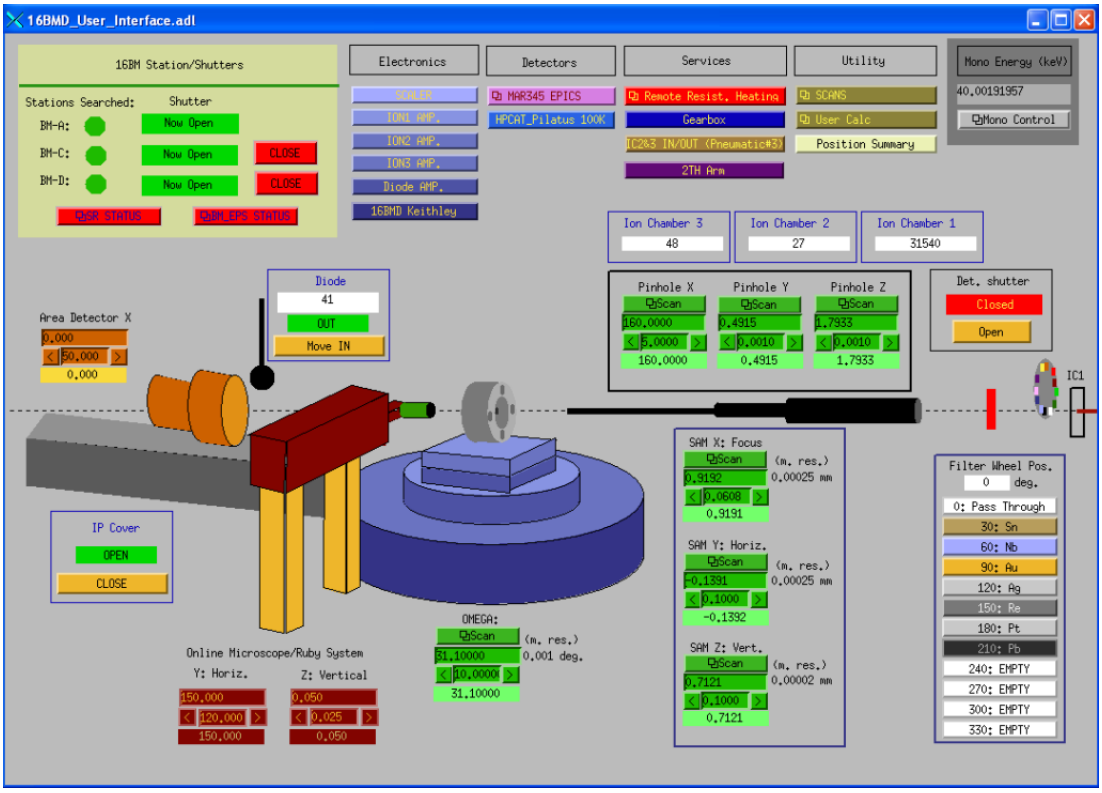

Figure 95 Argonne National Lab Advanced Light Source HPCAT 16-BM-D user interface screenshot

The monochromatic beam was calibrated to 29.2 keV. The vertical beam FWHM was 3.8 μm and the horizontal beam FWHM was 3.4μm. To improve sample statistics the sample was rastered 30μm^2 in the x-y plane and/or oscillated +/-5^o omega.

5.3.4 X-ray data processing with DIOPTAS and FullProf

The two-dimensional X-ray diffraction area detector data collected at each pressure were integrated using DIOPTAS, a python-based data processing software for synchrotron XRD data.[164] A screenshot of the DIOPTAS software with two-dimensional XRD data on the left and integrated one-dimensional XRD spectrum on the right is shown in Figure 96.

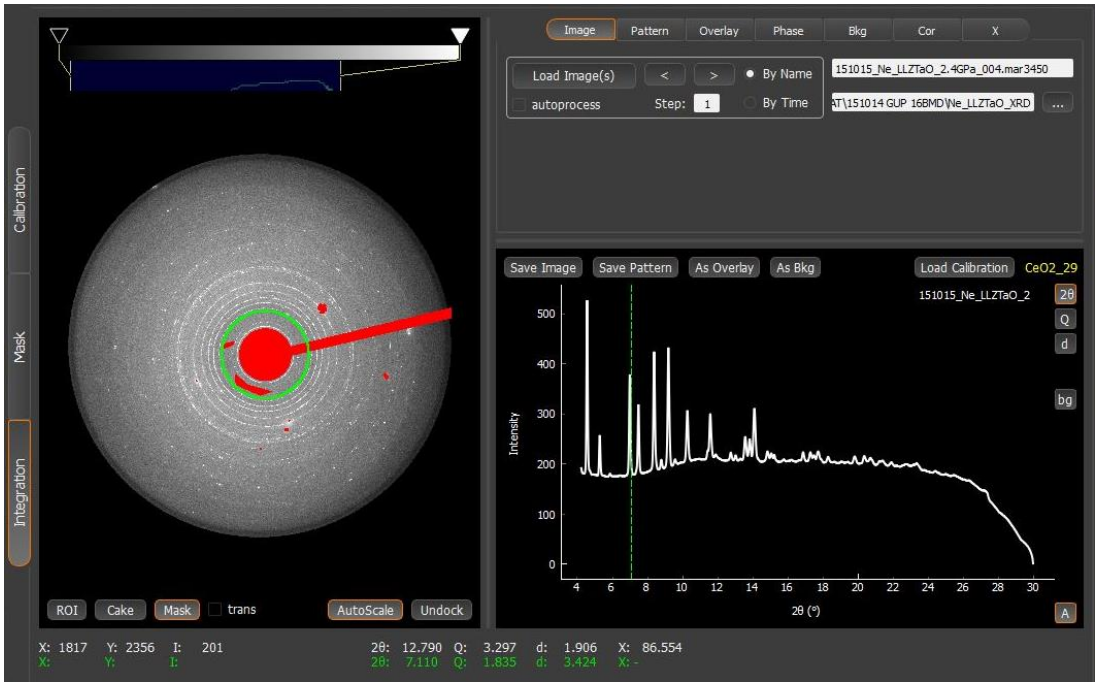

Figure 96 Screenshot of DIOPTAS software for data processing of two-dimensional X-ray diffraction area detector data; two-dimensional X-ray data (left) with masking (red) and integrated data (right)

The one-dimensional 2-theta vs. intensity XRD data was analyzed and refined using the FullProf software.[165] The patterns were refined until the chi-squared value was satisfactorily low or the best possible refinement was attained. A screen shot of the FullProf software and refinement process are shown in Figure 97.

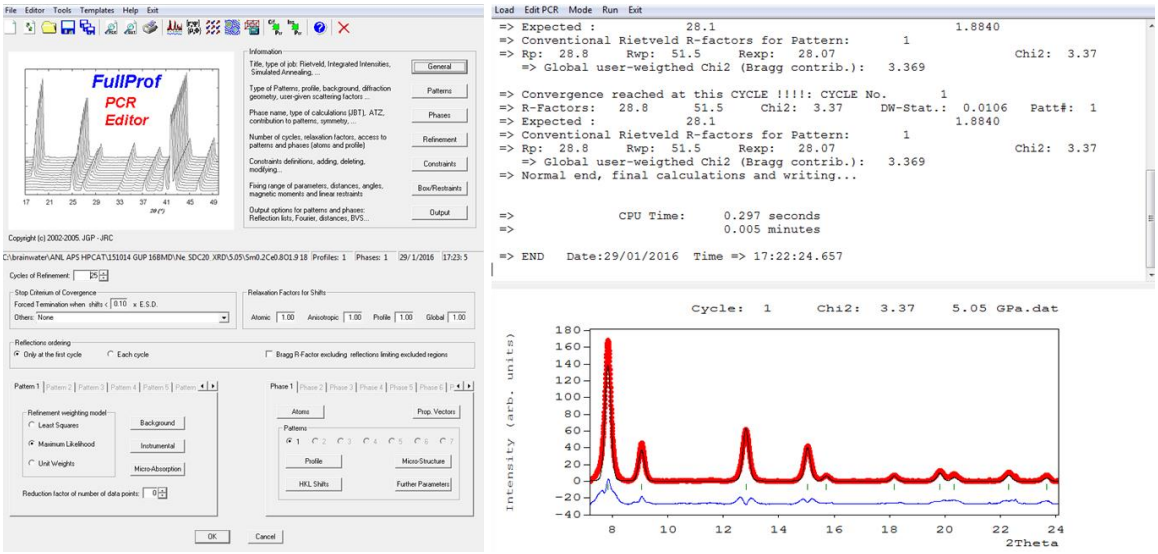

Figure 97 Screenshot of FullProf software used for Rietveld refinement of integrated X-ray diffraction data

5.4 Results and Discussion

5.4.1 High pressure electrical resistance study of Li-ion solid state ionic conductor - $Li_{6.7}La_3Zr_{1.7}Ta_{0.3}O_{12}$

The electrical conductivity of LLZTaO, prepared for the high pressure resistance measurements, was measured at ambient pressure from 55^{o}C to 115^{o}C and the data is shown in Figure 98. The total conductivity of LLZTaO prepared by solid state reaction is comparable to that reported in the previous literature[32] and the activation energy is 0.10eV. The conductivity measurement of LLZTaO with respect to temperature confirms that the as-fabricated powders are the correct phase.

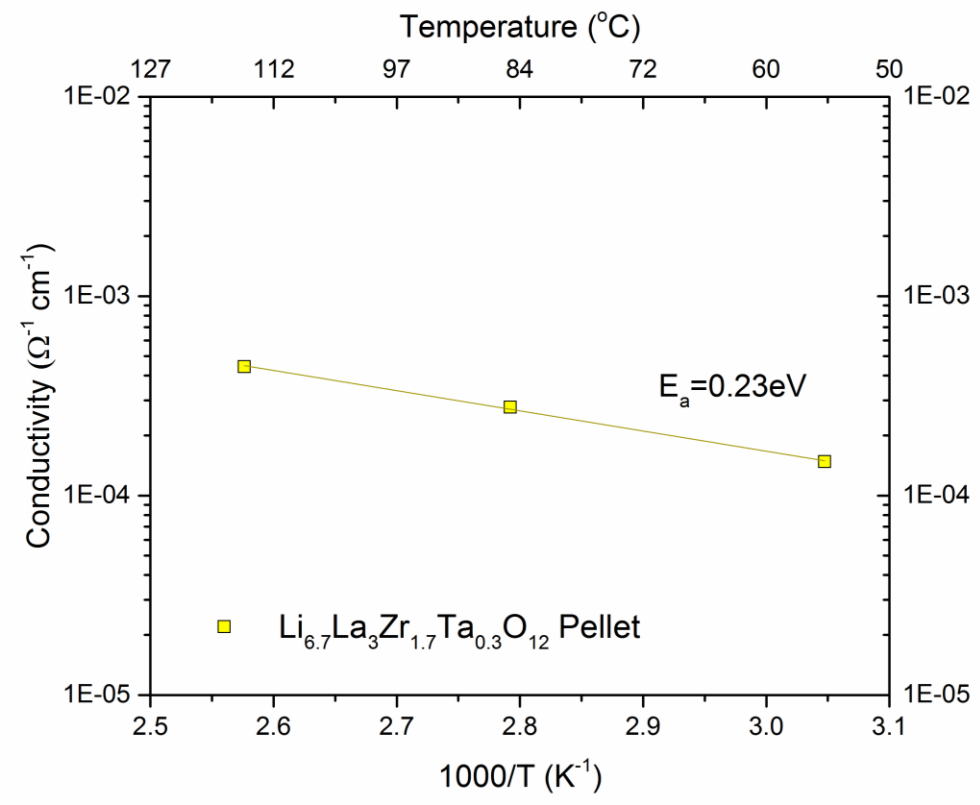

Figure 98 Electrical conductivity of LLZTaO pellet as a function of temperature with activation energy of 0.10eV.

Selected XRD patterns of LLZTaO at high pressure from 0.9 GPa to 16.6 GPa are shown in Figure 99. No phase transformation is observed over the pressure range. Peak shifting to higher 2θ position confirms lattice compression at high pressure. Reduction in peak intensity is due to reduction of sample volume in the X-ray path at high pressures. Non-hydrostatic condition at high pressures is confirmed due to broadening of diffraction peaks at small d-spacing. The XRD patterns were refined using the FulProf software package to determine the LLZTaO unit cell size at each pressure. The unit cell volume with respect to pressure from 0.9GPa to 16.6GPa is presented in Fig 100. The unit cell volume contraction at 16.6 GPa is ~8%.

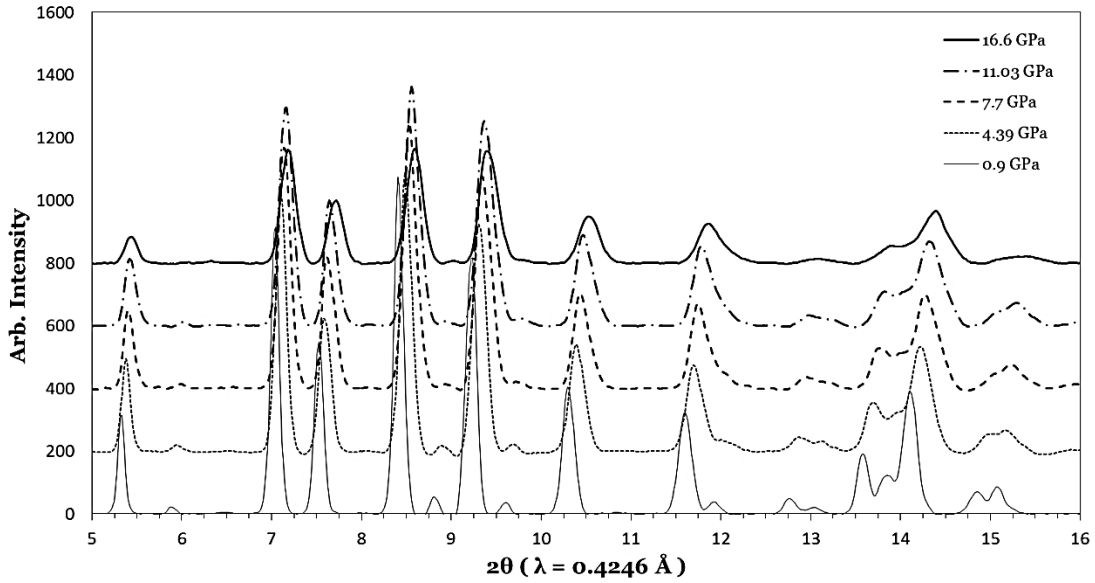

Figure 99 Synchrotron XRD patterns of LLZTaO from 0.9GPa to 16.6GPa

In Figure 100, the LLZTaO pressure-volume data is fit to the 4th order Birch-Murnaghan equation of state (EOS Fit 7) to determine the isothermal bulk modulus of the material and the results are listed in Table 8 where V_o is the ambient pressure unit cell volume, K_T is the isothermal bulk modulus, and K_T' is the pressure derivative of the isothermal bulk modulus. Due to slight increases in pressure during loading and assembly of the DAC, there is no ambient pressure measurement. The bulk modulus of LLZTaO with silicone oil PTM is K_T=58 GPa. The soft elastic properties of the LLZO family of materials is also reported by Ni, et al.[166]

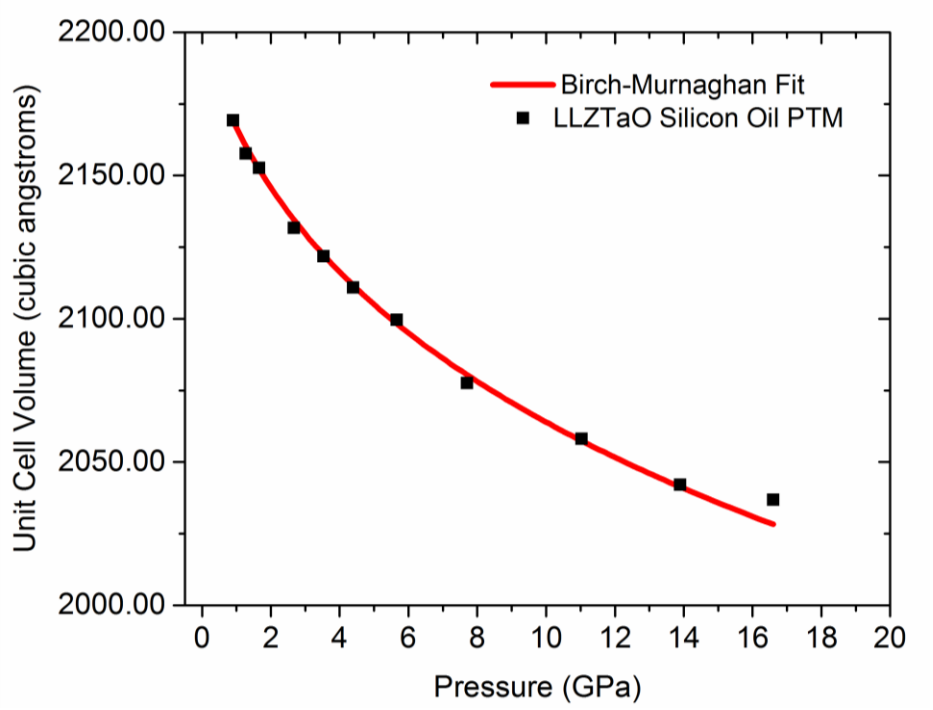

Figure 100 LLZTaO unit cell volume, refined from LLZTaO high pressure µ-XRD data from 0.9GPa to 16.6GPa

Table 8 EOS data for LLZTaO with silicon oil PTM from 4th order Brich-Murnaghan equation of state

	EOS Parameters for LLZTaO with Silicon Oil PTM
V_o (Å^3)	2197
K_T (GPa)	58
K_T'	32

Electrical resistance of the LLZTaO material as a function of pressure is reported in Figure 101. The data is reported for two compression-decompression cycles. All cycles are plotted independently in Figure 101 A-D and the data is plotted together in Figure 101E. The discrepancy in the first compression cycle, especially at low pressure is attributed to re-arrangement of the sample with respect to the electrodes. The P-R data

from the second cycle is considered most reliable, but all data is consistent and repeatable. Over the measured pressure range, the resistance of LLZTaO increases by approximately 1 order of magnitude. No discontinuity in the resistance data is measured, indicating no new, low energy transport pathways were formed at high pressure due to ion rearrangement.

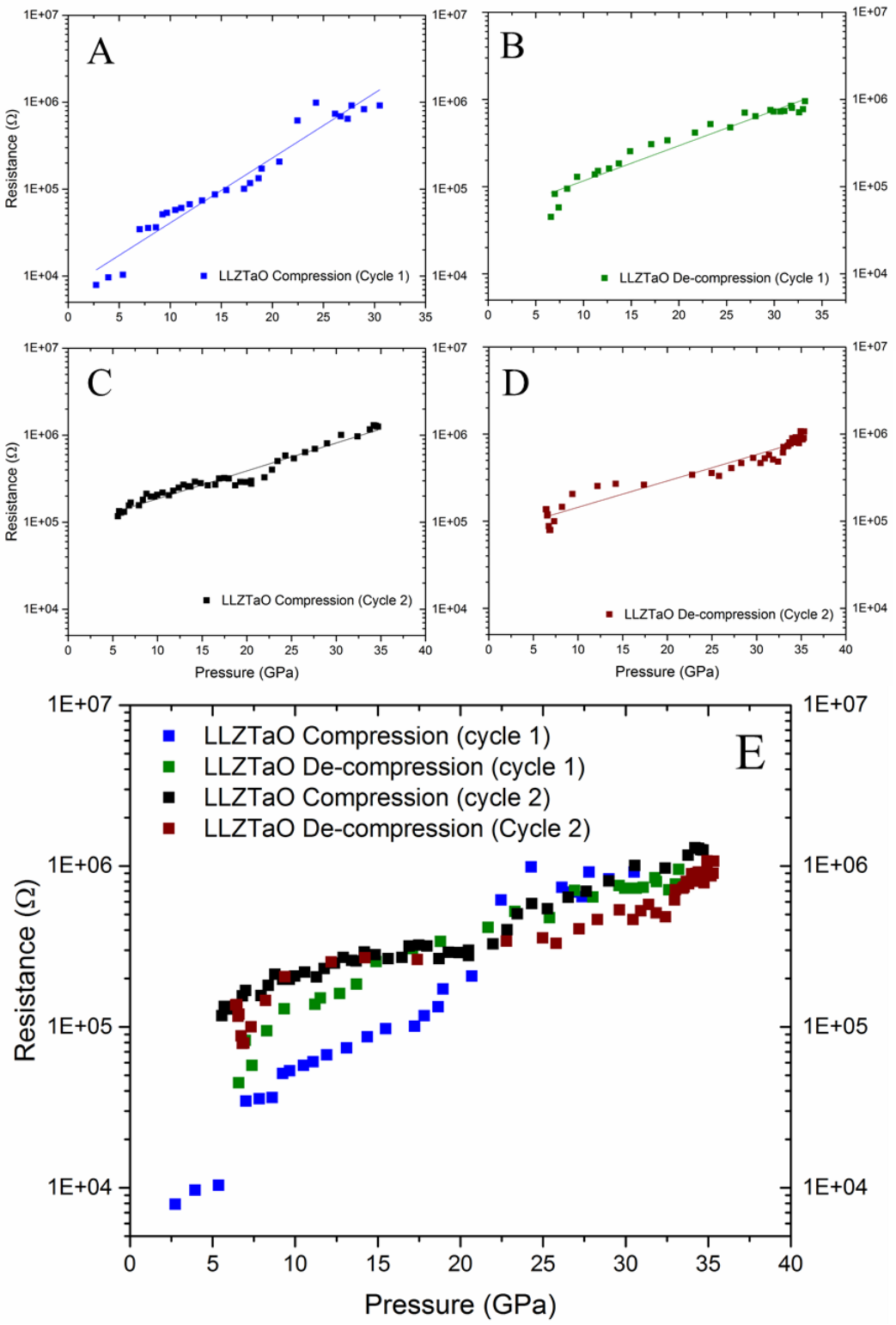

Figure 101 Pressure vs. resistance curves for $Li_{6.7}La_3Zr_{1.7}Ta_{0.3}O_{12}$ under compression and decompression. Data collected using a tungsten electrode equipped diamond anvil cell.

In collaboration with Dr. Saiful Islam and Dr. Benjamin Morgan of the University of Bath the mean-squared displacement for lithium (proportional to diffusion coefficient) was calculated by DFT and MD techniques. The calculated MSD data for Li^+ in LLZTaO is shown in Figure 102. While the simulation is not fully converged, the simulation is in agreement with the experimental P-R resistance data. Li^+ transport decreases significantly with increasing pressure up to 5 GPa and then remains almost constant to 35GPa. Our experimental data shows constant resistance increase with increasing pressure, up to 35GPa. An important factor not considered in the DFT calculation and MD simulations is transport along grain boundaries and particle interfaces of the LLZTaO sample. These factors might explain the discrepancy in the high pressure transport properties.

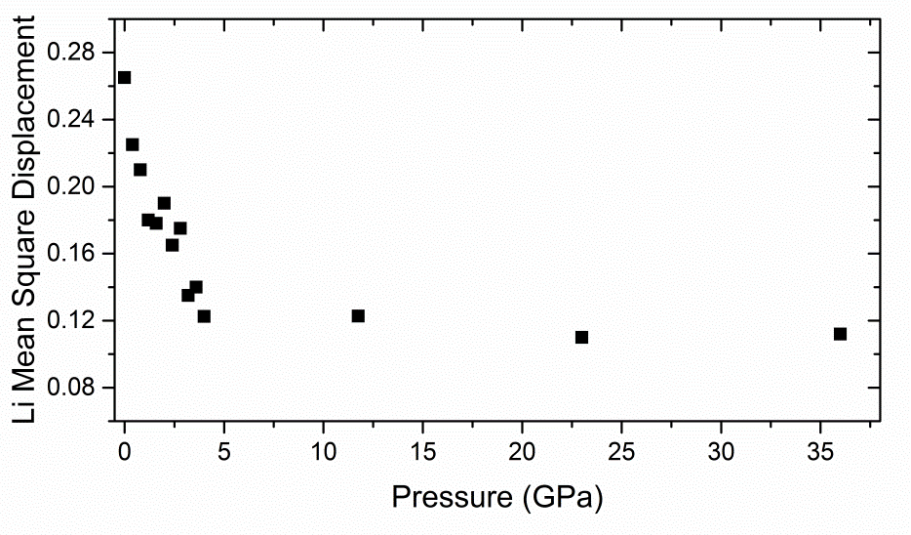

Figure 102 Calculated Li^+ mean square displacement (proportional to diffusion coefficient, D, and ionic conductivity, σ, assuming constant correlation factors) in Li6.7La3Zr1.7Ta0.3O12 as a function of pressure.

In Figure 103 the pressure-resistance curve is projected to the hypothetical negative pressure range assuming a linear relationship. The change in resistance of the sample from 0GPa to -35GPa is approximately one order of magnitude. If the relationship

of pressure and resistance remains linear in the dilatative strain region, we expect approximately one order of magnitude increase in transport properties due to tensile strain on the lattice.

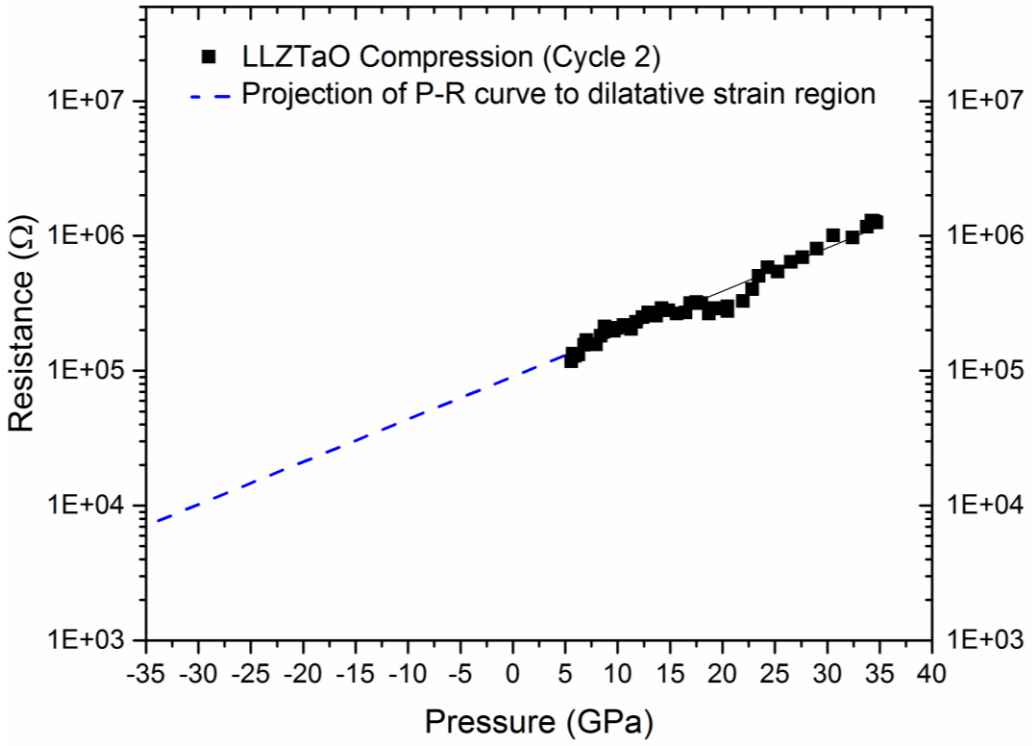

Figure 103 Pressure vs. resistance curve for Li6.7La3Zr1.7Ta0.3O12 under compression (Cycle 2) with projection of P-R data into hypothetical negative pressure, dilatative strain range

The data collected in this section suggests that the electrical properties of LLZTaO Li^+ conductor do not deviate from theoretical bulk calculations of the pressure effect on the material. The absence of structural transition measured by μ-XRD does not rule out minor changes in Li+ positions in the structure. Neutron diffraction has high cross section for Li^+ and is necessary to precisely determine Li+ positions in a crystal. These measurements show no significant deviation from predicted behavior of LLZTaO structure or transport properties at high pressure.

5.4.2 High pressure structural characterization of O^{2-} solid state ionic conductor – $Sm_{0.2}Ce_{0.8}O_{1.9}$

Figure 104 displays high pressure x-ray diffraction spectra taken up to ~20GPa for nanocrystalline SDC20 with (A) silicone oil as PTM and (B) no PTM. Rietveld refinement of the highest and lowest pressure spectra are included. In both spectra no structural transition is observed and the cubic fluorite-type structure remains up to ~20 GPa. Peak shifting to higher two-theta is consistent with volumetric contraction of the SDC20 lattice.

Peak depression and broadening as a function of pressure is observed in both sets of patterns but most noticeably in the SDC20 sample measured with no PTM (Figure 104B). While the (222) Bragg diffraction peak is distinguishable up to ~13 GPa in the SDC20 sample measured with silicon oil PTM, its intensity decreases drastically above ~5 GPa for the SDC20 measured without PTM. Similar peak intensity decrease and peak broadening is observed in the higher two-theta peaks. The peak depression and broadening, with most significance in the SDC20 without PTM sample, is consistent with quasi- and non-hydrostatic conditions due to silicone oil PTM[167] and no PTM used for the measurements. In non-hydrostatic and quasi-hydrostatic compression conditions a pressure gradient with sample distribution can form causing orientation-texture development as the sample tries to reoriente in order to minimize internal energy during the applied stress. It is noted that the raw pressure measurements for the SDC20 with silicon oil PTM sample, calibrated by ruby fluorescence, have been adjusted by 3 GPa so that the ambient pressure unit cell volume of SDC20 in silicon oil coincides with the known ambient pressure unit cell volume of SDC20.

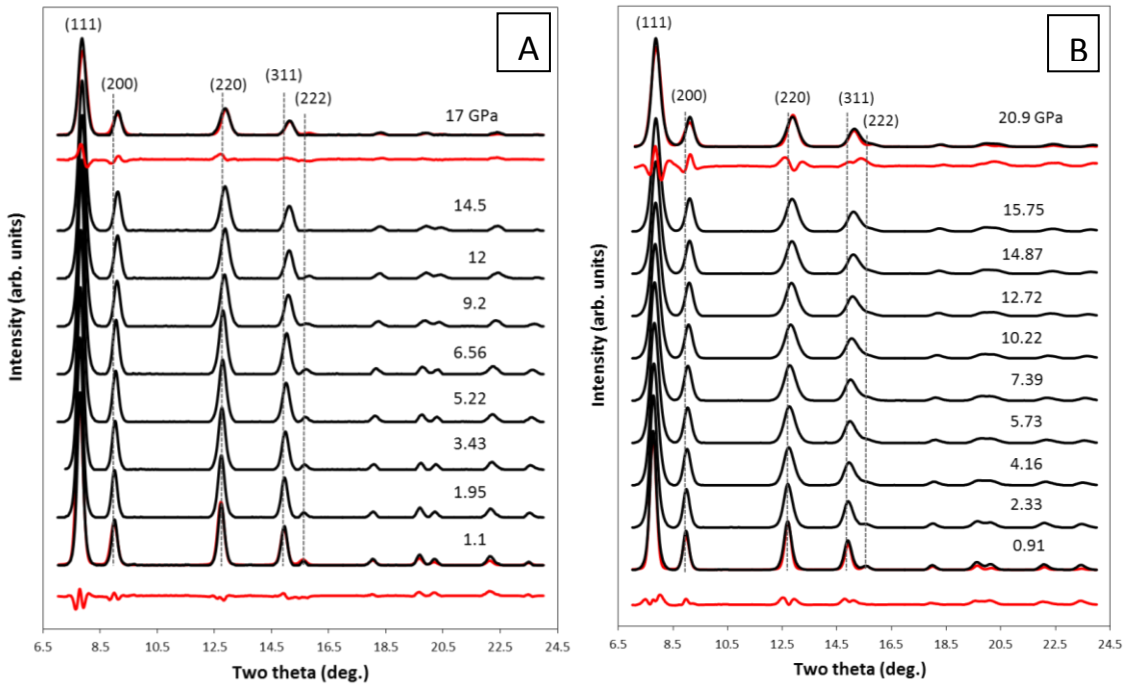

Figure 104 XRD patterns for SDC20 up to 20 GPa with (A) Silicone oil PTM and (B) no PTM. The red trace is the difference between the measured and fitted spectra.

To quantify the peak broadening as a function of pressure in the diffraction data the full width half maximum (FWHM) values for the (220) Bragg diffraction peak in both PTM conditions is given in Table 9. The (220) FWHM value for the sample measured with no PTM is 54.1% wider than that of SDC20 measured with silicon oil PTM at ~3.5 GPa. The (220) FWHM value for the sample measured at 15.75 GPa with no PTM is 31.6% wider than that of SDC20 measured with silicon oil PTM at 17 GPa.

Table 9 FWHM comparison of SDC (220) Bragg reflection with silicon oil PTM and without PTM

	Pressure (GPa)	FWHM (2-theta)
SDC20 w/ silicon oil PTM	3.43	0.27
	17	0.38
SDC20 w/o PTM	3.55	0.41
	15.75	0.5

Figure 105 displays the variation in unit cell volume for SDC20, refined from the XRD data, with and without silicon oil PTM up to ~20GPa. Volumetric strain up to 5% is observed in both measurements. The P-V curve is linear up to ~13GPa for both conditions. However, an apparent compressibility disruption is observed in the P-V curve around 15 GPa for the SDC20 data with silicon oil PTM. The observation is consistent with the reported effect of silicon oil as PTM[167] on the high-pressure compressibility of nanocrystalline CeO_2 by Wang et al.[168] and will be discussed in more detail in the following section.

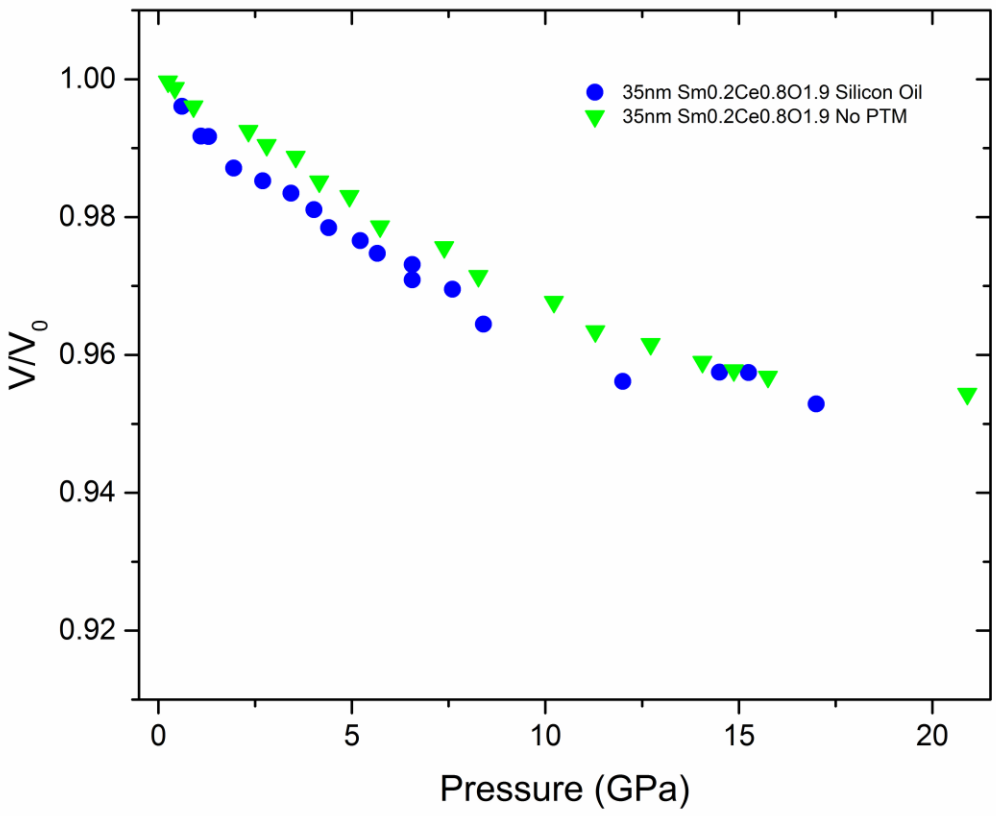

Figure 105 Pressure-Volume curves for nanocrystalline 35nm SDC20 with silicon oil PTM and without PTM. It is noted that the in-situ pressure calibration for the SDC20 with silicon oil PTM had an obvious error (in its zero pressure reference) so that has been re- adjusted by 3 GPa to match with V/Vo = 1.0 at P = 0 GPa condition.

In order to determine the relative effects of pressure on individual atomic plane compression, d-spacings for the (111), (200), (220), and (311) Bragg peaks were analyzed and relative d-spacings (d/d_o) are plotted in Figure 106. Interestingly, the (200) d-spacing shift is the most significant both for silicon oil PTM and without PTM. This relative d-spacing data is again consistent with the recently reported data on nanocrystalline CeO_2 by Wang et al.[168] The anomolous compressibility behavior around 15 GPa is found in (111), (200), (220), and (311) Bragg peaks of SDC20 in the silicon oil PTM sample. The effect is also observed in the (220) peak of the SDC20 sample measured without PTM.

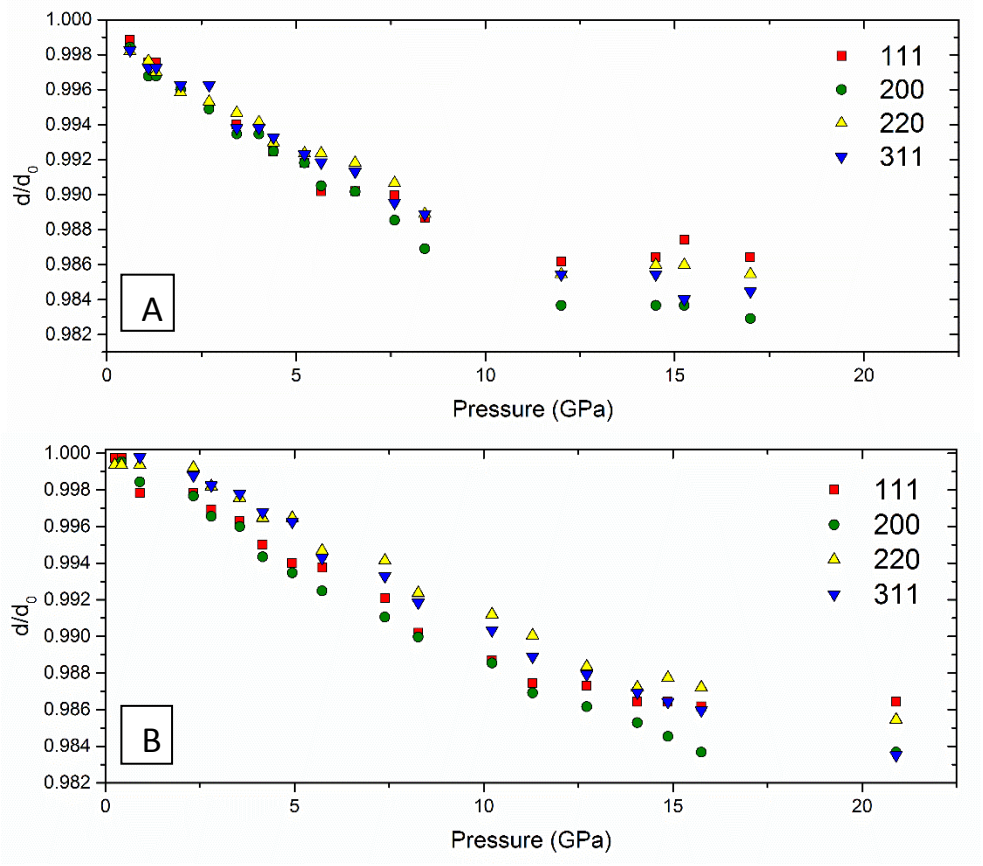

Figure 106 Variation of relative d-spacing (d/d0) for 35 nm SDC20 at (111), (200), (220) and (311) Bragg reflections as a function of pressure with (A) Silicon oil PTM, and (B) No PTM

In Figure 107, the pressure-volume data from both data sets are fit to the Birch-Murnaghan equation of state to determine the isothermal bulk modulus of the nanocrystalline SDC20 and the results are listed in Table 10 where V_o is the ambient pressure unit cell volume, K_T is the isothermal bulk modulus, K_T' is the pressure derivative of the isothermal bulk modulus, and K_T'' is the second pressure derivative of the isothermal bulk modulus. The ambient pressure unit cell volume for the SDC20 powders is fixed to V_o=160.41 Å^3. The bulk modulus of SDC20 with silicon oil PTM is K_T=157 GPa. It is noted that the anomalous compression behavior of nanocrystalline

SDC20 above 13GPa is not included in the fitting for the bulk modulus determination. The bulk modulus of SDC20 without PTM is K_T=188.67 GPa.

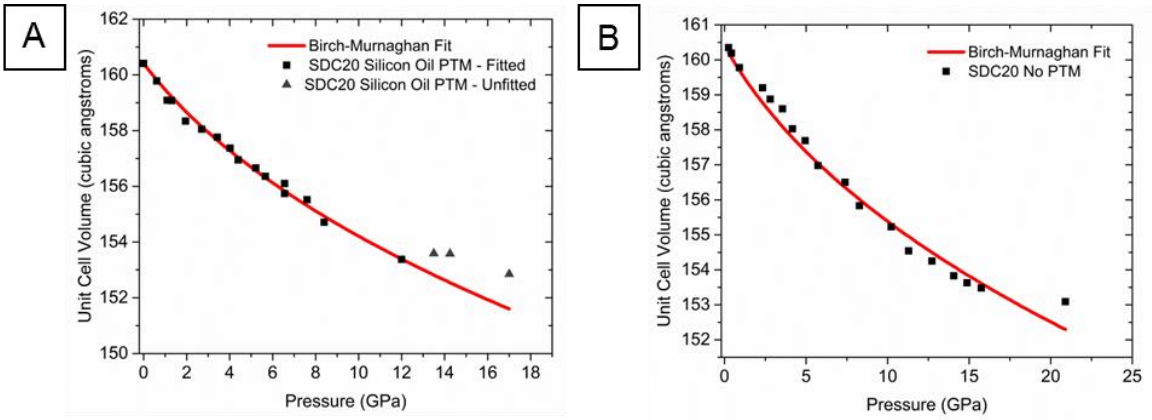

Figure 107 (A) EOS fit of SDC20 Silicon Oil PTM P-V data, (B) EOS fit of SDC20 with no PTM P-V data

Table 10 EOS data for SDC20 with and without silicon oil PTM

EOS Parameters for 35nm SDC20		
	Silicon Oil	No Pressure medium
V_o (Å^3)	160	160
K_T (GPa)	157	189
K_T'	29	39
K_T''	-4	-7

The highly defected nanocrystalline Sm-doped CeO_2 shows no structural phase transition up to 5% compressive lattice strain (~20 GPa). In comparison to reported P-V curves in the literature for CeO_2, our data is consistent.[168] Significant peak broadening and intensity reduction of the Bragg peaks with increasing pressure was observed. The broadening and intensity reduction can be attributed to a strain distribution within the sample in non- and quasi-hydrostatic conditions.

The observed compressibility anomaly of the nanocrystalline SDC20 sample observed above ~15GPa is partially attributed to the nonhomogeniety of silicon oil PTM above ~13GPa as reported by Klotz[167], however, a nanoparticle effect, proposed by Wang et al.[168] is also attributed to explain the abnormal behavior. In the mechanism proposed by Wang et al.[168] the outer shell of the ceria nanoparticle can form an amorphous shell under compression which causes a decrease in the apparent pressure of the nano grain CeO_2 particle core. The data for ~35nm SDC20 presented in this work extends the previous data interpretation of 4.7nm, 5.2nm and 12nm CeO_2 data presented by Wang et al. and confirms the similar effect in ~35nm nanoparticles of SDC20.

The relative d-spacing (d/d_0) data reveals the change in packing density of specific planes in the SDC structure, (111), (200), (220), and (311) as a function of pressure. Differences in compression and evidence of nonhydrosticity (spread of the relative d-spacing data) for each atomic plane is noticeable in the silicon oil PTM sample and the sample with no PTM. The (200) plane consistently shows the highest compressibility of all planes and the compressibility anomaly of nanocrystalline SDC20 is observed in all planes but most dramatically in the (111) plane.

The effect of defect concentration on elastic properties of SOFC electrolyte ionic conductors is important for understanding the effect of strain on transport properties and for the mechanical robustness of the high temperture energy conversion device. The reduction in bulk modulus of $Sm_{0.2}Ce_{0.8}O_{1.9}$ observed in our measurements by high pressure XRD is in agreement with preliminary results by Wang, Y. et al.[152] Samarium, Sm^{3+}, doping in the Ce site of CeO_2 creates oxygen vacancies, $V_o^{\cdot\cdot}$, which is responsible

for the decrease o the bulk modulus of the material. The bulk modulus determined by fitting a Birch-Murnaghan EOS curve to the data in this work is consistently lower for nanocrystalline SDC20 in comparison to the bulk CeO_2 properties reported (~210-220GPa)[169; 170], for both PTM conditions tested.

Theoretical model development of the strain effect on ion transport in ionic conducting films has been developed by Schichtel, Korte, Janek et al.[77-79; 114] Biaxial elastic strain at a coherent interface of two phases with similar symmetry but mismatched d-spacing is defined as ε_{12} where each phase d-spacing is represented by $d_{hkl,1}$ and $d_{hkl,2}$.[114] If isotropic mechanical properties are assumed, the isotropic pressure of the phase 1 thin film is related to the Young's modulus, Y_1, Poisson ratio, ν_1, and the biaxial elastic strain, ε_{12}, by Equation 34.

$$P = -\frac{2}{3}\frac{Y_1}{1-\nu_1}\varepsilon_{12} \tag{34}$$

Additionally, the bulk modulus is related to Young's modulus by equation 2, where K_1 is the bulk modulus of phase 1 (35).

$$Y_1 = 3K_1(1-2\nu_1) \tag{35}$$

Combining equation 1 and 2 yields the biaxial elastic strain relationship to the pressure, poisson's ratio and bulk modulus, given in Equation 36. The biaxial elastic strain is inversely dependent on the bulk modulus of phase 1.

$$\varepsilon_{12} = -\frac{3}{6}\frac{P(1-\nu_1)}{K_1(1-2\nu_1)} \tag{36}$$

In order to create maximum strain in the thin film ionic conductor without misfit dislocation generation, which have been shown to decrease ion transport[131; 133], a

material with low elastic modulus is most desirable to reduce the volume elastic energy of the film.[151] The volume elastic energy of the film is given by Equation 37.[151] As the modulus of the material decreases the film volume elastic energy decreases and misfit dislocation formation decreases.

$$Film\ volume\ elastic\ energy = Young's\ modulus * film\ thickness * coherency\ strain \quad (37)$$

As bulk modulus of the material decreases (increasing elasticity of the material) a larger strain can be accomodated in the lattice (before misfit dislocation generation) causing enhanced lattice expansion and faster ionic transport through the lattice. This result could effect the optimum dopant ratio to achieve the highest ionic conduction for common ionic conductors when fabricated as epitaxial thin films. For example, the optimum dopant concentration of 20% in bulk doped-ceria may not be the optimum dopant concentration for fast ionic transport at strained interfaces. This insight might prove to be crucially important for the optimization of ionic conductivity in strained ionic conductors. The effect of decreasing bulk modulus on misfit dislocation formation is summarized in Figure 108.

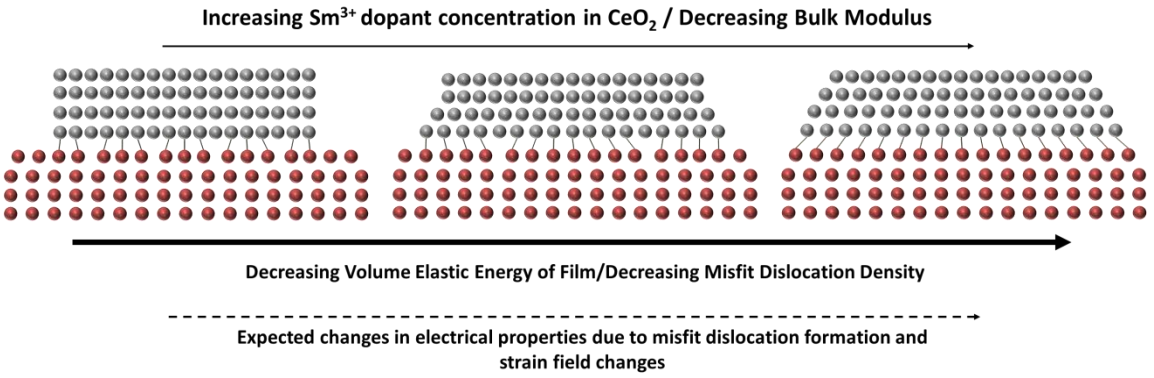

Figure 108 Schematic representation of bulk modulus dependent misfit dislocation formation in doped CeO_2 thin film on a single crystal substrate with $d_{substrate} > d_{CeO2}$ as a function of dopant concentration. As dopant concentration increases in CeO2, bulk modulus decreases and misfit dislocation decreases. The change in strain field and dislocation concentration are expected to have significant effects on ionic conductivity at the strained interface.

The presented experimental data is expected to be useful to compliment calculations of the effect of strain on energy barriers to ionic conductivity and advance the integrity of the calculation by providing experimental data on a relevant intermediate temperature SOFC electrolyte material. A computational simulation work on the strain effect by De Souza et al[82] uses the undoped-CeO_2 high pressure diamond anivl cell data of Duculos et al[171] to verify the computed lattice volume, V_{latt}, of CeO_2 with pressure. The P-V data of $Sm_{0.2}Ce_{0.8}O_{1.9}$ presented in this work will benefit further strain-effect computations by providing the P-V curve of the doped material, which is importantly shown to have different elastic properties from undoped-CeO_2. Also, the structural stability of $Sm_{0.2}Ce_{0.8}O_{1.9}$ has been experimentally verified up to 20 GPa. The experimental confirmation of reduced bulk modulus in heavily doped-CeO_2 provides new information about the interdependence of dopant concentration in doped CeO_2, misfit dislocation formation and the strain effect on ionic conductivity.

5.5 Conclusion

In this study, the effect of pressure on structure and transport properties of SDC20 and LLZTaO has been studied. In LLZTaO, a fast Li^+ conductor, no structural transitions were observed up to 35GPa. The isothermal bulk modulus of LLZTaO, K_T=58 GPa, was found by 4th order Birch-Murnaghan equation of state. A linear increase in resistance of the sample with compressive strain was measured, with no exception to the predicted pressure-resistance relationship in the material. As stated, the properties of LLZTaO under dilatative strain cannot be measured due to processing limitations of LLZTaO thin films. In order to extrapolate our results to the dilatative strain region, the P-R curve was extended to negative pressure with a linear fit. If the P-R relationship remains linear in the dilatative strain region, we expect no more than one order of magnitude increase in electrical properties at >7% strain. However, new mechanisms could drastically effect the electrical properties under dilatative strain and experimental work is necessary once LLZTaO films can be reliably fabricated.

The high pressure structure and bulk modulus of heavily doped $Sm_{0.2}Ce_{0.8}O_{1.9}$ (SDC) was studied by the diamond anvil technique and high pressure synchrotron XRD. Highly defected SDC20 does not show structural phase transitions up to 20GPa and the relative d-spacing for SDC20 with both silicon oil and no PTM with respect to pressure are consistent with previous literature reports.[168]

The bulk modulus of the highly defected SDC20 structure is less than the bulk modulus for pure CeO_2, which is consistent with “softening” of the structure due to oxygen vacancy defect concentration. The decrease in bulk modulus of SDC20 due to cation doping is expected to alter the volume elastic energy of thin film SDC20 and allow

the film to accommodate more strain before misfit dislocation generation occurs. Currently, the maximization of strain but prevention of dislocation formation is expected to provide the largest enhancement in ionic conductivity in strained ionic conductors. This result indicates that the optimum dopant concentration for fast ionic conductivity in bulk doped-CeO_2 will not necessarily be the same optimum concentration for strained thin film doped-CeO_2. This experimental work is a foundation for guiding dopant concentration optimization for maximum ionic conductivity in strained SDC20.

Conclusion

Solid-state electrolytes are critical components of solid-state energy conversion devices. Development of fast ion conductors for high performance devices is necessary to speed commercialization of these promising technologies. In this work, the effects at interfaces of solid-state ionic conductors on transport properties have been investigated and a number of conclusions have been drawn from three sets of experiments.

Importantly, the space-charge effect has not been recognized as a mechanism for altering transport properties in the materials studied in this work. All solid-state electrolytes used in solid oxide fuel cells and solid state batteries are heavily doped to create high concentrations of mobile defect charge carriers. The length of the space charge region at heterogeneous interfaces is dependent on charge carrier concentration. In heavily doped electrolytes the space charge region is expected to be extremely small (<1nm) and is not expected to greatly effect transport properties. The lack of space charge effects in this wide-ranging work is due to the selection of heavily-doped materials that were chosen for the studies, due to their practical application in energy devices.

Electrical properties of SDC20 bulk, thin film and nanocrystalline samples were characterized by impedance spectroscopy and concentration cell measurements. Electrical properties of nanocrystalline SDC20 samples were significantly higher than the properties of microcrystalline samples and the grain boundary resistance drop of the nanocrystalline sample was more significant than the grain bulk resistance change. Thin film SDC20 samples with varying interface to bulk volume ratio were fabricated by PLD

and no change in electrical properties due to interface dominated volume were measured. The mechanism for enhancement in the SDC20 nanocrystalline sample was determined to be the curvature effect on oxygen vacancy concentration at grain boundaries. Oxygen vacancy formation at the interface is more favorable than in the bulk and diffusion of oxygen vacancies to grain boundaries in nanoparticles with large curvature greatly reduces the grain boundary resistance of the nanocrystalline material and increases the total conductivity.

The BZY15/SDC20 interface was explored to determine if interfacial effects between the two important SOFC electrolyte materials would be beneficial for ionic conductivity. It has been concluded from the experimental work in this dissertation that the BZY15/SDC20 interface, as fabricated in the heterostructured samples, enhances ionic conductivity dramatically. Detailed HAADF STEM analysis shows that the crystalline SDC20 regions of the heterostructure sample are under significant strain due to the surrounding BZY15 phase. Although the exact strain in the SDC20 phase cannot be calculated from the data, the lattice mismatch of the BZY15 (011) and SDC20 (200) planes of ~8% ensures that significant strain is present in the nanocrystalline SDC20 regions of the heterostructure samples. It is concluded that the increase of more than one order of magnitude in electrical properties of the BZY15/SDC20 heterostructure is due to large dilatative strain in the SDC20 phase and high mobility of oxygen vacancies at the BZY15/SDC20 interface. DFT calculations and MD simulations of the oxygen anion diffusion coefficient in the SDC20 phase at the heavily strained BZY15/SDC20 interface conclude that the diffusion coefficient is enhanced by three orders of magnitude and so support the findings in this work.

High pressure structural and electrical measurements of LLZTaO and SDC20 have been carried out by the diamond anvil cell technique at the Advanced Photon Source at Argonne National Lab. Micro-XRD measurements of each ionic conductor reveal no structural phase transitions up to ~20 GPa. Electrical measurements of the Li^+ conductor, LLZTaO, up to 35GPa and >8% volumetric strain confirm reduced electrical conductivity in the material due to the strain effect of up to 1 order of magnitude. As expected, in the absence of crystal structure transitions or defect formation, pure compressive strain squeezes mass transport pathways and reduces charge carrier transport. The bulk modulus of both LLZTaO and SDC20 was calculated from the P-V data refined from the XRD patterns. In SDC20, the bulk modulus was measured to be ~180GPa, significantly lower than the bulk modulus of un-doped CeO_2 (~220 GPa). It is concluded that the bulk modulus of SDC20 is reduced due to oxygen vacancy formation in SDC20 by Sm^{3+} doping. The elastic properties of thin films are related to the strain effect by the elastic strain formation at heterogeneous interfaces. It is concluded that the doping concentration of doped-CeO_2 will dramatically change the strain effect on ionic conductivity in the material.

The experimental and computational work in this dissertation builds on the previous knowledge of interfacial effects on ionic conductivity in solid-state electrolytes. New interfacial effects have been identified and mechanisms for the experimentally-verified effects have been proposed. Strategic application of these and other interfacial effects on ionic conductivity will greatly enhance the performance of solid-state energy conversion and storage devices and speed the wide-spread adoption of these important technologies.

Recommendations

The work of this thesis has uncovered new interfacial effects on ionic conductivity in solid state electrolytes. There are a number of new and exciting possibilities for future research in this direction.

In general, harnessing interfacial effects in solid-state electrolytes offers new degrees of control in the development of fast ion conductors. The concentration and mobility of ionic and electronic charge carriers can be modified based on charged interfaces, strained interfaces or curved interfaces. As the understanding of interfacial effects on charge carriers deepens, applications of the effects will abound. For example, in the promising SDC20 SOFC electrolyte studied in this work, partial electronic conductivity of the electrolyte reduces the voltage efficiency of the cell. Although unsuccessfully attempted in this work in Section 3.5.4, electronic defect trapping interfaces could be introduced into the electrolyte and dramatically decrease electronic conductivity at SOFC operating conditions. The successfully applied electron trapping defects in SDC20 would improve SDC electrolyte SOFC performance by 20%. The same technique could be applied in other mixed conductors with large ionic conductivity but extremely large electronic conductivity.

New techniques for fabrication of dense, nanocrystalline functional ceramics should be vigorously pursued to prevent grain growth and enable nanostructured SDC20 electrolyte fabrication, which has been shown to enhance electrolyte conductivity by one order of magnitude. This work is expected to yield valuable results due to interfacial effects on charge transport. Suppression of grain growth at sintering temperatures is

difficult but the multi-step sintering technique used in this work showed significant improvement from traditional sintering. Other scalable sintering methods, such as microwave sintering, should be pursued to reduce the SDC20 grain size further and test the electrical properties of nanocrystalline samples. Exploration of sintering additives and the effect on sintering temperatures as well as on interfacial effects is also a direction that could yield profitable results.

The discovery of fast ion transport in thin SDC20 layers in the BZY15/SDC20 heterostructure samples is a significant achievement of this dissertation. Optimization of the heterostructure architecture to maximize transport properties is an apparent next step of the work. Other solid-state electrolytes, such as doped-Bi_2O_3, are promising candidates to be tested in the heterostructure configuration. Discovery of scalable techniques for fabrication of heterostructure electrolytes in solid-state devices is a critical need for translation of this work. Vertically-aligned heterostructure fabrication by PLD, attempted in this work, is a first step in that direction. Scalable fabrication techniques to implement interfacial effects in devices will require nano-scale control, which is lacking in large-scale ceramics manufacturing today. In order to take advantage of the interesting effects explored in this work, scalable fabrication techniques must be developed.

Exploration of strain effects on ionic conductivity by high pressure techniques put forward in this work represents a new strategy for studying the strain effect in solid-state electrolytes. In order to collect more reliable high pressure electrical data, the Paris-Edinburough type cell at ANL APS HPCAT 16-BM-D should be used. In the P-E cell the sample characteristic length is approximately 3mm, and significantly larger than the sample size of the DAC cell. The current collection probes in the P-E cell can be

configured to increase electrode area, reduce electrode spacing and reduce total sample resistance. Additionally, the P-E cell at 16-BM-D is equipped to measure at high pressure and temperature which is valuable for the oxygen and proton conducting electrolytes that were not able to be measured at high pressure and ambient temperature with the DAC cell. High pressure transference number measurements of oxygen anion conductors is expected to show a transition to proton conduction at high pressure and would be an interesting scientific pursuit.

The work outlined in this dissertation provides a strong foundation for future application of interfacial effects on ionic conductivity in solid-state ionic conductors. All future work that seeks to apply interfacial effects to devices will be a profitable endeavor and should be vigorously pursued to advance the development of high performance solid-state energy conversion and storage devices.

Appendix A: Technoeconomic analysis of low-temperature, internal reforming solid oxide fuel cell system

A.1 Introduction

Distributed and low carbon energy conversion devices are desired for energy scenarios that demand uninterruptable power, are particularly vulnerable during grid disruptions or where the provided energy is associated with a significantly unfavorable carbon ratio. Although the US electrical grid has been an economical solution for providing power to residential, commercial and industrial users, the current power grid has several disadvantages.[172]

- The grid has significant transmission and distribution losses.
- The total carbon emissions per kWh generated for grid power is large and contributes to human influenced climate change.
- The grid is vulnerable to inclement weather especially hurricanes, floods and tornadoes.
- The grid is increasingly susceptible to direct terrorist or cyberterrorist attacks.

A distributed generation model is beneficial for a variety of applications, especially where the disadvantages of the current grid are exaggerated.

Reciprocating engine generators (Natural Gas, Diesel) are currently employed as the state of the art emergency generation technology where uninterruptable power is necessary. Reciprocating engine generators (REGs) are reliable and have low initial capital cost (~$0.25/W) however they are not useful for baseload power supply (~ 10,000 hour lifetime) and have a large carbon to kWh ratio due to their low efficiency (~0.25). In this study the emergency power generation strategy at a large campus in the Southeast US was studied to determine the economic viability of replacing the REGs with intermediate

temperature fuel cells (ITFC). The use of ITFCs fueled by natural gas would reduce total O&M for emergency power generation, reduce carbon emissions from emergency power generation by 50%, decrease total cost of emergency power generation, and provide constant baseload electricity.

Solid Oxide Fuel cells (SOFCs) have been developed for alternative energy conversion of hydrocarbon fuels (primarily methane) to electricity with high energy efficiency and low carbon emissions. The SOFC's all-solid-state construction affords the system long operation lifetimes and low operation and maintenance (O&M) costs. High operation temperatures (~800^{o}C) of traditional SOFCs which were developed in the past 30 years based on Yttria-stabilized Zirconia (YSZ) electrolytes demand high associated capital costs to ensure high temperature stability of SOFC sealing components, interconnect materials and balance of plant (BOP) components. A new class of Intermediate Temperature Fuel Cells (ITFCs) composed of fast ion conducting solid-state electrolytes and all-solid-state components with high performance at 500^{o}C are being developed. Solid-state electrolytes with large ionic conductivity at low temperatures due to interfacial effects on charge carriers, presented in this dissertation, are under development to reduce resistance to mass transport below 500^{o}C. Technologies that enable fast fuel cell reactions at SOFC electrodes at low temperatures are also being developed. These technologies will be implemented to reach >200mW/cm^{2} power density at ≤500^{o}C while using natural gas as fuel.

The first part of this study looks at the effect of internal reforming and 500^{o}C operation temperature on ITFC capital cost using the 2012 Strategic Analysis report[173] "Manufacturing Cost Analysis of Stationary Fuel Cell Systems" as a baseline. A cost

analysis based on replacing the external reforming system with an internal reforming catalyst is conducted. Analysis of intermediate temperature cost savings are realized in three ways. Costs associated with the interconnect, sealing, and cathode connect materials are reduced due to the implementation of intermediate temperature material alternatives. The total capital cost is reduced by the cost of fuel cell and fuel processing balance of plant (BOP) components which are designed for the intermediate temperature range. Also, intermediate temperature operation is expected to extend the lifetime of the ITFC system and decrease fuel cell degradation rate. The effects of intermediate temperature operation are summarized in Table A-1.

Table A - 1 Fuel Cell System Cost and Lifetime savings from baseline values due to 500^{o}C target operating temperature

Component	Low Temperature Effect
Seals, Interconnects, Cathode Connect Materials	Replacement with low cost alternatives
Fuel Cell and Fuel Processing BOP BOM	Reduction of cost of parts near hot zone (replacement of ceramic parts with metal parts)
Degradation Rate	Reduction

In the second part of this study, the reduced ITFC capital cost is used in a combined ITFC/Grid emergency power generation model to calculate the economic viability and payback periods associated with a variety of model parameters.

A.2 Fuel cell capital cost analysis

The 2012 report[173] by Strategic Analysis considers the cost of Solid Oxide Fuel Cell (SOFC) systems ranging in size (1, 5, 25, 100kW) and manufacturing rate (100, 1000,

10,000, 50,000 systems/year). The fuel cell specifications for the Strategic Analysis cost analysis are listed in Table A-2.

Table A - 2 Summary of Strategic Analysis SOFC System configurations and operating conditions

Fuel Cell System Parameter/Cost Inputs	SA Fuel Cell System Configuration Characteristics
Fuel	Natural Gas
Oxidant	Ambient Air
Operation Temperature	819^{o}C
Fuel Processing	External Reforming system
CHP capability	Heat exchangers included
Inlet fuel pressure	1.4 atm
Power Electronics	Controls, inverters, sensors for full system operation
Electricity	110VAC
Start-up	Grid-reliant start-up; no batteries
Housing	Suitable for outdoor installation
Un-enumerated cost margin	10%
Degradation	20%/10 year
Net electrical System Eff.	49% HHV, 55% LHV
Installation Cost	Not included
Sales Margin	not included

In order to reduce the operating temperature and capital cost of the fuel cell system the technologies under development at Georgia Tech have been applied to modify the Strategic Analysis cost calculations. The Georgia Tech fuel cell system parameters are listed in Table A-3 and the changes to the baseline system are highlighted.

Table A - 3 Summary of Georgia Tech ITFC System configurations and operating conditions

Fuel Cell System Parameter/Cost Inputs	SA Fuel Cell System Configuration Characteristics
Fuel	Natural Gas + CO_2
Oxidant	Ambient Air
Operation Temperature	500°C
Fuel Processing	Internal Reforming system, $Ni_{0.05}Ru_{0.05}Ce_{0.9}O_2$ Catalyst
CHP capability	Heat exchangers included
Inlet fuel pressure	1.4 atm
Power Electronics	Controls, inverters, sensors for full system operation
Electricity	110VAC
Start-up	Grid-reliant start-up; no batteries
Housing	Suitable for outdoor installation
Un-enumerated cost margin	10%
Degradation	10%/10 year
Net electrical System Eff.	49% HHV, 55% LHV
Installation Cost	Not included
Sales Margin	not included

The Georgia Tech ITFC system diagram is shown in Figure A-1. The external reforming BOP components have been removed and inlet CO_2 has been added for internal reforming with $Ni_{0.05}Ru_{0.05}Ce_{0.9}O_2$ catalyst. The system is configured for combined heat and power (CHP) operation for building space heating and service water. Unspent fuel will be sent to the burner for heat generation. The water handling system has been removed from the baseline system due to the high coking tolerant Ni-$BaZr_{0.7}Ce_{0.1}Y_{0.1}Yb_{0.1}$ anode and sufficient oxygen anion conductivity to provide anode side water for carbon removal.

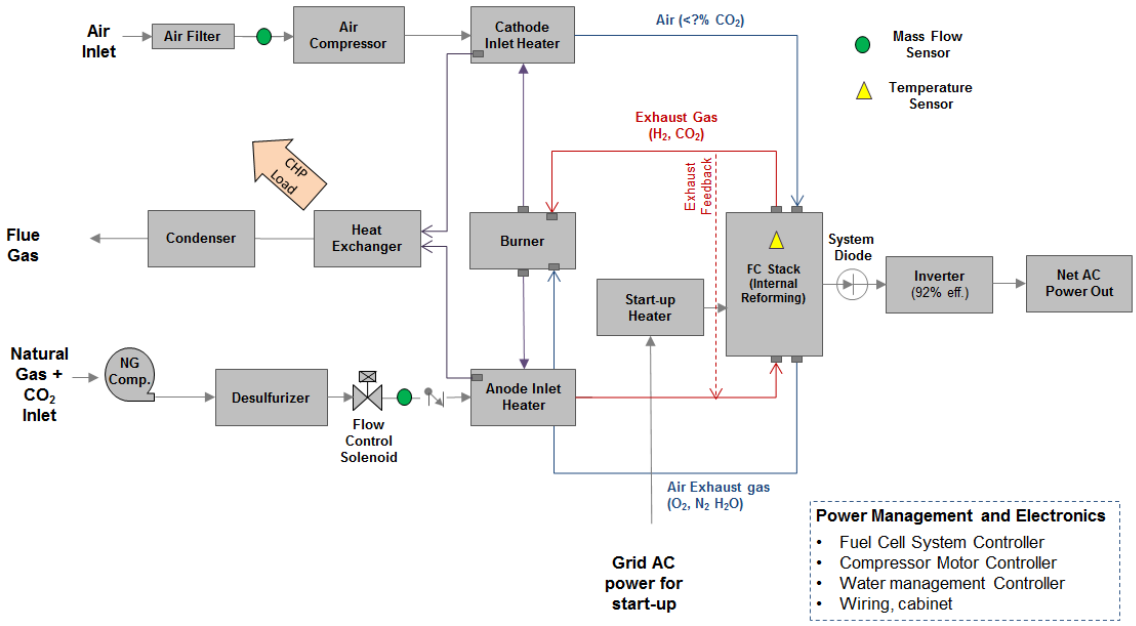

Figure A - 1 Summary of Georgia Tech ITFC System configurations and operating conditions

A.2.1 Internal reforming catalyst technology development

In order to reform methane in the fuel cell stack at intermediate temperature a catalyst other than Ni is necessary. In this work we are developing a $Ni_{0.05}Ru_{0.05}Ce_{0.9}O_2$ intermediate temperature methane reforming catalyst which has high conversion rates and selectivity of H_2 as seen in Figure A-2. By adding this catalyst to the ITFC anode, reforming can be accomplished in the fuel cell stack, at 500°C without the use of an external reforming reactor.

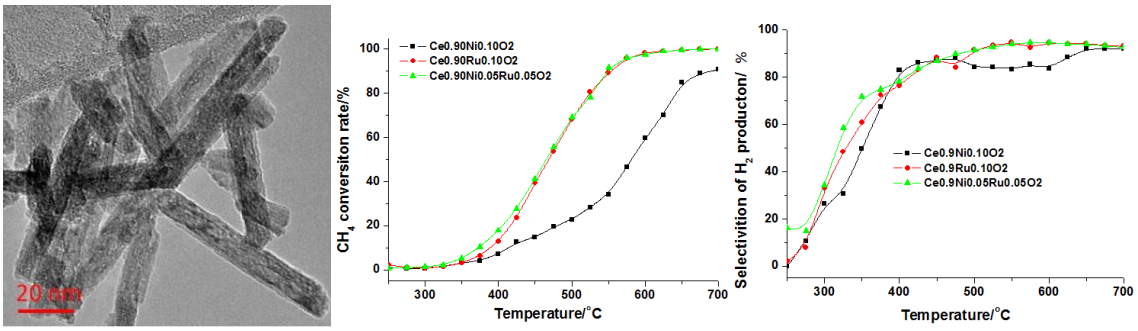

Figure A - 2 (Left) TEM image of Ni0.05Ru0.05Ce0.9O2 methane reforming catalyst; (Middle) Fraction of methane converted by reforming catalyst from 300oC to 700oC by

three ceria based catalysts; (Right) Selectivity for H2 production as a function of temperature for three ceria based catalysts

A.2.2 Internal reforming cost analysis

The $Ni_{0.05}Ru_{0.05}Ce_{0.9}O_2$ internal reforming catalyst loading is assumed to be 0.005 g/cm^2. Market price for Ru metal is \$1.76/g, Ni metal is \$0.012/g, and CeO_2 (99.5% purity) powder is \$0.025/g. The total cost of $Ni_{0.05}Ru_{0.05}Ce_{0.9}O_2$ catalyst per cm^2 is \$0.00031/cm^2. The power density of 281mW/cm^2 is used to determine total superficial anode surface area in each size specific fuel cell system and the area is over-sized by 10% for lifetime degradation. A spray coating and firing step is added to the fabrication process flow and the manufacturing cost is adjusted.

Figure A-3 shows the total system cost breakdown for the external reforming SA baseline and the internal reforming GT fuel cell. The costs for the reforming system and the reforming catalyst are marked on the charts for a relative comparison between fuel cell system sizes and production rates. It can be seen that the system costs for both cases are largely dependent on system size and manufacturing rate. Interestingly, the internal reforming modifications are cost effective only for the 1kW and 5kW systems. The total cost of the 25kW and 100kW systems with internal reforming are higher than the baseline external reforming systems. The specific cost for the catalyst coating and annealing steps may differ slightly from the costs used in the analysis dependent on final application method which may slightly influence the cost. However, the general trend of cost savings by internal reforming for small systems (≤5kW) and cost additions for large systems (≥25kW) is important for the design of low cost fuel cell systems. Of the additional cost due to internal reforming catalyst ~40% is due to added manufacturing steps and ~60% is

due to catalyst cost. Strategies to reduce catalyst loading will be explored to reduce the internal reforming system cost.

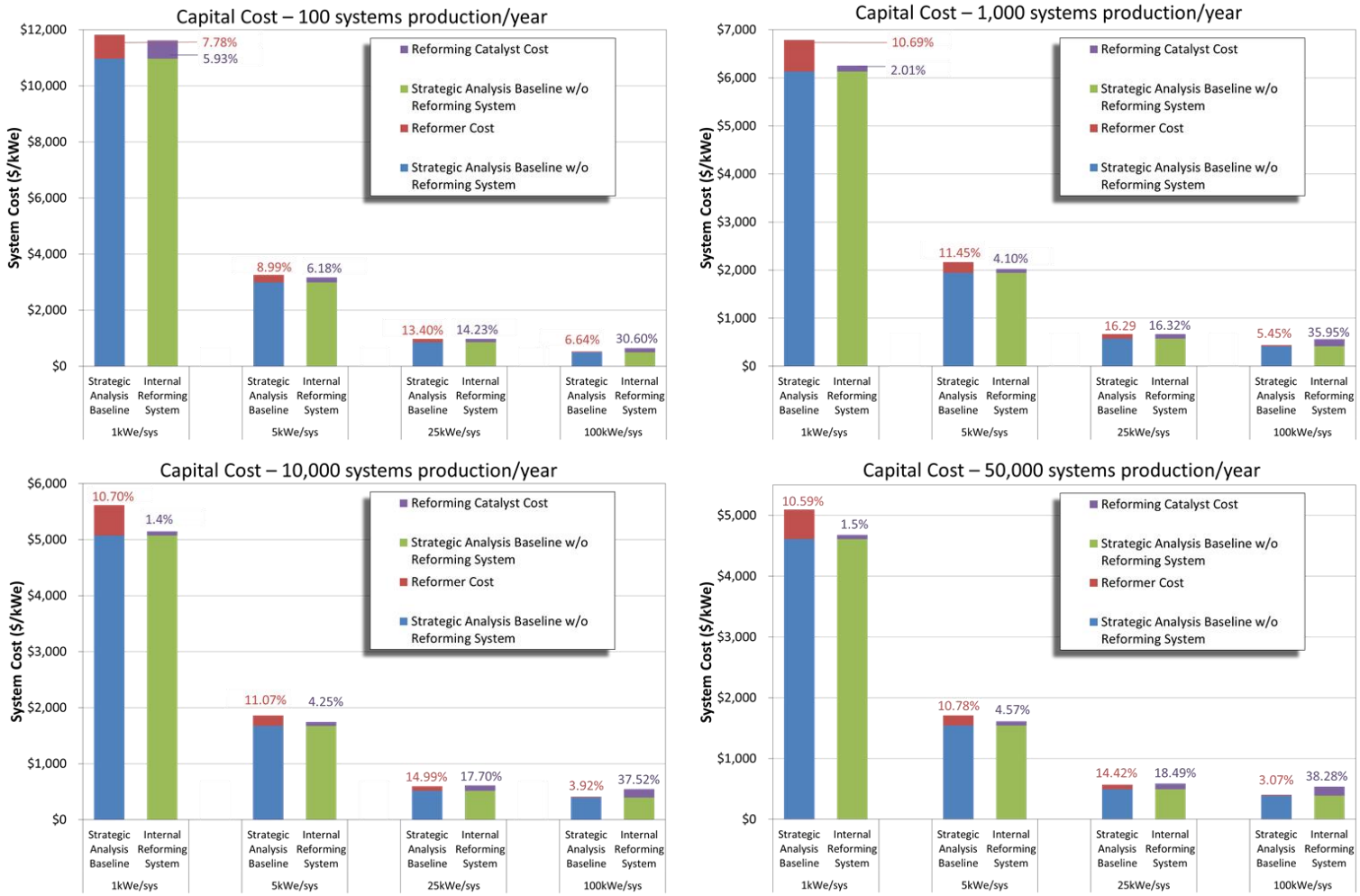

Figure A – 3 Total system cost comparison between Strategic Analysis cost baseline (blue) and Georgia Tech fuel cell system with internal reforming modifications (red)

The percentage changes in cost with and without internal reforming are listed in Table A-4. The baseline numbers used for the analysis are taken directly from the Strategic Analysis report.

Table A - 4 Cost Comparison of baseline strategic analysis system to internal reforming system with percentage changes in cost listed.

	Annual Production Rate	systems/year	100				1000			
	System Net Electric Power (Output)	kWnet	1	5	25	100	1	5	25	100
Strategic Analysis Cost	Total System	$/kWe	$11,827	$3,263	$981	$531	$6,786	$2,166	$671	$439
Internal Reforming Cost	Total System	$/kWe	$11,625	$3,179	$988	$650	$6,254	$2,023	$671	$566
Internal Reforming Cost Decrease Percentage			1.71%	2.58%	-0.73%	-22.47%	7.84%	6.59%	-0.03%	-28.93%
	Annual Production Rate	systems/year	10000				50000			
	System Net Electric Power (Output)	kWnet	1	5	25	100	1	5	25	100
Strategic Analysis Cost	Total System	$/kWe	$5,618	$1,863	$599	$414	$5,097	$1,708	$569	$402
Internal Reforming Cost	Total System	$/kWe	$5,147	$1,749	$613	$547	$4,678	$1,613	$590	$539
Internal Reforming Cost Decrease Percentage			8.40%	6.14%	-2.36%	-32.34%	8.22%	5.60%	-3.56%	-34.17%

An important metric that must be considered when switching from external reforming to internal reforming is fuel utilization. If the fuel utilization rate decreases when internal reforming catalyst is used, the total efficiency of the fuel cell will decrease and affect the capital cost and operation costs of the fuel cell system. In this study we assumed that the fuel utilization would remain constant when switching from external to internal reforming. Figure A-4 is an analysis of operation voltage v. power density (left) and operation voltage v. 100kW stack cost (right) for a fuel cell tested in our lab at 500^{o}C. Stack cost of \$0.136/cm^{2} is assumed from the system cost targets of the program and the SA report which states ~65% of system cost is from stack cost for 100kW system. The change in stack capital cost with voltage reflects the change in fuel cell area necessary to maintain 100kW at a given power density.

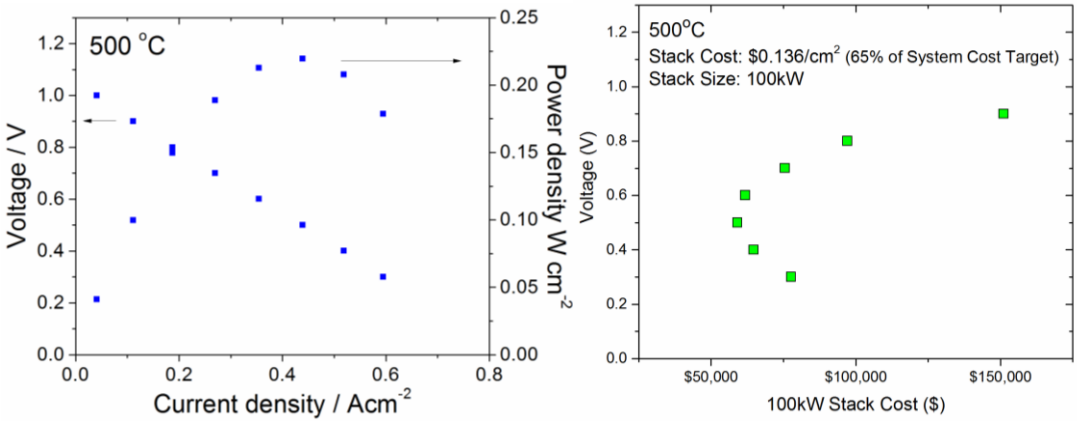

Figure A - 4 (left) I-V and I-P curve for Ni-SDC/Ni-BZCYYb (functional layer)/SDC electrolyte /LSCF commercial cathode at 500°C; (right) Stack cost v. Operation voltage for 500°C cell

The change in OPEX due to a decrease or increase in fuel utilization is modeled later in this report. As total efficiency of the cell (including fuel utilization) changes the payback period for each fuel cell system changes accordingly.

A.2.3 Intermediate temperature fuel cell technology development

In order to lower the SOFC operation temperature to the ITFC operation temperature of 500°C, new technologies are under development at Georgia Tech. At low temperature all fuel cell reactions become more sluggish, demanding new materials and component architectures to maintain high fuel cell performance.

Hollow nanofiber cathode

In order to enhance oxygen reduction reaction at the ITFC cathode at 500°C, a nanostructured hollow nanofiber cathode is being studied. SEM images of the nanofibers are shown in Figure A-5. The large surface area of the nanofiber cathode provides increased reaction sites for cathode reactions and the interconnectivity of the cathode fibers provides short conduction pathways to reduce polarization of the cathode. Intermediate operation temperature is ideal for this cathode architecture because it

prevents significant grain growth and enables long term stability. To further increase the rate of cathode reactions, catalyst nanoparticles will be infiltrated into the nanofiber cathode.

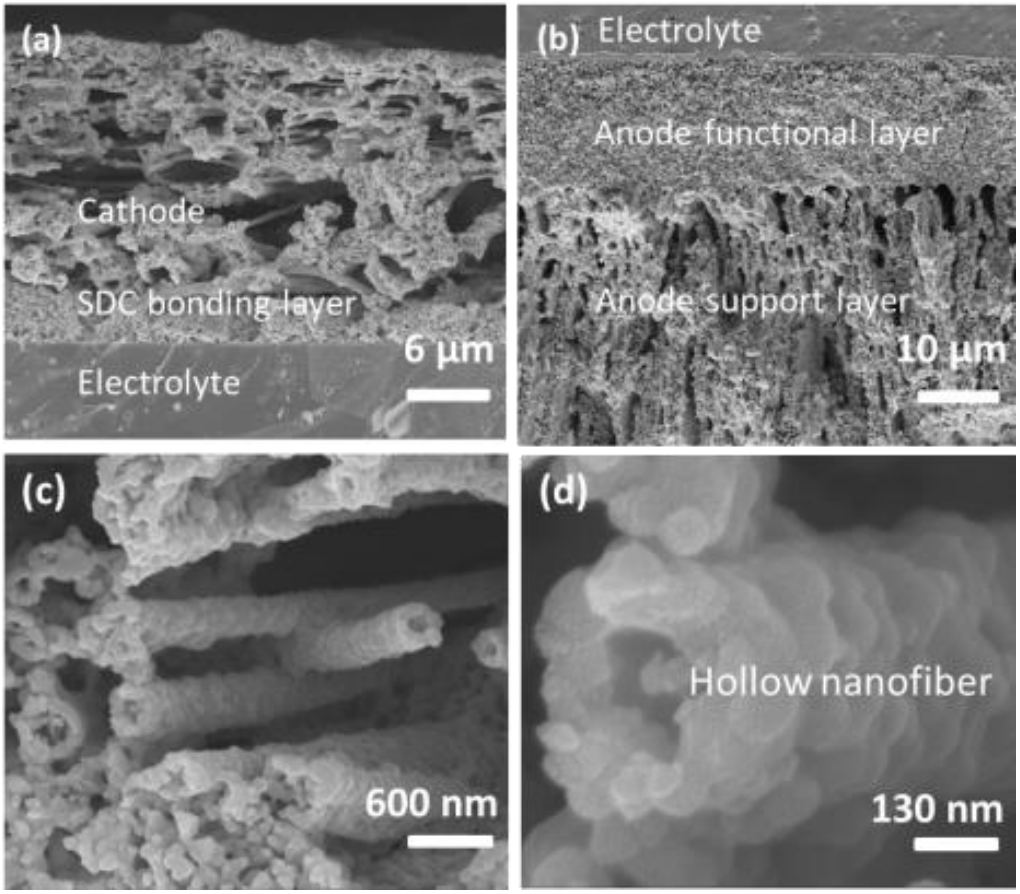

Figure A - 5 Cross-sectional images of a cell after being tested at 550 oC for ~260 h: (a) the cathode, the SDC bonding layer, and the SDC electrolyte showing good adhesion of the cathode to the electrolyte layer; (b) the anode-electrolyte interface showing the straight and open pores/channels for fast mass transfer; (c) a closer view of the cathode consisting of intact hollow fibers; and (d) an individual hollow fibers seen in (c).

Multifunctional Anode

In order to handle methane reforming, reduce concentration polarization, and improve fuel utilization at 500^{o}C, a multifunctional anode has been developed. The multifunctional has three zones for internal methane reforming, the water-gas shift reaction, and fuel oxidation, as seen in Figure A-6. The $Ni_{0.05}Ru_{0.05}Ce_{0.9}O_2$ anode catalyst

is active for methane reforming at 500°C. The oriented microstructure of the multifunctional anode eases the flow of fuel to the fuel oxidation reaction sites close to the electrolyte and facilitates the water-gas shift reaction. The active anode layer contains increased numbers of triple phase boundary sites for fuel oxidation to enhance anode fuel cell reaction rates.

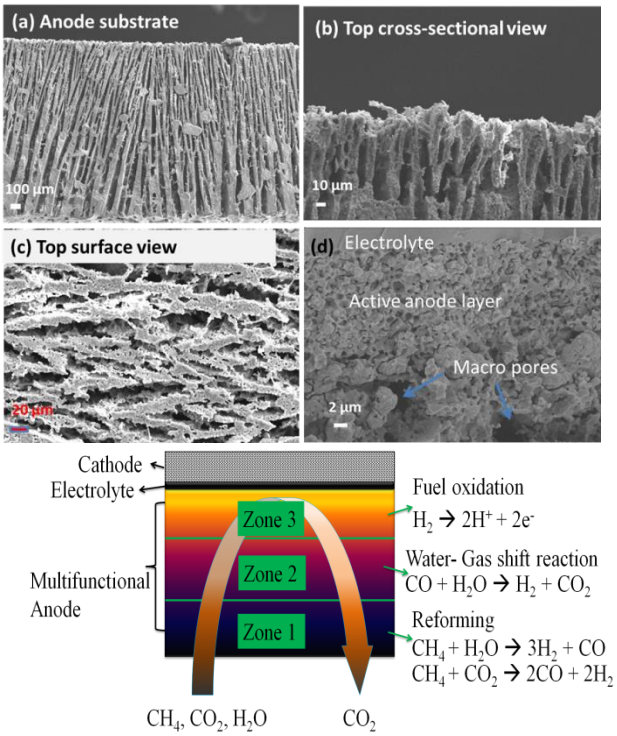

Figure A - 6 (Left) SEM images of zone 2 of the multifunctional anode (a-c) with oriented microstructure and of zone 3 containing the anode active layer(d); (Right) Schematic of multifunctional anode with 3 zones

Nanostructured and composite O^{2-}/H^{+} conducting solid state electrolyte

Resistance to charge flow in the ITFC solid state electrolyte at low temperatures is a large contributor to low current density and low power density at 500°C operation temperature. In order to improve ionic conductivity in the electrolyte material, we are developing technology that uses interfacial effects in nanostructured materials and at heterogeneous interfaces to dramatically enhance solid state transport. Schematics of the

electrolytes under development are shown in Figure A-7. The composite electrolyte also enhances fuel efficiency due to partial proton conductivity and water formation at the cathode. The oxygen anion conducting component of the electrolyte provides sufficient oxygen at the anode to prevent carbon coking.

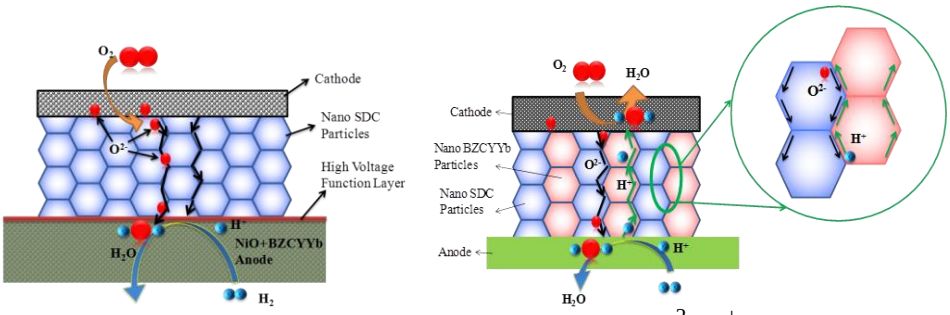

Figure A - 7 Schematic of nanostructured composite O^{2-}/H^{+} conducting solid state electrolyte under development at Georgia Tech

A.2.4 Intermediate temperature fuel cell cost analysis (500°C w/ external reforming)

In order to calculate the effect of ITFC operation temperature of 500°C on total system cost, the cost of several components of the ITFC were reduced systematically from the Strategic Analysis baseline. The cost reductions are summarized in Table A-5.

Table A - 5 Summary of adjustments made to Strategic Analysis baseline to account for temperature reduction from 819°C to 500°C

Component	Savings from baseline value due to reduced operation temperature
Seals, Interconnects, Cathode Connect Materials	75% reduction
Fuel Cell and Fuel Processing BOP BOM	20% reduction
Degradation Rate	8% reduction

Although our technical developments do not address all materials in the fuel cell stack, intermediate temperature operation makes possible the use of inexpensive

alternatives for the seals, interconnects, and cathode connect materials used in the fuel cell system. To account for this, the cost attributed to these components was reduced by 75%. Similarly, BOP materials located outside of the fuel cell stack but near the hot zone can be replaced with less expensive components when the stack temperature is reduced to 500^{o}C. In the intermediate temperature cost analysis, the cost of all fuel cell and fuel processing BOP materials are reduced by 20%. The expected lifetime of the ITFC is longer than the 819^{o}C SOFC so the degradation rate of the ITFC was decreased by 8%. Total cost comparison between the high temperature and intermediate temperatures are listed in Table A-6 and graphed in Figure A-8.

Table A - 6 Tabular cost comparison and cost savings (%) between Strategic Analysis baseline SOFC (819^{o}C) and Georgia Tech ITFC (500^{o}C) as a function of system size (kW) and manufacturing rate

	Annual Production Rate	systems/year	100				1000			
	System Net Electric Power (Output)	kWnet	1	5	25	100	1	5	25	100
Strategic Analysis Baseline SOFC Cost	Total System	$/kWe	11827.49	3263.183	981.321	531.014	6786.153	2166.131	670.571	439.032
ITFC (<500oC) Cost	Total System	$/kWe	10176.38	2816.808	795.1218	410.5305	6171.151	1918.89	550.3216	335.41
ITFC Cost Savings (%)			13.96%	13.68%	18.97%	22.69%	9.06%	11.41%	17.93%	23.60%

	Annual Production Rate	systems/year	10000				50000			
	System Net Electric Power (Output)	kWnet	1	5	25	100	1	5	25	100
Strategic Analysis Baseline SOFC Cost	Total System	$/kWe	5618.47	1862.971	598.862	413.611	5097.224	1708.278	569.426	401.951
ITFC (<500oC) Cost	Total System	$/kWe	5134.607	1644.658	486.2622	311.7056	4652.598	1502.434	458.8963	300.899
ITFC Cost Savings (%)			8.61%	11.72%	18.80%	24.64%	8.72%	12.05%	19.41%	25.14%

Figure A-8 shows the total system cost breakdown for the high temperature SA baseline fuel cell (819^{o}C) and the intermediate temperature GT fuel cell (<500^{o}C). The costs specifically associated with the high temperature operation are marked on the SA baseline charts for a relative comparison between fuel cell system sizes and production rates.

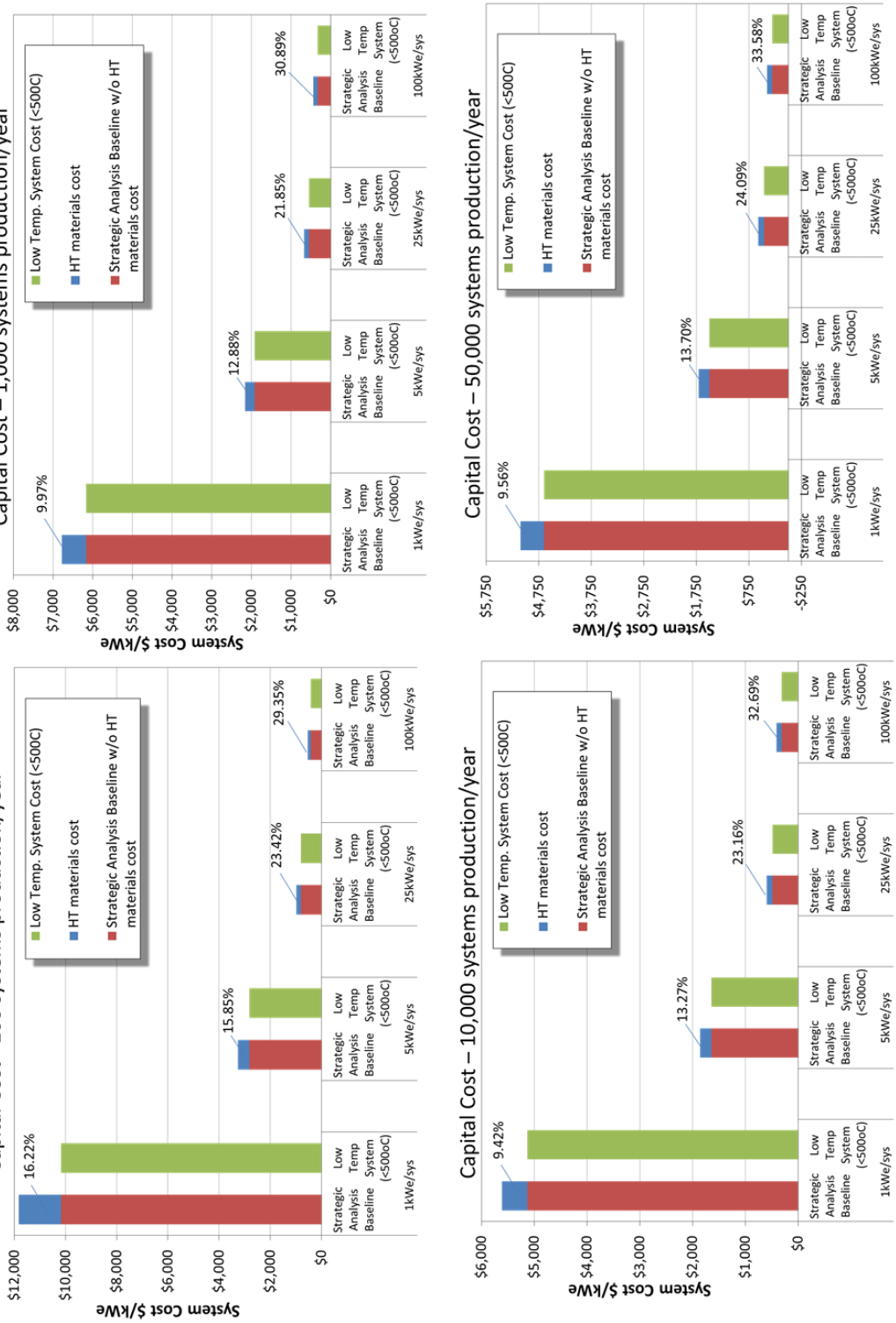

Figure A - 8 Graphical cost comparison and cost savings (%) between Strategic Analysis baseline SOFC (819°C) and Georgia Tech ITFC (500°C) as a function of system size (kW) and manufacturing rate

From the ITFC cost calculations it is apparent that a significant decrease in total cost, up to 33.58%, is realized by reducing the operating temperature from 819^{o}C to 500^{o}C. Importantly, the cost reduction is most significant for the largest system cost calculated (100kW) and it increases as manufacturing rate increases.

A.2.5 Intermediate temperature, internal reforming fuel cell cost analysis

A cost analysis of the combined intermediate temperature and internal reforming fuel cell is shown in Figure A-9 and compared to the Strategic Analysis baseline fuel cell with external reforming and high operation temperature. The largest cost savings are realized in the 1kW and 5kW intermediate temperature fuel cell systems with internal reforming.

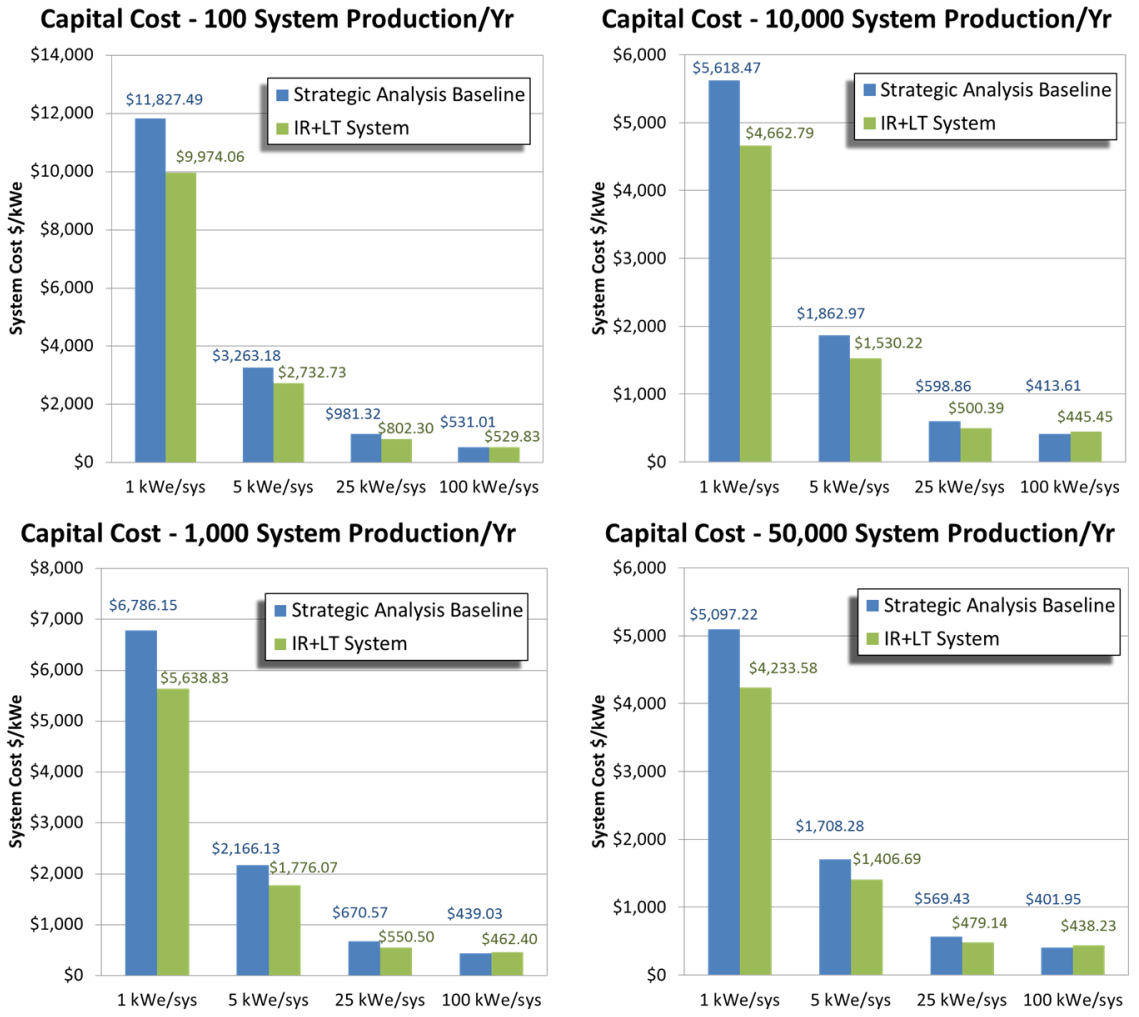

Figure A - 9 System cost comparison between External Reforming Strategic Analysis baseline SOFC (819°C –blue) and Georgia Tech intermediate temperature internal reforming fuel cell (500°C – green) as a function of system size (kW) and manufacturing rate

A.3 Techno-economic analysis for a combined electrical grid/ITFC emergency power generation model

Natural gas REGs are currently used to provide emergency power when grid power is interrupted in a variety of settings. On large campuses, such as universities and hospitals, emergency power is required to provide power for critical instrumentation and equipment as well as auxiliary lighting and ventilation when grid power is interrupted. In the US, distributed generation (DG) units account for over 200GW of capacity, most of which is provided by REGS.[172] REGs have been used for this purpose due to their low

cost however, these generators have low efficiency, short operation lifetimes, and require frequent maintenance. Fuel cells are a distributed stationary power generation technology that is cleaner than REGs with half the carbon to kWh ratio and can provide constant baseload affordable power which is useful for emergency generation during grid outages. Fuel cell systems are high efficiency distributed generation technologies that do not suffer from transmission and distribution losses and are less prone to attacks from direct terrorism, cyber terrorism, or natural disaster. The emergency generation model proposed here is also beneficial for ITFC long term stability because the ITFC is constantly at intermediate temperature and only undergoes thermal cycling for infrequent maintenance. Additionally, the natural gas distribution system is in place for current REG emergency power solutions. Gas pipeline installation costs and gas delivery volume concerns are mitigated by replacing the existing natural gas powered REG with an ITFC.

A.3.1 ITFC/Grid emergency power model

In this techno-economic analysis a model emergency power generation system including an ITFC is proposed to replace existing REG emergency power models. Cost modeling and payback period are calculated as a function of ITFC system capital cost, electricity price, and fuel cell total efficiency. System diagrams of the existing and proposed models are shown in Figure A-10.

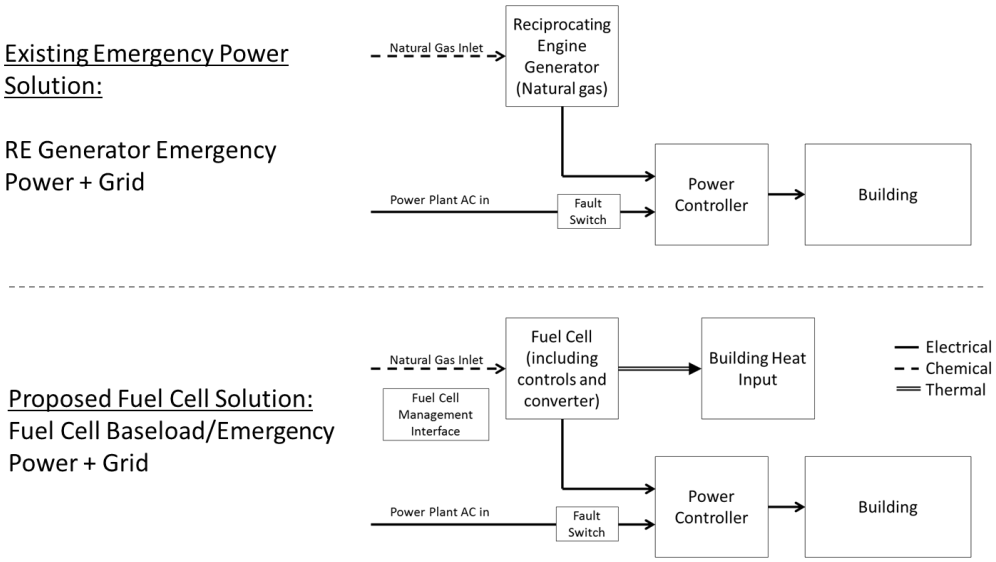

Figure A - 10 System diagrams of an existing emergency power solution including a REG and Grid power (Top) and the proposed ITFC solution which is supported by the grid but provides constant baseload

In the existing emergency power solution (Figure A-10 – Top) electricity for the building is provided by the electrical grid. In the event of a grid outage, the REG turns on and provides a constant load of power until the grid power is restored. When the grid power is restored the REG stops providing power. In this model the REG is powered by natural gas. In the proposed ITFC solution (Figure A-10 – Bottom), the ITFC is on perpetually, providing baseload power and providing emergency power during a grid outage. These operation scenarios are summarized in Figure A-11.

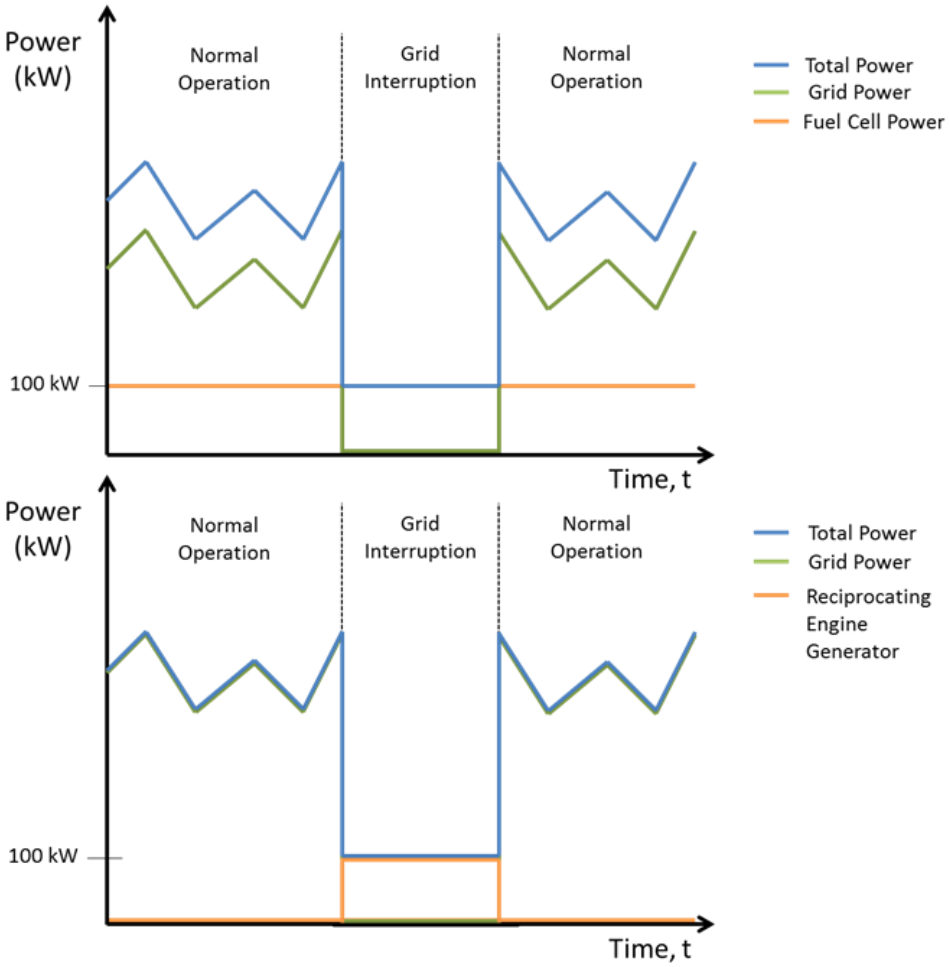

Figure A - 11 Grid outage operation schemes for ITFC/Grid model (Top) and REG/Grid model (Bottom)

The cost analysis was completed for a 3750 day period (~10 years) with grid power interruptions for 24 hours every 150 days. The 3750 day period is represented schematically in Figure A-12.

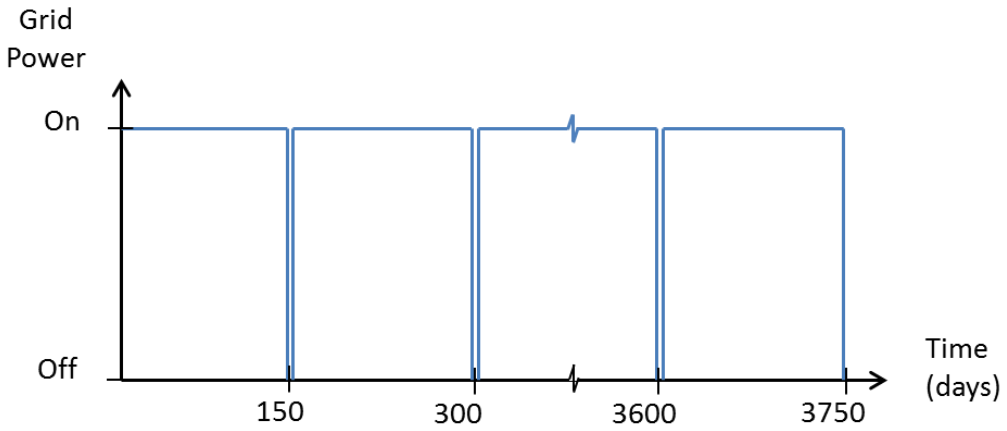

Figure A - 12 Grid outage model for ITFC cost analysis with 24 hour grid power outages in 150 day intervals

Input variables for the techno-economic analysis are listed in Table A-7. Values such as cost of grid electricity are listed with a baseline value but are varied during the modeling of that parameter.

Table A - 7 Techno-economic analysis emergency generation model baseline inputs

TEA emergency generation model inputs (3750 days)	Value	Unit
Cost of Grid Electricity	0.065	$/kWh
Cost of Natural Gas (interruptible)	5.17	$/Mcf
Cost of Natural Gas (uninterruptible)	6.64	$/Mcf
Fuel Cell Electrical Efficiency	0.5	
RE Generator Electrical Efficiency	0.25	
Natural Gas Heat Content	1025000	Btu/Mcf
Fuel Cell Heat Rate (at given efficiency)	6824.28327	Btu/kWh
Cost of Fuel Cell Electricity	0.04420804	$/kWh
Maximum MCFH (thousand cubic feet per hour)	3.328918668	MCFH
RE Generator Heat Rate (at given efficiency)	13648.56654	Btu/kWh
Cost of RE Generator Electricity	0.08841608	$/kWh
Total Power Demand	500	kW
Uninterrupted Power Demand	100	kW
100kW Reciprocating engine generator + installation capital cost	48712.37	$
100kW $7/W fuel cell capital cost + installation capital cost	730000	$
100kW $3/kW FC + installation capital cost	330000	$
100kW $1.5/W Fuel Cell capital cost + installation capital cost	180000	$
O&M Reciprocating engine generator	0.02	$/kWh

Table A – 7 (continued)

O&M Fuel Cell	0.02	$/kWh
# of Fuel Cell stack replacements	1	#/10 years
Thermal Capacity Utilization	0	%

In order to account for current SOFC capital costs ($7/W), the ITFC cost goal ($1.5/W), and for an median ITFC capital cost, 3 fuel cell system capital costs were analyzed; $7/W, $3/W, and $1.5/W. An example of the 3750 day total cost curves for three 100kW ITFC systems with $7/W, $3/W, and $1.5/W capital costs and the REG model system with grid electricity cost of $0.065/kWh is shown in Figure A-13. The payback period is the crossover in total cost of the ITFC/Grid model with the REG/Grid model. In this scenario only the $1.5/W system has a payback period within 10 years. The payback period is marked at ~2600 days. At 2600 days the ITFC/Grid system costs less to operate than the REG/Grid system.

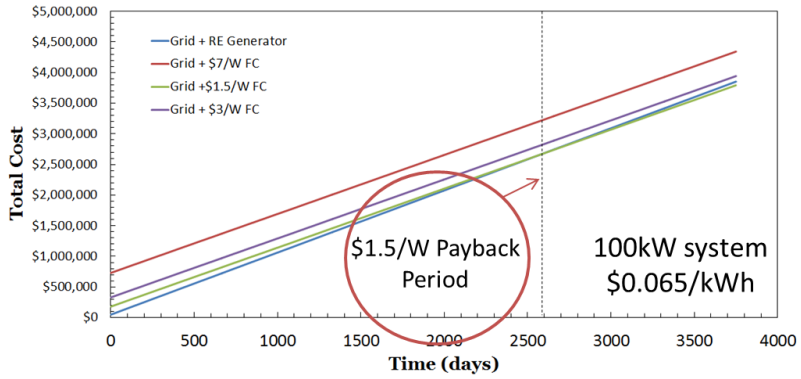

Figure A - 13 3750 day total cost curves for three 100kW ITFC systems with $7/W, $3/W, and $1.5/W capital costs and the REG model system with grid electricity cost of $0.065/kWh

A.3.2 ITFC/Grid Model pre-analysis considerations

Before proceeding with the modeling results two important competing factors should be mentioned that affect the viability of the ITFC/Grid emergency power solution. These are listed below;

- Is the natural gas pricing structure such that the gas supply is interruptible or uninterruptible?
- Is the heat for the building provided by a centralized plant?

During our research for this analysis, the difference in gas pricing for interruptible and uninterruptable was found to be significant and to have a large impact on the cost analysis if the gas supply must be uninterruptible to ensure emergency power continuity. At Georgia Tech the cost of interruptible natural gas is $5.17/mcf and the cost of uninterruptible natural gas is $6.64/mcf. This 20% increase in natural gas cost can have a significant effect on the total cost of the ITFC/Grid system. Additionally, at large campuses such as hospitals and universities, centralized steam plants provide steam to buildings for space heating and water service. In our model we were not able to use the waste heat because of the scale difference between the ITFC and steam plant made it not economically viable.

A.3.3 ITFC/Grid model cost analysis with variable electricity prices

Grid electricity prices fluctuate drastically in the US depending on location. A summary of grid electricity prices by US region, provided by the EIA, is shown in Table A-8. It is understood that the grid electricity cost will factor into both the ITFC/Grid and REG/Grid models and that US Regions with high grid electricity costs will be more attractive for the ITFC/Grid model. Further analysis will show the quantitative effect of grid electricity price on ITFC/Grid model payback period.

Table A - 8 Commercial and residential grid electricity prices by US Region

Table 5.6.A. Average Retail Price of Electricity to Ultimate Customers by End-Use Sector (www.eia.gov)

US Region	Commercial Prices as of March 2015 (cents/kWh)	Residential Prices as of March 2015 (cents/kWh)
New England	16.95	20.83
Middle Atlantic	13.52	15.78
East North Central	9.94	12.35
West North Central	8.62	10.42
South Atlantic	9.66	11.44
East South Central	10.25	10.46
West South Central	8.03	10.72
Mountain	9.47	11.45
Pacific Contiguous	12.32	13.73
Hawaii	28.14	31.2
Alaska	17.57	19.64

The payback period from the 3750 day total cost plots for a range of electricity prices have been collected and graphed in Figure A-14. A rapid decline in the payback period can be seen for all ITFC systems with increasing electricity cost. The five year mark indicates that the current SOFC technology ($7/W) will have a payback period of 5 years in this model scenario when the cost of electricity is ~$0.20/kWh. Alternatively, the target ITFC system ($1.5/W) will have a 5 year payback period at grid electricity costs of ~$0.08/kWh. The grid electricity price of $0.065/kWh at Georgia Tech, which is located in the Southeast US, makes fuel cell capital costs, even at the target ITFC cost of $1.5/W, prohibitive for ITFC economic viability in this model. However, in US Regions such as the Northeast the high electricity cost will significantly enhance the viability of the ITFC/Grid emergency power model.

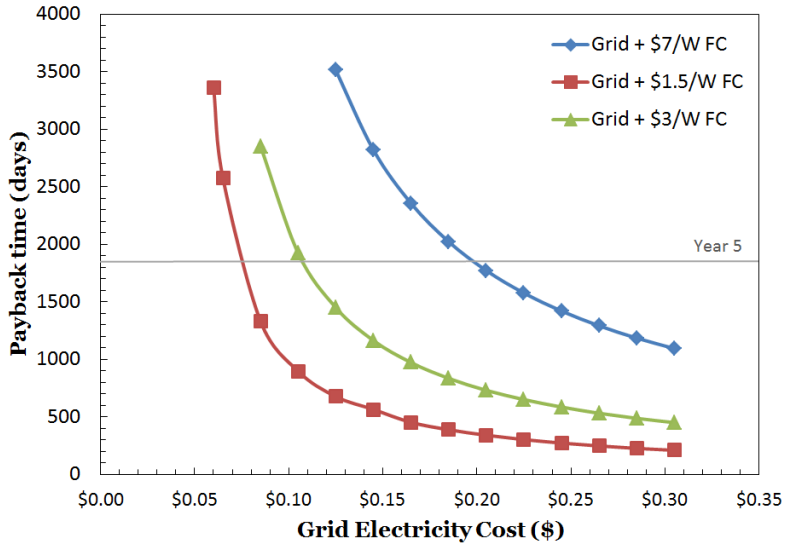

Figure A - 14 Payback period for ITFC/Grid emergency power solution for each ITFC system capital cost

For an ITFC/Grid system of 100kW, electricity cost of $0.20/kWh, and total fuel cell efficiency of 0.5 the payback period is 353 days, 756 days, and 1830 days for $1.5/W, $3/W, and $7/W system capital cost, respectively. The total accumulated cost savings (%) after 10 years for the $1.5/W, $3/W, and $7/W systems is 7.8%, 12.7%, 14.8%, respectively.

A.3.4 ITFC/Grid model cost analysis with variable fuel cell efficiency

The total ITFC capital cost calculated in this work includes the heat exchanger and accompanying components necessary for using the excess fuel cell heat for building space heating and service water. The total fuel cell efficiency depends on the amount of excess heat that can be used effectively in the CHP ITFC installation. On large campuses, the relatively small amount of heat generated by a 100kW ITFC system will not be price competitive with existing steam generation plants, however, there may be unique

applications for high quality ITFC heat. If a use for the excess heat can be found then the distributed ITFC total efficiency can reach >80%.

The payback period analysis for a range of ITFC total efficiencies have been calculated and plotted in Figure A-15. The payback period for each system has been calculated at three fixed grid electricity prices; $0.065/kWh (GT competitive price), $0.105/kWh and $0.145/kWh. The payback period decreases as ITFC total efficiency increases but has diminishing returns at efficiencies >60% when the cost of grid electricity is >$0.105/kWh. For example, the payback period for the $1.5/W ITFC changes by <200 days when total efficiency increases from 60% to 90% at $0.145/kWh grid electricity. However, the ITFC efficiency is critical for the case where grid electricity is $0.065/kWh. Only total efficiencies achievable using CHP will allow the ITFC to become economically viable.

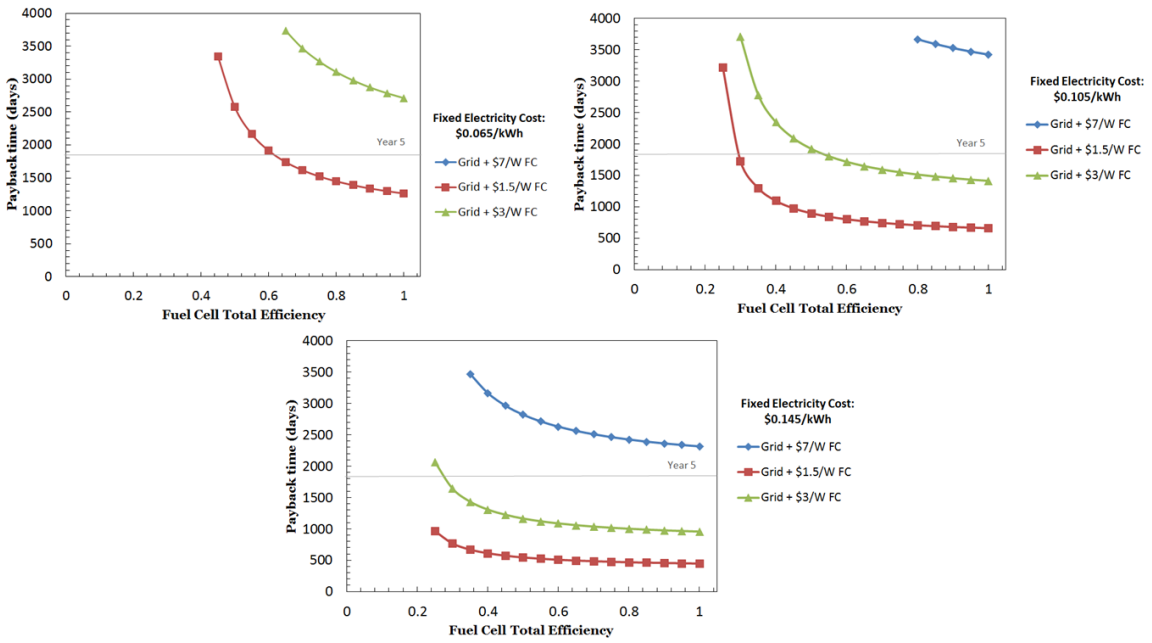

Figure A - 15 ITFC/Grid model payback periods as a function of fuel cell total efficiency at three fixed grid electricity prices

A.4 Conclusions

A preliminary cost analysis of an internal reforming SOFC with $Ni_{0.05}Ru_{0.05}Ce_{0.9}O_2$ catalyst and an ITFC (500^oC operation temperature) has been completed based on modifying the existing baseline 819^oC SOFC manufacturing capital costs put forward in the 2012 Strategic Analysis Report.[173] It is concluded that based on current cost inputs, the internal reforming strategy is most successful for fuel cell systems of small size (<5kW). Further investigation into the catalyst loading, composition, and application will be investigated to reduce the internal reforming catalyst cost. The effect of reducing the fuel cell operating temperature by >300^oC in the ITFC is dramatic, achieving >22% total capital cost reduction for the 100kW system. Fast ion conducting electrolytes must be developed to realize dramatic SOFC capital cost reduction at low temperatures while maintaining high performance.

A techno-economic analysis of the ITFC operating at 500^oC combined with grid electricity to provide emergency power and low cost baseload power was completed. In comparison to the existing REG/Grid emergency power model, the payback periods for the ITFC/Grid system were calculated as a function of fuel cell capital cost ($1.5/W, $3/W, $7/w) grid electricity cost ($0.065 - $0.30), and fuel cell total efficiency (25% - 100%). Payback periods decreased significantly as fuel cell capital costs decreased and grid electricity cost increased. Fuel total efficiency had a significant impact for low grid electricity costs but small effects on payback period at high grid electricity prices.

For a large hospital or university campus in the Southeast US, where emergency power is vitally necessary, the ITFC/Grid emergency power model is only economically viable when fuel cell capital costs reach $1.5/W or when fuel cell efficiency is >60%.

Boosting fuel cell efficiency by using waste heat from the fuel cell is not cost competitive with steam generation plants that currently exist on these campuses to provide space heating and water service. Unique implementations of the fuel cell excess heat are necessary to boost fuel cell total efficiency over 50%.

References

1. Obama, B. (2011). Remarks By the President on America's Energy Security (Georgetown University, Washington D.C., The White House).

2. Funke, K. (2013). Solid State Ionics: from Michael Faraday to green energy-the European dimension. *Sci Technol Adv Mater 14*, 50. 10.1088/1468-6996/14/4/043502

3. Palomares, V., Serras, P., Villaluenga, I., Hueso, K.B., Carretero-Gonzalez, J., and Rojo, T. (2012). Na-ion batteries, recent advances and present challenges to become low cost energy storage systems. *Energy & Environmental Science 5*, 5884-5901. 10.1039/c2ee02781j

4. Bates, J.B., Dudney, N.J., Lubben, D.C., Gruzalski, G.R., Kwak, B.S., Yu, X., and Zuhr, R.A. (1995). Thin-film rechargeable lithium batteries. *Journal of Power Sources 54*, 58-62. 10.1016/0378-7753(94)02040-A

5. Kreuer, K.D. (2003). Proton-conducting oxides. *Annual Review of Materials Research 33*, 333-359. 10.1146/annurev.matsci.33.022802.091825

6. Minh, N.Q. (1993). Ceramic Fuel-Cells. *Journal of the American Ceramic Society 76*, 563-588. 10.1111/j.1151-2916.1993.tb03645.x

7. Allen, P.C., and Lazarus, D. (1978). Effect of pressure on ionic conductivity in rubidium silver iodide and silver iodide. *Physical Review B 17*, 1913.

8. Rainwater, B.H. (2012). Electrical properties of BaZr0. 1Ce0. 7Y0. 1Yb0. 1O3-δ and its application in intermediate temperature solid oxide fuel cells. In School of Materials Science and Engineering (Atlanta, GA, Georgia Institute of Technology).

9. Fergus, J.W. (2006). Electrolytes for solid oxide fuel cells. *Journal of Power Sources 162*, 30-40. http://dx.doi.org/10.1016/j.jpowsour.2006.06.062

10. Iwahara, H. (1995). Technological challenges in the application of proton conducting ceramics. *Solid State Ionics 77*, 289-298. http://dx.doi.org/10.1016/0167-2738(95)00051-7

11. Yang, L., Choi, Y., Qin, W., Chen, H., Blinn, K., Liu, M., Liu, P., Bai, J., Tyson, T.A., and Liu, M. (2011). Promotion of water-mediated carbon removal by nanostructured barium oxide/nickel interfaces in solid oxide fuel cells. *Nat Commun 2*, 357. http://www.nature.com/ncomms/journal/v2/n6/suppinfo/ncomms1359_S1.html

12. Yang, L., Wang, S., Blinn, K., Liu, M., Liu, Z., Cheng, Z., and Liu, M. (2009). Enhanced sulfur and coking tolerance of a mixed ion conductor for SOFCs: BaZr0. 1Ce0. 7Y0. 2–xYbxO3–δ. *Science 326*, 126-129.

13. Kim, S., Hirayama, M., Taminato, S., and Kanno, R. (2013). Epitaxial growth and lithium ion conductivity of lithium-oxide garnet for an all solid-state battery electrolyte. *Dalton Transactions 42*, 13112-13117. 10.1039/C3DT51795K

14. Knauth, P. (2009). Inorganic solid Li ion conductors: An overview. *Solid State Ionics 180*, 911-916. 10.1016/j.ssi.2009.03.022

15. Thangadurai, V., and Weppner, W. (2005). Li6ALa2Nb2O12 (A= Ca, Sr, Ba): A New Class of Fast Lithium Ion Conductors with Garnet-Like Structure. *Journal of the American Ceramic Society 88*, 411-418. 10.1111/j.1551-2916.2005.00060.x

16. Belous, A., Novitskaya, G., Polyanetskaya, S., and Gornikov, Y.I. (1987). Properties of Ln2/3− xM3xTiO3 (Ln= Gd–Lu; M= Li, Na, K) Oxides. *Izv Akad Nauk SSSR, Neorg Mater 23*, 1330-1332.

17. LIN, Z. (1986). Phase Relationship and Electrical Conductivity of Li1+ XTi2-XGaXP3O12 and Li1+2XTi2-XMGXP3O12 Systems. *J CHIN SILIC SOC J Chin Silic Soc 14*, 23.

18. Cretin, M., and Fabry, P. (1999). Comparative study of lithium ion conductors in the system Li1+ xAlxA2-xIV (PO4) 3 with AIV. *Journal of the European Ceramic Society 19*, 2931-2940. 10.1016/S0955-2219(99)00055-2

19. Pradel, A., and Ribes, M. (1986). Electrical properties of lithium conductive silicon sulfide glasses prepared by twin roller quenching. *Solid State Ionics 18*, 351-355. 10.1016/0167-2738(86)90139-6

20. Bates, J., Dudney, N., Gruzalski, G., Zuhr, R., Choudhury, A., Luck, C., and Robertson, J. (1992). Electrical properties of amorphous lithium electrolyte thin films. *Solid State Ionics 53*, 647-654. 10.1016/0167-2738(92)90442-R

21. Thangadurai, V., Kaack, H., and Weppner, W.J. (2003). Novel Fast Lithium Ion Conduction in Garnet-Type Li5La3M2O12 (M= Nb, Ta). *Journal of the American Ceramic Society 86*, 437-440.

22. Murugan, R., Thangadurai, V., and Weppner, W. (2007). Fast Lithium Ion Conduction in Garnet-Type Li7La3Zr2O12. *Angewandte Chemie International Edition 46*, 7778-7781.

23. Geiger, C.A., Alekseev, E., Lazic, B., Fisch, M., Armbruster, T., Langner, R., Fechtelkord, M., Kim, N., Pettke, T., and Weppner, W. (2010). Crystal chemistry and stability of "Li7La3Zr2O12" garnet: a fast lithium-ion conductor. *Inorganic chemistry 50*, 1089-1097.

24. Cussen, E.J. (2006). The structure of lithium garnets: cation disorder and clustering in a new family of fast Li+ conductors. *Chemical communications*, 412-413.

25. Buschmann, H., Dölle, J., Berendts, S., Kuhn, A., Bottke, P., Wilkening, M., Heitjans, P., Senyshyn, A., Ehrenberg, H., and Lotnyk, A. (2011). Structure and dynamics of the fast lithium ion conductor "Li7La3Zr2O12". *Physical Chemistry Chemical Physics 13*, 19378-19392.

26. Kotobuki, M., Munakata, H., Kanamura, K., Sato, Y., and Yoshida, T. (2010). Compatibility of Li7La3Zr2O12 solid electrolyte to all-solid-state battery using Li metal anode. *J Electrochem Soc 157*, A1076-A1079.

27. Xie, H., Alonso, J.A., Li, Y., Fernández-Díaz, M.T., and Goodenough, J.B. (2011). Lithium Distribution in Aluminum-Free Cubic Li7La3Zr2O12. *Chemistry of Materials 23*, 3587-3589.

28. Takada, K. (2013). Progress and prospective of solid-state lithium batteries. *Acta Materialia 61*, 759-770.

29. Shimonishi, Y., Toda, A., Zhang, T., Hirano, A., Imanishi, N., Yamamoto, O., and Takeda, Y. (2011). Synthesis of garnet-type Li7− xLa3Zr2O12− 1/2x and its stability in aqueous solutions. *Solid State Ionics 183*, 48-53.

30. Thangadurai, V., and Weppner, W. (2005). Li6ALa2Ta2O12 (A= Sr, Ba): Novel Garnet-Like Oxides for Fast Lithium Ion Conduction. *Advanced Functional Materials 15*, 107-112.

31. Thangadurai, V., and Weppner, W. (2005). Investigations on electrical conductivity and chemical compatibility between fast lithium ion conducting garnet-like Li6BaLa2Ta2O12 and lithium battery cathodes. *Journal of Power Sources 142*, 339-344.

32. Wang, Y., and Lai, W. (2012). High Ionic Conductivity Lithium Garnet Oxides of Li7− xLa3Zr2− xTaxO12 Compositions. *Electrochemical and Solid-State Letters 15*, A68-A71.

33. Fuller, T.F., and Harb, J. (2015). Electrochemical Engineering, pp. 6, Chapter 9.

34. Korte, C., Peters, A., Janek, J., Hesse, D., and Zakharov, N. (2008). Ionic conductivity and activation energy for oxygen ion transport in superlattices—the semicoherent multilayer system YSZ (ZrO 2+ 9.5 mol% Y 2 O 3)/Y 2 O 3. *Physical Chemistry Chemical Physics 10*, 4623-4635.

35. Korte, C., Schichtel, N., Hesse, D., and Janek, J. (2009). Influence of interface structure on mass transport in phase boundaries between different ionic materials. *Monatshefte für Chemie-Chemical Monthly 140*, 1069-1080. 10.1007/s00706-009-0125-7

36. Kosacki, I., Rouleau, C.M., Becher, P.F., Bentley, J., and Lowndes, D.H. (2004). Surface/interface-related conductivity in nanometer thick YSZ films. *Electrochemical and solid-state letters 7*, A459-A461.

37. Kosacki, I., Rouleau, C.M., Becher, P.F., Bentley, J., and Lowndes, D.H. (2005). Nanoscale effects on the ionic conductivity in highly textured YSZ thin films. *Solid State Ionics 176*, 1319-1326. http://dx.doi.org/10.1016/j.ssi.2005.02.021

38. Li, B., Zhang, J., Kaspar, T., Shutthanandan, V., Ewing, R.C., and Lian, J. (2013). Multilayered YSZ/GZO films with greatly enhanced ionic conduction for low temperature solid oxide fuel cells. *Physical Chemistry Chemical Physics 15*, 1296-1301.

39. Pergolesi, D., Fabbri, E., Cook, S.N., Roddatis, V., Traversa, E., and Kilner, J.A. (2012). Tensile Lattice Distortion Does Not Affect Oxygen Transport in Yttria-Stabilized Zirconia-CeO2 Heterointerfaces. *ACS Nano 6*, 10524-10534. 10.1021/nn302812m

40. Peters, A., Korte, C., Hesse, D., Zakharov, N., and Janek, J. (2007). Ionic conductivity and activation energy for oxygen ion transport in superlattices—The multilayer system CSZ (ZrO2/CaO)/Al2O3. *Solid State Ionics 178*, 67-76.

41. Rushton, M.J.D., and Chroneos, A. (2014). Impact of uniaxial strain and doping on oxygen diffusion in CeO2. *Scientific Reports 4*, 6068. 10.1038/srep06068

42. Yang, F., Zhao, X.F., and Xiao, P. (2010). Electrical properties of YSZ/Al2O3 composite and YSZ/Al2O3 interface studied by impedance spectroscopy and finite element modelling. *Solid State Ionics 181*, 783-789. 10.1016/j.ssi.2010.04.036

43. Kant, K.M., Esposito, V., and Pryds, N. (2012). Strain induced ionic conductivity enhancement in epitaxial Ce0. 9Gd0. 1O2− δ thin films. *Applied Physics Letters 100*, 033105.

44. Foster, L.E. (2005). Nanotechnology: Science, Innovation, and Opportunity (Prentice Hall PTR).

45. Li, X., Lin, Y., Chen, H., and Roco, M.C. (2007). Worldwide nanotechnology development: a comparative study of USPTO, EPO, and JPO patents (1976–2004). *Journal of Nanoparticle Research 9*, 977-1002.

46. Ju, Y.S., and Goodson, K.E. (1999). Phonon scattering in silicon films with thickness of order 100 nm. *Applied Physics Letters 74*, 3005-3007. doi:http://dx.doi.org/10.1063/1.123994

47. Nath, P., and Chopra, K.L. (1974). Thermal conductivity of copper films. *Thin Solid Films 20*, 53-62. http://dx.doi.org/10.1016/0040-6090(74)90033-9

48. Yu, X.Y., Chen, G., Verma, A., and Smith, J.S. (1995). Temperature dependence of thermophysical properties of GaAs/AlAs periodic structure. *Applied Physics Letters 67*, 3554-3556. doi:http://dx.doi.org/10.1063/1.114919

49. Huijben, M., Brinkman, A., Koster, G., Rijnders, G., Hilgenkamp, H., and Blank, D.H.A. (2009). Structure-Property Relation of SrTiO3/LaAlO3 Interfaces. *Advanced Materials 21*, 1665-1677. 10.1002/adma.200801448

50. Ohtomo, A., and Hwang, H.Y. (2004). A high-mobility electron gas at the LaAlO3/SrTiO3 heterointerface. *Nature 427,* 423-426.

51. Bolotin, K.I., Sikes, K.J., Jiang, Z., Klima, M., Fudenberg, G., Hone, J., Kim, P., and Stormer, H.L. (2008). Ultrahigh electron mobility in suspended graphene. *Solid State Communications 146,* 351-355. http://dx.doi.org/10.1016/j.ssc.2008.02.024

52. Despotuli, A., Andreeva, A., and Rambabu, B. (2005). Nanoionics of advanced superionic conductors. *Ionics 11,* 306-314. 10.1007/BF02430394

53. Maier, J. (2002). Nano-sized mixed conductors (Aspects of nano-ionics. Part III). *Solid State Ionics 148,* 367-374. http://dx.doi.org/10.1016/S0167-2738(02)00075-9

54. Maier, J. (2002). Thermodynamic aspects and morphology of nano-structured ion conductors: Aspects of nano-ionics Part I. *Solid State Ionics 154,* 291-301.

55. Maier, J. (2003). Defect chemistry and ion transport in nanostructured materials: Part II. Aspects of nanoionics. *Solid State Ionics 157*, 327-334. http://dx.doi.org/10.1016/S0167-2738(02)00229-1

56. Tuller, H.L. (2000). Ionic conduction in nanocrystalline materials. *Solid State Ionics 131,* 143-157.

57. Maier, J. (2014). Pushing Nanoionics to the Limits: Charge Carrier Chemistry in Extremely Small Systems. *Chemistry of Materials 26*, 348-360. 10.1021/cm4021657

58. Liang, C.C. (1973). CONDUCTION CHARACTERISTICS OF LITHIUM IODIDE ALUMINUM OXIDE SOLID ELECTROLYTES. *J Electrochem Soc 120,* 1289-1292. 10.1149/1.2403248

59. Wagner Jr, J.B. (1980). Transport in compounds containing a dispersed second phase. *Materials Research Bulletin 15*, 1691-1701. http://dx.doi.org/10.1016/0025-5408(80)90187-7

60. Shahi, K., and Wagner Jr, J. (1982). Enhanced ionic conduction in dispersed solid electrolyte systems (DSES) and/or multiphase systems: Agl Al2O3, Agl SiO2, Agl Fly ash, and Agl AgBr. *Journal of Solid State Chemistry 42,* 107-119. 10.1016/0022-4596(82)90256-0

61. Maier, J. (1984). Enhancement of the ionic conductivity in solid-solid dispersions by surface induced defects. *Ber Bunsen-Ges Phys Chem Chem Phys 88,* 1057-1062.

62. Maier, J. (1985). SPACE-CHARGE REGIONS IN SOLID 2 PHASE SYSTEMS AND THEIR CONDUCTION CONTRIBUTION .2. CONTACT EQUILIBRIUM AT THE INTERFACE OF 2 IONIC CONDUCTORS AND THE RELATED CONDUCTIVITY EFFECT. *Ber Bunsen-Ges Phys Chem Chem Phys 89,* 355-362.

63. Maier, J. (1985). Space charge regions in solid two-phase systems and their conduction contribution—I. Conductance enhancement in the system ionic conductor-'inert' phase and application on AgC1:Al2O3 and AgC1:SiO2. *Journal of Physics and Chemistry of Solids 46*, 309-320. http://dx.doi.org/10.1016/0022-3697(85)90172-6

64. Maier, J. (1987). Composite electrolytes. *Materials chemistry and physics 17*, 485-498. 10.1016/0254-0584(87)90098-8

65. Maier, J. (1987). Defect chemistry and ionic conductivity in thin films. *Solid State Ionics 23*, 59-67. http://dx.doi.org/10.1016/0167-2738(87)90082-8

66. Maier, J. (1987). DEFECT CHEMISTRY AND CONDUCTIVITY EFFECTS IN HETEROGENEOUS SOLID ELECTROLYTES. *J Electrochem Soc 134*, 1524-1535. 10.1149/1.2100703

67. Maier, J. (1988). On the electronic conductivity of composite electrolytes. *Solid State Ionics 28–30, Part 2*, 1073-1077. http://dx.doi.org/10.1016/0167-2738(88)90333-5

68. Maier, J. (1989). SPACE-CHARGE REGIONS IN SOLID 2 PHASE SYSTEMS AND THEIR CONDUCTION CONTRIBUTION .4. THE BEHAVIOR OF MINORITY CHARGE-CARRIERS .A. CONCENTRATION PROFILES, CONDUCTIVITY CONTRIBUTION, DETERMINATION BY GENERALIZED WAGNER-HEBB-PROCEDURE. *Ber Bunsen-Ges Phys Chem Chem Phys 93*, 1468-1473.

69. Dudney, N.J. (1985). EFFECT OF INTERFACIAL SPACE-CHARGE POLARIZATION ON THE IONIC-CONDUCTIVITY OF COMPOSITE ELECTROLYTES. *Journal of the American Ceramic Society 68*, 538-545. 10.1111/j.1151-2916.1985.tb11520.x

70. Wang, J.C., and Dudney, N.J. (1986). Model for the composition dependence of conductivity of an ionic conductor containing submicron particles of an insulator. *Solid State Ionics 18–19, Part 1*, 112-116. http://dx.doi.org/10.1016/0167-2738(86)90096-2

71. Dudney, N.J. (1988). Enhanced ionic conductivity in composite electrolytes. *Solid State Ionics 28*, 1065-1072. http://dx.doi.org/10.1016/0167-2738(88)90332-3

72. Nakamura, O., and Goodenough, J.B. (1982). Conductivity enhancement of lithium bromide monohydrate by Al2O3 particles. *Solid State Ionics 7*, 119-123. http://dx.doi.org/10.1016/0167-2738(82)90004-2

73. Shukla, A.K., Manoharan, R., and Goodenough, J.B. (1988). Enhancement of ionic conductivity by dispersed oxide inclusions: Influence of oxide isoelectric point and cation size. *Solid State Ionics 26*, 5-10. http://dx.doi.org/10.1016/0167-2738(88)90238-X

74. Maier, J. (2009). Nanoionics: ionic charge carriers in small systems. *Physical Chemistry Chemical Physics 11*, 3011-3022. 10.1039/B902586N

75. Leonhardt, M., Jamnik, J., and Maier, J. (1999). In situ monitoring and quantitative analysis of oxygen diffusion through schottky-barriers in SrTiO3 bicrystals. *Electrochemical and solid-state letters 2*, 333-335.

76. Sayle, T., Parker, S., and Catlow, C. (1994). The role of oxygen vacancies on ceria surfaces in the oxidation of carbon monoxide. *Surface Science 316*, 329-336.

77. Korte, C., Keppner, J., Peters, A., Schichtel, N., Aydin, H., and Janek, J. (2014). Coherency strain and its effect on ionic conductivity and diffusion in solid electrolytes - an improved model for nanocrystalline thin films and a review of experimental data. *Physical Chemistry Chemical Physics 16*, 24575-24591. 10.1039/c4cp03055a

78. Korte, C., Peters, A., Janek, J., Hesse, D., and Zakharov, N. (2008). Ionic conductivity and activation energy for oxygen ion transport in superlattices - The semicoherent multilayer system YSZ (ZrO2 + 9.5 mol% Y2O3)/Y2O3. *Physical Chemistry Chemical Physics 10*, 4623-4635.

79. Korte, C., Schichtel, N., Hesse, D., and Janek, J. (2009). Influence of interface structure on mass transport in phase boundaries between different ionic materials : EExperimental studies and formal considerations. *Monatshefte fur Chemie 140*, 1069-1080.

80. Garcia-Barriocanal, J., Rivera-Calzada, A., Varela, M., Sefrioui, Z., Iborra, E., Leon, C., Pennycook, S.J., and Santamaria, J. (2008). Colossal ionic conductivity at interfaces of epitaxial ZrO2: Y2O3/SrTiO3 heterostructures. *Science 321*, 676-680.

81. Tuller, H.L., and Bishop, S.R. (2011). Point defects in oxides: tailoring materials through defect engineering. *Annual Review of Materials Research 41*, 369-398.

82. De Souza, R.A., Ramadan, A., and Hörner, S. (2012). Modifying the barriers for oxygen-vacancy migration in fluorite-structured CeO 2 electrolytes through strain: a computer simulation study. *Energy & Environmental Science 5*, 5445-5453.

83. Buffat, P., and Borel, J. (1976). Melting of Gold Clusters. *Phys Rev A 13*, 2287.

84. Villain, S., Knauth, P., and Schwitzgebel, G. (1997). Electrodeposition of Nanocrystalline Silver: Study of Grain Growth by Measurement of Reversible Electromotive Force. *The Journal of Physical Chemistry B 101*, 7452-7454.

85. Gräf, C.P., Heim, U., and Schwitzgebel, G. (2000). Potentiometrical investigations of nanocrystalline copper. *Solid State Ionics 131*, 165-174. http://dx.doi.org/10.1016/S0167-2738(00)00631-7

86. Gerhardt, R., Nowick, A.S., Mochel, M.E., and Dumler, I. (1986). Grain-Boundary Effect in Ceria Doped with Trivalent Cations: II, Microstructure and Microanalysis. *Journal of the American Ceramic Society 69*, 647-651. 10.1111/j.1151-2916.1986.tb07465.x

87. Gerhardt, R., and Nowick, A.S. (1986). Grain-Boundary Effect in Ceria Doped with Trivalent Cations: I, Electrical Measurements. *Journal of the American Ceramic Society 69*, 641-646. 10.1111/j.1151-2916.1986.tb07464.x

88. Tuller, H., and Nowick, A. (1979). Defect structure and electrical properties of nonstoichiometric CeO2 single crystals. *J Electrochem Soc 126*, 209-217.

89. Huang, K., Feng, M., and Goodenough, J.B. (1998). Synthesis and electrical properties of dense Ce0. 9Gd0. 1O1. 95 ceramics. *Journal of the American Ceramic Society 81*, 357-362.

90. Wang, S., Kobayashi, T., Dokiya, M., and Hashimoto, T. (2000). Electrical and Ionic Conductivity of Gd-Doped Ceria. *J Electrochem Soc 147*, 3606-3609.

91. Omar, S., Wachsman, E.D., Jones, J.L., and Nino, J.C. (2009). Crystal structure–ionic conductivity relationships in doped ceria systems. *Journal of the American Ceramic Society 92*, 2674-2681.

92. Jung, G.-B., Huang, T.-J., and Chang, C.-L. (2002). Effect of temperature and dopant concentration on the conductivity of samaria-doped ceria electrolyte. *Journal of Solid State Electrochemistry 6*, 225-230.

93. Tschöpe, A., Sommer, E., and Birringer, R. (2001). Grain size-dependent electrical conductivity of polycrystalline cerium oxide: I. Experiments. *Solid State Ionics 139*, 255-265.

94. Souza, E., Chueh, W., Jung, W., Muccillo, E., and Haile, S. (2012). Ionic and electronic conductivity of nanostructured, samaria-doped ceria. *J Electrochem Soc 159*, K127-K135.

95. Anselmi-Tamburini, U., Maglia, F., Chiodelli, G., Tacca, A., Spinolo, G., Riello, P., Bucella, S., and Munir, Z.A. (2006). Nanoscale effects on the ionic conductivity of highly doped bulk nanometric cerium oxide. *Advanced Functional Materials 16*, 2363-2368.

96. Shirpour, M., Gregori, G., Merkle, R., and Maier, J. (2011). On the proton conductivity in pure and gadolinium doped nanocrystalline cerium oxide. *Physical Chemistry Chemical Physics 13*, 937-940.

97. Bellino, M.G., Lamas, D.G., and Walsöe de Reca, N.E. (2006). Enhanced Ionic Conductivity in Nanostructured, Heavily Doped Ceria Ceramics. *Advanced Functional Materials 16*, 107-113. 10.1002/adfm.200500186

98. Kim, S., and Maier, J. (2004). Partial electronic and ionic conduction in nanocrystalline ceria: role of space charge. *Journal of the European Ceramic Society 24*, 1919-1923. http://dx.doi.org/10.1016/S0955-2219(03)00525-9

99. Kim, S., and Maier, J. (2002). On the conductivity mechanism of nanocrystalline ceria. *J Electrochem Soc 149*, J73-J83.

100. Blom, D.A., and Chiang, Y.-M. (1996). Interfacial Segregation in Ionic Conductors: Ceria. *MRS Online Proceedings Library Archive 458*, null-null. doi:10.1557/PROC-458-127

101. Guo, X., Sigle, W., and Maier, J. (2003). Blocking Grain Boundaries in Yttria-Doped and Undoped Ceria Ceramics of High Purity. *Journal of the American Ceramic Society 86*, 77-87.

102. Chen, I.W., and Wang, X.H. (2000). Sintering dense nanocrystalline ceramics without final-stage grain growth. *Nature 404*, 168-171. 10.1038/35004548

103. Souza, E., Chueh, W., Muccillo, E., and Haile, S. (2010). Ionic and Electronic Conductivity of Nanometer Sized Samaria-Doped Ceria Ceramics. Paper presented at: Meeting Abstracts (The Electrochemical Society).

104. Liao, S.C., Chen, Y.J., Kear, B.H., and Mayo, W.E. (1998). High pressure/low temperature sintering of nanocrystalline alumina. *Nanostructured Materials 10*, 1063-1079. http://dx.doi.org/10.1016/S0965-9773(98)00125-1

105. Clark, D.E., Folz, D.C., and West, J.K. (2000). Processing materials with microwave energy. *Materials Science and Engineering: A 287*, 153-158. http://dx.doi.org/10.1016/S0921-5093(00)00768-1

106. Kim, H.N., Kim, D.K., and Chang, S.N. (2008). Shock compaction of Gd-doped ceria ceramics. *International Journal of Modern Physics B 22*, 1686-1691. 10.1142/s0217979208047262

107. Maglia, F., Tredici, I.G., and Anselmi-Tamburini, U. (2013). Densification and properties of bulk nanocrystalline functional ceramics with grain size below 50 nm. *Journal of the European Ceramic Society 33*, 1045-1066. http://dx.doi.org/10.1016/j.jeurceramsoc.2012.12.004

108. Fredenburg, D.A., Koller, D.D., Coe, J.D., and Kiyanda, C.B. (2014). The influence of morphology on the low- and high-strain-rate compaction response of CeO2 powders. *Journal of Applied Physics 115*, 10. 10.1063/1.4868356

109. Fredenburg, D.A., Dennis-Koller, D., and Dattelbaum, D.M. (2012). SHOCK CONSOLIDATION RESPONSE OF CeO2 POWDERS. In Shock Compression of Condensed Matter - 2011, Pts 1 and 2, M.L. Elert, W.T. Buttler, J.P. Borg, J.L. Jordan, and T.J. Vogler, eds. (Melville, Amer Inst Physics). 10.1063/1.3686564

110. Dai, C., and Thadhani, N.N. (2011). Shock-compression response of magnetic Fe3O4 nanoparticles. *Acta Materialia 59*, 785-796. 10.1016/j.actamat.2010.10.022

111. Vogler, T.J., Lee, M.Y., and Grady, D.E. (2007). Static and dynamic compaction of ceramic powders. *Int J Solids Struct 44*, 636-658. 10.1016/j.ijsolstr.2006.05.001

112. Guo, X.X., and Maier, J. (2009). Ionically Conducting Two-Dimensional Heterostructures. *Advanced Materials 21*, 2619-2631. 10.1002/adma.200900412

113. Sata, N., Eberman, K., Eberl, K., and Maier, J. (2000). Mesoscopic fast ion conduction in nanometre-scale planar heterostructures. *Nature 408*, 946-949. 10.1038/35050047

114. Schichtel, N., Korte, C., Hesse, D., and Janek, J. (2009). Elastic strain at interfaces and its influence on ionic conductivity in nanoscaled solid electrolyte thin films—theoretical considerations and experimental studies. *Physical Chemistry Chemical Physics 11*, 3043-3048. 10.1039/B900148D

115. Chu, M., Sun, Y., Aghoram, U., and Thompson, S.E. (2009). Strain: a solution for higher carrier mobility in nanoscale MOSFETs. *Annual Review of Materials Research 39*, 203-229.

116. Sanna, S., Esposito, V., Tebano, A., Licoccia, S., Traversa, E., and Balestrino, G. (2010). Enhancement of Ionic Conductivity in Sm-Doped Ceria/Yttria-Stabilized Zirconia Heteroepitaxial Structures. *Small 6*, 1863-1867.

117. Peters, A., Korte, C., Hesse, D., Zakharov, N., and Janek, J. (2007). Ionic conductivity and activation energy for oxygen ion transport in superlattices — The multilayer system CSZ (ZrO2+CaO)/Al2O3. *Solid State Ionics 178*, 67-76. http://dx.doi.org/10.1016/j.ssi.2006.12.004

118. Liu, M., Ding, D., Bai, Y., He, T., and Liu, M. (2012). An Efficient SOFC Based on Samaria-Doped Ceria (SDC) Electrolyte. *J Electrochem Soc 159*, B661.

119. MacManus-Driscoll, J.L., Zerrer, P., Wang, H., Yang, H., Yoon, J., Fouchet, A., Yu, R., Blamire, M.G., and Jia, Q. (2008). Strain control and spontaneous phase ordering in vertical nanocomposite heteroepitaxial thin films. *Nature materials 7*, 314-320.

120. Su, Q., Yoon, D., Chen, A., Khatkhatay, F., Manthiram, A., and Wang, H. (2013). Vertically aligned nanocomposite electrolytes with superior out-of-plane ionic conductivity for solid oxide fuel cells. *Journal of Power Sources 242*, 455-463.

121. Su, Q., Yoon, D., Sisman, Z., Khatkhatay, F., Jia, Q., Manthiram, A., and Wang, H. (2013). Vertically aligned nanocomposite La0. 8Sr0. 2MnO3-δ/Zr0. 92Y0. 08O1. 96 thin films as electrode/electrolyte interfacial layer for solid oxide reversible fuel cells. *International journal of hydrogen energy 38*, 16320-16327.

122. Yoon, J., Cho, S., Kim, J.-H., Lee, J., Bi, Z., Serquis, A., Zhang, X., Manthiram, A., and Wang, H. (2009). Vertically Aligned Nanocomposite Thin Films as a Cathode/Electrolyte Interface Layer for Thin-Film Solid Oxide Fuel Cells. *Advanced Functional Materials 19*, 3868-3873. 10.1002/adfm.200901338

123. Zhang, W., Chen, A., Bi, Z., Jia, Q., MacManus-Driscoll, J.L., and Wang, H. (2014). Interfacial coupling in heteroepitaxial vertically aligned nanocomposite thin films: From lateral to vertical control. *Current Opinion in Solid State and Materials Science 18*, 6-18.

124. Zhang, W., Jian, J., Chen, A., Jiao, L., Khatkhatay, F., Li, L., Chu, F., Jia, Q., MacManus-Driscoll, J.L., and Wang, H. (2014). Strain relaxation and enhanced perpendicular magnetic anisotropy in BiFeO3: CoFe2O4 vertically aligned nanocomposite thin films. *Applied Physics Letters 104*, 062402.

125. Speakman, S.A. (2012). Introduction to High Resolution X-Ray Diffraction of Epitaxial Thin Films (MIT LL).

126. Kim, H.-R., Kim, J.-C., Lee, K.-R., Ji, H.-I., Lee, H.-W., Lee, J.-H., and Son, J.-W. (2011). 'Illusional'nano-size effect due to artifacts of in-plane conductivity measurements of ultra-thin films. *Physical Chemistry Chemical Physics 13*, 6133-6137.

127. Sanna, S., Esposito, V., Pergolesi, D., Orsini, A., Tebano, A., Licoccia, S., Balestrino, G., and Traversa, E. (2009). Fabrication and Electrochemical Properties of Epitaxial Samarium-Doped Ceria Films on SrTiO3-Buffered MgO Substrates. *Advanced Functional Materials 19*, 1713-1719.

128. Rainwater, B.H. (2012). Electrical properties of BaZr0.1Ce0.7Y0.1Yb0.1O3-δ and its application in intermediate temperature solid oxide fuel cells.

129. Iguchi, F., Sata, N., Tsurui, T., and Yugami, H. (2007). Microstructures and grain boundary conductivity of BaZr1−xYxO3 (x = 0.05, 0.10, 0.15) ceramics. *Solid State Ionics 178*, 691-695. http://dx.doi.org/10.1016/j.ssi.2007.02.019

130. Yang, S.M., Lee, S., Jian, J., Zhang, W., Lu, P., Jia, Q., Wang, H., Noh, T.W., Kalinin, S.V., and MacManus-Driscoll, J.L. (2015). Strongly enhanced oxygen ion transport through samarium-doped CeO2 nanopillars in nanocomposite films. *Nature communications 6*.

131. Marrocchelli, D., Sun, L., and Yildiz, B. (2015). Dislocations in SrTiO3: easy to reduce but not so fast for oxygen transport. *Journal of the American Chemical Society 137*, 4735-4748.

132. Yang, N., Cantoni, C., Foglietti, V., Tebano, A., Belianinov, A., Strelcov, E., Jesse, S., Di Castro, D., Di Bartolomeo, E., and Licoccia, S. (2015). Defective interfaces in Yttrium-doped Barium Zirconate films and consequences on proton conduction. *Nano letters 15*, 2343-2349.

133. Sun, L., Marrocchelli, D., and Yildiz, B. (2015). Edge dislocation slows down oxide ion diffusion in doped CeO2 by segregation of charged defects. *Nature communications 6*.

134. Laio, A., Bernard, S., Chiarotti, G.L., Scandolo, S., and Tosatti, E. (2000). Physics of iron at Earth's core conditions. *Science 287*, 1027-1030. 10.1126/science.287.5455.1027

135. Kingma, K.J., Meade, C., Hemley, R.J., Mao, H.K., and Veblen, D.R. (1993). MICROSTRUCTURAL OBSERVATIONS OF ALPHA-QUARTZ AMORPHIZATION. *Science 259*, 666-669.

136. Hemley, R.J., Mao, H.K., Shen, G.Y., Badro, J., Gillet, P., Hanfland, M., and Hausermann, D. (1997). X-ray imaging of stress and strain of diamond, iron, and tungsten at megabar pressures. *Science 276*, 1242-1245. 10.1126/science.276.5316.1242

137. Funamori, N., and Jeanloz, R. (1997). High-pressure transformation of Al2O3. *Science 278*, 1109-1111. 10.1126/science.278.5340.1109

138. Eremets, M.I., Shimizu, K., Kobayashi, T.C., and Amaya, K. (1998). Metallic CsI at Pressures of up to 220 Gigapascals. *Science 281*, 1333-1335. 10.1126/science.281.5381.1333

139. Han, Y., Gao, C., Ma, Y., Liu, H., Pan, Y., Luo, J., Li, M., He, C., Huang, X., Zou, G., Li, Y., Li, X., and Liu, J. (2005). Integrated microcircuit on a diamond anvil for high-pressure electrical resistivity measurement. *Applied Physics Letters 86*, 064104. doi:http://dx.doi.org/10.1063/1.1863444

140. He, C., Gao, C., Ma, Y., Li, M., Hao, A., Huang, X., Liu, B., Zhang, D., Yu, C., Zou, G., Li, Y., Li, H., Li, X., and Liu, J. (2007). In situ electrical impedance spectroscopy under high pressure on diamond anvil cell. *Applied Physics Letters 91*, 092124. doi:http://dx.doi.org/10.1063/1.2778760

141. Weir, S.T., Akella, J., Aracne-Ruddle, C., Vohra, Y.K., and Catledge, S.A. (2000). Epitaxial diamond encapsulation of metal microprobes for high pressure experiments. *Applied Physics Letters 77*, 3400-3402. doi:http://dx.doi.org/10.1063/1.1326838

142. Matsuoka, T., and Shimizu, K. (2009). Direct observation of a pressure-induced metal-to-semiconductor transition in lithium. *Nature 458*, 186-189. 10.1038/nature07827

143. Jayaraman, A. (1983). Diamond anvil cell and high-pressure physical investigations. *Reviews of Modern Physics 55*, 65.

144. Zhao, J., Liu, Z., Gordon, R.A., Takarabe, K., Reid, J., and Tse, J.S. (2015). Pressure-induced phase transition and electrical properties of thermoelectric Al-doped Mg2Si. *Journal of Applied Physics 118*, 145902. doi:http://dx.doi.org/10.1063/1.4933069

145. Radzilowski, R.H., and Kummer, J.T. (1971). The Hydrostatic Pressure Dependence of the Ionic Conductivity of β-Aluminas. *J Electrochem Soc 118*, 714-716. 10.1149/1.2408152

146. Yoon, D., and Lazarus, D. (1972). Pressure dependence of ionic conductivity in KCl, NaCl, KBr, and NaBr. *Physical Review B 5*, 4935.

147. Hughes, H. (1955). The pressure effect on the electrical conductivity of peridot. *Journal of Geophysical Research 60*, 187-191.

148. Kafalas, J., and Cava, R. (1979). Effect of Pressure and Composition on Fast Na+ ion Transport in the System Na1+XZr2SiXP3-XO12. *Amsterdam Netherlands; Lake Geneva, WI USA: North-Holland Country of Publication: Netherlands*, 419-422.

149. Samara, G. (1984). High-pressure studies of ionic conductivity in solids. *Solid state physics 38*, 1-80.

150. M'Peko, J.-C., and de Souza, M.F. (2003). Ionic transport in polycrystalline zirconia and Frenkel's space-charge layer postulation. *Applied Physics Letters 83*, 737-739. doi:http://dx.doi.org/10.1063/1.1595729

151. Cammarata, R., Sieradzki, K., and Spaepen, F. (2000). Simple model for interface stresses with application to misfit dislocation generation in epitaxial thin films. *Journal of applied physics 87*, 1227-1234.

152. Wang, Y., Duncan, K., Wachsman, E.D., and Ebrahimi, F. (2007). The effect of oxygen vacancy concentration on the elastic modulus of fluorite-structured oxides. *Solid State Ionics 178*, 53-58. http://dx.doi.org/10.1016/j.ssi.2006.11.003

153. Burbano, M., Marrocchelli, D., Yildiz, B., Tuller, H.L., Norberg, S.T., Hull, S., Madden, P.A., and Watson, G.W. (2011). A dipole polarizable potential for reduced and doped CeO2 obtained from first principles. *Journal of Physics: Condensed Matter 23*, 255402.

154. Cussen, E.J. (2010). Structure and ionic conductivity in lithium garnets. *Journal of Materials Chemistry 20*, 5167-5173.

155. Cussen, E.J., Yip, T.W., O'Neill, G., and O'Callaghan, M.P. (2011). A comparison of the transport properties of lithium-stuffed garnets and the conventional phases Li3Ln3Te2O12. *Journal of Solid State Chemistry 184*, 470-475.

156. Logéat, A., Köhler, T., Eisele, U., Stiaszny, B., Harzer, A., Tovar, M., Senyshyn, A., Ehrenberg, H., and Kozinsky, B. (2012). From order to disorder: The structure of lithium-conducting garnets Li 7− x La 3 Ta x Zr 2− x O 12 (x= 0–2). *Solid State Ionics 206*, 33-38.

157. Murugan, R., Weppner, W., Schmid-Beurmann, P., and Thangadurai, V. (2008). Structure and lithium ion conductivity of garnet-like Li5La3Sb2O12 and Li6SrLa2Sb2O12. *Materials Research Bulletin 43*, 2579-2591.

158. O'Callaghan, M.P., Lynham, D.R., Cussen, E.J., and Chen, G.Z. (2006). Structure and ionic-transport properties of lithium-containing garnets Li(3)Ln(3)Te(2)O(12) (Ln = Y, Pr, Nd, Sm-Lu). *Chemistry of Materials 18*, 4681-4689. Doi 10.1021/Cm060992t

159. O'Callaghan, M.P., Powell, A.S., Titman, J.J., Chen, G.Z., and Cussen, E.J. (2008). Switching on Fast Lithium Ion Conductivity in Garnets: The Structure and Transport Properties of Li3+ x Nd3Te2− x Sb x O12. *Chemistry of Materials 20*, 2360-2369.

160. Hayashi, H., Sagawa, R., Inaba, H., and Kawamura, K. (2000). Molecular dynamics calculations on ceria-based solid electrolytes with different radius dopants. *Solid State Ionics 131*, 281-290. http://dx.doi.org/10.1016/S0167-2738(00)00675-5

161. Amsif, M., Marrero-Lopez, D., Ruiz-Morales, J., Savvin, S., Gabás, M., and Nunez, P. (2011). Influence of rare-earth doping on the microstructure and conductivity of BaCe 0.9 Ln 0.1 O 3− δ proton conductors. *Journal of Power Sources 196*, 3461-3469.

162. Velisavljevic, N., Chesnut, G.N., Vohra, Y.K., Weir, S.T., Malba, V., and Akella, J. (2002). Structural and electrical properties of beryllium metal to 66 GPa studied using designer diamond anvils. *Physical Review B 65*, 172107.

163. Park, C., Popov, D., Ikuta, D., Lin, C., Kenney-Benson, C., Rod, E., Bommananvar, A., and Shen, G. (2015). New developments in micro-X-ray diffraction and X-ray absorption spectroscopy for high-pressure research at 16-BM-D at the Advanced Photon Source. *Review of Scientific Instruments 86*, 072205.

164. Prescher, C., and Prakapenka, V.B. (2015). DIOPTAS: a program for reduction of two-dimensional X-ray diffraction data and data exploration. *High Pressure Research 35*, 223-230.

165. Rodriguez-Carvajal, J. (1993). FULLPROF 98. Program for Rietveld Pattern Matching Analysis of Powder Patterns, unspublished results, Grenoble, 1998.(b) Rodriguez-Carvajal, J. *Physica B 55*, 192.

166. Ni, J.E., Case, E.D., Sakamoto, J.S., Rangasamy, E., and Wolfenstine, J.B. (2012). Room temperature elastic moduli and Vickers hardness of hot-pressed LLZO cubic garnet. *J Mater Sci 47*, 7978-7985. 10.1007/s10853-012-6687-5

167. Klotz, S., Chervin, J.C., Munsch, P., and Marchand, G.L. (2009). Hydrostatic limits of 11 pressure transmitting media. *Journal of Physics D: Applied Physics 42*, 075413.

168. Wang, Q., He, D., Peng, F., Lei, L., Liu, P., Yin, S., Wang, P., Xu, C., and Liu, J. (2014). Unusual Compression Behavior of Nanocrystalline CeO2. *Scientific reports 4*.

169. Gerward, L., Staun Olsen, J., Petit, L., Vaitheeswaran, G., Kanchana, V., and Svane, A. (2005). Bulk modulus of CeO2 and PrO2—An experimental and theoretical

study. *Journal of Alloys and Compounds 400*, 56-61. http://dx.doi.org/10.1016/j.jallcom.2005.04.008

170. Jiang, Y., Adams, J.B., and van Schilfgaarde, M. (2005). Density-functional calculation of CeO2 surfaces and prediction of effects of oxygen partial pressure and temperature on stabilities. *The Journal of chemical physics 123*, 064701.

171. Duclos, S.J., Vohra, Y.K., Ruoff, A.L., Jayaraman, A., and Espinosa, G. (1988). High-pressure x-ray diffraction study of CeO 2 to 70 GPa and pressure-induced phase transformation from the fluorite structure. *Physical Review B 38*, 7755.

172. (2007). "The potential benefits of distributed generation and rate-related issues that may impede their expansion". *US Department of Energy*.

173. James, B.D., Spisak, A.B., and Colella, W.G. (2012). Manufacturing cost analysis of stationary fuel cell systems. *Strategic Analysis Inc Arlington VA, September*.